



SAPIENZA
UNIVERSITÀ DI ROMA

Department of Chemistry
and Technology of Drug

PhD in Pharmaceutical Sciences
XXXVII Cycle

Development of materials with increasing structural
complexity: from Chiral Stationary Phases to Covalent
Organic Polymers and Metal-Organic Frameworks

S.S.D. CHEM-05/A

Supervisor
Prof. Claudio Villani

Co-supervisor
Prof. Josep Puigmartí-Luis

Candidate
Maria Aurora Guarducci
1677290

Academic Year: 2023-2024

The Ph.D thesis was held at:

Department of Chemistry and Technology Drugs
Sapienza Università di Roma

Department of Physical Chemistry
Universitat de Barcelona

Table of contents

Abstract.....	11
---------------	----

Part A

Chapter 1

1. Chirality and its role in compounds of pharmacological interest.....	18
1.1 The chromatographic approach for the separation of chiral compounds....	20
1.2 Chiral Stationary Phases.....	23
1.3 Donor-acceptor phases: Brush-Type or Pirkle-Type CSPs.....	28
1.3.1 Main chiral stationary phases Pirkle-Type.....	34
1.4 From high performance Liquid Chromatography (HPLC) to Ultra High- Performance Liquid Chromatography (UHPLC).....	41
1.4.1 Application of Chiral Stationary Pirkle Phases in UHPLC.....	45
1.5 Whelk-O1 as chiral solvating agent at NMR.....	49
1.6 Inverted Chirality Column Approach (ICCA).....	56
1.7 Docking Studies for understanding enantioseparation.....	59
1.7.1 Molecular docking for donor-acceptor chiral selectors.....	62

Chapter 2

2. Objectives of this thesis in the field of CSPs.....	64
--	----

Chapter 3

3. Materials and Methods.....	66
3.1 Chemicals and Reagents.....	66
3.2 Instrumentation.....	66

3.3 Software.....	67
3.4 Synthesis of (<i>R,R</i>) and (<i>S,S</i>)-Sel1.....	68
3.4.1 Synthesis of 6-(allyloxy)-1-naphtoyl chloride.....	68
3.4.2 Synthesis of <i>N</i> -((1 <i>S</i> ,2 <i>S</i>)-2-aminocyclohexyl)-3,5-dinitrobenzamide.....	70
3.4.3 Synthesis of (<i>R,R</i>)- and (<i>S,S</i>)-Sel1.....	71
3.5 Synthesis of (<i>R,R</i>)- and (<i>S,S</i>)-Sel2.....	78
3.6 Immobilization on Silica.....	80
3.6.1 Characterization of (<i>S,S</i>)-CSP1 and (<i>S,S</i>)-CSP2.....	82
3.7 LC Packing Column.....	83
3.8 Molecular Docking.....	84

Chapter 4

4. Results and Discussion.....	85
4.1 Preliminary evaluation of chiral capabilities: NMR studies.....	85
4.2 HPLC enantioseparation.....	90
4.3 Molecular Docking results.....	92

Chapter 5

5. Conclusions and future perspectives.....	97
--	-----------

Chapter 6

6. References.....	99
---------------------------	-----------

Part B

Chapter 7

7. Introduction about different types of materials.....	110
7.1 Covalent Organic Polymers (COPs).....	111
7.2 Covalent Organic Frameworks (COFs).....	114
7.2.1 Synthetic methods.....	116
7.3 Conversion of a non-porous covalent organic polymer into a porous covalent organic framework.....	119
7.4 Catalysis.....	122
7.4.1 Heterogeneous catalysis.....	124
7.4.2 Development of Surface Organometallic Chemistry (SOMC).....	127
7.5 Role of copper in catalysis.....	129
7.5.1 Copper (I)-Catalysed Alkyne-Azide cycloaddition (CuAAC) “click” reaction.....	131
7.5.2 Application of triazoles.....	138
7.6 Potential toxicity of copper.....	143

Chapter 8

8. Objectives of this thesis in the COP field.....	145
--	-----

Chapter 9

9. Materials and Methods.....	147
9.1 Chemicals and Reagents.....	147
9.2 Instruments.....	147
9.3 Synthesis of COP.....	150
9.4 Synthesis of Cu ²⁺ @COP and Cu ⁺ @COP.....	151

9.5 Synthesis of 1,2,3-triazole (1-11) through homogeneous phase, Cu ²⁺ @COP, Cu ⁺ @COP.....	153
--	-----

Chapter 10

10. Results and Discussion.....	164
10.1 Characterization of the COP.....	164
10.2 Characterization of the Cu ²⁺ @COP and Cu ⁺ @COP.....	166
10.3 Catalytic application in CuAAC “click” reaction.....	172

Chapter 11

11. Conclusions and future perspectives.....	177
--	-----

Chapter 12

12. References.....	179
---------------------	-----

Part C

Chapter 13

13. Introduction to Metal Organic Frameworks (MOFs).....	189
13.1 Synthetic Approaches.....	193
13.2 Green approaches for the synthesis of MOFs.....	198
13.2.1 Metal precursors and organic and organic linkers for the synthesis of sustainable MOFs.....	203
13.3 Using a micellar approach as a novel sustainable MOF synthesis strategy.....	206
13.4 Applications.....	209
13.5 Cu-CAT-1.....	214
13.6 Mn-BTC.....	216

Chapter 14

14. Objectives of this thesis in the MOFs field.....	217
--	-----

Chapter 15

15. Materials and Methods.....	220
15.1 Chemical and reagents.....	220
15.2 Instruments.....	220
15.3 Synthesis of Cu-CAT-1 nanoparticles.....	223
15.4 Synthesis of Mn-BTC nanoparticles.....	225

Chapter 16

16.	Results and Discussion.....	228
16.1	Characterization of Cu-CAT-1 nanoparticles.....	228
16.2	Characterization of Mn-BTC nanoparticles.....	237
16.3	Preparation of the substrate for electrochemical studies.....	242

Chapter 17

17.	Iron based MOFs.....	245
17.1	MIL-100 (Fe): synthesis, characterization and application in drug delivery.....	248
17.2	MIL-53 (Fe): synthesis, characterization and application in drug delivery.....	251
17.3	Doping of MOFs with second metals.....	253

Chapter 18

18.	Materials and Methods.....	256
18.1	Chemical and reagents.....	256
18.2	Instruments.....	256
18.3	Synthesis of MIL-100 (Fe) nanoparticles.....	257
18.4	Synthesis of MIL-53 (Fe) nanoparticles.....	259
18.5	Synthesis of magnesium-doped MIL-100 (Fe) nanoparticles.....	261
18.6	Synthesis of magnesium-doped MIL-53 (Fe) nanoparticles.....	263

Chapter 19

19.	Results and Discussion.....	265
19.1	Characterization of MIL-100 (Fe) nanoparticles.....	265

19.2	Characterization of magnesium-doped MIL-100 (Fe) nanoparticles.....	270
19.3	Characterization of MIL-53 (Fe) nanoparticles.....	275
19.4	Characterization of magnesium-doped MIL-53 (Fe) nanoparticles.....	278

Chapter 20

20.	Conclusions and future perspectives.....	282
------------	--	------------

Chapter 21

21.	References.....	284
------------	-----------------	------------

General conclusions and perspectives.....	298
--	------------

List of publications and contributions to conferences.....	303
---	------------

Abstract

The engineering of artificial functional materials is one of the most dynamic scientific fields of the contemporary era. It is considered a multidisciplinary area that combines chemistry, physics, materials and computational science to design and synthesize new materials with properties optimized for specific assets and function. One of the first materials to be discovered was zeolites in the mid-1700s. Zeolites are microporous, generally crystalline minerals composed mainly of aluminosilicates of alkali or alkaline earth metals, such as sodium, potassium or calcium. They are characterized by a regular three-dimensional composed of silica (SiO_4) and alumina (AlO_4), which form cavities and channels at the molecular level. This class of microporous silicates is mainly used in catalysis, adsorption-separation, and ion exchange. The final structure of zeolites is highly unpredictable since it depends on several variables, such as the synthesis solvents, the direction agents in the structure, and the mineralizers.

The true revolution in materials occurred in the 20th century with the advent of polymers, including groundbreaking like plastics and nylon. The 21st century has seen growing attention to nanometric-sized materials, such as carbon nanotubes, graphene and nanoparticles. These materials have unique physical and chemical properties, such as greater mechanical resistance and superior electrical conductivity. Graphene is a two-dimensional material composed of a single layer of carbon atoms arranged in a honeycomb (hexagonal) structure. Among its various properties, high electrical and thermal conductivity, mechanical resistance and flexibility stand out. It is a material used mainly in electrochemistry, for example, for the construction of supercapacitors and batteries. Another category of nanomaterials includes by carbon nanotubes (CNTs), which are cylindrical structures composed of one or more layers of

graphene rolled into a tubular shape. They can be classified into single-walled carbon nanotubes (SWNTs) and multi-walled carbon nanotubes (MWNTs), depending on the number of graphene layers present. These exhibit properties and applications like graphene.

Nanomaterials are also crucial for applications as separation phases, where their porosity plays a key role in enhancing performance and efficiency. Starting from separation techniques, the most widespread one is liquid chromatography, which involves the use of a solid stationary phase. The principal material used as the solid support for synthesizing stationary phases is silica, which consists of particles exhibiting permanent mesoporosity. The silica surface is covered with silanol groups (Si-OH) which are responsible for polar interactions and can act as acidic active sites. The silica surface can be chemically modified through derivatization processes to introduce various functionalities, thus broadening its applications. A classic example is silica modified with alkyl chains, such as C18 silica (octadecylsilane), widely used in reversed-phase chromatography (RP-HPLC). Moreover, silica can be efficiently derivatized with a wide array of specifically designed chiral molecules for separating enantiomers. Based on these modifications, the characteristics of chiral stationary phases are determined by the presence of chiral selectors and can be predicted with reasonable accuracy. Many stationary phases are currently available commercially, with one of the most notable being Pirkle's Whelk-O1, composed of silica derivatized with (1-(3,5-dinitrobenzamide)-1,2,3,4-tetrahydrophenanthrene). This stationary phase has proven to be one of the most commercially promising, as it can resolve various enantiomers under different experimental conditions.

In recent years, research has focused on the study of covalent organic materials, which represent a very broad class that includes Covalent Organic Polymers (or COP), materials whose complexity varies depending on the precursors and can

also present porous or non-porous structures. Their complexity relies on various factors, one above all the synthetic approach. The kinetic aspect of bond formation plays a crucial role in determining the material's structural organization. A higher rate of bond formation tends to increase the likelihood of irregularities or defects in the atomic arrangement, thereby promoting the formation of an amorphous structure. This is because rapid kinetics limit the time available for atoms to arrange into an ordered, crystalline structure, resulting in a disordered or amorphous state. For this reason, compounds that act as reaction modulators are frequently and voluntarily used in their synthesis. These materials are used primarily in the field of metal-heterogeneous organic catalysis; this is due to their insoluble nature in common organic solvents, their strong affinity for metals that allows them to be used as reaction catalysts, but above all, to be quickly recovered from the reaction environment and reused, thus advancing the entire process towards a more sustainable chemistry. The frameworks materials can be classified in Covalent Organic Frameworks (COFs) and Metal Organic Frameworks (MOFs). MOFs and COFs are crystalline porous materials, and they can be readily self-assembled from different molecular building pieces that interact with one another through covalent bonds or coordinated interactions. They have high porosity and large surface area that led to a wide range of applications. The main difference between MOFs and COFs lies in the constituents: in the first case there is an organic molecule that acts as a linker and a metal ion that act as nodes. These elements establish coordination interactions between them; in the second case, at least two organic molecules are present in the structure that establish covalent bonds, giving greater stability to the entire system compared to MOFs. Both materials can serve as carriers, due to their porosity, making them for electrochemical applications, purification, chromatographic separation, as well as catalysis, storage and gas adsorption.

Although there are numerous synthetic methods to obtain these materials, current research focuses on developing approaches to reduce the environmental impact of often harmful organic solvents. However, the use of aqueous solvents as an alternative is often limited due to the poor insolubility of the organic precursors in water.

This thesis presents the development of various materials described in three parts, each reflecting progressive increase in structural complexity.

In the first part, the synthesis of two chiral selectors is described, their structure was designed starting from the commercially available Whelk-O1 selector. A preliminary study on their chiral discrimination capabilities was conducted by NMR, using one of selector as chiral solvating agent (CSA) towards ibuprofen. Once synthesized and characterized, the chiral selectors were anchored on silica. The CSPs obtained were packed in chromatographic columns tested on different racemic mixtures in specific experimental conditions. Finally, based on the obtained chromatographic data, molecular docking studies were conducted in presence of the best resolved racemate to analyse the significant interactions between the selectors and the selectands. Therefore, in this first part of the thesis we focused on preparation of a material that does not present a high intrinsic structural complexity, but this is only due to the structure of the anchored selector, which determines its properties.

In the second part of the thesis a Covalent Organic Polymer (COP) based on amide bonds is presented. This is a material that is structurally more complex than the case of the CSP presented in the first part. This has been characterized from a chemical-morphological point of view and its amorphous and non-porous structure has been revealed. As mentioned above, a fundamental aspect to consider in the synthesis of covalent organic materials is the kinetics of bond formation; in this case, the amide bond formation occurs so quickly that it does

not allow an ordered and crystalline structure. Due to the potential good coordination capacity, the prepared COPs were modified with different metals including copper and the resulting doped COPs have been tested. Initially, Cu^{2+} @COP was obtained, which was reduced in the presence of ascorbic acid, obtaining Cu^+ @COP. In both cases, a chemical-morphological characterization was carried out, in addition to a careful analysis of the oxidation state of copper to confirm the reduction of the metal. The metal-organic supports obtained were used as potential catalysts in the CuAAC “click” reaction. After optimization of reaction conditions, product yields of Cu^+ @COP were compared with those obtained in homogeneous phase conditions, by using copper sulphate, and in addition, with those in heterogeneous phase but in presence of Cu^{2+} @COP and ascorbic acid, as a reducing agent. As for all heterogeneous solid catalysts, Cu^+ @COP is removed by simple filtration, while the final product is purified through a crystallization process. Although it has not reached the optimal characteristics of crystallinity, surface area and porosity, this material has shown promising results as heterogeneous catalyst working in water media.

In the third part of this thesis, a micellar approach has been employed to synthesize nanoscale porous crystalline materials, as previously documented in literature, resulting in MOFs with potential applications in supercapacitors and drug delivery. In short, the micellar approach employs two surfactants, SDS and CTAB, that form a micellar medium within which the MOFs grow. In particular, copper and manganese-based MOF nanoparticles (Cu-CAT-1 and Mn-BTC respectively) were synthesized and were chemically and morphologically characterized. Data obtained were compared with those reported in the literature using conventional synthetic methods. Morphological analysis demonstrates that nanoparticles were produced through the micellar approach, whereas conventional methods yielded fibrous structures several micrometres in length.

Given the well-established conductivity properties of Cu-CAT-1, these materials are currently being investigated for supercapacitor applications due to their favourable electrochemical characteristics and their enhanced processability due to their nanoscale dimension. If results will be promising, they will be used for the construction of asymmetric supercapacitors. The same approach has been used and optimized for synthesising iron-based MOFs (MIL-53 (Fe) and MIL-100 (Fe) respectively) at the nanometric scale. Also in this case, materials were fully characterized and results compared with those reported in the literature. Furthermore, a synthetic protocol has been developed and optimized to dope these systems with a biocompatible metal ion, magnesium. We have generated two MOF systems, i.e. magnesium-doped MIL-100 (Fe) and magnesium-doped MIL-53 (Fe)). Looking to the applicability, MIL-100 (Fe) and MIL-53 (Fe) are already known in the literature to have good properties as drug-carriers due to their excellent structural properties and low toxicity. This project aims to evaluate the potential toxicity and biocompatibility of these materials when shaped into nanoparticles at the nanoscale. Special attention will be given to magnesium doped systems, focusing on how the presence of magnesium influences these properties. In this case, synthesizing MOFs in nanoparticles form offers a significant advantage for in vivo applications, as these materials can more easily penetrate cells. On the contrary, conventional approaches, often produce microsized MOF crystals with polyhedral shapes, limiting their in vivo applicability. In this last part, we can highlight how, compared to the previous sections, prepared materials show a greater intrinsic structural complexity together with high crystallinity, porosity and surface area.

Part A

1. Chirality and its role in compounds of pharmacological interest

Chirality describes a spatial stereochemical arrangement of atoms in a molecule in which simple symmetry operations, such as reflection at a molecular level, make it non-superimposable on its mirror image, this is due to the presence in a molecule of stereogenic centers, axes or planes. Molecules with this characteristic are called chiral, while if they don't have this property are achiral. Chirality is a Greek word and means "handedness", derived from the word stem $\chi\epsilon\iota\omicron$ (hand). Enantiomers are defined as chiral molecules that are non-superimposable mirror images of each other. A mixture with equal proportions of both enantiomers is called racemate or racemic mixture. The chiral center can have an absolute configuration of type R, S, using CIP rules or D, L, dextrose and levogyre, moreover they can be represented by the signs (+) and (-). Differentiating two enantiomers is highly challenging since they have the same physical chemical properties, such as the refractive index, melting or boiling temperature, and spectroscopic characteristics. Specifically, one enantiomer will rotate in one direction (i.e. clockwise) while the other enantiomer rotates equally in the opposite direction (counterclockwise). As an alternative, the two enantiomeric species can interact with a chiral organic molecule with defined stereochemistry. This is made possible by the formation of diastereomeric derivatives or adducts, which are not specular compounds but rather have different spatial orientations and the same molecular formula and atom connectivity. [1] This suggests that the two enantiomeric species have distinct chemical-physical properties that allow them to be distinguished from one another. The concept of chirality also plays a fundamental role in biology, especially in biochemistry; many biological

macromolecules are chiral since amino acids and carbohydrates are themselves chiral.

Research has made significant investments in examining the effects of chirality, especially in the context of biologically active compounds. Enantiomeric chiral molecules thus generally show different physiological effects, they have a different taste, smell, toxicity and pharmacological action as a drug. Drug's pharmacological behavior is influenced by its interactions with chiral systems including proteins, enzymes, and receptors and thanks to the effects of these interactions aspects such as toxicity, metabolism, elimination and therapeutic efficacy are affected. During the drug discovery and development phases, the racemic mixture and both single enantiomers need to be tested separately for their pharmacological activity and toxicity. Determining the racemic mixture, extracting pure single enantiomers, and using analytical techniques to track them (for example, in bodily fluids) have thus become crucial. [2-3] For instance, two enantiomers may exhibit identical pharmacological activity but differ in potency, as in the case of (*R*)- and (*S*)-Warfarin. [4] These enantiomers are specifically metabolized differently by the human body; enantiomer (*S*) is eliminated more quickly than the enantiomer (*R*), resulting in a shorter-lasting pharmacological effect. The enantiomers may also exhibit opposite pharmacological activity; this is the case with the opioid agonist (*3S, 4R*)-Pinacedol and the antagonist (*3R, 4S*)-Pinacedol. [5] Another possibility is that just one of the two enantiomeric species possesses all the therapeutic properties, with the other being inactive, or in the worst case responsible for side effects, the best-known case is Thalidomide. [6-7]

1.1 The chromatographic approach for the separation of chiral compounds

Liquid Chromatography (LC), which measures the rate at which mixture constituents migrate into a stationary immobilized phase carried by a mobile phase known as an eluent, is one of the most used methods for separating and isolating chiral compounds. There are two approaches (**Figure 1**) to obtain enantiopure molecules:

- *Chiral approach*: which includes the enantioselective synthesis of the required enantiomer, using chiral and auxiliary tuning, catalysts or stereoselective enzymes. [8-9]
- *Racemic approach*: which provides the resolution of a racemic mixture in single enantiomers by indirect and direct methods. [10-11]

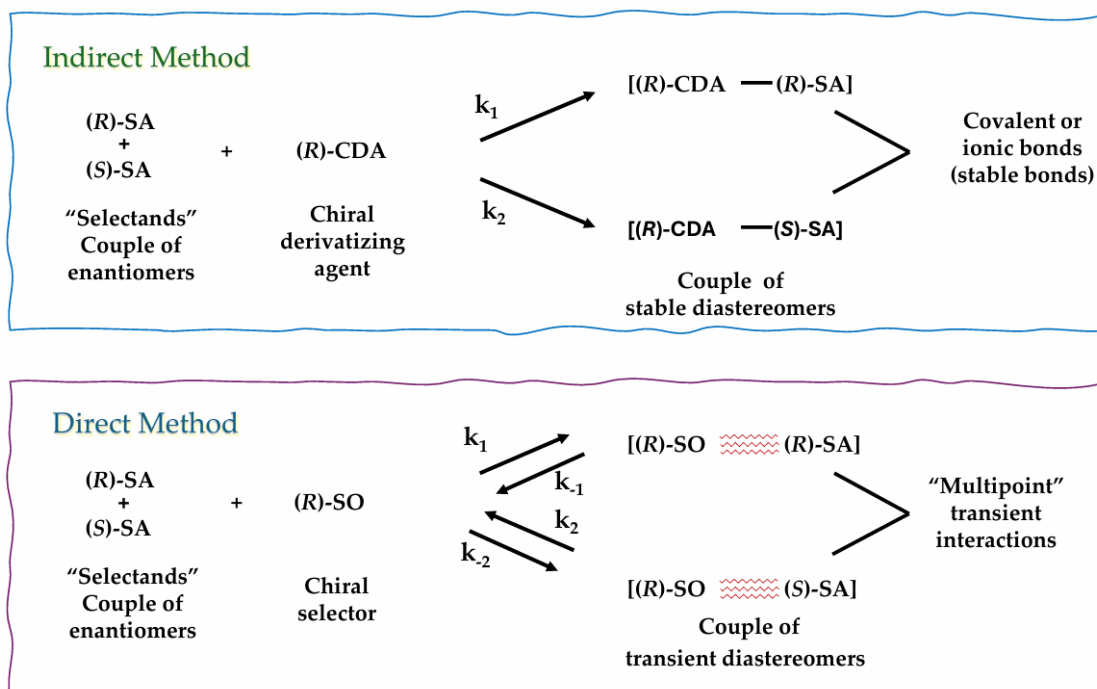


Figure 1. Schematic illustration about Indirect and Direct approach through which is possible to obtain enantiopure molecules.

The indirect method involves a mixture of enantiomers, equimolar or enriched with one of the two species, reacted with a defined stereochemistry compound, this leads to the covalent formation of a pair of diastereoisomers. [12] This requires a prior chiral derivatization which is helpful and efficient but has some limitations that must be considered despite the large number and variety of optically active chemicals created for indirect analysis. Initially, there should be just one enantiomer of the chiral derivatization agent (CDA), or it should have a significant enantiomeric excess previously determined by other measures. A mistake would unavoidably be made if these circumstances weren't met; the existence of a second enantiomer would cause the development of a second pair of diastereomers, for a total of four stereoisomers. As a result, the analyte's enantiomeric and diastereomeric compositions would not coincide. The reagent must also remain stable throughout time and in the conditions used to perform the derivatization reaction. The two enantiomers' derivatization reaction might not go to completion, which would mean that the resultant diastereomeric composition might not match the original enantiomeric one. All these variables are, of course, controllable if a trustworthy technique for figuring out the enantiomeric composition is created and proven. The indirect method works particularly well when a drug is being analyzed more than once; but it is not appropriate for analytical controls of drugs with different structures because the method needs to be carefully adjusted before it can be used with confidence to determine the enantiomeric composition of a drug. The term "*selector*" refers to that chiral molecule that is used to distinguish between enantiomers. It interacts differentially with the two enantiomers, recognizing and separating them. For example, in chiral chromatography, the chiral selector is often a component of the stationary phase that could interact differently with each enantiomer. The

word "*selectand*" represents the chiral molecule that is being separated or analyzed. In other words, it is the compound whose enantiomers are to be separated or analyzed using a chiral selector.

Right now, the direct chromatographic resolution approach for enantiomers is preferred since it does not imply prior derivatization, and lower sample manipulation is required to obtain results more quickly and reliably. [13] In this case a chiral selector in the chromatographic system that must preferentially connect with one of the mixture's enantiomers to produce temporary diastereomeric complexes makes it feasible to resolve the enantiomers directly. The retention times on the column vary depending on the stability of the enantiomeric complex that is formed; the enantiomer that forms the less stable complex will elute first. The chiral selector might be a part of the stationary phase immobilized in the chromatographic support, or it can be present as an addition in the mobile phase, in this case it is called Chiral Stationary Phase (CSP).

1.2 Chiral Stationary Phases

Many CSPs have been developed for HPLC by different research groups over the course of the last years. Davankov, Pirkle, Okamoto, Blaschke, Allenmark, Hermansson, Armstrong, Gasparrini and Lindner have all produced some of the most groundbreaking works in this regard. The direct resolution of enantiomers became possible with the development of chiral stationary phases (CSPs), eliminating the need for an indirect approach of chromatographic separation that required a derivatization step beforehand. [14-15] There are different types of CSP that can be classified as follows:

- **Macromolecular selectors**: Biopolymer- derived (proteins, polysaccharide derivatives); Synthetic polymers (polytartaramides, poly(meth)acrylamides);
- **Macrocyclic selectors**: Cyclodextrins; Macrocyclic antibiotics; Chiral crown ethers;
- **Low-molecular mass selectors**: donor-acceptor (Pirkle-type) selectors; Chiral ion-exchange type selectors; Ligand exchange selectors (chelating agents).

Polysaccharide-based CSPs

In enantioselective liquid chromatography, polysaccharide selectors have a long history of use. The first studies conducted in the 1970s by Hesse and Hagel used microcrystalline cellulose triacetate (MCTA) as a polymer selection material in the absence of supporting beads. [16-17] Simple cross-linked beads made of polysaccharide derivatives without support have also been suggested as chiral separation methods, and they have demonstrated an increase in load capacity, albeit with certain drawbacks concerning their kinetic and hydrodynamic characteristics. [18-19] Okamoto *et al.* discovered in 1984 a way to solve the mechanical stability issue with MCTA: applying a thin layer of roughly 20% by

weight of microporous silica beads (pore size: 1000 Å) on the surface of cellulose derivatives. [20] The efficiency of these coated polysaccharide CSPs, which are based on derivatives of cellulose and amylose (such as carbamate and esters), was significantly increased. The phases with polysaccharides are highly adaptable and can be employed in supercritical fluid chromatography, normal, reversed and polar-organic elution modes. [21-22]

Then significant progress has been made in identifying immobilized CSPs that exhibit greater resistance to “non-standard” solvents such as dichloromethane, chloroform, ethyl acetate, tetrahydrofuran, dioxane, toluene and acetone. In this way it is clear that the physically adsorbed polymer layer expanding and/or dissolving once coated CSPs are exposed to various solvents, the column is eventually destroyed by the selector switch being removed. [23]

Cyclodextrin-based CSPs

Armstrong and DeMond introduced cyclodextrin-related (CSPsCDs), which are based on α -, β -, γ - cyclodextrins. [24] Their hydrophilic surface and hydrophobic voids enable them to form inclusion complexes, which enables them to contain a variety of kinds of chemicals. The elution conditions that can be employed for CD-based CSPs [25-26] (encompassing conditions NP, PO, RP and SFC) [27-28] and the molecular recognition processes that are active under these specific conditions are multimodal. An interesting work that examines in detail the mechanisms of these CSPs for newly synthesized cyclodextrin derivatives, is that of Scriba *et al* from 2016. [29]

Macrocyclic antibiotics CSPs

Macrocyclic antibiotics are a class of macrocyclic natural compounds discovered by Armstrong *et al.* and used as potential chiral selectors. In addition to polysaccharide CSPs, they currently constitute the second largest group of CSPs on the market. [30-31] The glycopeptides that are most frequently employed as chiral selectors are Vancomycin and Teicoplanin; as reported in **Figure 2**, the second structure has an extra ionizable amino group in comparison to the second structure. The Vancomycin-modified silica that Armstrong *et al.* developed in 1994 was the first CSP of this class to be characterized. [32] Several analogs of glycopeptide antibiotic family, [33] including Vancomycin [32], Teicoplanin [34], Ristocetin A [35] and Teicoplanin Aglycone [36], have since been proposed as strong chiral selectors with analogous selectivity characteristics. Moreover, Avoparcin [33], Glycopeptide A-40, 926 [37-38], Hepta-Tyr [39], Novancomycin [40] and Eremomycin [41-42] have been investigated as chiral selectors in HPLC. All CSPs described are particularly useful in the separation of natural and synthetic non-derivatized amino acids [43] and tiny peptides. [44] The multimodal applicability of macrocyclic antibiotic CSPs in elution mode NP, PO, RP, [45] and SFC [46] contributes to their versatility. The most successful organic mode was found to be polar (methanol with acetic acid up to 1% and triethylamine), [47] followed by Hilic. [48] It is challenging to determine the chiral recognition process for them with certainty because of their structural complexity. Numerous possible interactions, such as different hydrogen donor/acceptor sites, aromatic rings for π - π interaction, acid and basic groups that might be engaged in electrostatic interactions, are present in all of these selectors. It is evident that sufficient steric limitations involving the

stereoselective connection to some of these sites exist in addition to a certain degree of conformational flexibility.

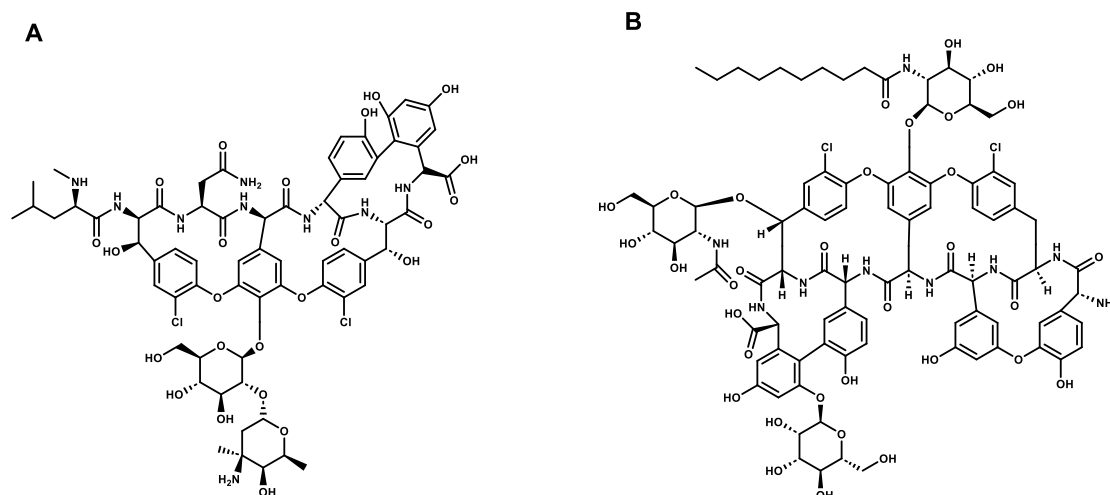


Figure 2. A) Structure of Vancomycin. B) Structure of Teicoplanin.

Proteins CSPs

Numerous protein-based CSPs, that have been tested in research settings and are well documented in scientific literature, have been developed with the help of Allenmark, Hermansson, Miwa, Haginaka and others. [49-52] Promising proteins include human serum albumin (HSA), [53] which is currently utilized more for drug-protein binding studies than for enantiomer separation; α 1-acid glycoprotein (AGP), [54] another plasma protein with altered binding characteristic in immobilized form because of the reticulation protocols used; crude ovomucoid (OVM) [55], which demonstrated a strong chiral recognition ability and cellobioidrolase I (CBH I). [56] Among these, AGP and OVM seem to have greater enantiomer separation capacities, encompassing a broad range of basic racemates, neutral drugs, and acids, as well as other pharmaceutical items. HAS preferably solves chiral acid compounds, while CBH preferably solves basic

chiral compounds (β -blockers). [57] Retention and enantioselectivity are largely controlled by experimental parameters like pH, buffer type and ionic strength, type and content of organic modifiers (typically 1- or 2-propanol and acetonitrile, respectively), additives (alkylamine or quaternate ammonium salts, hydrophobic carboxylic acids, alkyl sulfonates), and temperature. There is a sensitive dependence of separation factors on pH and modifier variations, which might impact the number of accessible selective and non-selective adsorption sites rather differently. [58-60] It should be emphasized that proteins could undergo conformational changes based on the experimental settings given above, which could impact the capacity to resolve enantiomers.

1.3 Donor-acceptor phases: Brush-Type or Pirkle-Type CSPs

A class of chiral stationary phases known as “*Brush-Type*” or “*Pirkle-Type*” was made possible by the proposal of the first chiral stationary phases linked to a siliceous support with completely synthetic selectors in the 1970s. [61-62] These chiral stationary phases are distinguished by the presence of synthetic organic molecules with defined stereochemistry, very simple structure, low molecular weight, and one or two stereogenic centers, that acts as a chiral selector. They are effectively used for the resolution of mixtures of enantiomers, both in analytical and preparative way or chromatography. These chiral selectors perform at least some of the following tasks, thanks to their structural features that are helpful for chiral discrimination: a hydrogen bonding potential; an aromatic group with π -acid or π -basic character; and the potential for dipole-dipole interactions; large, non-flexible, non-polar groups that can serve as efficient steric barriers to regulate conformational interactions (**Figure 3**).

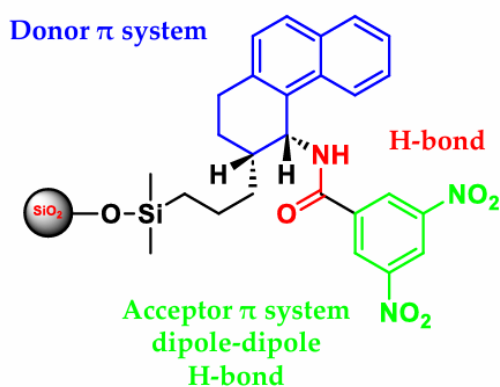


Figure 3. Structure of the chiral selector in the stationary phase (*R,R*)-Whelk-O1 and interactions of the different parts of the chiral selector.

These selectors are therefore also called "multiple interaction" selectors and respond to the main characteristics that must have a chiral stationary phase: they are very stable, have a wide field of application and have high chromatographic efficiency, therefore being suitable for preparative chromatography. Furthermore, the employed chiral selectors are frequently synthesized in both enantiomeric forms. The ability to obtain stationary phases with inverted chirality and, consequently, reverse the order of elution of the two enantiomers is a very useful characteristic. This is especially important for the quantitative determination of enantiomeric excess in situations where one of the two enantiomers is present only in traces and for the detection of impurities. [63] The high sample loading capacity of Pirkle chiral stationary phases is another benefit, particularly when contrasted with chiral protein stationary phases, those containing macrocyclic antibiotics, and those based on cyclodextrins. This characteristic encourages their preparative use in preclinical drug discovery research, an area in which chiral stationary phases of type Pirkle have shown to be particularly effective and compatible. [64-66] Among the chiral stationary phases of type Pirkle, Whelk-O1 appears to have the most widespread distribution to date in both academic and industrial laboratories. It is also the model whose chiral recognition mechanism has been thoroughly examined: on the one hand, it was logically designed based on mechanistic considerations; on the other hand, it has been the focus of a thorough investigation by multiple researchers using a variety of techniques, such as chromatography, [67] thermodynamics, [68] NMR, [69] X-Ray diffraction [70] and computational methods. [71-72] Pirkle and Welch initially designed the Whelk-O1 phase as a chiral stationary phase specific for the naproxen. Naproxen was the only commercially available Nonsteroidal Anti-Inflammatory Drugs (NSAIDs) to be sold as a single enantiomer, there was a great deal of interest in its asymmetric

synthesis and chromatographic resolution. [73-74] They primarily used the principle of reciprocity as the starting point for their research. The principle of reciprocity could be applied to the system of selective separation when selectors and selectands change roles and belong to two or more forms of congeners, analogues and isomers. Specifically, both selector and selectand enantiomers need to be accessible for chiral recognition. [75] Chiral solvating agents (CSA) were used in nuclear magnetic resonance (NMR) spectroscopy to differentiate enantiomers, thereby demonstrating the principle of reciprocity through reversal of selectand and selector roles. Pirkle started that by using the right optically active amines as solvents, it is possible to cause the enantiomers of secondary and tertiary alcohols to have non-equivalent NMR spectra. [76] This phenomenon also occurs in the reverse way: in optically active alcohols, amino enantiomers may exhibit non-equivalent NMR spectra. [77] He consequently discovered that, for a particular pair of chemicals, the functions of an enantiomeric solute and a CSA can be swapped out. [78]

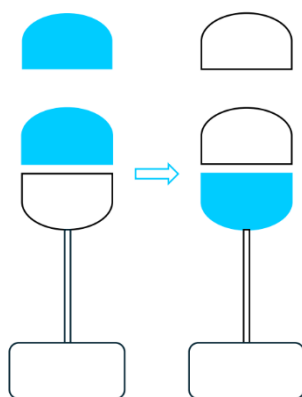


Figure 4. Graphic representation of the principle of reciprocity. A single enantiomer of a racemic mixture that separates into the left chiral stationary phase, when it is used to produce a second chiral stationary phase (right), will allow the resolution of the

enantiomers of analytes that are structurally like the chiral selector of the first chiral stationary phase.

The principle of reciprocity was later extended by Pirkle to enantioselective liquid chromatography, [79] emphasizing that one can use a chiral stationary phase to develop others: if a chiral stationary phase made of (+)-A retains (+)-B, then a stationary phase made of immobilized (+)-B should selectively retain (+)-A (**Figure 4**). [80-81] The idea was further developed by Pirkle and Pochapsky, who noted that the idea behind this “bootstrapping” approach of designing reciprocal stationary chiral phases from compounds that in turn resolve on preexisting chiral stationary phases is predicated on the idea that if two molecules exhibit chiral mutual recognition, it is irrelevant which of them is connected to a stationary support for that recognition to occur. This is not strictly true, as chiral stationary phase immobilization frequently influences chiral recognition; within certain bounds, reciprocity serves as a helpful guide for chiral stationary phase design. [82] One striking example of the novo construction of a chiral stationary phase for a specific selection based precisely on the principle of reciprocity is the resolution of Naproxen (**Figure 5A**) by Pirkle and his colleagues. [83] In an attempt to develop a selector for improved enantioselectivity of Naproxen, they used two chiral stationary phases easily accessible and easy to use: the CSP-1 phase, consisting of (*S*)-Naproxen immobilized on silica gel via an ester bond (**Figure 5B**), and the CSP-2 phase, consisting of (*S*)-Naproxen immobilized on silica gel through an ionic interaction (**Figure 5C**).

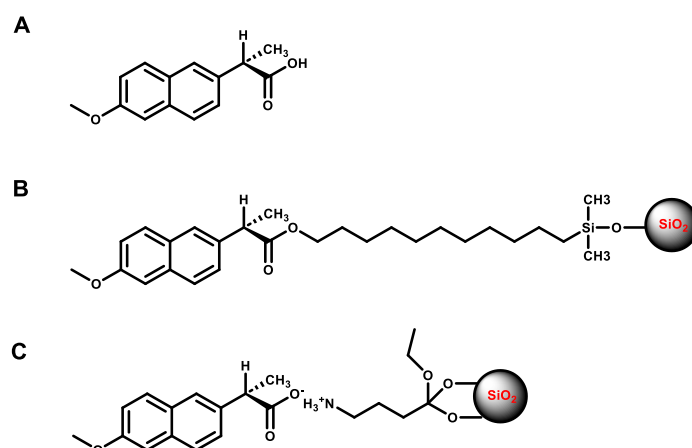


Figure 5. A) Structure of (*S*)-Naproxen. B) Chiral Stationary Phase CSP-1. C) Chiral Stationary Phase CSP-2.

As a consequence of this study, a new chiral stationary phase containing the Whelk-O1 selector was created. This selector demonstrated a high degree of enantioselectivity for Naproxen ($\alpha = 2.25$), which had never been seen observed before for synthetic products, and also was shown to be an effective agent in the separation of numerous structurally related NSAIDs as well as several other racemic mixtures. Scientists saved a great deal of time and money by using an immobilized target molecule to make it easier to evaluate selectors for that specific target chromatographically. This method was also far more practical than the methods employed in the research of molecular recognition. Other benefits of the developed method include: the amount of the selector needed for the analysis is small and recoverable; results are unaffected by small concentrations of impurities in the sample; the stationary phase used for the analysis can be used again for the purification and/or resolution of the selector; the analysis time is relatively short; and chromatographic analysis can be performed at different temperatures, allowing thermodynamic parameters that form the basis of the molecular recognition process to be studied. Through a series of advancements

and the constant application of logical planning. [84] Pirkle *et al.* also created chiral stationary phases for certain analytes, such as various medications and enhanced enantiomeric selectivity. Pirkle *et al.* have created a great deal of chiral stationary phases in more than 30 years of effort; some of these have gone on to become commercial products and are still in high demand by scientists worldwide. [85] Several generations of chiral stationary phases of the Pirkle type with small molecules have been developed based on the general principles set by these pioneers. The aim is to resolve many racemic mixtures that have not been separated and to further improve enantioselectivity process.

1.3.1 Main chiral stationary phases Pirkle type

The three kinds of chiral stationary phases of the Pirkle Type that are now in use are π electron acceptors/donors, π electron acceptors, and π donors. The phases Whelk-O1, Whelk-O2 and ULMO are found in the first group; DACH-DNB, Pirkle 1-J, α -Burke 2, β -Gem 1, Leucine and Phenylglycine are found in the second type; and Naphthyleucine in the third class.

Whelk-O1

1-(3,5-dinitrobenzamide)-1,2,3,4-tetrahydrophenantrene is the basis of the chiral stationary phase Whelk-O1. Racemates of many different functional group classes, such as amide, epoxides, esters, urea, carbamates, ethers, aziridines, phosphonates, aldehydes, ketones, carboxylic acids, and alcohols, can be separated through this phase. The great selectivity of this π electron acceptor/donor phase enables the resolution of a large range of non-derivatized racemates. Commonly utilized in normal phase liquid chromatography (NPLC), Whelk-O1 is a well-known chiral stationary phase. Hydrogen bonding and π - π interactions, which are especially potent in alkane-based eluents frequently utilized in NPLC, are the main mechanisms driving the interaction between chiral analytes and the Whelk-O1 phase. Although the Whelk-O1 column's preferred elution mode is NPLC, its application in reverse phase liquid chromatography (RPLC) has also been investigated, albeit in an unsystematic fashion thus far. [86] When converting from NPLC to RPLC, it is typically believed that there will be a decrease in enantioselectivity and resolution. This is related to that RPLC, as opposed to NPLC, typically favors hydrophobicity-driven interactions as the major mode of interaction between the stationary phase

and analytes. [87] In many cases, the great flexibility found on the Whelk-O1 column offers alternative selectivity and competes favorably with chiral stationary phases generated from polysaccharides. Additional benefits encompass extended column life, superior efficiency, reversal of the elution sequence, and exceptional load capacity.

Whelk-O2

The Whelk-O2 phase is the three-bonded covalent version of the Whelk-O1 phase: it maintains the same chiral selector, but the bonding procedure involves a tri-alkoxy-organosilane (**Figure 6**). In most cases, the enantioselectivities remain the same, allowing for a separation ability similar to that of Whelk-O1. When utilizing mobile phases that contain potent chemical modifiers like trifluoroacetic acid, the Whelk-O2 phase is especially recommended as it is designed to enhance the stability and resistance of the stationary phase Whelk-O1. A wide range of substances, particularly those of pharmaceutical and chemical importance, can benefit from Whelk-O2 excellent enantioselectivity. It is also very adaptable, robust, and produces highly reproducible results, all of which are essential for reliable analytical and preparative separations.

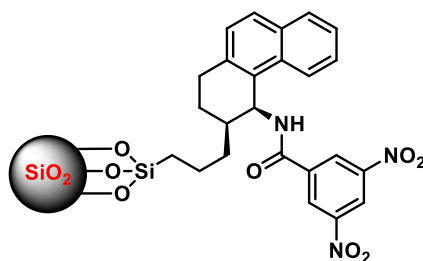


Figure 6. Structure of Whelk-O2 CSP.

Ulmo

The scientists Lindner, Maier and Uray created the ULMO chiral stationary phase. The basis of ULMO is diphenylethylenediamine derivative known as 3,5-dinitrobenzoyl (**Figure 7**). Aril-carbinol enantiomers can be effectively separated using this phase, which is also capable of distinguishing the enantiomers of many other groups of racemates.

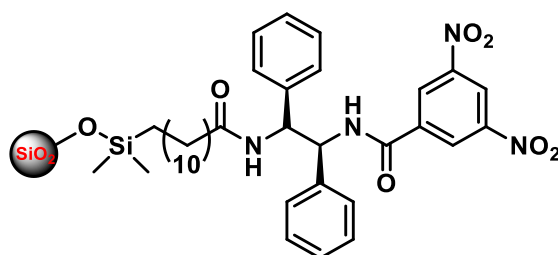


Figure 7. Structure of ULMO CSP.

DACH-DNB

Gasparri, Misiti and Villani designed the DACH-DNB chiral stationary phase. [88] A broad range of racemates, including amides, alcohols, esters, ketones, acid, sulfoxides, phosphines, selenoxides, phosphonates, thiophosphenotoxins, phosphonylenes, phosphine-boranes, β -lactams, organometallics, atropisomers and heterocycles, can be resolved by DACH-DNB phase, which contains the 3,5-dinitrobenzoyl derivative of 1,2-diaminocyclohexane (**Figure 8**).

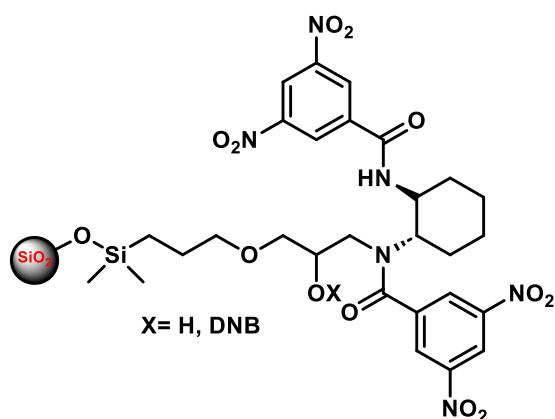


Figure 8. Structure of DACH-DNB CSP.

Pirkle 1-J

Chiral selector in Pirkle 1-J phase is the 3-(3,5-dinitrobenzamide)-4-phenyl- β -lactam (**Figure 9**). The unique structure of β -lactam compounds modifies their molecular recognition characteristics, making them highly advantageous in the direct isolation of non-derivatized β -blocker enantiomers. This is a significant class of cardiovascular drugs, where the enantiomers frequently exhibit distinct pharmacological activity. Aril-propionic acids and other NSAID enantiomers can also be efficacy separated.

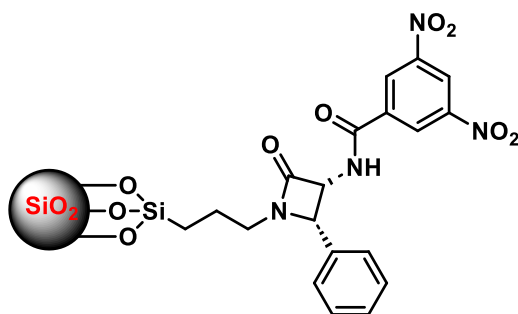


Figure 9. Structure of Pirkle 1-J CSP.

α -Burke 2

Derivative from dimethyl-*N*-3,5-dinitro-benzoyl- α -amino-2,2-dimethyl-4-pentenyl phosphate covalently bonded to 5 μm silica, the α -Burke 2 phase was initially made by J. A. Burke (**Figure 10**). The α -Burke 2 was specifically designed to directly separate enantiomers of β -blockers without chemical derivatization, but this chiral phase also resolves enantiomers of many compounds separated on chiral π -acceptor Pirkle stationary phases.

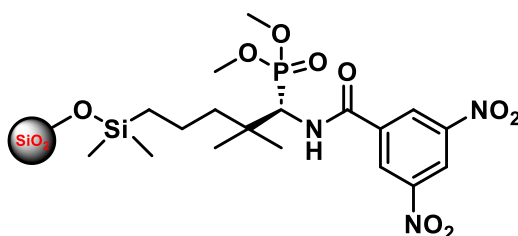


Figure 10. Structure of α -Burke 2 CSP.

β -Gem 1

Within the β -Gem 1 chiral stationary phase, 5 μm of silica is functionalized with *N*-3,5-dinitrobenzoyl-3-amino-3-phenyl-2-(1,1-dimethylene)-propanoate via ester bond (**Figure 11**). This chiral phase outperforms its widely used equivalent, phenylglycine, for numerous analytes. It can distinguish between the anilide derivatives of several different chiral carboxylic acids, including non-steroidal anti-inflammatory drugs.

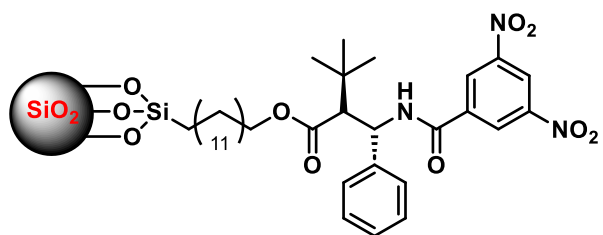


Figure 11. Structure of β -Gem 1 CSP.

Leucine

The basis for the Leucine chiral stationary phase is the 3,5-dinitrobenzoyl-leucine derivative, which is covalently bonded to aminopropyl silica measuring 5 μm (**Figure 12**). The π -acceptor phase exhibits enhanced enantioselectivity towards many kinds of chemicals, such as benzodiazepine compounds.

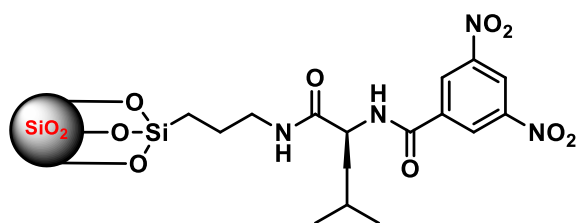


Figure 12. Structure of Leucine CSP.

Phenylglycine

The chiral stationary phase phenylglycine is based on the derivative 3,5-dinitrobenzoyl-phenylglycine, covalently bounded to 5 μm of aminopropyl silica (**Figure 13**). Numerous compounds with π -basic groups can be resolved in this phase, such as aryl-substituted cyclic sulfoxides, bi- β -naphthol cyclic, sulfoxides and their analogues, α -indanol and α -tetralol analogues, and aryl-substituted hydantoins.

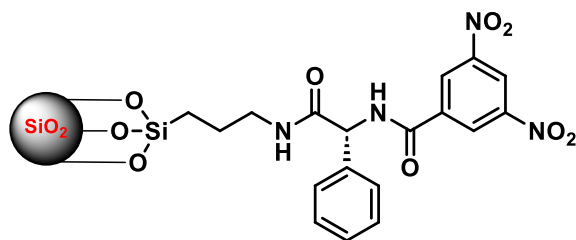


Figure 13. Structure of phenylglycine CSP.

Naphthyleucine

The naphthyleucine stationary chiral phase is based on *N*-(1-naphthyl) leucine, covalently bound to 5 μm of silica through an ester bond (**Figure 14**). This phase discriminates DNB derivatives of amino acids like free acid if used in reverse phase mode. In the classical normal phase, this chiral stationary phase can resolve the amides and esters of DNB amines, alcohols, and amino acids.

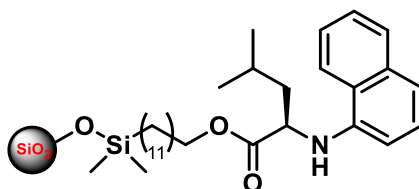


Figure 14. Structure of Naphthyleucine CSP.

1.4 From High Performance Liquid Chromatography (HPLC) to Ultra High-Performance Liquid Chromatography (UHPLC)

Being the most well-known method of separation, liquid chromatography (LC) relies on the physical separation of analytes through dispersion and interactions between a stationary phase and a flowing liquid, or mobile phase. In high performance liquid chromatography (HPLC) a selector is typically linked to a porous particle that is tightly packed inside the column as the stationary phase, it's about a LC where the mobile phase is restricted to flow through a column using a pumping system. The solid particles, primarily silica-based, that make up the adsorbing phase in the packed columns can undergo various functional group derivatizations. Thermodynamic laws, which account for the distribution of analytes between the two phases, control the different kinds of interactions. Chromatography involves a few different parameters to consider. For example, the resolution (R_s) indicates how well one analyte is separated from another in the chromatographic process. This parameter is dependent on two thermodynamic factors: “ k ” (see **equation 1.1**) namely retention factor and “ α ” (see **equation 1.2**) namely selectivity factor.

$$k = \frac{t_R - t_0}{t_0} \quad \text{Eq. 1.1}$$

$$\alpha = \frac{k_A}{k_B} \quad \text{Eq. 1.2}$$

Moreover, a kinetic one: N is the *efficiency*, concerning the number of theoretical plates (**equation 1.3**):

$$N = \frac{L}{H} \quad \text{Eq. 1.3}$$

L is the length of the column, H is the height equivalent to a theoretical plate, t_R is the retention time, t_0 is the hold-up time. *Efficiency* measures the separation power and performance provided by the column; it can be expressed either by the number of theoretical plates (N) or by the height equivalent to a theoretical plate (H). Thus, the higher the efficiency, the narrower the peak shape. All three parameters affect R_s , but while the first two depend on the chemistry of the stationary phase, efficiency is instead related to the length of the column (L) and inversely proportional to the particle size (d_p). UHPLC, which stands for ultra-high pressure liquid chromatography, was first used by Jorgenson in 1997. This group was the first to report the usage of 1.0-1.5 μm silica-based non-porous particles filled nano-columns on a system prototype compatible with very high pressures up to 4100 bar reached in a study in 1997 and 7200 bar reached in 2003. [89-90] Pressure-compatible UHPLC systems operating in the 600-1400 bar range have been commercialized throughout the last ten years. Many sensing devices, such as ultraviolet (UV), ultraviolet diode matrix detector (UV-DAD), evaporative light diffusion detector (ELSD), crown aerosol discharge (CAD), refractive index (RI), fluorescence detector (FD), and mass spectrometry (MS), have improved in design and can all be coupled to UHPLC. Reducing analysis time while maintaining equal kinetic parameters is one of the primary benefits of using UHPLC over HPLC. Because there are so many samples in environmental, such as foods and chemical analyses, where productivity needs to be increased, this high productivity feature is intriguing. The pharmaceutical industry is another factor that propels quick separations. In applications like quality control, pharmacokinetics, and drug metabolism, increased productivity and decreased costs are especially important during the drug discovery and development process. [91-92] The first commercial columns made for UHPLC had dimensions of 2.1x50 mm and 2.1x100 mm and were packed with 1.7 μm particles. [93] The

particles were composed of an organic/inorganic hybrid bridge ethylene derivatized with groups C_{18} and had a mean pore size of 130 Å. [94] They were totally porous. The columns were intended for RP separations of analytes with molecular weights below about 5 kDa. Maximum efficiencies of 280.00 plates/m have been reported for these columns, corrected for system dispersion. [95] Many more surface compounds on hybrid particles and sub-2 μm silica have been introduced in the last twenty years. [96] UHPLC columns were sold for hydrophilic interaction chromatography, [97] normal phase, [98], RP mode, dimensional exclusion and ion exchange. UHPLC columns are now available for separations of analytes up to ~2 MDa, including biopolymers and industrial polymers. [99-101] In order to enhance the kinetic performance of the existing UHPLC technology, a system with a pressure capability over the 1200-1400 bar limit could be helpful. Nevertheless, the construction of such a system would be challenging, as there are currently no pumping or injection technologies that can function in such environments. [102] Therefore, increasing the mobile phase's temperature is an intriguing way to enhance the kinetic performance in UHPLC. [103] At high temperatures ($>60^\circ$), the mobile phase's viscosity is reduced (up to 13 times between 20° and 180° for a 60:40 MeOH-Water mixture), which results in low column pressure drop and increased analyte diffusion coefficients. [104] Consequently, increasing the flow rate can boost output, while extending the column length can boost resolution and efficiency. Temperatures between 150° and 200° are particularly significant for improving performance, but they can also be exceedingly dangerous for the UV cell, sample and column stability. In UHPLC a temperature range of 60-100 $^\circ\text{C}$ seems to be a decent compromise since it still offers high kinetic performance without causing issues with compound and column degradation. [105] Although the performance of modern UHPLC equipment is both revolutionary and evolutionary, it has limitations as well. For

example, the cost of equipment is considerably higher (20-50%), and certain UHPLC systems can cause issues when trying to run older HPLC procedures. [106] Furthermore, even if the supply of UHPLC columns is expanding quickly, it is still limited, especially for modes other than reverse phase, like dimensional exclusion chromatography and ion exchange chromatography. [107] Lastly, for labs without UHPLC equipment, UHPLC procedures must be “converted” to standard HPLC method settings. Because different UHPLC system platforms have varied dispersion volume, viscous heating, and system permanence, it can be more challenging to transfer methods between laboratories, particularly for high resolution methods. [108-109]

1.4.1 Application of Chiral Stationary Pirkle Phases in UHPLC

While the transition from HPLC to achiral UHPLC occurred easily in 2004, the UHPLC transition by using CSPs occurred only 10 years later. Pirkle type stationary phases were the first to be produced in the UHPLC format and have since been used intensively for the last fifteen years. [110] This occurred because the requirement to screen enormous libraries of chiral molecules encouraged the development of chiral separations that were quicker and more effective than those that could be achieved on the standard types of chiral stationary phases, which are made up of particles that are between 3-5 μm . The time needed for analysis has significantly changed: if until only fifteen years ago, the standard time required to perform chiral separations was several tens of minutes, today numerous examples of chiral separations performed in minutes have been reported. [111] Cancellieri *et al.* in 2010 created the first Pirkle type chiral stationary phase to be employed in UHPLC by functionalizing 1.9 μm fully porous particles (FPPs) with the DACH-DNB selector (**Figure 15**). [112]

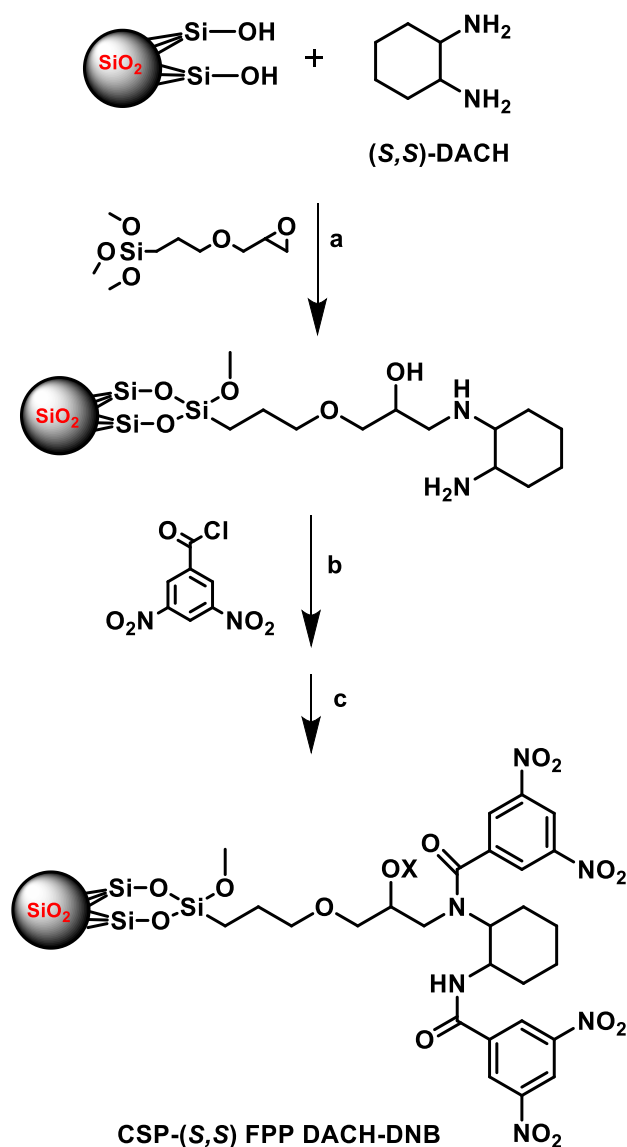


Figure 15. Synthetic procedure of FPP DACH-DNB CSPs. a) GOPTMS, MeOH, reflux, 7.5h; b) THF, T= 0 °C (addition) then reflux; c) trimethylsilyl-imidazole, toluene reflux, 4h (X=H or DNB). [112]

Comparing the kinetic performance of the sub 2 μm FPP-DACH-DNB chiral stationary phase packed column with those of 4.3 μm and 2.6 μm diameter, a significant increase in efficiency and a reduction in analysis time is recorded (**Figure 15**).

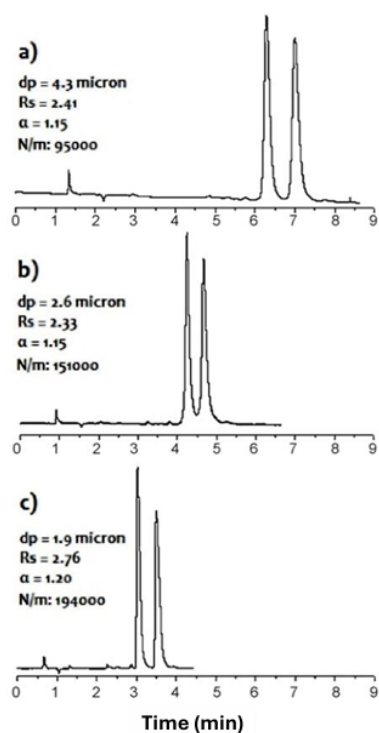


Figure 16. 2-Methoxyphenylsulfoxide enantiomer separation chromatograms of FPP DACH-DNB columns **a)** 4.3 μm ; **b)** 2.6 μm ; **c)** 1.9 μm . [Rs: resolution; α : selectivity; N/m: efficiency] [112]

After a few years, FPPs below 2 microns were functionalized using the Whelk-O1 chiral selector. [113] Excellent chromatographic performance, including a very wide resolution and very symmetrical and narrow peak in ultrafast separations, have been made possible using this chiral stationary phase (**Figure 17**). [114]

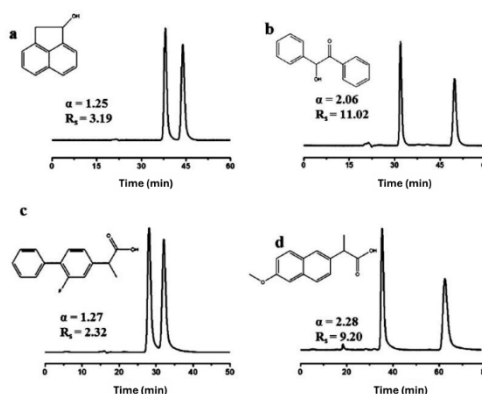


Figure 17. Examples of ultra-fast enantioseparations performed with Whelk-O1 particles less than 2 microns. **a)** Acenaphthenol and **b)** Benzoin separated in normal phase mode; **c)** Flurbiprofen and **d)** Naproxen separated in polar organic mode.

Studies on Supercritical Fluid Chromatography (SFC) have also been conducted; these studies have successfully used chromatographic columns packed with particles of FPP Whelk-O1 below 2 microns for fast screening of a library of 129 racemic compounds (agrochemicals, β -blockers, organic acids and antidepressant) with significantly different physics-chemical properties. By using these columns even basic racemic mixtures can be resolved, which are difficult to separate on the Whelk-O1 stationary phase consisting of larger particles. [115] The Pirkle chiral selectors are undoubtedly one of the most effective instances of the significant benefits that may be attained, even in the chiral separations field, by employing tiny particles with enhanced mass transfer characteristics. It has been much easier to prepare small chiral particles in recent years, and it has been demonstrated that these phases can be employed in a wide range of chromatographic modes and pressure regimes.

1.5 Whelk-O1 as chiral solvating agent at NMR

The presence of a chiral species can modify the stereochemical course of reactions, the properties of enantiomers, or confer chiral characteristics to normal achiral materials. From an applied point of view, separation, determination of the absolute configuration and enantiomeric purity of optical isomers, this principle has taken various forms. Chirality identification is most frequently used in the liquid phase since there are several ways to identify diastereoisomeric interactions in a solution. [116] Boiling point, density, and dipole moment discrepancies between individual enantiomers and their mixtures are examples of extrinsic features that are not very useful in understanding reverse interactions. It has been demonstrated that effective methods are those that detect the variations in the energy with which enantiomers interact with their chiral environment or that reveal spectrum differences between enantiomers in that environment. [117] Pirkle reported the first observation of this phenomena, observing distinct ^{19}F NMR resonances for the enantiomers of (trifluoromethyl)-phenylcarbinol in 1-phenylethylamine, an optically active solvent. Following that, the method became well-liked as a simple substitute for the traditional solutions to the frequently challenging issue of figuring out enantiomeric purity and absolute configuration. [118] To perturb the NMR spectra of enantiomeric solutes in different ways, chiral additives, known as chiral diamagnetic solvating agents (CSA) were used. In general, both the CSA and the solute are hydrogen bond donors or acceptors, and their complementary functionality allows an interaction characterized by their ability to form bonds with appropriate enantiomeric solutes to generate different complexes. CSAs can be acids, amines, alcohols, sulfoxides or cyclic molecules such as peptides or cyclodextrins, which interact with appropriate enantiomeric solutes. Near its asymmetric center, the

CSA nearly always has a group of high diamagnetic anisotropy. This property is helpful in converting the various mean spatial environments of solute nuclei into distinct magnetic environments that can be measured using the NMR technique. When Pirkle chiral selectors are soluble, they can be easily used as chiral solvating agents in NMR spectroscopy. By forming host-guest systems in solution, enantiopurity can be measured, the absolute configuration can be determined, or stereomutation processes can be investigated using NMR experiments at variable temperature (VT-NMR). [119-120] This type of experiment is useful when dealing with conformational chirality in which enantiomers interact with each other only by rotating around individual bonds, at a rate that depends on temperature and time. Furthermore, they could rotate slow enough to consider them stereochemical stable at room temperature; in such case, they are referred to be atropoisomers. To create safe and effective medications, conformational enantiomers must carefully consider the fact that they might interconnect on highly diverse time scales. [121] In contrast, configurational chirality is caused by the presence of a classical stereogenic center, which is easily detectable during the drug design process. [122] The pharmacological and pharmacokinetic properties of configurational and structural enantiomers might change significantly, leading to significant variations in the therapeutic index or adverse effects between two enantiomeric species. [123-127] Conformational enantiomer separation using high-performance liquid chromatography (HPLC) has become a viable option due to technological advancements and the creation of new chiral stationary phases. [128-130] When used in conjunction with NMR, this method provides invaluable assistance in deciphering the stereomutation process of atropoisomers and determining the precise configuration. [131-133] The chiral selector Whelk-O1 and the quick interchange enantiomeric conformations of two distinct medicinal

compounds like anti-HIV medication, Nevirapine (NVP) and antiepileptic medication Oxcarbazepine (OXC) have been studied by Franzini *et al.* (**Figure 18**). [134]

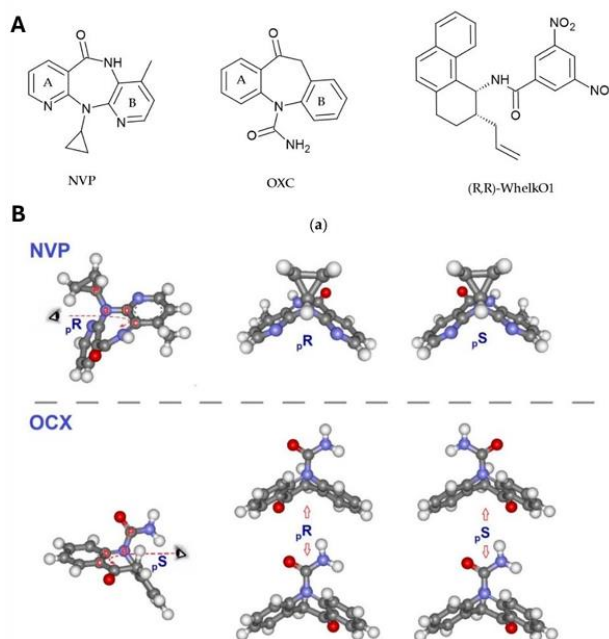


Figure 18. A) Structures of Nevirapine (NVP), Oxcarbazepine (OXC) and the soluble analogue of chiral selector (*R,R*)-Whelk-O1. B) Conformational enantiomeric forms of NVP and OXC. [134]

Compounds characterized by a seven-member non-planar ring in their molecular skeleton are known to be chiral, since the absence of flatness allows the existence of two conformational enantiomers, sometimes rapid exchange, typical of dibenzoazepinic and diazepinic systems. [135-137] The researchers took advantage of the Whelk-O1 selector's capacity to distinguish between the enantiomers of substances examined using variable temperature NMR (VT-NMR) or variable temperature HPLC (VT-HPLC). The chromatographic selector (*R,R*)-Whelk-O1 has good selectivity, so the authors used it as CSA for NMR. They added its soluble analogue in stoichiometric quantities to a solution of

Nevirapine, and the splitting of the methyl group singlet into two resolved peaks reveals the formation of two diastereomeric adducts, which were caused by the reversible association between the analyte and the chiral solvating agent.

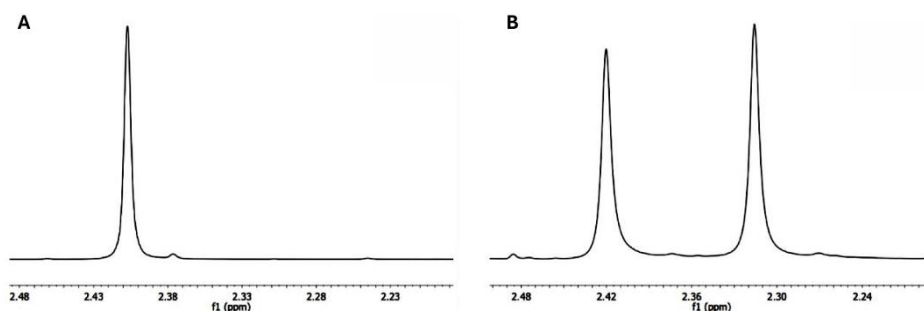


Figure 19. A) ^1H NMR signal corresponding to the methyl protons in NVP and B) in the solution with CSA (*R,R*) Whelk-O1. [134]

The two diastereomeric adducts start to exchange as the temperature rises, and +49 °C is the point at which coalescence occurs (**Figure 20**), generating a single signal at a temperature of +52 °C. By comparing the simulated and experimental spectra, the velocity constant at each temperature was found. Nevirapine's racemization barrier was found to be 16.7 kcal/mol, which is in line with results from dynamic chromatography tests as well as those found in published literature and determined by VT-NMR analysis of the fast exchange profile of methylene diasterotopic protons in the seven-member ring further supported the OXC enantiomerization barrier. The temperature range that was measured from +30° to +133°. At the temperature of coalescence (+112 kcal/mol), neither the chiral stationary phase nor the chiral solvating agent had any discernible disruptive effects on the enantiomerization barriers.

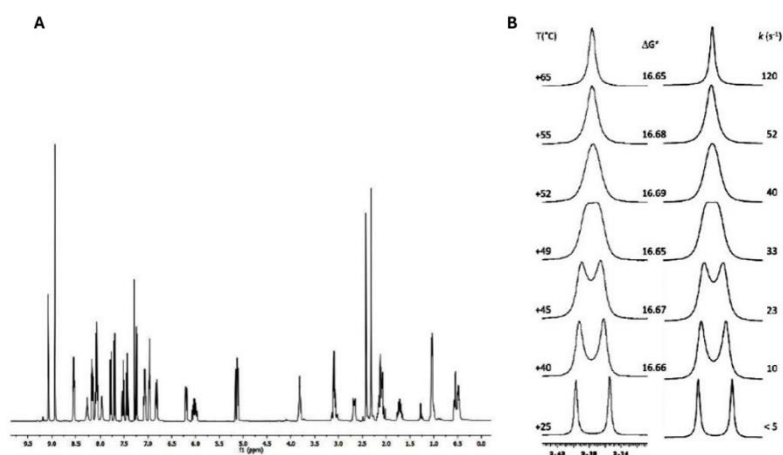


Figure 20. A) ¹H NMR of an equimolar solution of (*R,R*)-Whelk-O1 and NVP and B) progressive coalescence of the signals of the methyl groups monitored by VT-NMR. [134]

To show that there are two structural enantiomers for both NVP or OXC and to quantify their enantiomer barriers by VT-HPLC, a screening process was started using a chiral (*R,R*)- Whelk-O1 stationary phase. The experimental peak profiles provide information about the kinetic parameters of the column interconversion. A progressive coalescence of the peaks in a single big peak for both substances was seen by increasing the temperature of the chromatographic column in a range between -50° and 25° degrees (HPLC was repeated in wide range of temperatures).

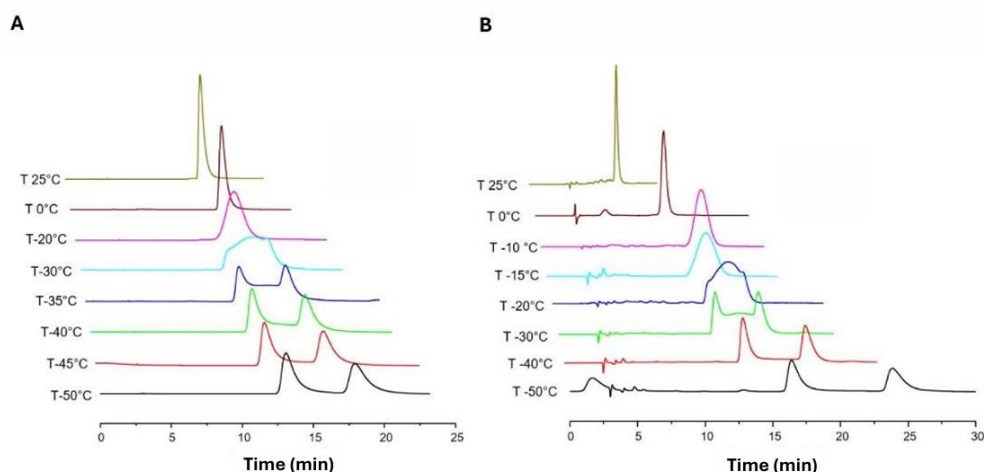


Figure 21. VT-HPLC elution profiles recorded for **A)** NVP and **B)** OXC. [134]

This is an example of a column enantiomerization that can be easily investigated using VT-HPLC since it happens on a time scale similar to the elution process. The results show only very small differences between the elution profiles of the two compounds, which show a similar temperature-dependent pattern (**Figure 21**). NVP exhibits a single peak at room temperature, suggesting a quick interconversion between the two enantiomeric conformers: at lower temperatures, however, a steady expansion and any typical plateau-shaped elution profiles are visible. Finally, at $-50\text{ }^{\circ}\text{C}$ some of the processes of isomerization are slowed down enough to reveal two well resolved peaks. The appearance of distinctive plateau-shaped patterns at intermediate temperatures suggests a dynamic process of column interconversion. When using computational approaches and a variable temperature NMR study to calculate the energy barrier for the enantiomerization of structural enantiomers of NVPs, the results almost match the literature-reported value. Since VT-HPLC NMR is appropriate for studying the stereomutation processes of stereolabile compounds and is applicable within an even wider range of enantiomerization activation energies than VT-HPLC, the authors also used VT-NMR to measure

the enantiomerization barriers of both NVP and OXC and to solidify data obtained from VT-HPLC. [138]

1.6 Inverted Chirality Column Approach (ICCA)

The basis of the “Inverted Chirality Column Approach” (ICCA) approach is the inversion of the order of elution of a given enantiomeric pair following column switching, under identical chemical conditions. [139] When natural selectors like proteins or polysaccharides are present, this method isn’t possible to apply. It is highly helpful for the enantiomeric analysis of the trace when the minor enantiomer follows the main one and is partly obscured by the main enantiomer’s tailing: on the chiral stationary phase (CSP) with opposite configuration, the track enantiomer is eluted first, enabling a more exact and accurate quantification by peak area integration. [140] The enantiomeric excess (*ee*) value of non-racemic mixtures can be determined using this method even in the absence of pure enantiomeric standards. [141] Using chiral stationary phases with the same selectivity but opposite chirality, ICCA’s approach is predicated on the potential to reverse the enantiomer’s elution order while preserving almost similar enantiomeric retention (Figure 22).

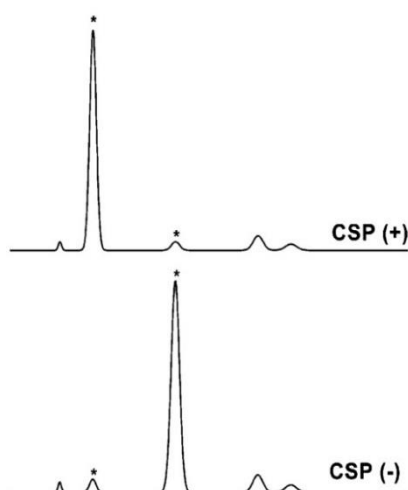


Figure 22. Chromatograms of a non-racemic mixture performed on two stationary phases with opposite chirality: CSP (+) and CSP (-).

When a racemic mixture is analyzed on stationary phases with selectors with opposite chirality CSP (-) and CSP (+), conventional detectors only show that these have the same chromatographic profile; however, chiro detectors, which produce double signals for the two resolved enantiomers, clearly show the order of inverted elution (**Figure 23**).

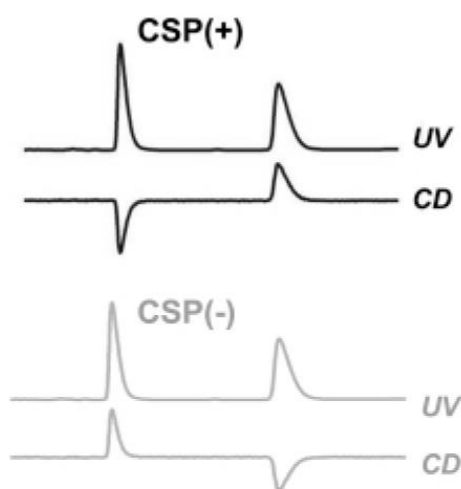


Figure 23. Chromatograms of a racemic mixture performed on two stationary phases with opposite chirality CSP (+) and CSP (-) with UV and CD detectors.

A further advantage of this approach is to be able to choose the configuration of the selector that produces a chromatographic profile with the most convenient elution order, that is, with the enantiomer of the eluting track first. As a result, it is simple to do the analysis of the enantiomeric trace by selecting the chiral stationary phase that permits the previously specified order of elution. This considerably improves sensitivity and enables a more precise quantification by integrating the peak area. [142-143] In the research by Ianni et al. the scientists used the ICCA method to perform an indirect analysis on an asymmetric synthesis, or the addition of butan-2-one to *trans*- β -nitrostyrene catalyzed by (*S*)-

proline, resulting in the formation of the enantiomeric pair (3*S*,4*R*)-3-methyl-4-phenyl-5-nitropentan-2-one and (3*R*,4*S*)-3-methyl-4-phenyl-5-pentan-2-one as the main product. To separate and determine the enantiomeric excess of the phytocannabinoids present in medicinal marijuana, Mazzocanti *et al.* devised an enantioselective approach via UHPSFC (Ultra-High Performance Supercritical Fluid Chromatography) using the ICCA method. Because plant extracts are highly enriched complex mixtures and frequently do not have minor enantiomers available as reference samples, the study's authors employed the ICCA method with columns that had stationary phases of the (FSC-1) Pirkle type (*R,R*)-Whelk-O1 and (FSC-2) (*S,S*)-Whelk-O2.

1.7 Docking Studies for understanding enantioseparation

The science of enantioseparation has effectively used both liquid chromatography and enantioselective chromatography techniques in recent decades. Even with the enormous amount of research in these areas, there is still much to learn about the mechanism of stereoselective interaction. Retention and enantioseparation can really be aided by a variety of non-covalent interactions as well as other effects, for example, they can affect the directional noncovalent interactions at the base of the stereoselective bond, the non-stereoselective adsorption of solid support analytes and the strong long-range interactions involved in the primary non-stereoselective bond. These interactions are controlled by the complementarity of functional groups, such as hydrogen bonds (HB), π - π interactions, dipole-dipole stacking and emerging halogen bonds (XB), steric factors resulting from the spatial arrangement of the selector binding site, selector conformational changes induced by selectand binding, hydrophobic effects and solvation effects. This high level of complexity particularly affects high molecular weight selectors such as polysaccharide derivatives. [144-145] For several years, cheminformatics and molecular modeling have been used in conjunction with chromatographic studies and retention models, FT-IR and NMR spectroscopy techniques, X-Ray crystallography analysis and computational methods to gather data on the structure and binding strength of selector-selectand complexes as well as the kind of non-covalent interactions involved. Specifically, computational tools helped overcome some drawbacks from earlier methods, such as limited dependability of solid-state models to describe complexes in solution and low solubility of some selectors, which were noted for X-Ray crystallography and spectroscopy, respectively. [146] Molecular docking is generally used to simulate the interaction between enantiomer pairs

and the active site of the selector, to predict both the energy and geometry of the selector and bond (**Figure 23**). A docking process consists of two general steps: scoring or classifying hooked conformations (selector-selectand mutual orientations) and conducting a conformational search using different techniques. [147] The majority of research on enantioseparation published used Autodock and AutoDock Tools as a graphical interface. [148] To determine the binding conformations of the selectand to the selector, AutoDock uses the Lamarckian Genetic Algorithm, that describe the three-dimensional arrangement of the molecules involved in docking using geometric variables of state that, in this specific case, are the selector-selectand distance, the orientation of selectand with respect to the selector and the degrees of torsional freedom (number of rotating bonds) of selectand enantiomers. [149] AutoGrid, an AutoDock module that produces a condensed version of the selection, is used to create three-dimensional grid boxes during the pre-docking stage. Every kind of chiral analyte atom is positioned in the computational space profiled by the grid box, and the interaction energy between each atom of the selector is computed and assigned to a grid point. During docking, maps are utilized to extract the energies of interaction between the enantiomers and the selection. Maps are made up of all the gathered grid points for a specific type of atom. Upon completion of the docking calculations, multiple sets of enantiomer conformers are acquired. The molecular dynamics (MD) simulation was first used in chromatography by Giddings and Eyring in the middle of the last century. [150] It illustrates how molecules move, vibrate, spread and interact over time (**Figure 23**). A trajectory, which charts the locations and velocities of chiral partners in the system and their variations over time, is the data set that results from the MD experiment. [151] The trajectory data set can be used to calculate all the system's dynamic and equilibrium characteristics. Given that the solvent can have a significant impact

on the energy of various complex orientations, the solvent can either be explicitly or implicitly treated when parameterizing it in MD simulations. Selectand enantiomers in selectors can be modeled by combining docking computations and MD simulations. [152-154]

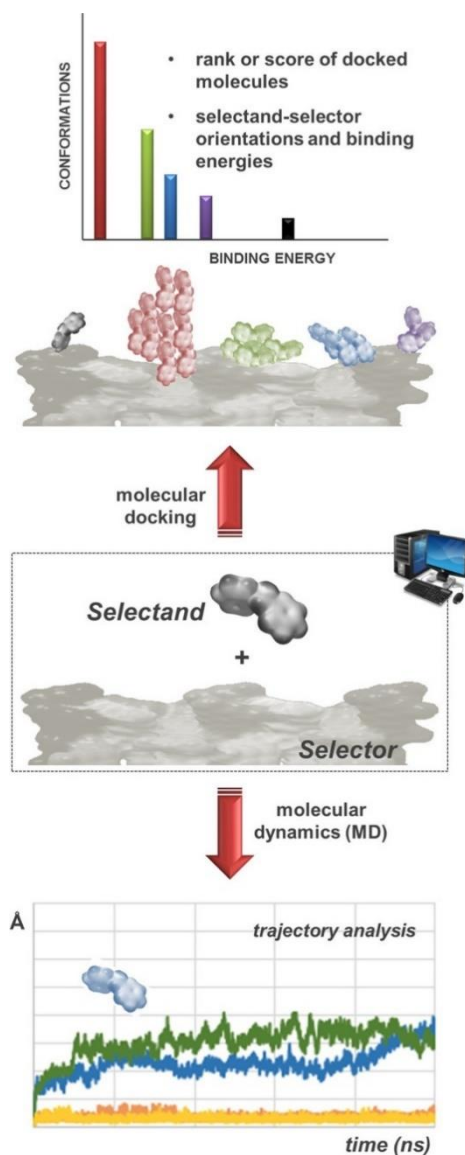


Figure 23. Docking and Molecular Dynamics (MD) application in liquid-phase enantioseparations. [154]

1.7.1 Molecular docking for donor-acceptor chiral selectors

Donor-Acceptor chiral selectors, also known as “*Brush*” or “*Pirkle selectors*”, are made up of tiny molecules that are fixed in a silica matrix. Complementary electrostatic interactions like HB, π - π interactions, and dipole-dipole stacking can be executed by these CSPs. Numerous investigations of the solvation at the Whelk-O1 interface and the docking modes of various selector switches have been conducted using MD simulations. [155-156] Gasparrini *et al.* have produced an intriguing study, which involves a generic scheme based on a “almost flexible” systematic and automatic docking technique to examine stereoselective recognition mechanisms. The scheme is validated on a leucine-containing Pirkle selector. [157-158] In order to study the enantioseparation of six closely related aromatic analytes **1-6** out of four polyproline-based CSPs I-IV, Cann and Ashtari recently employed MD simulations (**Figure 24**). MD simulations were conducted on a patterned surface with 16 polyprolines, 64 silanol groups, 48 trimethylsilyl terminals and 128 fixed Si atoms in this work. Each solvent combination, selector, and analyte were considered. The impact of two distinct mobile phases on chiral identification was taken into consideration in the theoretical investigation. These were water/methanol (MeOH) as a polar mobile phase and n-hexane/2-propanol as a non-polar mixture.

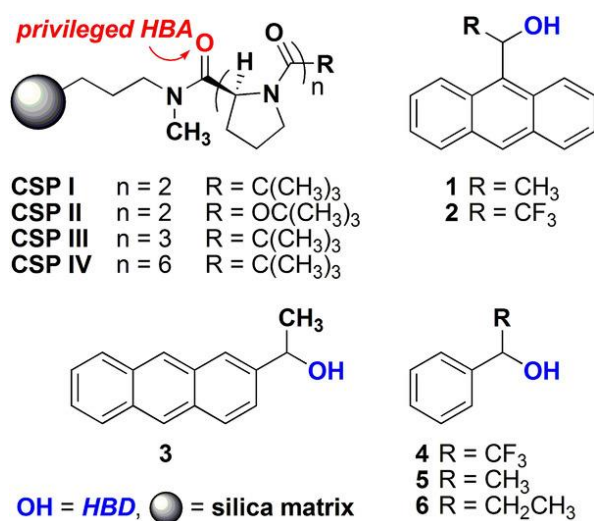


Figure 24. Structures of Pirkle-Type polyproline selectors and aromatic alcohols (1-6) as selectands in MD simulations. [159]

Furthermore, the chosen chiral selectors made it possible to examine how oligomer length and terminal group affect selectivity because of the deliberate structural modification made in the CSP series. Based on this, the following data produced by the simulations: water/methanol elution conditions result in a different recognition mechanism compared to NP elution conditions; overcrowding at the interface increases for CSP IV; affecting the arrangement of the analyte's attachment on the surface; carbonyl oxygens near the Si layer have been shown to be preferentially involved in chiral recognition as acceptors of hydrogen bonds; HB is the main interaction governing recognition and selectivity coupled with steric encumbrance effects on the chiral surface. The computed selectivity's were compared with the experimental values whenever possible, and a good overall agreement was found.

2. Objectives of this thesis in the field of CSPs

Based on the Whelk-O1 selector, two totally synthetic structures have been designed and synthesized in order to reproduce the same interactions of the Pirkle Type selector. We began by examining the chiral stationary phase DACH-DNB which was characterized by the 3,5-dinitrobenzoyl derivative of 1,2-diaminocyclohexane and has the capacity to separate several racemates, including alcohols, esters, ketones, acids, sulphides, phosphines, selenoxides, phosphonates, thiophosphinosides, phosphine selenides, phosphine adducts with borane, β -lactams, organometallics, atropoisomers and heterocycles. Simultaneously, the chiral stationary phase Whelk-O1, whose structure is based on 1-(3,5-dinitrobenzamido)-1,2,3,4-tetrahydrophenantrene, was also considered. This phase provides the separation of racemates belonging to numerous families, such as amides, epoxides, esters, urea, carbamates, ethers, aziridines, phosphonates, aldehydes, ketones, carboxylic acids and alcohols; moreover, being an electron acceptor/donor phase π allows a broad selectivity, permitting the resolution of a broad range of non-derivatized racemates. The combination of the structures of these stationary phases gave rise to the idea of designing and synthesizing two new selectors. Starting from 6-hydroxy-1-naphthoic acid, the hydroxyl group is functionalized by a sequence of synthetic steps and then this procedure yields 6-(allyloxy)-1-naphthyl chloride. The latter compound then reacts with either (*R,R*) or (*S,S*)-*t*-butyl(2-(3,5-dinitrobenzamido)cyclohexyl) carbamate. Two structures (*R,R*)**Sel1** and (*S,S*)**Sel1**, with distinct stereochemistry are prepared. It was possible to synthesize a second selector, **Sel2**, which was likewise obtained in both configurations, and which simplified the structure of **Sel1** by removing the naphthalene moiety. The following steps were performed: first a *click thiol-ene*

reaction was carried out in order to facilitate the anchoring of the selectors on silica, obtaining four distinct stationary phases which were used after packing chromatographic columns with a geometry of 150x4.6 mm x LD. Several racemic combinations were then injected into these columns to evaluate their ability to separate enantiomers; in particular 1-(9-anthryl)-2,2,2-trifluoroethanol and 1,1'-bi-(2-naphthol) were promising. Based on the obtained results, further studies of molecular docking with **Sel1** and **Sel2** respectively with 1,1'-bi-(2-naphthol) were carried out to assess the type of interactions which are established between the selectors and the selectand and to explain the order of elution. In addition, a racemic mixture of **Sel1** was injected into the (*R,R*) Whelk-O1 column and showed good separation capabilities with very high resolution. Finally, NMR studies have been conducted, particularly between **Sel1** and Ibuprofen, which has further confirmed the detection capabilities of the selectors.

3. Materials and Methods

3.1 Chemicals and Reagents

6-Hydroxy-1-naphtoic acid, (1*R*,2*R*)-*N*-Boc-1,2-cyclohexanediamine, (1*S*,2*S*)-*N*-Boc-1,2-cyclohexanediamine, acryloyl chloride, and all solvents and reagents used were supplied by Merck life science (Darmstadt, Germany). Spherical Kromasil Silica 100 silica gel (pore size 100 Å, particle size 5.0 µm, specific surface area 320 m² g⁻¹) was purchased from Eka Nobel (Bohus, Sweden). Pre-coated silica gel F₂₅₄ sheets for TLC from Merck (Darmstadt, Germany) were used for reaction monitoring.

3.2 Instrumentation

The ¹H- and ¹³C- NMR spectra were obtained with either deuterated chloroform (CDCl₃) or deuterated methanol (CD₃OD) solution using a Bruker spectrometer. ¹H NMR spectra were obtained at 400 MHz, while ¹³C spectra were at 100 MHz. Resonances are expressed in parts per million (ppm) in relation to tetramethyl silane. The chromatographic analyses were conducted by JASCO liquid analytical chromatography (Tokyo, Japan), equipped with a 20 µl loop Rheodyne universal injector, two pump systems JASCO PU 980 and Jasco PU 1580 CO₂ and two detectors: spectrophotometric detector (Jasco UV 975) and circular dichroism detector (Jasco UV/CD 995). FT-IR spectra were obtained by Jasco FT/IR-6800. The instrument uses a Diffuse Reflectance Accessory (DRIFT) to analyze solid samples.

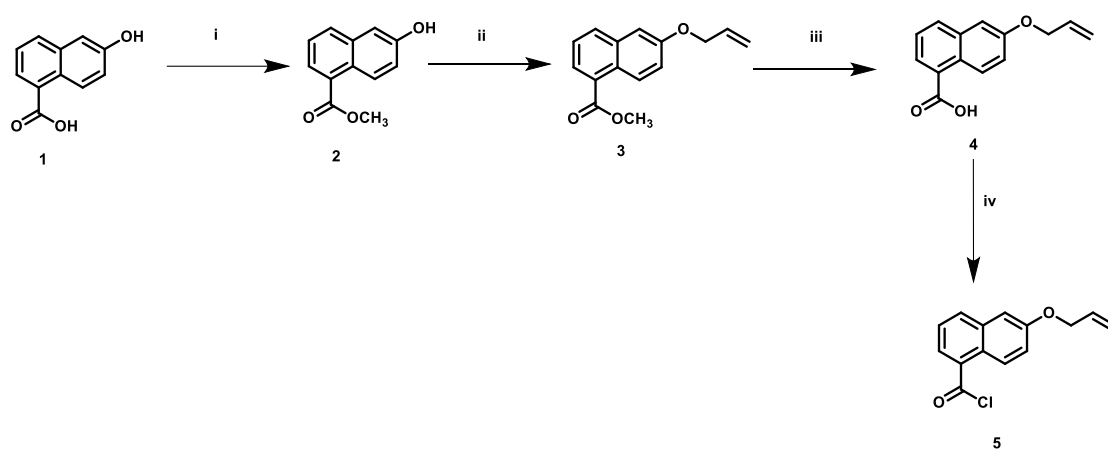
3.3 Software

The acquisition of the chromatograms was carried out using the Borwin software for the JASCO chromatograph (Tokyo, Japan). Processing of the chromatograms was carried out using Origin 6.0 software and processing of the NMR spectra using MestreNova.

3.4 Synthesis of (*R,R*) and (*S,S*)-Sel1

Each step of synthesis obtained a good product yield and was characterized using ^1H -NMR, ^{13}C -NMR and FT-IR.

3.4.1 Synthesis of 6-(allyloxy)-1-naphtoyl chloride

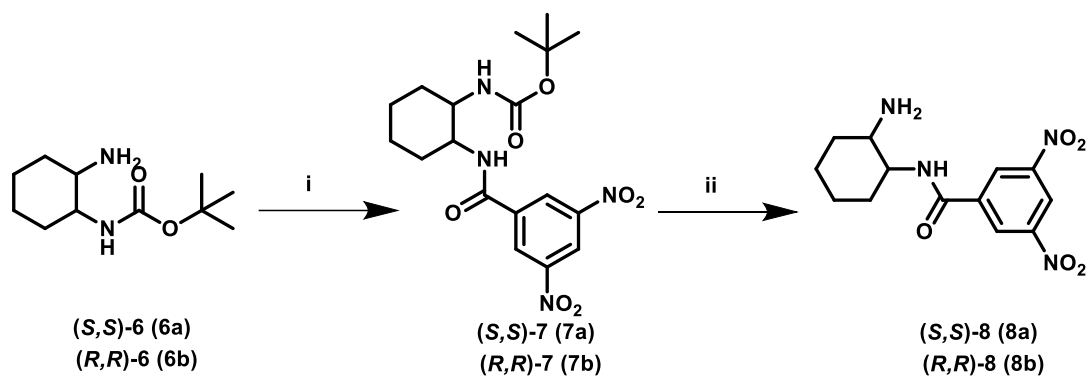


Scheme 1. Synthesis of 6-(allyloxy)-1-naphtoyl chloride (**5**). **i)** SOCl_2 , MeOH, R.T., 3h, (yield: 91%). **ii)** Allyl bromide, K_2CO_3 , DMF dry, N_2 , R.T., 12h (yield: 68%). **iii)** 2N KOH, THF, 50 °C, 12h (yield: 86%) **iv)** SOCl_2 , reflux, N_2 (not isolated), 3h.

For the synthesis of intermediate **5**, 6-hydroxy-1-naphtoic acid **1** was solubilised in methanol, and then thionyl chloride was added. The ester derivative **2** was dissolved in *N,N*-dimethylformamide at room temperature in presence of potassium carbonate. The solution was magnetically stirred under inert atmosphere, due to the presence of nitrogen flow, and placed in an ice bath. Subsequently, allyl-bromide is added drop by drop to promote the substitution and the consequent formation of intermediate **3**. The intermediate **3** is then hydrolysed in a solution of tetrahydrofuran and potassium hydroxide to obtain

intermediate **4**. Finally, the treatment with thionyl chloride provided the desired acyl chloride **5**.

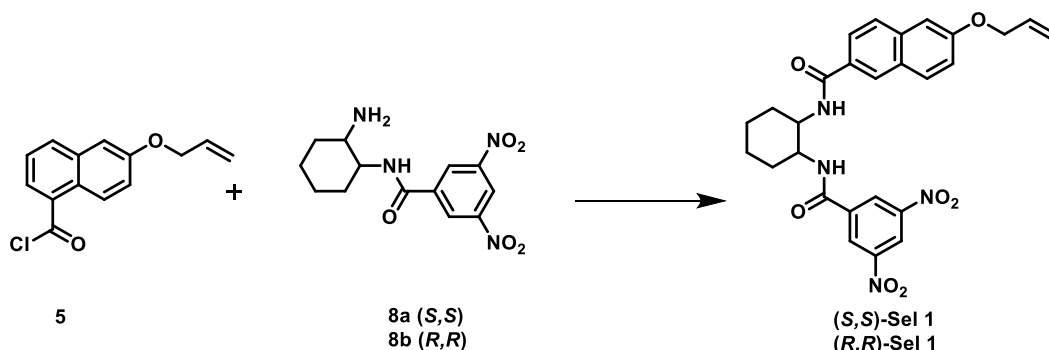
3.4.2 Synthesis of *N*-((1*S*,2*S*)-2-aminocyclohexyl)-3,5-dinitrobenzamide (**8a**; **8b**)



Scheme 2. Synthesis of *N*-((1*S*,2*S*)-2-aminocyclohexyl)-3,5-dinitrobenzamide **8a** and *N*-((1*R*,2*R*)-2-aminocyclohexyl)-3,5-dinitrobenzamide **8b**. **i**) 3,5-dinitrobenzoyl chloride, TEA, CHCl₃ dry, N₂, 3h (yield: 90%). **ii**) 12 N HCl, THF, 50 °C, 2h (yield: 93%).

For the synthesis of the desired amine [(*S,S*)-(**8**)], namely **8a**, (*S,S*)-*N*-Boc-1,2-cyclohexanediamine **6a** was dissolved in chloroform and then diisopropylethylamine was added to the solution. A solution of dinitrobenzoyl chloride also solubilised in chloroform, was then added drop by drop to the solution obtained, which was kept in an inert atmosphere, due to the presence of nitrogen flow, and placed in an ice bath. Subsequently, the carbamate **7a** thus produced was solubilised in dichloromethane and deprotected by acidification with trifluoroacetic acid, obtaining amine **8a**. The same procedure was used to obtain **8b** starting from (*R,R*)-*N*-Boc-1,2-cyclohexanediamine **6b**.

3.4.3 Synthesis of (*R,R*)- and (*S,S*)-Sel1



Scheme 3. Synthesis of (*R,R*)-Sel1 and (*S,S*)-Sel1.

(*S,S*)-Sel1 and (*R,R*)-Sel1 were synthesized starting from intermediate **5**, which was dissolved in anhydrous chloroform; then diisopropyl ethylamine and intermediate **8a** and **8b** were added. This reaction has led to obtaining a good product (yield 68.5%).

General procedure for synthesis of intermediate 2

Preparation of the methyl ester intermediate of methyl 6-hydroxy-1-naphtoate: 6-hydroxy-1-naphtoic acid (940.0 mg; 5 mmol) was solubilized in methanol ($V=10.0$ mL), then thionyl chloride (5 mmol; 0.36 mL; $d=1.64$ g/mL) was added drop by drop. The reaction was left at 65 °C and its course is monitored by TLC until complete after 3 hours (Mobile Phase: EtOAc /Hex 2:1). The product was concentrated at rotavapor to remove the excess of thionyl chloride and methanol. The following organic product was extracted by liquid extraction of ethyl acetate and water (3x20 ml). The organic phase was first washed with an aqueous solution saturated with NaHCO_3 and then with an aqueous solution saturated

with sodium chloride. Finally, the intermediate **2** was dried over anhydrous Na₂SO₄ and concentrated at rotavapor.

Quantity obtained: 499.0 mg (C₁₂H₁₀O₃; MW: 202.21).

Aspect: White solid.

Yield: 91.0%.

¹H-NMR (400 MHz, Methanol-d₄, δ, ppm): 8.54 (1H, d, 1H_{Ar}, J = 9.1 Hz), 7.75 (1H, d, 1H_{Ar}, J = 7.2 Hz), 7.68 (1H, d, 1H_{Ar}), 7.22 (dd, 1H_{Ar}, J = 8.2 Hz, J = 7.8 Hz), 7.02 (2H, d, 2H_{Ar}, J = 8.6 Hz), 3.78 (s, 3H, -CH₃).

¹³C{H}-NMR (101 MHz, Methanol-d₄, δ, ppm): 168.33, 155.25, 135.79, 131.38, 126.95, 126.84, 126.75, 125.80, 124.51, 119.52, 109.25, 51.13.

FT-IR-ATR (ν_{max}/cm⁻¹): 3389, 2952, 2918, 2544, 1690, 1623.

General procedure for synthesis of intermediate **3**

Preparation of the methyl 6-(allyloxy)-1-naphtoate: starting from intermediate **2** (467.10 mg; 2.31 mmol) which was dissolved in *N,N*-dimethyl formamide anhydrous (V= 12.0 mL), then the potassium carbonate (658.52 mg; 4.62 mmol) was added. The solution was magnetically stirred under inert atmosphere, due to the presence of nitrogen flow, subsequently, allyl bromide was added drop by drop (2.31 mmol; 0.19 mL; d= 1.40 g/mL) at 0 °C. The reaction was left overnight at room temperature; its course is controlled by TLC until it finished (mobile phase: EtOAc/n-Hexane 3:1). Then was quenched by the addition of a NaOH solution 0.1 M and the organic product was extracted by ethyl acetate (3x20 mL). Finally, the intermediate **3** was dried over anhydrous Na₂SO₄ and concentrated at rotavapor.

Quantity obtained: 298.0 mg (C₁₅H₁₄O₃; MW: 242.27).

Aspect: White solid.

Yield: 52.0%.

¹H NMR (400 MHz, Chloroform-d, δ , ppm): 8.65 (d, 1H, $1H_{Ar}$, J = 9.4 Hz), 7.85 (d, 1H, $1H_{Ar}$, J = 7.3 Hz), 7.71 (d, 1H, $1H_{Ar}$, J = 8.2 Hz), 7.27 (t, 1H, $1H_{Ar}$, J = 7.8 Hz), 7.12 (dd, 1H, $1H_{Ar}$, J = 9.4 Hz, J = 2.7 Hz), 6.99 (d, 1H, $1H_{Ar}$, J = 2.6 Hz), 5.95 (m, 1H -CH=, J = 22.5 Hz, J = 10.5 Hz, J = 5.3 Hz), 5.30 (d, 1H, =CH₂, J = 17.3 Hz), 5.15 (d, 1H, =CH₂, J = 10.5 Hz), 4.49 (d, 2H, -CH₂, J = 5.3 Hz), 3.81 (s, 3H, -CH₃).

¹³C{H}- NMR (101 MHz, Chloroform-d, δ , ppm): 168.14, 156.51, 135.30, 133.00, 132.14, 127.97, 127.54, 127.03; 126.88; 125.10; 120.58; 117.94; 107.63; 68.80; 52.13.

FT-IR-ATR (ν_{max}/cm^{-1}): 3081, 3017, 1623, 1595, 1430, 1130.

General procedure for synthesis of intermediate 4

Preparation of the 6-(allyloxy)-1-naphthoic acid: starting from intermediate 3 (363.40 mg; 1.50 mmol) which was solubilized in MeOH (V= 3.0 mL), then a solution of KOH 1M (V= 2.0 mL) was added. The solution was magnetically stirred and placed in a bath at 50 °C. The course of the reaction is controlled by TLC until complete after 2 hours (Mobile Phase: AcOEt/n-Hexane 3:1). Once the hydrolysis was finished the solution was acidified with HCl up to pH~4, then the organic product was extracted with ethyl acetate (3x20 mL). Finally, the intermediate 4 was dried over anhydrous Na₂SO₄ and concentrated at rotavapor.

Quantity obtained: 322.5 mg (C₁₄H₁₂O₃; MW: 228.24).

Aspect: White solid.

Yield: 94.0%.

¹H NMR (400 MHz, Chloroform-d, δ , ppm): 8.93 (d, 1H, $1H_{Ar}$, J = 9.5 Hz), 8.17 (d, 1H, $1H_{Ar}$, J = 6.4 Hz), 7.88 (d, 1H, $1H_{Ar}$, J = 8.2 Hz), 7.42 (t, 1H, $1H_{Ar}$, J = 7.8 Hz), 7.27 (dd, 1H, $1H_{Ar}$, J = 9.5, J = 2.7 Hz), 7.13 (d, 1H, $1H_{Ar}$, J = 2.6 Hz), 6.06 (m, 1H, -

CH=, J = 22.5 Hz, J=10.5 Hz, J=5.3 Hz), 5.41 (dd, 2H, =CH₂, J = 17.3 Hz, J=1.4 Hz), 5.27 (dd, 2H, =CH₂, J = 10.5 Hz, J=1.3 Hz), 4.60 (d, 2H, -CH₂, J = 5.3 Hz).

¹³C{H}- NMR (101 MHz, Chloroform-d, δ, ppm): 173.12, 156.56, 135.43, 133.33, 132.96, 129.51, 127.64, 127.17, 125.66, 125.15, 120.88, 118.01, 107.79, 68.83.

FT-IR-ATR (ν_{max}/cm⁻¹) 3061, 1673, 1421, 1237.

General procedure for synthesis of intermediate 7a and 7b

Preparation of the t-butyl (2-(3,5-dinitrobenzamido) cyclohexyl) carbamate: 7a and 7b were synthesized starting from **6a** and **6b** (100.0 mg; 0.47 mmol). They were dissolved in anhydrous chloroform (V= 15.0 mL); then diisopropyl ethylamine (0.47 mmol; 0.082 mL; d= 740 g/mL) was added to this solution. The reactions were magnetically stirred under inert atmosphere, due to the presence of nitrogen flow and placed in an ice bath. A solution of 3,5-dinitrobenzoyl chloride (108.0 mg; 0.47 mmol) was then added drop by drop and solubilized in chloroform anhydrous. The course of the reaction was controlled by TLC until complete after 12 hours (Mobile Phase: AcOEt/n-Hexane 1:1). Then the reactions were quenched by the addition of a NaOH solution 0.1 M, and the organic product is extracted by ethyl acetate (3x20 mL). Then, the organic phases were washed with saturated aqueous solution of NaHCO₃ (1x20mL), and finally, the intermediates **7a** and **7b** were dried over anhydrous Na₂SO₄ and concentrated at rotavapor.

Quantity obtained: 190.45 mg (C₁₈H₂₄N₄O₇; Mw: 408.16).

Aspect: White Solid.

Yield: 99.0%.

¹H NMR (400 MHz, Chloroform-d, δ, ppm) 9.07 (s, 1H, 1H_{Ar}), 9.02 (s, 2H, 2H_{Ar}), 8.06 (d, 1H, -NHCO-OCH₃, J = 5.7 Hz), 4.62 (d, 1H, -NHCO-, J = 7.4 Hz), 3.65 (m, 1H, -CH), 3.49 (m, 1H, -CH), 2.32 (d, 1H, J = 13.2 Hz), 1.97 (d, 1H, -CH, J = 7.8 Hz),

1.78 (s, 1H, -CH), 1.72 (d, 1H, -CH, J = 8.0 Hz), 1.33 (d, 2H, -CH₂, J = 11.1 Hz), 1.29 (s, 9H, (-CH₃)₃), 1.18 – 1.10 (m, 1H, -CH).

¹³C{H}- NMR (101 MHz, Chloroform-d, δ, ppm): 161.96, 157.96, 148.62, 138.03, 127.32, 120.82, 80.76, 80.76, 58.35, 53.19, 31.95, 28.21, 24.60.

FT-IR-ATR (ν_{max}/cm⁻¹) 3081, 3017, 1623, 1595, 1430, 1130.

General procedure for synthesis of intermediate 8a and 8b

Preparation of the N-(2-aminocyclohexyl)-3,5-dinitrobenzamide: 8a and 8b were synthesized starting from intermediate **7a** and **7b** (169.10 mg; 0.41 mmol) which were solubilized in dichloromethane anhydrous (V= 5.0 mL), then trifluoroacetic acid (0.82 mmol; 0.063 mL; d= 1.49 g/mL) was added at 0° C. The reactions were left at a temperature of 35 °C overnight, and TLC monitors their course until it is complete (Mobile Phase: AcOEt/n-Hexane 1:1). The reactions were concentrated to remove the solvent and then were made some washes with n-hexane and diethyl ether and concentrated at rotavapor in order to remove the excess of trifluoroacetic acid.

Quantity obtained: 132.9 mg (C₁₃H₁₆N₄O₅; Mw: 308.29).

Aspect: Yellow Solid.

Yield: 79.0%.

¹H NMR (400 MHz, Chloroform-d, δ, ppm): 9.04 (dd, 3H, 3H_{Ar}, J = 16.1, J= 2.0 Hz), 3.99 (td, 1H, -CH, J = 11.3, J=4.3 Hz), 3.02 (td, 1H, -CH, J = 11.3, J=4.2 Hz), 2.06 (dd, 2H, -CH₂), 1.96 (dd, 2H, J = 11.3, J=2.5 Hz), 1.79 (dd, 2H, J = 7.7, J=2.1 Hz), 1.35 (dd, 2H, J = 9.2, J=5.4 Hz).

¹³C{H}- NMR (101 MHz, MeOD₄, δ, ppm): 164.51, 148.59, 137.26, 127.40, 120.69, 54.69, 51.77, 30.89, 29.76, 24.16, 23.55.

FT-IR-ATR (ν_{max}/cm⁻¹) 3241, 2857, 1620, 1340.

General procedure for synthesis of (*R,R*)-Sel1 and (*S,S*)-Sel1

Preparation of the 6-(allyloxy)-*N*-(2-(3,5-dinitrobenzamido) cyclohexyl)-2-naphthamide: (*R,R*)-Sel1 and (*S,S*)-Sel1 were synthesized starting from intermediate 4 (98.40 mg; 0.43 mmol) that was allowed to react in thionyl chloride (V= 2.0 mL) under inert atmosphere, for the presence of nitrogen flow, at a temperature of 85 °C. The reaction was left for three hours and half obtaining the intermediate 5. Subsequently, the product obtained was concentrated at rotavapor to remove excess thionyl chloride. Intermediate 5 was supplemented with anhydrous chloroform (V= 20.0 mL); then diisopropyl ethylamine (0.43 mmol; V= 0.074 mL), and intermediate 8a and 8b (132.91 mg; 0.43 mmol) were added, respectively, in the two reactions. The reactions were magnetically stirred under inert atmosphere, due to the presence of nitrogen flow, at room temperature for 24 hours and its course was monitored through TLC until it is complete (Mobile Phase: AcOEt/n-Hexane 3:1). Both the products were extracted with ethyl acetate (3x20 mL), the organic phases were washed first with a water solution of NaOH 1M up to pH~8, then with a water solution of HCl 2N up to pH~4. The final products were purified through a chromatographic column with silica gel. Mobile Phase: AcOEt/n-Hexane 1:1.

Quantity obtained: 152.0 mg (C₂₇H₂₆N₄O₇; MW: 518.53);

Aspect: Brown Solid.

Yield: 69.0%.

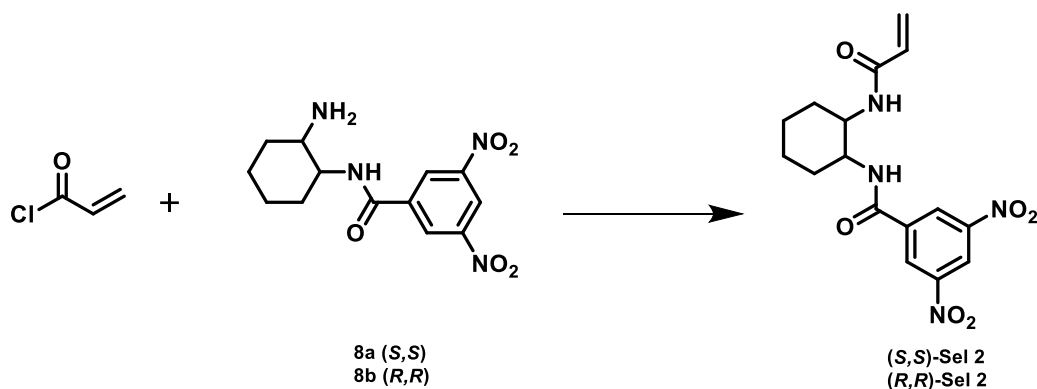
¹H NMR (400 MHz, CDCl₃, δ, ppm): 8.66 (d, 1H, 1H_{Ar}, J = 8.5 Hz), 8.42 (s, 3H), 7.61 – 7.41 (m, 2H, 2H_{Ar}), 7.19 (s, 1H, 1H_{Ar}), 7.18 – 7.03 (m, 2H, 2H_{Ar}), 6.83 (d, 1H, 1H_{Ar}, J = 2.4 Hz), 6.71 (d, 1H, 1H_{Ar}, J = 8.5 Hz), 6.52 (dd, 1H, 1H_{Ar}, J = 9.2, J=2.5 Hz), 6.01 (m, 2H, -CH₂, J = 22.6, J=10.6, J=5.4 Hz), 5.39 (dd, 1H, J = 17.3, J=1.3 Hz), 5.27 (dd, 1H, J = 10.5, J=1.1 Hz), 4.45 (d, 2H, J = 5.4 Hz), 4.03 (dt, 1H, J = 10.2, J=5.5 Hz),

2.40 – 2.11 (m, 2H), 2.06 – 1.84 (m, 2H), 1.75 – 1.53 (m, 1H), 1.41 (d, 3H, J = 38.6 Hz), 1.28 – 1.09 (m, 1H).

$^{13}\text{C}\{\text{H}\}$ - NMR (101 MHz, Chloroform-*d*, δ , ppm): 161.96, 157.96, 148.62, 138.03, 127.32, 120.82, 80.76, 80.76, 58.35, 53.19, 31.95, 28.21, 24.60.

FT-IR-ATR ($\nu_{\text{max}}/\text{cm}^{-1}$) 3081, 3017, 1623, 1595, 1430, 1130.

3.5 Synthesis of (*R,R*)- and (*S,S*)-Sel2



Scheme 4. Synthesis of (*R,R*) and (*S,S*)-Sel2

The synthesis of (*S,S*)-Sel2 and (*R,R*)-Sel2 started from **8a** and **8b**, respectively. They were solubilized in anhydrous chloroform, and then triethylamine and acryloyl chloride were added drop by drop at 0 °C.

General procedure for synthesis of (*R,R*)-Sel1 and (*S,S*)-Sel2

Preparation of the *N*-(2-acrylamidocyclohexyl)-3,5-dinitrobenzamide: starting from intermediated **8a** and **8b** (214.65 mg; 0.93 mmol) which were solubilized in anhydrous chloroform ($V = 3.0$ mL), then triethylamine (2.79 mmol; 0.38 mL; $d = 726$ g/cm³) and finally acryloyl chloride (1.86 mmol; 0.235 mL; 1.11 g/mL) was added drop by drop at 0° C. The reaction was magnetically stirred in an inert atmosphere under nitrogen flow at room temperature overnight, and its course was monitored through TLC until it is complete (Mobile Phase: AcOEt/ *n*-Hexane 1:1). Then, the organic product was extracted by ethyl acetate (3x20 mL) and dried over anhydrous Na₂SO₄.

Quantity obtained: 195.0 mg (C₁₆H₁₈N₄O₆; Mw: 362.34);

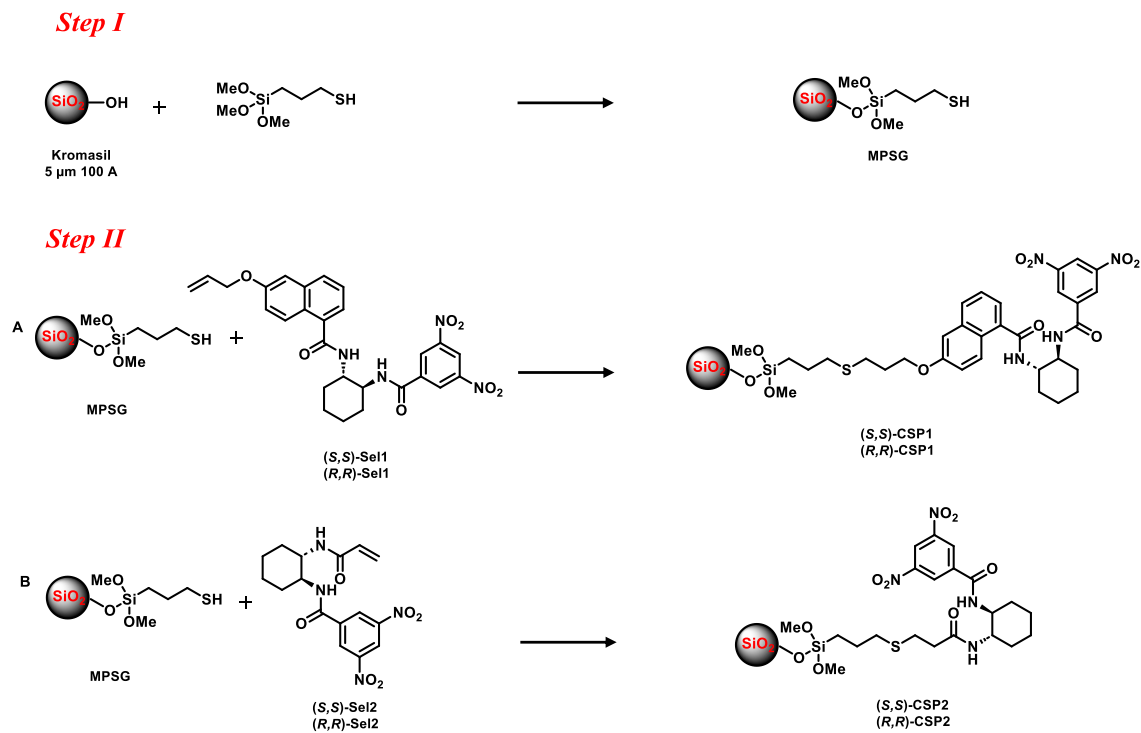
Aspect: Brown Solid.

Yield: 98.0%.

¹H NMR (400 MHz, CDCl₃, δ, ppm): 9.37 (1H, s, H_{Ar}), 9.07 (2H, s, H_{Ar}), 8.27 (1H, s, -NH-), 7.02 (1H, s, -NH-), 6.18 (1H, -CH=CH₂, m, J=2 Hz), 5.87 (2H, -CH=CH₂, m, J=2Hz), 3.32 (2H, m, J= 2Hz), 3.25 (2H, m, J= 4Hz), 1.66 (2H_{Al}, m, J= 2Hz), 1.61 (1H_{Al}, m, J= 2Hz), 1.44 (1H_{Al}, m, J= 2.4 Hz), 1,35 (2H_{Al}, m, J= 4Hz), 1.22 (2H_{Al}, m, J=4Hz).

¹³C{H}- NMR (101 MHz, Chloroform-d, δ, ppm): 25.01, 30.85, 50.09, 51.32, 121.62, 124.46, 127.75, 128.04, 138.55, 147.54, 166.42, 167.57.

3.6 Immobilization on silica



Scheme 5. Activation of silica gel and immobilization of selectors. **Step I:** Preparation of mercaptopropyl-silica gel MPSG. **Step II:** A synthesis of (S,S)-CSP1 and Step II B synthesis of (S,S)-CSP2.

Step I: Preparation of mercaptopropyl-silica gel

6.40 g of Kromasil Silica (5 μ , 100 \AA , 320 m²/g), previously dried at reduced pressure (0.1 mmHg at 120 °C for 2 h), was dispersed in 90.0 mL of dry toluene at 60° C. Finally, a solution of (3-mercaptopropyl) trimethoxysilane (3.26 g; 16.59 mmol) in 3.0 mL of dry toluene was added dropwise over 20 min. The reaction was stirred for 20 h at 60 °C under an inert atmosphere due to the presence of nitrogen. The modified silica, MPSG silica, was isolated by filtration, washed with toluene, methanol, and dichloromethane (30.0 mL each), and then dried at

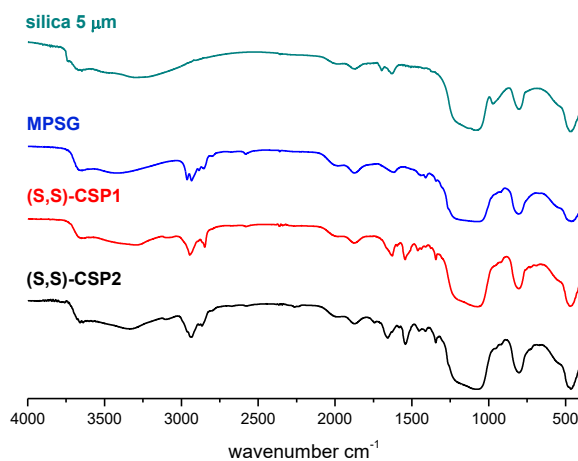
reduced pressure (0.1 mmHg; T= 60 °C), until the weight is constant (7.13 g; weight increment 11%).

Step II: Anchoring of selectors on mercaptopropyl silica

The (*S,S*)-**Sel1** (0.50 g; 0.87 mmol) was dissolved in 40.0 mL of chloroform (ethanol stabilized, filtered on neutral aluminum oxide, under a nitrogen atmosphere, and degassed with helium). 3.15 g of MPSG-silica was dispersed in the solution previously obtained. 2,2'-azobis(2-methylpropionitrile), AIBN (0.072 g; 0.44mmol) was added to the reaction flask three times (at the start, after 2 and 4 h). The reaction was stirred for 6 h at 90° C. Modified silica was filtered, washed with chloroform, acetone and dichloromethane, and dried at reduced pressure (0.1 mmHg; T= 50 °C) up to constant weight (3.28 g; weight increment 4%). The (*S,S*)-**Sel2** (0.20 g; 0.54 mmol) was anchored in the same way onto 2.34 g of MPSG-silica previously obtained. Modified silica was filtered, washed with chloroform, acetone and dichloromethane, and dried at reduced pressure (0.1 mmHg; T= 50 °C) up to constant weight (2.45 g; weight increment 5 %).

3.6.1 Characterization of (S,S)-CSP1 and (S,S)-CSP2

FT-IR- DRIFT



Kromasil 5 μm 100 Å (v_{\max}/cm^{-1}): 3296 (v: -OH), 1086 (v: Si-O).

Kromasil MPSG (v_{\max}/cm^{-1}): 2938 (v: -CH₂), 2847 (v: -CH₂), 1096 (v: Si-O).

(S,S)-CSP1 (v_{\max}/cm^{-1}): 3278 (v: CO-NH), 3278 (v: -CH₂), 2944 (v: -CH₂), 1682 (v: C=O); 1344 (v: -NO₂), 1078 (v: Si-O).

(S,S)-CSP2 (v_{\max}/cm^{-1}): 3278 (v: CO-NH), 3278 (v: -CH₂), 2944 (v: -CH₂), 1682 (v: C=O); 1344 (v: -NO₂), 1078 (v: Si-O).

Elemental Analysis

	Surface Area (m ² /g)	%C	%H	%S	%N	Selector (μm/g)	Selector (μm/m ²)
MPSG	320	5.00	1.00	2.03	0.15	630.07	2.2
(S,S)-CSP1	320	7.65	1.18	1.98	0.58	103.50	0.35
(R,R)-CSP-2	320	7.98	1.14	2.00	0.74	132.05	0.45

3.7 LC Packing column

A stainless-steel column (150x4.6 mm L x I.D.) was packed by the slurry method. About 2.5 g of CSP was used to pack the column, which was dispersed in chloroform/isopropanol 80:20 and sonicated for 20 min. The slurry was instantly pumped into the column by methanol, and the packing pressure was 700 bar.

3.8 Molecular Docking

Structures of **(S,S)-Sel1**, **(S,S)-Sel2** and 1,1'-bi-(2-naphthol) were submitted to conformational search according to the algorithm implemented in the software package SPARTAN 10, v. 1.1.0 (Wavefunction, Inc., Irvine, CA, USA). Inside a window of 3 kcal such an analysis afforded just one conformation of 1,1'-bi-(2-naphthol) in M or P configuration (i.e., **(M)-Guest** and **(P)-Guest**), while two more representative geometries of **(S,S)-Sel2** and three of **(S,S)-Sel1**. Next, rigid dockings between the structures of the **(S,S)-Sel2** host and the M and P 1,1'-bi-(2-naphthol) guest were performed using the homemade computer program MolInE. [181] The same computational procedure was repeated for the dockings between the structures of the **(S,S)-Sel1** host and the M and P 1,1'-bi-(2-naphthol) guest. The host-guest approach options set were 50 directions of translation and 256 relative orientations of the guest to host for each couple of host-guest conformations. Molecular Mechanics optimizations of all the adduct geometries obtained by the rigid-docking algorithm were next performed using the Batchmin computer program, with the following options set: MM2* Force Field, PR conjugate gradient minimization. Finally, again resorting to the Spartan program, all the geometries of adducts **(S,S)-Sel2/(P)-Guest** and **(S,S)-Sel2/(M)-Guest** were also submitted to equilibrium geometry optimization by resorting to the following five independent semiempirical levels of theory AM1, PM3, PM6, RM1, MNDO. Also the **(S,S)-Sel1/(P)-Guest** and **(S,S)-Sel1/(M)-Guest** adducts were subjected to geometry optimization but, in this case, limited only to the semi-empirical PM3 level of theory.

4. Results and Discussion

The idea of the project is if it is conceivable to suggest an experimental strategy for people who wish to approach the construction of novel stationary phases with wholly synthetic selectors, considering the adaptability of fully synthetic selectors in tackling even difficult problems. The experimental process is broken down into the following steps: a) synthesize chiral molecules that are capable of multiple interactions (hydrogen bonding and Van der Waals interactions); b) assess enantioselective capabilities; c) after this capacity is assessed, anchor the selectors to silica; d) assess the CSPs from a thermodynamic perspective; e) assess the stability of the introduced selector-selectand using molecular docking techniques.

4.1 Preliminary evaluation of chiral capabilities: NMR studies

We investigated the enantioselective properties of the synthesized selectors using them as chiral solvating agents (CSAs) in NMR spectroscopy. Chiral solvating agents induce chemical shift inequalities of specific (proton) signals of enantiomers in NMR spectra. In this context, CDCl₃ was selected as the solvent, and the presence of a chiral solvating agent, specifically (*S,S*)-**Se11**, was used to induce distinct chemical shifts of the proton signals of the alpha-hydrogen of ibuprofen enantiomers. Two prepared samples were employed: one contained an equimolar solution of the selector and ibuprofen in CDCl₃ (50 mM, at 25°C), while the other consisted solely of ibuprofen under similar conditions. Both

samples underwent ^1H -NMR spectroscopy, and the respective spectra were registered and compared. The comparative analysis revealed that in the presence of the selector **(S,S)-Sel1**, the proton on the stereogenic centre of ibuprofen exhibited signal splitting, as depicted in **Figure 25**. This splitting phenomenon suggests a pronounced enantioselectivity of **(S,S)-Sel1**.

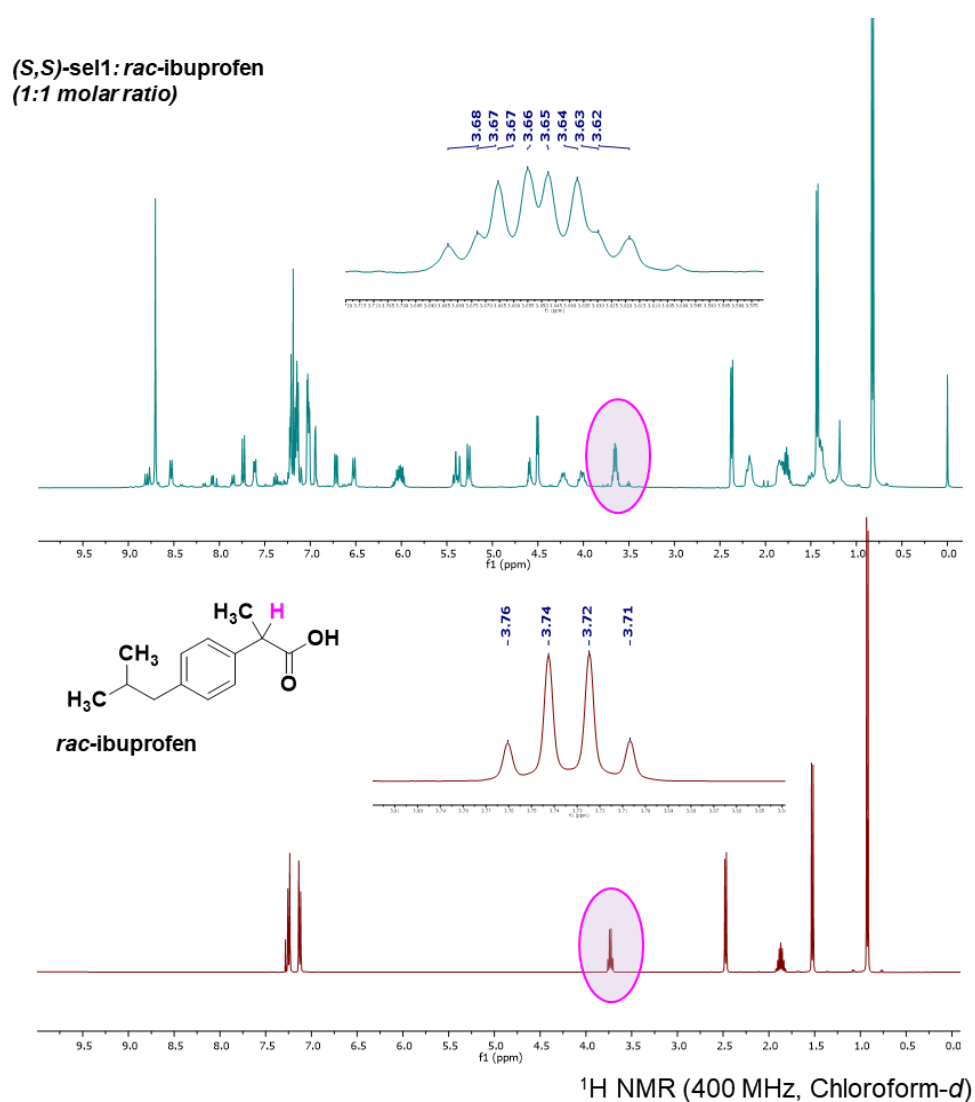


Figure 25. Comparison between the two ^1H NMR spectra.

Moreover, in order to assign the signals of ^1H NMR spectra to *S*- and *R*-enantiomers of ibuprofen, the single enantiomers were also tested in the presence of **(*S,S*)-Sel1** as shown in **Figure 26**.

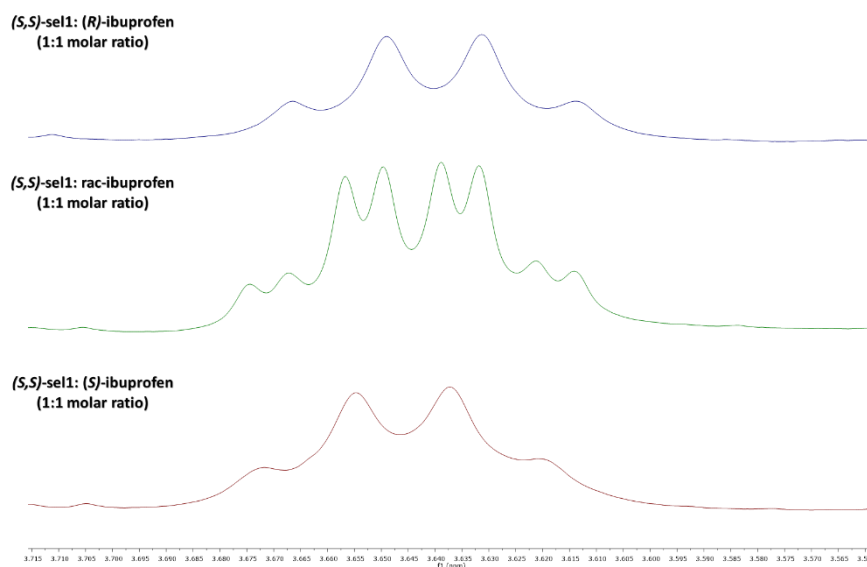


Figure 26. ^1H NMR spectra to *S*- and *R*- enantiomers of Ibuprofen in the presence of **(*S,S*)-Sel1**.

The enantioselective recognition capacity of selectors obtained was also assessed by injecting a mixture of **Sel1** enantiomers onto a column (*R,R*)-Whelk-O1 5 μm (250x4.6 mm LxID). The analysis shows that the two enantiomers are solved with an α value of 3.17. The **(*R,R*)-Sel1** is eluted at 12.17 minutes, and the **(*S,S*)-Sel1** elutes at 30.58 minutes (**Figure 27 and Table 1**).

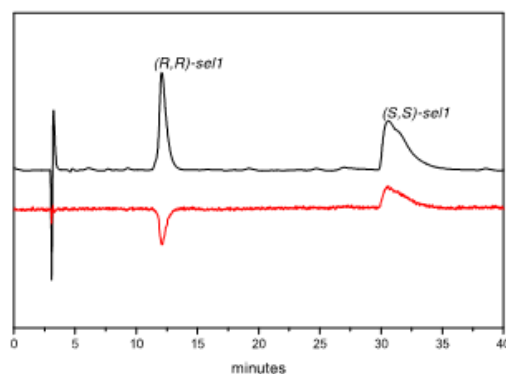


Figure 27. Chromatogram of (*S,S*)- and (*R,R*)-**Sel1**. Column: (*R,R*)-Whelk-O1 5 μ m (250x4.6 mm LxID Mobile phase, n-Hexane/Chloroform (40/60% v/v)+0.5 % MeOH. Flow rate, 1 mL/min; UV wavelength, 280 nm (black trace top); CD wavelength 280 nm (red trace bottom).

	Rt (min)	<i>k</i>	α
(<i>R,R</i>)- Sel1	12.17	2.69	3.17
(<i>S,S</i>)- Sel1	30.58	8.52	

Table 1. Resolution and selectivity parameters of **Sel1** and **Sel2** condition reported in **Figure 27**.

Although not considered orthodox, the effective separation of the racemate of **Sel1** on a chiral column instills confidence in its enantioselective capabilities. Therefore, given the very good separation of the racemate of **Sel1** on the Whelk-O1 column, we have subsequently packed (*S,S*)-**CSP1**. This decision was made to evaluate the separation proficiency of analytes sharing structural similarities with Whelk-O1, specifically with the presence of groups capable of hydrogen bond interactions and bulky aromatic groups within these analytes. These preliminary studies on the enantio-recognition capability in a solution of the

developed selectors provided us with a starting point to assess whether it was worthwhile to proceed with the chromatographic evaluation.

4.2 HPLC enantioseparation

To determine the enantioselective capability of the stationary phase, we inject racemic compounds, such as 1-(9-anthryl)-2,2,2-trifluoroethanol and 1,1'-bi-(2-naphthol), containing functional groups that can interact with the selector (namely, hydroxyl groups for hydrogen bond interactions and bulky aromatic groups for van der Waals interactions). Then, we carried out a mobile phase optimization process to find the best eluent to analyze such compounds. The results show that the most effective eluent for **(S,S)-CSP1** (**Figure 28**) is n-hexane/chloroform (70/30% v/v) and n-hexane/chloroform (80/20% v/v) for **(S,S)-CSP2** (**Figure 29**). The parameters obtained from enantiomeric separation such as selectivity factor (α), resolution (R_s), and retention times (R_t) are indicated in **Table 2**. The same analytes were injected for both columns, and the chromatograms show discrete separation capacity for racemic mixtures.

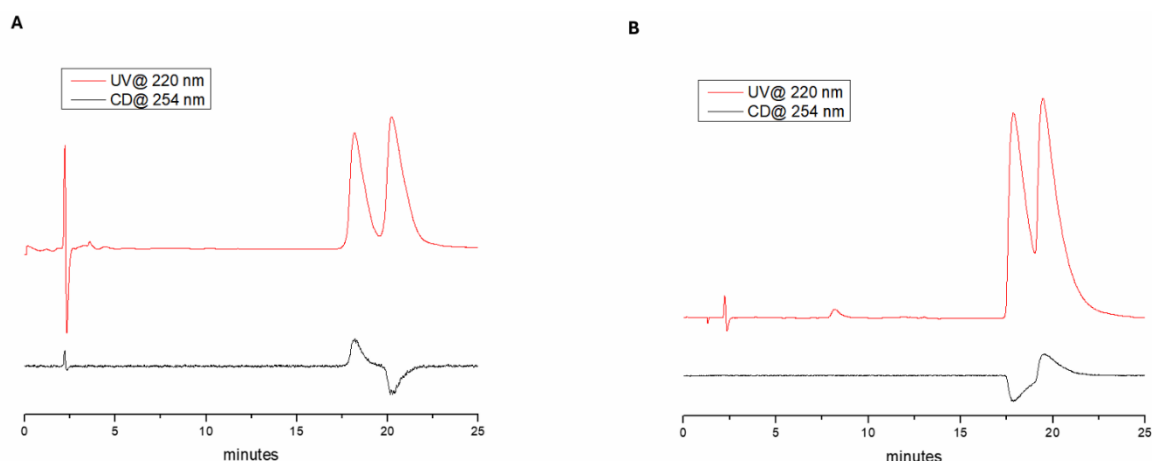


Figure 28. **A)** Chromatogram of 1-(9-anthryl)-2,2,2-trifluoroethanol in **(S,S)-CSP1**. Mobile phase, n-hexane/chloroform (70/30 % v/v). Flow rate, 1 ml/min; UV wavelength 220 nm; CD wavelength 254 nm. **B)** Chromatogram of 1,1'-bi-(2-naphthol) in **(S,S)-CSP1**.

Mobile Phase, n-hexane/chloroform (70/30 % v/v). Flow rate, 1 ml/min; UV wavelength 220 nm; CD wavelength 254 nm.

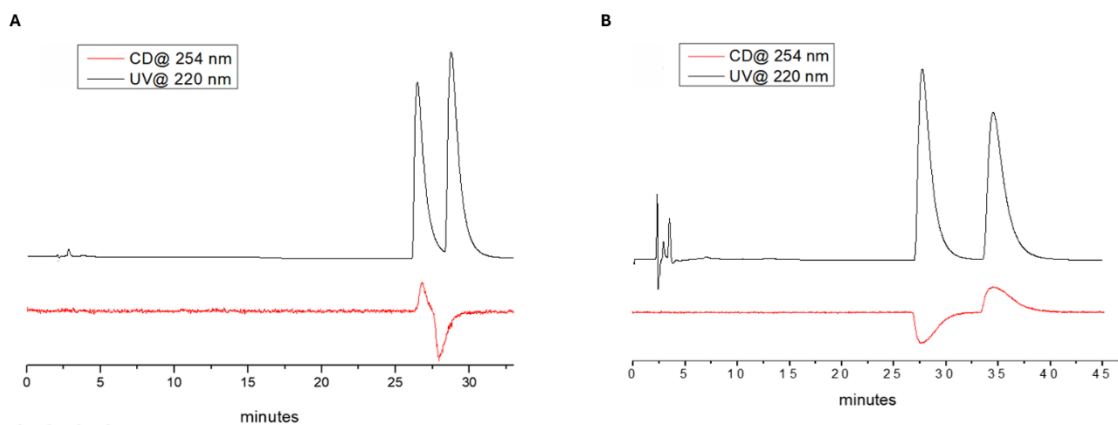


Figure 29. **A)** Chromatogram of 1-(9-anthryl)-2,2,2-trifluoroethanol in (*S,S*)-CSP2. Mobile Phase, n-hexane/chloroform (80/20 % v/v). Flow rate, 1 ml/min; UV wavelength 220 nm; CD wavelength 254 nm. **B)** Chromatogram of 1,1'-bi-(2-naphthol) in (*S,S*)-CSP2. Mobile Phase, n-hexane/chloroform (80/20 % v/v). Flow rate, 1 ml/min; UV wavelength 220 nm; CD wavelength 254 nm.

Column	Sample	k_1	k_2	α	R_s	$Rt1$	$Rt2$
(<i>S,S</i>)-CSP1	1-(9-Anthryl)-2,2,2-trifluoroethanol	7.60	8.60	1.13	1.37	17.92	20.01
	1,1'-Bi-(2-Naphthol)	7.03	7.74	1.10	1.09	17.87	19.45
(<i>S,S</i>)-CSP2	1-(9-Anthryl)-2,2,2-trifluoroethanol	12.17	13.29	1.09	1.24	26.45	28.70
	1,1'-Bi-(2-Naphthol)	12.41	15.71	1.27	1.63	27.36	34.09

Table 2. Resolution and selectivity parameters of (*S,S*)-CSP1 and (*S,S*)-CSP2 for racemates. Condition used are reported in **Figure 28** and **Figure 29** respectively.

4.3 Molecular Docking results

In **Figure 30** are reported the chromatograms of single enantiomers of 1,1'-Bi-(2-Naphthol), showing that the elution order on the (*S,S*)-CSPs is (*M*)- as first eluted and (*P*)- as second eluted enantiomer.

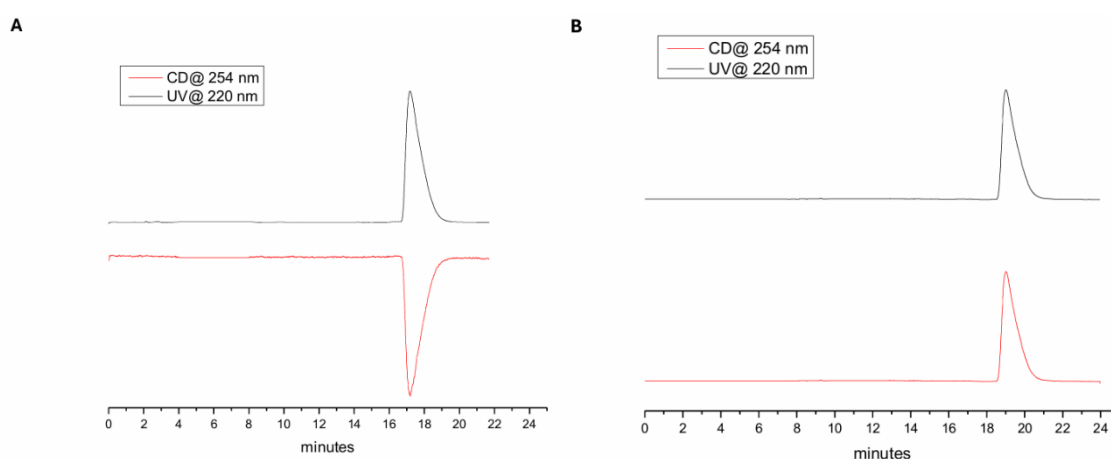


Figure 30. **A)** Chromatograms of (*M*)-1,1'-bi-(2-naphthol) and **B)** (*P*)-1,1'-bi-(2-naphthol) on (*S,S*)-CSP1. Mobile Phase, n-hexane/chloroform (70/30 % v/v). Flow rate, 1 ml/min; UV wavelength 220 nm; CD wavelength 254 nm.

From the docking analysis performed at the MM2* molecular mechanics level of theory between the (*S,S*)-Sel2 host and the (*M*)-1,1'-bi-(2-naphthol) guest structures (complex hereafter quoted with the acronym (*S,S*)-Sel2/(*M*)-Guest), within an energy window of 30 kcal they were obtained 188 adduct-geometries. In the same energy window, the docking performed between the (*S,S*)-Sel2 host and the (*P*)-1,1'-bi-(2-naphthol) guest structures (complex hereafter quoted with the acronym (*S,S*)-Sel2/(*P*)-Guest) afforded instead 96 adduct-geometries. The enantio-discrimination resulting by difference in energy stability accords with

the experimental data (i.e., *(S,S)*-Sel2/*(P)*-Guest most stable of the *(S,S)*-Sel2/*(M)*-Guest adduct), although the estimated Docking Energy Difference (DDE) values of -1.54 kcal is much more extensive with respect to the experimental one, that amounts to only -0.14 kcal. However, this difference is totally compatible with what was expected in consideration of the initial, necessarily not too high, level of calculation adopted (i.e. molecular mechanics). In answer to this consideration, all the 188 adduct-geometries of *(S,S)*-Sel2/*(M)*-Guest and 96 adduct-geometries of *(S,S)*-Sel2/*(P)*-Guest were submitted to further geometry-optimization steps (independent one to each other) based on the following five semiempirical Hamiltonians: 1) AM1; 2) PM3; 2) PM6; 2) RM1; 2) MNDO. Also in this case, the order of the assessed enantio-discrimination data appears correct, with the obtained DDE values now resulting quantitatively much more coherent with the experimental datum (Table 3).

	DDE	
	(BiNP-BiNM)	a
	kcal	
Experimental	-0.14	1.27
MM2*	-1.54	13.46
AM1	-0.79	3.82
PM3	-0.17	1.34
PM6	-0.88	4.43
RM1	-0.76	3.59
MNDO	-0.29	1.64

Table 3. Enantio-discrimination of racemic 1,1'-bi-(2-naphthol) estimated by docking analysis and compared with the relevant experimental data.

In particular, the best agreement has been obtained by using the PM3 Hamiltonian that, compared with the experimental one, afforded a $DDE_{PM3} - DDE_{Exp}$ difference of only -0.03 kcal, corresponding to a difference in resolution $a_{PM3} - a_{Exp}$ of 0.07 units. Thus, it seems reasonable to be able to extract from the structures of the diastereomeric adducts obtained with the best computational agreement information regarding the mechanism underlying the observed enantioselectivity. This can be done by analyzing the 3D structure of the most stable diastereomeric adducts, which are reported in **Figure 31**. Within the **(S,S)-Sel2/(P)-Guest** structure it is well visible the establishment of three effective H-Bonds between the host and guest geometries. Two of these involve the participation of the electron-accepting N-H framework of the amide group departing from the DNB-moiety of the CSP and the electron-donor C=O framework of the amide group bound to the propenyl of the CSP which interact with one of the (P)-1,1'-Bi-(2-Naphthol)'s OH groups (left side of **Figure 31**). The third H-Bond is instead established between the oxygen of one nitro-group belonging to the CSP and the electron-accepting hydrogen of the remaining (P)-1,1'-Bi-(2-Naphthol)'s hydroxyl group. Unlike this, within the **(S,S)-CSP/(M)-Guest** structure it is instead visible the establishment of only two H-Bonds (right side of **Figure 31**), which involve the same electron-accepting and electron-donor groups observed in its diastereomeric adduct, while it is absent the involvement of the CSP's nitro-groups within the formation of additional secondary bonds with the (M)-1,1'-Bi-(2-Naphthol) guest, because of a greater distance existing between the moiety endowed with complementary reactivity.

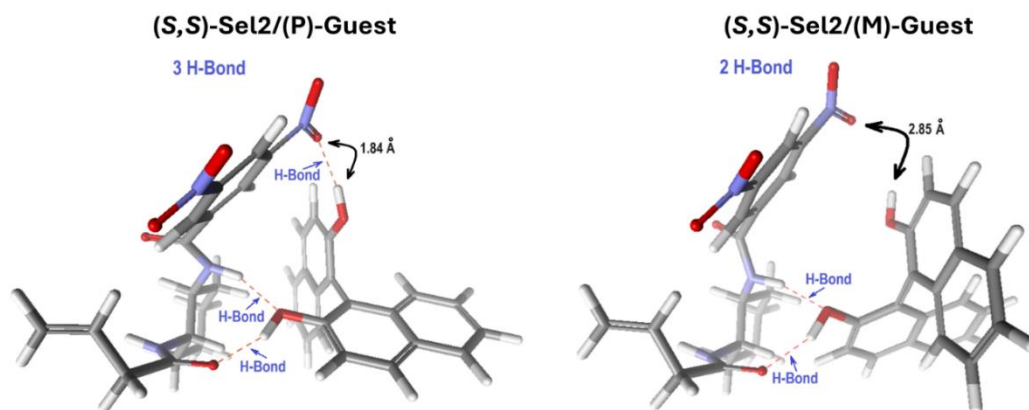


Figure 31. Most stable geometries of the diastereomeric **(S,S)-Sel2/(P)-Guest** and **(S,S)-Sel2/(M)-Guest** adducts were assessed by docking approach.

This different propensity in the formation of H-Bonds seems to be the basis of the discriminating behaviour of the analysed CSP towards the chiral structure of 1,1'-Bi-(2-Naphthol). Taking into consideration that for the just above considered dockings between selector **(S,S)-Sel2** and **(M)/(P)-Guests** the best final result has been obtained by resorting to a semiempirical optimization of the adducts with the PM3 Hamiltonian, also in order to perform a new additional docking-simulation among selector **(S,S)-Sel1** and **(M)/(P)-Guests** we replayed all the same computational steps of calculus only limited to the PM3 semi-empirical level of theory. The obtained results afforded a $DDE_{PSSb-MSSb}$ value of -0.0527 kcal, which corresponds to a selectivity factor a of 1.08 units a very minimal enantio-discrimination. However, comparison between calculated and experimental data puts in evidence a correct enantiomers' elution order, as well as a good agreement between the relevant ^{sel1}DDE values, with the $^{sel1}DDE_{PM3} - ^{sel1}DDE_{Exp}$ difference amounting to only -0.04 kcal, which corresponds to a resolution disagreement $^{sel1}a_{PM3} - ^{sel1}a_{Exp}$ of only 0.02 units. As in the case of the already

considered **Sel2**, in order to obtain some possible information regarding the mechanism with which the correlate, although quite modest, experimental enantio-discrimination obtained by **Sel1** takes place, we analyzed the 3D structures of the energetically most stable diastereomeric adducts **(S,S)-Sel1/(P)-Guest** and **(S,S)-Sel1/(M)-Guest** afforded by calculation (see **Figure 32**). From their inspection, while the **(S,S)-Sel1/(P)-Guest** adduct show a 3D structure very similar to the one already described for **(S,S)-Sel2/(P)-Guest** (although with the absence of the third H-Bond between the nitro-group's oxygen belonging to the CSP and the H-bond donor hydroxyl group of the (P)-1,1'-Bi-(2-Naphthol)), the **(S,S)-Sel1/(M)-Guest** displays a geometry quite different from that observed for **(S,S)-Sel2/(M)-Guest**, with the establishment, in this case, of only one H-Bond, but also of a new favorable pi-pi interaction between one of the two 2-Naphthol's moieties of **(M)-Guest** and the 3,5-dinitrobenzoyl group of **Sel1** (see **Figure 33**).

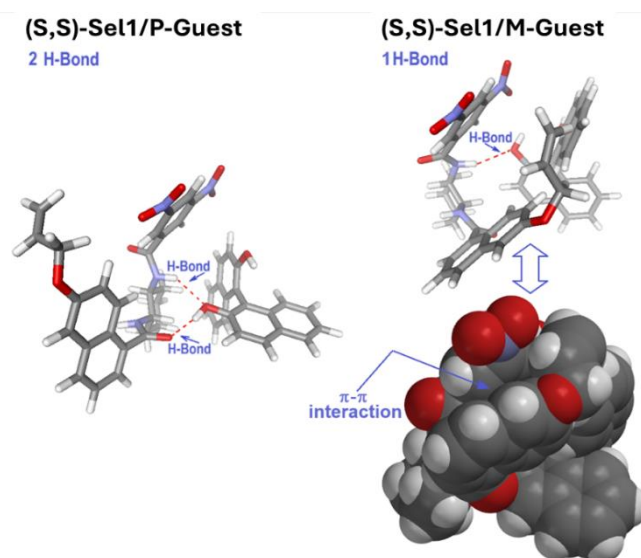


Figure 32. Most stable geometries of the diastereomeric **(S,S)-Sel1/(P)-Guest** and **(S,S)-Sel1/(M)-Guest** adducts assessed by docking approach.

5. Conclusions and future perspectives

The aim of this project was to design the synthesis of two novel selectors, based on the commercial Whelk-O1 and DACH-DNB: **Sel1** and **Sel2**; the latter represents the structural exemplification of the former. These were first characterized from a chemical point of view and subsequently an evaluation of their chiral recognition capabilities was carried out using **Sel1** as CSA. ¹H-NMR studies were conducted to further confirm the chiral recognition capabilities of **Sel1** against Ibuprofen; from the analysis of an equimolar host/guest mixture the splitting of the proton signal connected to the stereogenic center of the enantiomer is evident in the presence of the selector. Subsequently, the two selectors were anchored on silica to obtain four stationary phases which were packed to obtain the corresponding chromatographic columns. These were tested with the mixtures of 1-(9-anthryl)-2,2,2-trifluoroethanol and 1,1'-bi-(2-naphthol), in different mobile phase conditions revealing a good enantioseparation capacity. The best separation was obtained with the stationary phase (*S,S*)-CSP2 against 1,1'-bi-(2-naphthol) which revealed an α value equal to 1.27 in n-Hexane/Chloroform 80/20 conditions. To further understand the chiral recognition properties, molecular docking studies were performed on both selectors using binaphthol as guest. Thanks to these it was possible to understand the interactions that are established between the selectors and the two enantiomers of binaphthol because of which the order of elution of the species will also be determined. The future goals are to promote an optimization of the general procedure starting from the anchoring the selectors on silica, in order to improve the loading, to the packing of the columns. A further goal is to promote the expansion of the structural design of the Pirkle Type selectors library in order to broaden the possibility of obtaining new stationary phase. **Sel1** and **Sel2**

represent only the starting point of the study for the expansion of the library of possible Pirkle Type selectors for the synthesis of new stationary phases.

6. References

- [1] C. Fernandes, M. Tiritan, M. Pinto. *Chromatographia* **2013**, 76, 15-16.
- [2] E. R. Francotte. *Journal of Chromatography A* **2001**, 906, 379.
- [3] N. M. Maier, W. Lindner. *Chirality in Drug Research* **2006**.
- [4] M. Ohara, Y. Suzuki, S. Shinohara, I. Y. Gong, C. L. Schmerk, R. G. Tirona, U. I. Schwarz, L. H. Cavallari, R. B. Kim, H. Takahashi. *Clinical Pharmacokinetics* **2019**, 58, 8.
- [5] A. Hutt. *Smith and Williams' Introduction to the Principles of Drug Design and Action* **2019**, 97-166.
- [6] R. A. Shalliker. *Journal of Separation Science* **2009**, 32, 2903.
- [7] E. J. Ariëns. *European Journal of Clinical Pharmacology* **1984**, 26, 663.
- [8] E. R. Francotte. *Journal of Chromatography A* **2001**, 906, 1-2.
- [9] E. Francotte, W. Lindner. *Chirality in Drug Research* **2007**, 33.
- [10] D. R. Taylor, K. Maher. *Journal of Chromatography Science* **1992**, 30, 3.
- [11] J. Haginaka. *Journal of Pharmaceutical and Biomedical Analysis* **2002**, 27, 3-4.
- [12] T. Toyo'oka. *Journal of Biochemical and Biophysical Methods* **2002**, 54, 1-3.
- [13] Y. Zhang, D. R. Wu, D. B. Wang-Iverson, A. A. Tymiak. *Drug Discovery Today* **2005**, 10, 8.
- [14] W.H. Pirkle, T.C. Pochapsky. *Chemical Reviews* **1989**, 89, 2, 347-362.
- [15] W. Lindner, E. Francotte. *Wiley* **2006**.
- [16] G. Hesse, R. Hagel. *Chromatographia* **1973**, 6, 277.
- [17] G. Hesse, R. Hagel. *Justs Lleblgs Annalen der Chemie* **1976**, 6, 996-1008.
- [18] E. Francotte, R.M. Wolf. *Chirality* **1991**, 43-55.
- [19] T. Ikai, C. Yamamoto, M. Kamigaito, Y. Okamoto. *Journal of Separation Science* **2007**, 30, 7, 971-978.

- [20] Y. Okamoto, M. Kawashima, K. Hatada. *Journal of American Chemical Society* **1984**, *106*, *18*, 5357-5359.
- [21] E. P. Sousa, M. E. Tiritan, R.V. Oliveira, C. M. Afonso, Q. B. Cass, M. M. Pinto. *Chirality* **2004**, *16*, 279.
- [22] Q. B. Cass, A. L. G. Degani, N. M. Cassiano. *Journal of Liquid Chromatography and Related Technologies* **2003**, *26*, 2083.
- [23] T. Zhang, C. Kientzy, P. Franco, A. Ohnishi, Y. Kagamihara, H. Kurosawa. *Journal of Chromatography A*. **2005**, *1075*, 65.
- [24] D.W. Armstrong, W. DeMond. *Journal of Chromatography Science* **1984**, *22*, 411.
- [25] D.W. Armstrong, W. DeMond, T.-N, Pham, J.-J. Vallon. *Journal of Chromatography B*. **1996**, *687*, 303-336.
- [26] C.R. Mitchell, D.W. Armstrong. *Chiral Separations* **2004**, 61.
- [27] S.C. Chang, G.L. Reid III, S. Chen, C.D. Chang, D.W. Armstrong. *Trends in Analytical Chemistry* **1993**, *12*, *4*, 144-153.
- [28] D.W. Armstrong, S. Chen, C. Chang, S. Chang. *Journal of Liquid Chromatography* **1997**, *20*, 3279.
- [29] G.K.E. Scriba. *Journal of Chromatography A* **2016**, *1467*, 56.
- [30] T.J. Ward, A.B. Farris III. *Journal of Chromatography A* **2001**, *906*, 73.
- [31] I. Ilisz, R. Berkecz, A. Peter. *Journal of Separation Science* **2006**, *29*, 1305.
- [32] D.W. Armstrong, Y. Tang, S. Chen, Y. Zhou, C. Bagwill, J.R. Chen. *Analytical Chemistry* **1994**, *66*, 1473.
- [33] K. H. Ekbord-Ott, J. P. Kullman, X. Wang, K. Gahm, L. He, D. W. Armstrong. *Chirality* **1998**, *10*, 627.
- [34] D.W. Armstrong, Y. Liu, K.H. Ekborgott. *Chirality* **1995**, *7*, 474.
- [35] K. Ekborg-Ott, Y. Liu, D.W. Armstrong. *Chirality* **1998**, *10*, 434.
- [36] A. Berthod, X. Chen, J.P. Kullman, D.W. Armstrong, F. Gasparrini, I. D'Acquarica, C. Villani, A. Carotti. *Analytical Chemistry* **2000**, *72*, 1767.

- [37] A. Berthod, T. Yu, J.P. Kullman, D.W. Armstrong, F. Gasparrini, I. D'Acquarica, D. Misiti, A. Carotti. *Journal of Chromatography A* **2000**, 987, 113.
- [38] I. D'Acquarica, F. Gasparrini, D. Misiti, G. Zappia, C. Cimarelli, G. Palmieri, A. Carotti, S. Cellamare, C. Villani. *Tetrahedron: Asymmetry* **2000**, 11, 2375.
- [39] S. Fanali, G. D'Orazio, M.G. Quaglia, A. Rocco. *Journal of Chromatography A* **2004**, 1051, 247.
- [40] G.S. Ding, X.J. Huang, Y. Liu, J.D. Wang. *Chromatographia* **2004**, 59, 443.
- [41] K. Petrusevska, M.A. Kuznetsov, K. Gedicke, V. Meshko, S.M. Staroverov, A. Seidel-Morgenstern. *Journal of Separation Science* **2006**, 29, 1447.
- [42] S.M. Staroverov, M.A. Kuznetsov, P.N. Nesterenko, G.G. Vasiarov, G.S. Katrukha, G.B. Fedorova. *Journal of Chromatography A* **2006**, 1108, 263.
- [43] T.E. Beesley, J.-T Lee, J. Liq. *Journal of Liquid Chromatography and Related Technologies* **2009**, 32, 11-12.
- [44] I. Ilisz, R. Berkecz, A. Peter. *Journal of Separation Science* **2006**, 29, 1305.
- [45] Y. Liu, A. Berthod, C.R. Mitchell, T.L Xiao, B. Zhang, D.W. Armstrong *Journal of Chromatography A* **2002**, 978, 185.
- [46] T.E. Beesley, J.T. Lee, A.X. Wang. *Chiral Separation Techniques* **2001**, 25.
- [47] C. Wang, C. Jiang, D.W. Armstrong. *Journal of Separation Science* **2008**, 31, 1980.
- [48] K. Ekborg-Ott, Y. Liu, D.W. Armstrong. *Chirality* **1998**, 10, 434.
- [48] A. Berthod, X. Chen, J.P. Kullman, D.W. Armstrong, F. Gasparrini, I. D'Acquarica, C. Villani, A. Carotti. *Analytical Chemistry* **2000**, 72, 1767.
- [49] S. G. Allenmark, S. Andersson. *Journal of Chromatography A* **1994**, 666, 167.
- [50] J. Haginaka. *Journal of Chromatography A* **2001**, 906, 253.
- [51] M. C. Millot. *Journal of Chromatography B* **2003**, 797, 131.
- [52] J. Haginaka. *Journal of Chromatography B* **2008**, 875, 12.

- [53] E. Domenici, C. Brett, P. Salvadori, G. Felix, I. Cahagne, S. Motellier, I. W. Wainer. *Chromatographia* **1990**, 29, 170.
- [54] J. Hermansson. *Journal of Chromatography* **1983**, 169, 71.
- [55] T. Miwa, M. Ichikawa, M. Tsuno, T. Hattori, T. Miyakawa, M. Kayano, Y. Miyake. *Chemical and Pharmaceutical Bulletin* **1987**, 35, 682.
- [56] P. Erlandsson, I. Marle, L. Hansson, R. Isaksson, C. Petterson, G. Petterson. *Journal of the American Chemical Society* **1990**, 112, 4573.
- [57] J. Chen, W.A. Korfmacher, Y. Hsieh. *Journal of Chromatography B* **2005**, 820, 1.
- [58] T. Fornstedt, P. Sajonz, G. Guiochon. *Journal of the American Chemical Society* **2007**, 1164, 235.
- [59] T. Fornstedt, G. Götmar, M. Andersson, G. Guiochon. *Journal of the American Chemical Society* **1999**, 121, 1164.
- [60] G. Goetmar, J. Samuelsson, A. Karlsson, T. Fornstedt. *Journal of the American Chemical Society* **2007**, 1156, 3.
- [61] W. Pirkle, D. House. *The Journal of Organic Chemistry* **1979**, 44, 1957.
- [62] F. Mikes, G. Boshart. *Journal of Chromatography* **1978**, 149, 455.
- [63] E. Badaloni, W. Cabri, A. Ciogli, R. Deias, F. Gasparri, F. Giorgi, A. Vigevano, C. Villani. *Analytical Chemistry* **2007**, 79, 15.
- [64] P. Macaudiere, A. Tambute, M. Caude, R. Rosset, M. A. Almebik, I. W. Wainr. *Journal of Chromatography A* **1986**, 371.
- [65] A. M. Blum, K. G. Lynam, E. C. Nicolas. *Chirality* **1994**, 6, 4.
- [66] C. M. Kraml, D. Zhou, N. Byrne, O. McConnell. *Journal of Chromatography A* **2005**, 1100, 1.
- [67] W.H. Pirkle, C.J. Welch. *Journal of Chromatography A* **1994**, 683, 2.
- [68] J. Dungelová, J. Lehotay, J. Krupcik, J. Cizmárik, T. Welsch, D. W. Armstrong. *Journal of Chromatographic Science* **2004**, 42, 3.

- [69] G. E. Job, A. Shvets, W. H. Pirkle, S. Kuwahara, M. Kosaka, Y. Kasai, H. Taji, K. Fujita, M. Watanabe, N. Harada. *Journal of Chromatography A* **2004**, 1055, 1-2.
- [70] M. E. Koscho, P. L. Spence, W. H. Pirkle. *Tetrahedron Asymmetry* **2005**, 16, 19.
- [71] A. Del Rio, J. M. Hayes, P. Piras, C. Roussel. *Chirality* **2004**, 16.
- [72] C. F. Zhao, S. Diemert, N. M. Cann. *Journal of Chromatography A* **2009**, 1216, 32.
- [73] C. J. Welch. *Journal of Chromatography A* **1994**, 666, 1-2.
- [74] W. H. Pirkle, R. Däppen. *Journal of Chromatography A* **1987**, 404.
- [75] V. Schurig. *Molecules* **2016**, 21, 11.
- [76] W. H. Pirkle. *Journal of the American Chemical Society* **1966**, 88, 8.
- [77] W. H. Pirkle, T. G. Burlingame, S. D. Beare. *Tetrahedron Letters* **1968**, 9, 56.
- [78] W. H. Pirkle, D. J. Hoover. *Top Stereochem* **1982**, 13, 263-331.
- [79] W. H. Pirkle, D. W. House, J. M. Finn. *Journal of Chromatography A* **1980**, 192, 1C.
- [80] W. H. Pirkle, H. H. Myung, B. Bank. *Journal of Chromatography A* **1984**, 316C.
- [81] W. H. Pirkle, T. C. Pochapsky, J. A. Burke, K. C. Deming. *Chiral Separations* **1988**, 23-25.
- [82] W. H. Pirkle, T. C. Pochapsky. *Chemical Reviews* **1989**, 89, 2.
- [83] W. H. Pirkle, C. J. Welch, R. S. Readnour. *Analytical Chemistry* **1991**, 63, 1.
- [84] W. H. Pirkle, C. J. Welch. *Journal of Liquid Chromatography* **1991**, 14, 1.
- [85] G. Felix, A. Berthod. *Separation and Purification Reviews* **2007**, 36, 4.
- [86] Y. Okamoto, T. Ikai. *Chemical Society Reviews* **2008**, 37, 2593-2608.
- [87] S. Manetto, G. Mazzocanti, V. Mileo, E. Moretti, C. Villani, F. Gasparri. *Journal of Chromatography A* **2023**, 1705, 464177.
- [88] F. Gasparri, F. Maggio, D. Misiti, C. Villani, F. Andreolini, G. Mapelli. *Resolution Chromatography* **1994**, 17, 1.

- [89] J. E. MacNair, K. C. Lewis, J. W. Jorgenson. *Analytical Chemistry* **1997**, 69, 983-989.
- [90] A. D. Jerkovich, J. S. Mellors, J. W. Jorgenson. *LC GC Eur*, **2003**, 16, 20-23.
- [91] S. Fekete, I. Kohler, S. Rudaz, D. Guillarme. *Journal of Pharmaceutical and Biomedical Analysis* **2014**, 97, 105-119.
- [92] S. Fakete, J. Schappler, J.-L. Veuthey, D. Guillarme. *Trends in Analytical Chemistry* **2014**, 63, 2-13.
- [93] J. R. Mazzeo, U. D. Neue, M. Kele, R. Plumb. *Analytical Chemistry* **2005**, 77, 460A-467A.
- [94] K. D. Wyndham, J. E. O' Gara, T. H. Walter, K. H. Glose, N. L. Lawrence, B. A. Alden. *Analytical Chemistry* **2003**, 75, 6781-6788.
- [95] K. J. Fountain, U. D. Neue, E. S. Grumbach, D. M. Diehl. *Journal of Chromatography A* **2009**, 1216, 5979-5988.
- [96] K. J. Fountain, P. C. Iraneta. *UHPLC in Life Sciences* **2012**, 29-66.
- [97] D.V. McCalley. *Chromatography monographs* **2012**, 164-185.
- [98] D. Kotoni, A. Ciogli, C. Molinaro, I. D'Acquarica, J. Kocergin, T. Szczerba. *Analytical Chemistry* **2012**, 84, 6805-6813.
- [99] M. Janco, J. N. Alexander IV, E. S. P. Bouvier, D. Morrison. *Journal of Separation Science* **2013**, 36, 2718-2727.
- [100] J. C. Rea, Y. J. Wang, T. Zhang. *Ultra-High Performance Liquid Chromatography and its Applications* **2013**, 235-252.
- [101] E. S. P. Bouvier, S. M. Koza. *Trends in Analytical Chemistry* **2014**, 36, 85-94.
- [102] N. Wu, J. A. Lippert, M. L. Lee. *Journal of Chromatography A* **2001**, 911, 1-12.
- [103] D. T. T. Nguyen, D. Guillarme, S. Heinisch, M. P. Barrioulet, J. L. Rocca, S. Rudaz. *Journal of Chromatography A* **2007**, 1167, 76-84.
- [104] S. Heinisch, J. L. Rocca. *Journal of Chromatography A* **2009**, 1216, 642-658.

- [105] H. G. Gika, G. Theodoridis, J. Extance, A. M. Edge, I. D. Wilson. *Journal of Chromatography B* **2008**, 871, 279-287.
- [106] M. W. Dong. *LC-GC North America* **2013**, 31, 868-880.
- [107] R. E. Majors. *LC-GC North America* **2013**, 31, 537.
- [108] M. Dong, D. Guillarme, S. Fekete, R. Rangelova, J. Richards, D. Prudhomme. *LC-GC North America* **2014**.
- [109] M. W. Dong, K. Zhang. *Trends in Analytical Chemistry* **2014**, 63, 21-30.
- [110] M. Catani, O. H. Ismail, S. Felletti, F. Gasparrini, L. Pasti, V. Costa, A. Cavazzini. *American Pharmaceutical Review* **2017**, 20, 4.
- [111] D. C. Patel, Z. S. Breitbach, M. F. Wahab, C. L. Barhate, D. W. Armstrong. *Analytical Chemistry* **2015**, 87, 18.
- [112] G. Cancelliere, A. Ciogli, I. D'Acquarica, F. Gasparrini, J. Kocergin, D. Misiti, M. Pierini, H. Ritchie, P. Simone, C. Villani. *Journal of Chromatography A* **2010**, 1217, 12, 990-999.
- [113] D. Kotoni, A. Ciogli, I. D'Acquarica, J. Kocergin, T. Szczerba, H. Ritchie, C. Villani, F. Gasparrini. *Journal of Chromatography A* **2012**, 1269.
- [114] C. Villani, I. D'Acquarica, F. Gasparrini, D. Kotoni, M. Pierini, A. Ciogli, H. Ritchie, J. Kocergin. *LC-GC Europe* **2014**, 27, 3.
- [115] L. Sciascera, O. Ismail, A. Ciogli, D. Kotoni, A. Cavazzini, L. Botta, T. Szczerba, J. Kocergin, C. Villani, F. Gasparrini. *Journal of Chromatography A* **2015**, 1383.
- [116] A. Horeau, J. P. Guetté. *Tetrahedron* **1974**, 30, 13.
- [117] M. Raban, K. Mislow. *Tetrahedron Letters* **1965**, 6, 48.
- [118] Y. Shvo, E. C. Taylor, K. Mislow, M. Raban. *Journal of American Chemical Society* **1967**, 89, 19.
- [119] L. Yang, R. T. Williamson, M. Christensen, W. Schafer, C. Welch. *ACS Central Science* **2016**, 2, 5.

- [120] D. Casarini, S. Davalli, L. Lunazzi, D. Macciantelli. *Journal of Organic Chemistry* **1989**, *54*, 19.
- [121] S. R. Laplante, L. D. Fader, K. R. Fandrlick, D. R. Fandrlick , O. Hucke, R. Kemper, S. P. F. Miller, P. J. Edwards. *Journal of Medicinal Chemistry* **2011**, *54*, 20.
- [122] J. Clayden, W. J. Moran, P. J. Edwards, S. R. Laplante. *Angewandte Chemie - International Edition* **2009**, *48*, 35.
- [123] M. Simonyi. *Advances in Drug Research* **1997**, *30*.
- [124] G. B. Baker, T. I. Prior. *Annals of Medicine* **2002**, *34*, 7-8.
- [125] M. Abram, M. Jakubiec, K. Kamiński. *ChemMedChem* **2019**, *14*, 20.
- [126] P. Eveleigh, E. C. Hulme, C. Schudt, N. J. M. Birdsall. *Molecular Pharmacology* **1989**, *35*, 4.
- [127] S. R. LaPlante, P. Forgione, C. Boucher, R. Coulombe, J. Gillard, O. Hucke, A. Jakalian, M. A. Joly, G. Kukolj, C. Lemke, R. McCollum, S. Titolo, P. L. Beaulieu, T. Stammers. *Journal of Medicinal Chemistry* **2014**, *57*, 5.
- [128] T. Q. Yan, F. Riley, L. Philippe, J. Davoren, L. Cox, C. Orozco, B. Rai, M. Hardink. *Journal of Chromatography A* **2015**, *1398*.
- [129] L. Zhang, Y. Hu, E. Galella, F. P. Tomasella, W. P. Fish. *Journal of Pharmaceutical Analysis* **2017**, *7*, 3.
- [130] J. Dai, C. Wang, S. C. Traeger, L. Discenza, M. T. Obermeier, A. A. Tymiak, Y. Zhang. *Journal of Chromatography A* **2017**, *1487*.
- [131] R. Costil, A. J. Sterling, F. Duarte, J. Clayden. *Angewandte Chemie - International Edition* **2020**, *59*, 42.
- [132] A. Ciogli, S. Vivek Kumar, M. Mancinelli, A. Mazzanti, S. Perumal, C. Severi, C. Villani. *Organic and Biomolecular Chemistry* **2016**, *14*, 47.
- [133] S. Levi Mortera, R. Sabia, M. Pierini, F. Gasparrini, C. Villani. *Chemical Communications* **2012**, *48*, 26.

- [134] R. Franzini, M. Pierini, A. Mazzanti, A. Iazzetti, A. Ciogli, C. Villani. *International Journal of Molecular* **2021**, 22, 1.
- [135] B. Paizs, M. Simonyi. *Chirality* **1999**, 11, 8.
- [136] H. Tabata, N. Wada, Y. Takada, T. Oshitari, H. Takahashi, H. Natsugari. *Journal of Organic Chemistry* **2011**, 76, 12.
- [137] Y. Kanase, M. Kuniyoshi, H. Tabata, Y. Takahashi, S. Kayama, S. Wakamatsu, T. Oshitari, H. Natsugari, H. Takahashi. *Synthesis (Germany)* **2015**, 47, 24.
- [138] D. Casarini, L. Lunazzi, A. Mazzanti. *European Journal of Organic Chemistry* **2010**, 11.
- [139] M. Okamoto. *Journal of Pharmaceutical and Biomedical Analysis* **2002**, 27, 3-4, 401-407.
- [140] E. Badaloni, W. Cabri, A. Ciogli, I. D'Acquarica, R. Deias, F. Gasparrini, F. Giorgi, D. Kotoni, C. Villani. *Journal of Chromatography A* 2010, 1217, 7, 1020-1032.
- [141] E. Badaloni, W. Cabri, A. Ciogli, I. D'Acquarica, R. Deias, F. Gasparrini, F. Giorgi, D. Kotoni, C. Villani. *Journal of Chromatography A* **2010**, 1217, 7.
- [142] V. R. Meyer. *Chirality* **1995**, 7, 8.
- [143] J. A. Perry, J. D. Rateike, T. J. Szczerba. *Journal of Chromatography A* **1987**, 389 C.
- [144] B. Chankvetadze. *Journal of Chromatography A* **2018**, 1567, 2-25.
- [145] P. Peluso, V. Mamane, E. Aubert, S. Cossu. *Journal of Chromatography A* **2014**, 1345, 182-192.
- [146] G. K. E. Scriba *Journal of Chromatography A* **2016**, 1467, 56-78.
- [147] M. Karthikeyan, R. Vyas. *Practical Chemoinformatics* **2014**, 195-197.
- [148] G. M. Morris, D. S. Goodsell, R. Halliday, S. Huey, W. E. Hart, R. K. Belew, A. J. Olson. *Journal of Computational Chemistry* **1998**, 19, 1639-1662.

- [149] G. M. Morris, R. Huey, W. Lindstrom, M. F. Sanner, R. K. Belew, D. S. Goodsell, A. J. Olson. *Journal of Computational Chemistry* **2009**, 30, 2785-2791.
- [150] J. C. Giddings, H. Eyring. *Journal of Physical Chemistry* **1955**, 59, 416-421.
- [151] D. C. Young. *Computational Drug Design* **2009**, 294.
- [152] H. Alonso, A. A. Bliznyuk, J. E. Gready. *Medicinal Research Reviews* **2006**, 26, 531-568.
- [153] A. Hospital, J. R. Goñi, M. Orozco, J. L. Gelpi. *Advanced Application in Bioinformatics Chemistry* **2015**, 8, 37-47.
- [154] P. Peluso, A. Dessì, R. Dallochio, V. Mamage, S. Cossu. *Electrophoresis* **2019**, 40, 15, 1881-1896.
- [155] C. F. Zhao, N. M. Cann. *Journal of Chromatography A* 2006, 1131, 110-129.
- [156] K. Hall, M. Ashtari, N. M. Cann. *Journal of Chemical Physics* **2012**, 136, 114705.
- [157] S. Alcaro, F. Gasparri, O. Incani, S. Mecucci, D. Misiti, M. Pierini, C. Villani. *Journal of Computational Chemistry* **2000**, 21, 515-530.
- [158] S. Alcaro, F. Gasparri, O. Incani, L. Caglioti, M. Pierini, C. Villani. *Journal of Computational Chemistry* **2007**, 28, 1119-1128.
- [159] S. Alcaro, F. Gasparri, O. Incani, L. Caglioti, M. Pierini, C. Villani. *Journal of Computational Chemistry* **2007**, 28, 6, 1119-1128.

Part B

7. Introduction about different types of materials

The development and diversification of synthetic techniques allowed to obtain an impressive number of materials, and the increasingly advanced analytical techniques allow to recognize the differences in their characteristics. When Gilbert N. Lewis developed Lewis point structures of covalent compounds in 1916, he first proposed the concept of sharing electrons between surrounding atoms, essential to defining a covalent bond. [1-2] Fritz London [3] and Walter Heitler established the covalent bond in terms of overlapping atomic orbitals eleven years later. [4-5] Since then, covalent bonds, the strongest bonds in nature, have been the key to the construction of every type of molecule and, in materials science, they can be used to create materials that are more chemically stable and durable than most electrostatic bonds, such as coordination bonds, hydrogen bonds and hydrophobic bonds. The fact that covalent polymerization products like nylon, polyethylene, polystyrene, polyamide and others have so many applications in daily life is not surprising. [6] Covalent organic polymeric materials (COPs) are among the several materials examined; in 2005 they were integrated by Covalent Organic Frameworks (COFs) presenting dynamic bonds, compared to the COPs structural order and long-range crystallinity. Metal Organic Frameworks are created when coordination interactions take the place of covalent bonds. [7] A coordination bond, also known as a dative covalent bond, is a chemical bond in which both electrons come from the same atom. These materials are also known as porous coordination polymers (PCP), which are two- or three- dimensional porous crystalline solids made up of metal ions acting as nodes and organic ligands acting as linkers. [8]

7.1 Covalent Organic Polymers (COPs)

During the synthetic process, cross-linking between linear polymer chains has been utilized to create three-dimensional (3D) materials since the early 1960s. [9-10] These polymers are created by incorporating monomers that can sometimes be involved in polymerization processes (radical, anionic, cationic and condensation). The most successful family of these materials is based on the polystyrene divinylbenzene system, which are widely produced as resins and membranes for a variety of applications, such as synthesis support, water softening and purification. Molecular porogens were employed in conjunction with the copolymerization technique in the late 1980s to produce molecular imprinted polymers (MIP). These materials have been thoroughly investigated in solid phase extraction and detection applications. They have moderate Brunauer-Emmett-Teller (BET) surface areas (200-800 m²/g) and can be divided into mesoporous and microporous categories in dependence on average pores dimension. Numerous terms have been used to describe microporous materials of various kinds, such as conjugated microporous polymers (CMP), porous organic structures (POF), intrinsically microporous polymers (PIM) and porous aromatic structures (PAF). Despite being amorphous, these materials often exhibit significant internal surface areas, which can be attributed to mesopores and micropores made of stiff multitopic building blocks. They are insoluble materials based on light elements such as C, H, O, N, F and S atoms, through by covalent bonds. Porous organic polymers (POPs) are often made up of multitopic monomer units, which have three or more connection points, on the contrary in the classical synthesis of microporous polymers ditopic crosslinkers (such as divinylbenzene) are used to join long chains of polymerized monomers. Crosslinking in POPs is determined by the valence of the monomeric or co-

monomeric units, this is formed between building blocks that are usually rigid structures, on the contrary in polymeric gels crosslinking occurs between chains that have greater flexibility. They can exhibit variable porosity, permanent microporosity when made of rigid monomers, but also a mesoporous structure. In addition, cross-linked polymer gels, which often develop between side chains and flexible chains, differ from those in POP, which form between stiff building blocks. POPs, like many other porous materials, can achieve permanent microporosity only if they are made of relatively rigid monomers that, once interacted to form a cross-linked structure, give rise to pores with relatively rigid walls. Although POP's amorphous nature results as a drawback it can also be an advantage because it allows essential elements to be swiftly extracted from a reaction mixture without waiting for crystals to form. [11] Generally, when we talk about COPs we refer to porous structures, but there are also non-porous counterparts, in this case the precursors used are often conjugated systems, such as aromatic structures, which establish covalent bonds between them and form large structures. The methods used to create non-porous COP vary, including synthesis in solvothermal conditions, assisted by microwave, and at room temperature. Non-porous COP is characterized by large gaps or cavities, in contrast to their porous counterpart. This lack of porosity often occurs because of densely packed polymer chains or a specific type of monomer that does not result in open structures. Non-porous COP have exceptional mechanical stability due to strong covalent connections and are also chemically inert and resistant to harsh chemical conditions. Their stability at high temperatures makes them suitable for use in high-temperature applications. Additionally, non-porous COP may exhibit intriguing optical characteristics, including electronic and fluorescence, that depend on the initial monomer. [12] Due to their solid and insoluble nature, they can be employed in the field of heterogeneous catalysis. At times, working

in tandem with several metal species may also be feasible to generate metal-catalysts. Although these materials lack the intrinsic porosity necessary for high-capacity gas storage, non-porous COP can participate in gas separation processes due to the selective adsorption properties on their surfaces. Lastly, they have applications in the field of electronics as well. These include possible conductive materials, semiconductor used in organic electronic devices and optoelectronics utilized in solar cells and light-emitting diodes sensors (LEDs). [13]

7.2 Covalent Organic Frameworks (COFs)

In 2005, Yaghi *et al.* demonstrated the utility of the topological design principle in their synthesis of porous organic frameworks linked by covalent bonds, which were the first successful examples of covalent organic frameworks (COFs). [14] Covalent porous crystalline polymers allow the intricate integration of organic constituent materials into a structure that is precisely organized down to the atomic level. As in the case of organic polymers, COF are composed of light elements bound by covalent interactions, have low mass densities, high thermal stability and provide permanent porosity. Two-dimensional (2D) and three-dimensional (3D) COFs can be distinguished based on the dimensions of the construction elements. The covalently bound structure of COF bidimensional is restricted to 2D sheets, which stack further to create an eclipsed layer structure with periodic row alignment. Thanks to the presence of π interactions that are established between the precursors is possible to construct systems that involve columnar stacking, which would otherwise be impossible in the presence of other types of bonding. Conversely, 3D COFs are characterized by a three-dimensional extension of structure through constituent elements. In addition, 3D COFs have several open sites, low densities and high specific surface areas, making them excellent options for gas storage. [15] The reversible formation of covalent bonds, which can be formed, broken and reformed, is the result of dynamic covalent chemistry (DCC), which triggers the COF formation. Irreversible reactions are a challenging method for crystallizing organic polymers bonded to solids. [16] DCC is therefore thermodynamically controlled, as opposite to normal covalent bond formation, and provides reversible reaction systems with “error control” and “proofreading” features, which result in the formation of more thermodynamically stable structures. Self-repair feedback lowers the frequency

of defects and aids in the production of an ordered structure, while polymer skeleton formation happens concurrently with the crystallization process when the DCC approach is used. Finally, COF is a material which is characterized by high thermodynamic stability and an organized crystal structure. [15] To achieve thermodynamic control in reversible processes, two important factors in COF design and synthesis must be considered: the constituent element and the synthesis method, which includes reaction methods and conditions. A production of a crystalline and ordered structure was accomplished when the COF formation reaction is reversible, and if the geometry of the building blocks inside the COF must be carefully conserved. The first requirement states that the building blocks have reactive groups that provide the dynamic formation of the covalent bond; in other words, they must not have any irreversible collateral reactions, and the reaction system must only contain interchangeable monomers, oligomers and polymers under thermodynamic control. For the second behaviour, the building blocks must be conformationally fixed in order to direct bond formation. Since these structures are highly crystalline, X-Ray diffraction (XRD) is the main technique utilized for characterization; solid state NMR, elemental analysis, X-Ray photoelectric spectroscopy and infrared spectroscopy are employed to support XRD data.

7.2.1 Synthetic methods

Highly structured covalent networks can only be formed by modifying the thermodynamic equilibrium during covalent bond formation. To produce thermodynamically stable crystalline polymer structures, reaction methods and conditions such as temperature, pressure and the presence or absence of a mold must be considered. Solvothermal and microwave assisted strategies are also used in more recent synthetic approaches.

Solvothermal Synthesis

To synthesize COFs, a typical solvothermal procedure involves placing monomers and mixed solvents inside a Pyrex tube, which is then degassed using cycles of freezing, pumping, and thawing. The sealed tube is heated at a specific temperature for a set amount of time to allow for a reaction. The resulting precipitate is collected, cleaned with appropriate solvents, and then vacuum-dried to obtain a solid powder. When synthesizing highly crystalline COFs, the choice of reaction media and conditions should consider factors such as solubility, reaction rate, crystal nucleation, crystal growth rate, and the structure's "self-repair" ability. Solvent ratios and combinations are crucial in balancing structure creation and crystallization. Maintaining the reversibility of the reaction requires proper temperature control, typically in the range of 85 °C to 120 °C, depending on the chemical reactivity of the components. To prevent water molecules from causing a reverse reaction, the reaction environment must be closed. Cooper *et al.* developed a high-productivity methodology for dynamic covalent reactions in a microwave reactor to synthesize COF bonded to boron ester quickly. [17-18] A powerful alternative to the solvothermal approach could

be the microwave protocol. Compared to solvothermal methods, microwave synthesis offers several advantages, firstly it may be used on a large scale since it shortens the reaction time; moreover, the microwave solvent extraction method more effectively eliminates residues and contaminants trapped in the structures, which encourages improved porosity. Lastly, a sealed microwave synthesis vessel is not necessary.

Ionthermal synthesis

Thomas *et al.* investigated the production of triazine COF by ionthermic synthesis. [19-20] A crystalline conjugated triazine COF with solid chemical and thermal stability is produced by using the cyclotrimerization of aromatic nitrile building blocks in ZnCl₂ melted at 400°C. The trimerization reaction, which appears to be partially reversible, is catalysed by ZnCl₂, which also serves as the solvent. However, the harsh reaction conditions limit the yield of COFs. As a result, most COFs obtained using this synthetic approach are amorphous materials with no long-range molecular organization.

Synthesis of thin films oriented on graphene surfaces

The COFs produced through this synthetic approach are insoluble monolayers or powders that cannot be consistently integrated into actual devices or interfaced with electrodes. This makes the process of creating COF thin films on a substrate highly relevant from a scientific and technological standpoint. COF 2D film stacked over single-layer graphene surfaces was synthesized and characterized, as reported by Dichtel *et al.* graphene has been successfully used to make a variety of COF films, including COF-5, TP-COF, NiPc-COF, HHTP-DPB-COF and ZnPc-PPE-COF. The reaction time can be used to modify the

thickness of these films. According to grazing incidence X-Ray diffraction tests, thin films show strong crystallinity and vertical layer alignment. [21-23]

7.3 Conversion of a non-porous covalent organic polymer into a porous covalent organic framework

Non-porous and disordered structures do not allow COPs' applicability in areas that require higher surface areas and structural order. Recent advances report on the dynamic transformation of COPs into COFs, which offer enhanced porosity and crystallinity. This method is facilitated by substituting organic linkers within the COP structure, enabling structural modifications through reversible bonding mechanisms. Research has indicated that massive π electron systems, planar structures and intramolecular hydrogen bonds may be able to partially reduce local and/or non-local energy levels, promoting the development of more stable COF. In order to facilitate this transformation, the linker is replaced inside the non-porous polymer. By substituting suitable organic linkers for imine linkages, Zeng *et al.* were able to successfully switch COP-1, a non-porous imine amorphous polymer, into COF-1-4, a structure with high porosity and crystallinity. [24] As study model, imino COP-1 was used, and the 2,5-dihydroxy-1,4-benzenedicarboxaldehyde (L1) was chosen as a substitute linker. In detail, the compounds 1,3,5-tris(4-amidophenyl) triazine and 1,4-phthalaldehyde were combined to create COP-1 (Figure 33).

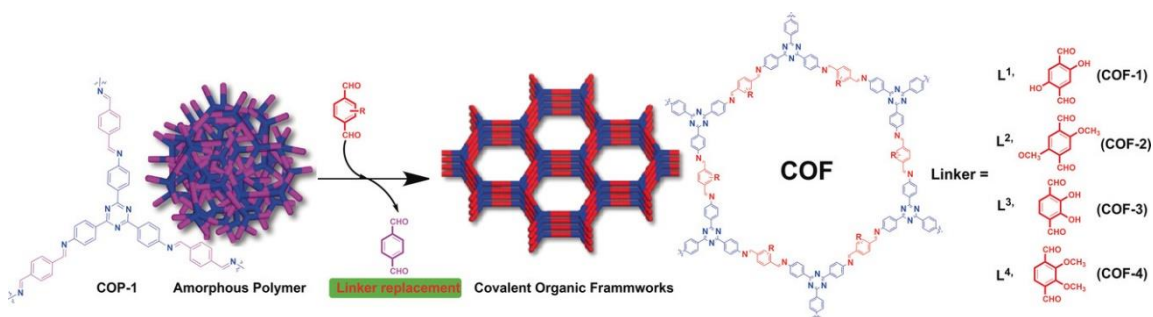


Figure 33. Conversion of amorphous COP-1 to COF using linker exchange strategy. [24]

The system was characterized by FT-IR spectroscopy, X-Ray diffraction, thermal stability analysis and SEM after this linker replacement procedure. Following a 72-hour analysis, the elongation band C=N of the COP-1 at 1621 cm^{-1} (**Figure 34**) is significantly attenuated. In parallel, bands were also observed at 3434 and 1617 cm^{-1} , corresponding to the elongation bands OH and C=N, respectively. These findings suggest that the desired COF-1 product has formed. The crystal structure of the COF-1 has been studied using XRD, which shows a strong peak at $2\Theta = 2.74^\circ$ corresponding to the crystallin plane (100) and other relatively weak peak positions at $2\Theta = 4.78, 5.54, 7.40, 9.78$ and 25.52° , respectively, corresponding to the crystallin plane (110, 200, 210, 220, 001 respectively). On the contrary, no apparent diffraction peak was observed by COP-1 due to its amorphous phase.

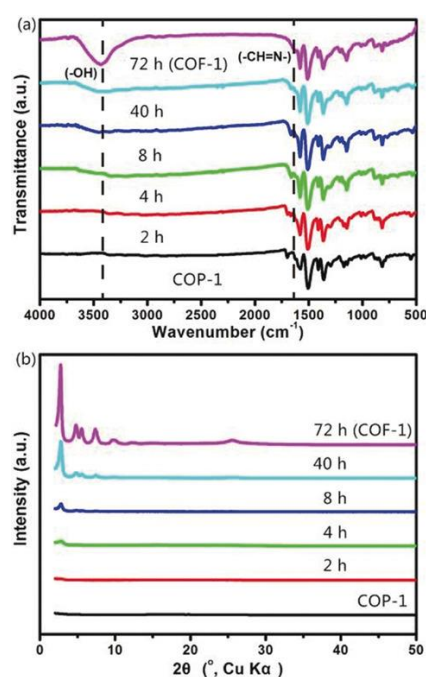


Figure 34. A) FTIR spectra of COP-1 and COF-1 obtained at different times and at different conversion stages: COP-1, 2 h, 4 h, 8 h, 40 h and 72 h (COF-1). B) PXRD models for COP-1 and COF-1 obtained at different times and at different conversion stages: COP-1, 2 h, 4 h, 8 h, 40 h and 72 h (COF-1). [24]

The resulting COF still exhibits good thermal stability, as demonstrated by the TGA evaluation of the COF-1. The morphology of these materials was analysed using field emission scanning electron microscopy (SEM). COP-1 is a yellow powder that aggregates into 1 μm microspheres and has a homogeneous particle size of around 150 nm. With a particle size of roughly 1 μm , COF-1, a dark red powder, has a petal-shaped morphology. When comparing COF-1-4 to the same COF generated from a one-step synthesis, the porosity of COF-1-4 is determined through the study of nitrogen adsorption, revealing an ultra-high porosity and larger surface area. Other linkers have also been explored to assess the flexibility of this synthetic strategy. In all cases, COF have been produced in every instance with significant porosity, crystallinity and stability, often better than the corresponding one-step synthesis. [24]

7.4 Catalysis

The term "catalysis" was first introduced by the Swedish chemist Jöns Jacob Berzelius in 1835, marking the beginning of a significant concept in chemistry. However, it was not until 1894 that Wilhelm Ostwald provided a more precise definition, describing catalysis as "the acceleration of a slow chemical process by the presence of a foreign material." [25] Consequentially, a catalyst is a substance that lowers the activation energy of a reaction, thereby increasing the reaction rate by forming transient bonds with the reactant molecules. For over a century, catalysis has played a crucial role in the synthesis of a vast array of chemical substances, supporting many industrial and laboratory processes. [26] There are three primary types of catalysis: biological (or enzymatic), homogeneous, and heterogeneous, each exhibiting distinct mechanisms and applications. [27] Enzymes are elaborate molecular catalysts primarily responsible for substrate specific reaction in vast biochemical networks. [28-29] The most recent field, enzymatic catalysis, has grown quickly and is now used in numerous industrial applications. Homogeneous catalysts usually have some significant benefit respect their heterogenous counterparts. Since catalysts often have all sites accessible, they can be used in the formation of metal complexes. Furthermore, chemoselectivity, regioselectivity, and/or catalyst enantioselectivity are frequently controllable. Despite these benefits, a significant drawback of homogeneous catalytic systems over heterogeneous catalysts persists: the challenge of separating the reaction products from the catalyst and any by-products and reaction media. This issue occurs because, unless the substance is extremely volatile, the most widely utilized separation technique, distillation, requires high temperatures. Many homogeneous catalysts are thermosensitive, in fact they decompose at temperatures below 150° C. Decomposition of the

catalyst, which is often costly, occurs due to the thermal stress induced by the product's distillation even at low pressure. Loss of the catalyst also occurs in other traditional procedures like extraction or chromatography. [30]

7.4.1 Heterogeneous catalysis

In heterogeneous catalysis, the reagents and catalyst exist in different phases. Typically, the reagents and products are in liquid or gaseous form, while the catalyst is in a solid state. Because the catalyst is in a different phase from the reagents and products, it can be easily separated and recovered from the reaction mixture. This makes the catalyst reusable and reduces operating costs, which is a key advantage of heterogeneous catalysis. Another benefit of heterogeneous catalysts over homogeneous catalysts is their higher mechanical and thermal stability, making them better suited for processes that require extreme reaction conditions, such as high pressures and temperatures. One of the main disadvantages is that most reactions occur on the catalyst's surface, necessitating the transport of reagents to the surface and the removal of products from it. This requirement can limit the reaction rate, especially in catalysts with small specific surface areas or in liquid-phase systems. Additionally, heterogeneous phase catalysts are less adaptable in terms of reaction control compared to their homogeneous counterparts, which can be easily tailored by modifying the catalyst's molecular structure or changing the reaction conditions. Once developed, heterogeneous catalysts are less likely to undergo further modification. Moreover, the synthesis of heterogeneous catalysts can be expensive and complex, as specific procedures are often required to achieve desired characteristics such as a high specific surface area or a uniform distribution of active sites. In recent decades, significant research has focused on the use of recyclable catalysts for organic synthesis to minimize waste generation and enhance catalyst efficiency. [31-32] This focus on recyclable catalysts represents one of the primary objectives of contemporary scientific research: to promote a more environmentally friendly, safe, and sustainable approach to

chemistry. [33-34] So today, the heterogenization of homogeneous catalysts on solid support is one of main interest of scientists. The most popular materials as solid supports for catalyst are polymers and porous silica. [35-37] Mesoporous silica exhibits enhanced physical characteristics, including a porous structure and higher surface areas. [38] However, silica surface modification is not the best solution to anchor catalyst, due to the presence of residual surface silanol groups that strongly interact with catalytic system. [39-40] Polymer substrates on the other hand, do not have these issues, but they also lack well-defined ultra-large pores. [41] Even with the advent of large-pore resins, low-bulge polymers, [42-46] and mesoporous polymers, the limiting of diffusion and the bulge of the polymer are still drawbacks. [47] New possibilities for heterogeneous catalysis have been created by recent advancements in the production of nanoporous polymers, such as the zeolites [48-51], porous organic polymers (POPs), metal organic frameworks and covalent organic frameworks. [52-55] Among these porous crystalline materials, zeolites have been widely used in the petroleum industry and have growing potential for use in environmental catalysis; they represent a significant class of heterogeneous catalysts. These are crystalline aluminosilicates with four connections and three-dimensional structures made of units of SiO_4 and AlO_4 that have the same angles and a Si/Al ratio higher than one. Additional tetrahedral-coordinated atoms like Ge, B and Ti can be added to the structure to enhance the zeolite family. Due to their exceptional stability and limited pore size, zeolites have been used as heterogeneous catalysts under difficult conditions since the 1960s, immediately after the first synthesis of these materials. However, they may be unsuitable when processing reagents with molecular dimensions greater than their micropore. [56-57] The high surface area of mesoporous silica allows for a high concentration of active sites per unit mass, and its pores facilitate mass transfer. Mesoporous silica enables catalytic

reactions involving substrates and/or bulky products. While mesoporous silica has long-range ordering of regular mesopores, the pore walls enclosing these pores are amorphous, unlike the crystallography defined pore walls in zeolites. The amorphous state of mesoporous silica suggests that zeolites inherently have higher stability and catalytic activity. Innovative methods have been developed to create micro-mesoporous crystalline materials, which contain an organized system of mesopores with walls made of crystalline microporous material, to overcome these limitations. [58-60] In recent years, scientists have shown increased interest in MOFs. A combination of inorganic nodes (metal ions or clusters) and organic linkers to create 3D coordination networks. The resulting MOF structures are different both from purely inorganic zeolites and mesoporous silica materials. [61-64]

7.4.2 Development of Surface Organometallic Chemistry (SOMC)

A relatively novel synthetic approach for creating single-site molecules with homogeneous functions is surface organometallic chemistry (SOMC), which has emerged as a significant advancement in catalysis over the past two decades. This technique involves the chemisorption of well-defined organometallic molecular fragments onto solid surfaces to produce immobilized reactive species. By providing precise control over the structure and reactivity of the catalyst, SOMC enhances the performance of catalytic systems, offering advantages such as improved selectivity and stability, as well as reduced leaching of active species into the reaction medium (**Figure 35**). [65-66]

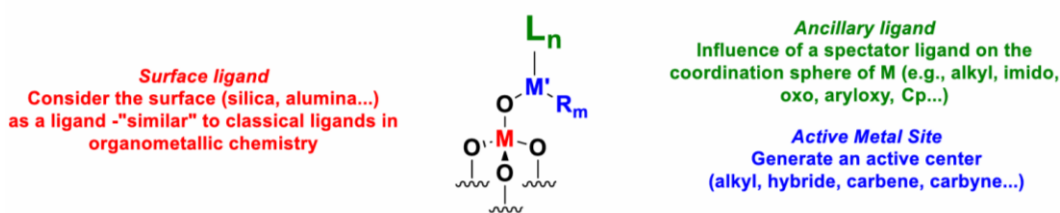


Figure 35. Simplified illustration of a grafted organometallic complex.

In contrast to homogeneous organometallic precursors, which often exhibit significantly lower catalytic activity—and in some cases, no catalytic activity at all—supported organometallic species can be much more effective. [67] Moreover, the supported organometallic species often avoid the typical deactivation pathways associated with bi- or multimolecular degradation found in homogeneous catalysis, resulting in more stable reactive catalytic species. [68] Following grafting onto supports, many organometallic species maintain their stability against oxygen, water, and temperature variations.

When constructing these complexes, it is generally preferred that the solid support is crystalline and possesses a high degree of porosity; thus, the choice of ligand is crucial. The ligand should be flexible and structurally identifiable, encouraging effective coordination with the metal. Additionally, the type of metal used plays a decisive role in determining catalyst performance. Other critical factors include the metal's nuclearity and oxidation state, the reaction conditions, and the compatibility of the catalytic species. Proper structure determination is made easier, even in reactive atmospheres and during catalysis, by the uniformity and simplicity of the supported catalysts. Infrared (IR), fine-structure, nuclear magnetic resonance (NMR), X-Ray adsorption edge (XANES), extended X-Ray adsorption (EXAFS), and atomic-resolution aberration-corrected transmission scanning electron microscopy are among the complementary techniques used in catalyst characterization in reactive atmospheres. The highly homogeneous nature of well-prepared supported species is demonstrated by data from XANES, IR, NMR and microscopy. By identifying media as ligands with electron donor qualities that influence reactivity and catalysis, these characterization approaches help discover surface metal complexes and clusters, including ligands and metal-structure bonding support. [70]

7.5 Role of copper in catalysis

Many metals, such as nickel, palladium, gold, and copper, have strong catalytic activity. Copper is particularly versatile as it can act through one or two electron processes, allowing it to access oxidation states Cu (0), Cu (I), Cu (II), and Cu (III). This versatility makes copper chemistry incredibly rich. Like palladium, organometallic intermediates involving copper can mediate both radical pathways and potent two-electron bonding pathways. Additionally, copper's various oxidation states are closely associated with various distinct functional groups through Lewis's acid interactions or π coordination. As a result, copper has a broad variety of actions. [71] Copper is well-known for its ability to activate terminal alkynes and its ease of coordination with heteroatoms and π bonds. Over a century ago, Ullman and Goldberg discovered that C-C and C-N cross-coupling reactions of aryl arenas or halides with nucleophiles such as amines, phenols, or carboxylic acids. In the last 20 years, their research in this area has really taken off. Compared to expensive transition metal catalysts, copper is a more practical and sustainable metal to use because it is a plentiful resource on Earth. [72] Copper is also involved in other reactions, including the Chan-Lam reaction, which forms C-N and C-S bonds; Michael Reaction; Glaser Coupling; cyclopropanation; oxidation reactions (converting alcohols to ketones or aldehydes); reduction reactions (nitroarenes being reduced to anilines because of the presence of hydrazine and Cu^(II)); cyclization; C-H bond formation. Finally, copper is involved in the well-known Copper (I)-catalysed alkyne-azide cycloaddition (CuAAC) or "click" reaction, that provide the formation of triazoles (Table 4).

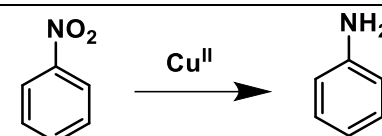
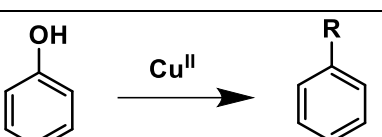
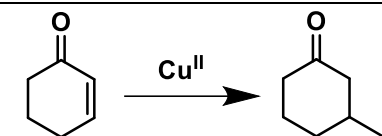
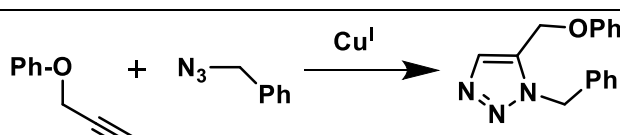
Type of Reaction	Scheme
Ullman Cross Coupling	$2 \text{ R-C}_6\text{H}_4\text{-X} \xrightarrow{\text{Cu}^{\text{II}}} \text{R-C}_6\text{H}_4\text{-C}_6\text{H}_4\text{-R}$ <p style="text-align: center;">X= I, Br</p>
Chan-Lam Reaction	$\text{R-NH}_2 + \text{Ph-B(OH)}_2 \xrightarrow{\text{Cu}^{\text{II}}} \text{R-NH-Ph}$
Reduction	 <p style="text-align: center;"> $\text{C}_6\text{H}_5\text{NO}_2 \xrightarrow{\text{Cu}^{\text{II}}} \text{C}_6\text{H}_5\text{NH}_2$ </p>
Oxidation	 <p style="text-align: center;"> $\text{C}_6\text{H}_5\text{OH} \xrightarrow{\text{Cu}^{\text{II}}} \text{C}_6\text{H}_4\text{R}$ </p> <p style="text-align: center;">R= CHO, COR'</p>
Michael Addition	 <p style="text-align: center;"> $\text{C}_6\text{H}_{10}\text{O} \xrightarrow{\text{Cu}^{\text{II}}} \text{C}_6\text{H}_{11}\text{O}$ </p>
Glaser Coupling	$2 \text{ Ph-C}\equiv\text{C-H} \xrightarrow{\text{Cu}^{\text{I}}} \text{Ph-C}\equiv\text{C-C}\equiv\text{C-Ph}$
CuAAC "click" reaction	 <p style="text-align: center;"> $\text{Ph-O-C}\equiv\text{C-H} + \text{N}_3\text{-CH}_2\text{-Ph} \xrightarrow{\text{Cu}^{\text{I}}} \text{Ph-O-CH}_2\text{-N=N-N-CH}_2\text{-Ph}$ </p>

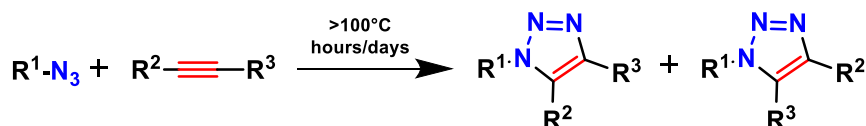
Table 4. Main reactions catalysed by copper.

7.5.1 Copper (I)-Catalysed Alkyne-Azide cycloaddition (CuAAC) “click” reaction

The definition of “*Click Chemistry*” is that “reactions must be modular, wide-ranging give very high yields, generate only harmless by-products that can be removed by non-chromatographic methods and be stereospecific, but not necessarily enantioselective”. [72] The most popular click reactions that have been modified to satisfy these requirements are: cycloaddition reactions (e.g., Diels-Alder reaction and 1,3-dipolar cycloaddition of Huisgen are the most common examples); [73-74] heterocyclic electrophiles (such as epoxides, aziridins, aziridinium ions) nucleophilic ring opening processes; non-aldocarbonyl compound reactions (urea, oxides, and hydrazoans), and added to carbon-carbon multiple bonds (especially Michael addition and thiol-ene chemistry). [75] Numerous scientific fields, including preparative organic synthesis, bio-conjugation, drug discovery, polymer and material science, and nanotechnology have been significantly impacted using click reactions. Furthermore, the potential of click chemistry to introduce desirable features into traditional polymers has garnered global attention, especially when paired with controlled/living polymerization techniques. These responses, however, might not be sufficient in some applications that display three-dimensional surface models or scaffolding, especially if spatial and temporal controls are also needed. [76-77] In 2001, Sharpless coined the term “click chemistry” to describe a set of reactions that produce strong bonds, enabling the rapid assembly of molecules with specific functions. The CuAAC reaction is a prime example of this concept. [78] In the original paper, it was noted that organic azides had the potential to be very selective yet highly energetic functional groups in organic synthesis. Their dipolar cycloadditions with olefins and alkynes were included in the reactions

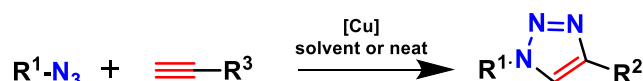
that satisfy the click criteria. It has been known for more than a century that terminal or internal alkynes react thermally with organic azides (**Scheme 6**). In 1893, A. Michael created the first 1,2,3-triazole by combining diethyl acetylenedicarboxybutyl carbonate and phenyl azide. Huisgen *et al.* investigated the reaction in detail between the 1950s and the 1970s. Even at higher temperatures, the reaction is very exothermic, but for inactivated reagents, the high activation barrier leads to very low reaction rates. Furthermore, both the dipole-HOMO and dipole-LUMO- controlled pathways function in these cycloadditions since the discrepancies in HOMO-LUMO energy levels for azides and alkynes are comparable in magnitude. Consequently, symmetric replacement of an alkyne generally results in a combination of products 1,2,3-triazol regioisomers. [79-80]

A

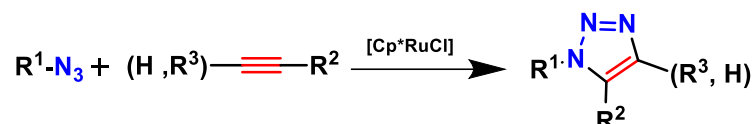


Reactions are faster when R² and R³ are withdrawing groups

B



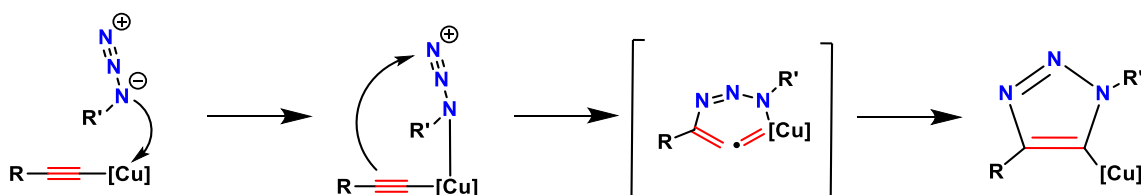
C



Scheme 6. **A)** Thermal cycloaddition of azides and alkynes usually requires prolonged heating and produces regioisomers mixtures of 1,4 and 1,5. **B)** CuAAC produces only 1,4 disubstituted-1,2,3-triazoles at room temperature with excellent yields. **C)** RuAAC

reaction proceeds with both terminal and internal alkynes and produces 1,5-disubstituted and completely 1,4,5-trisubstituted-1,2,3-triazoles.

With the use of copper catalyst (**Scheme 6B**), the reaction's mechanism and the product are significantly altered, becoming a series of distinct steps that lead to the creation of a 5-triazolyl copper intermediate. The nucleophilic β -carbon of copper acetyl chloride and the electrophilic terminal nitrogen of the coordinated organic azide create the crucial link in the creation of the C-N bond (**Scheme 7**).



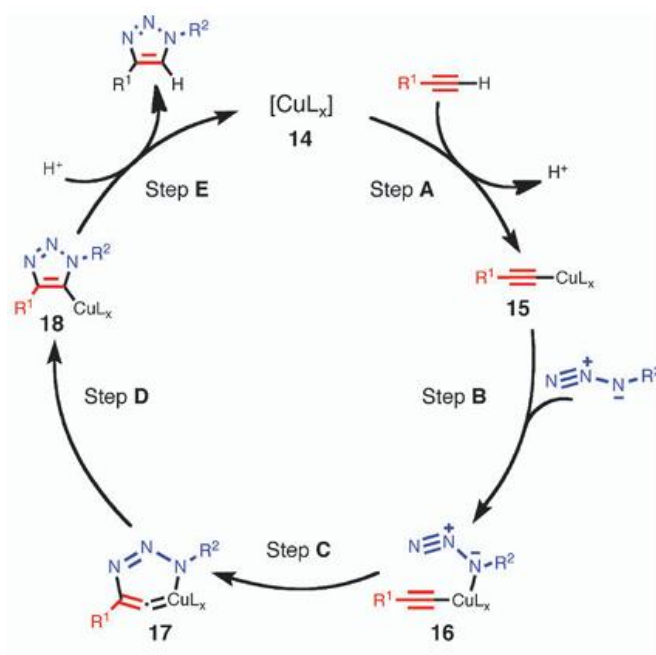
Scheme 7. Simplified representation of proposed steps for the formation of the C-N bond in the reaction of copper acetyls (i) with organic azides. [Cu] denote a monometallic centre in CuL_x or a cluster of-/oligometallic $\text{Cu}_x \text{L}_y$.

Compared to the thermal process, the CuAAC speed is improved by a factor of 10^7 , making it conveniently quick at room temperature and below. The primary, secondary, tertiary, aliphatic, aromatic and heteroaromatic azides typically react well with variably replaced terminal alkynes. The steric and electronic properties of the groups connected to the azide and alkyne centres do not significantly affect the reaction. Most organic and inorganic functional groups have little effect on the reaction, which makes protective group chemistry nearly unnecessary. The process happens in various protic and aprotic solvents, including water. Strong dipolar moment, aromatic character, ability to accept hydrogen bonds, and excellent chemical stability (usually inert under severe hydrolytic conditions, oxidizing and reducing, even at high temperature) are some of the favourable

qualities of the 1,2,3-triazole heterocycle. [81] As a result, it can engage in various beneficial interactions with surface, biological molecules, and organic and inorganic materials. For instance, it can function as a hydrolytically stable amide bond replacement. To date, azide-alkyne cycloaddition has only been reliably, simply, and 1,4-regiospecifically catalysed by copper. To be sure, no efficient catalyst has yet been developed to convert azides and terminal alkynes into 1,4-triazoles using any of the other metals known to catalyse different alkyne conversions. Many investigations were conducted on complexes of Ag (I), Pd (0/II), Pt (II), Au (I/III), Hg (II), which were unable to synthesize triazoles in synthetically usable yields; their impact on the cycloaddition's selectivity and speed was hardly perceptible. Cu (I) possesses a unique catalytic activity explained by its quick interchange of these and other ligands in its coordination sphere, especially under aqueous conditions, and by its capacity to involve terminal alkynes in both σ and π contacts. The initial C-N bond is formed when an organic azide acts as a ligand by a combination of synergistic alkyne nucleophilic activation and azide electrophilic activation. It was discovered in 2005 that cyclopentadienyl ruthenium complexes include internal alkynes in cycloaddition and catalyse the production of complementary 1,5 disubstituted triazole by azides and terminal alkynes (**Scheme 6C**). [82] These differences indicate that this twin process, known as RuAAC (azide-alkyne cycloaddition catalyzed by ruthenium), is mechanistically quite like that catalyzed by copper. RuAAC has a great range of applications and compatibility, however compared to CuAAC, the reaction is more susceptible to solvents and the steric requirements of azide substituents. [83] The applications of this reaction are currently being investigated. Since its invention, the CuAAC has been used under various experimental settings, highlighting its durability and compatibility with many functional groups, solvents, and additives, independent

of the catalyst source. Copper(I) can come from a variety of sources, including coordination complexes like $[\text{Cu}(\text{CH}_3\text{CN})_4]\text{PF}_6$ and $[\text{Cu}(\text{CH}_3\text{CN})_4]\text{OTf}$, as well as copper salts (iodide, bromide, chloride, acetate). [84] However, in general, it is not advised to utilize copper iodide due to its potential to act as a bridge binder for metal, which can lead to the development of polynuclear acetyl complexes that bind the catalyst and obstruct the productive catalytic cycle. Furthermore, under some circumstances, 1-iodoalkynes and 5-iodothydrines may be formed by copper iodide (I). [85] Copper exists in three oxidation states: 0, +1, +2. From a thermodynamic perspective, +1 is the least stable. The cuprous ion may oxidize to a Cu (II) species that is not catalytically active or disproportionate to a combination of Cu (II) and Cu (0). The capacity of Cu (II) to mediate these Glaser-type alkyne coupling reactions can compromise the production of triazoles while causing undesirable byproducts to arise when present in sufficient amounts. Fokin *et al.* presented ascorbate, a mild reducing agent, as a suitable and workable substitute for oxygen-free circumstance. [86] Its combination with an easily accessible and stable copper salt (II), like copper acetate (II) or copper sulphate (II) pentahydrate, was quickly accepted as the method of choice for the preparation synthesis of 1,2,3-triazoles. In **Scheme 8** the catalytic cycle for the CuAAC "click" reaction has been proposed in detail. Due to the well-known easiness of this phase, copper acetylurum (I) is formed through an exothermic process that most likely involves a complicated intermediate of π -alkyne copper (**Step A**). The alkyne terminal hydrogen is greatly acidified by copper alkyne π -coordination, which puts it in the proper range for deprotonation in an aqueous media and produces a σ -acetyl chloride. The azide is then activated by copper coordination (**Step B**), forming the intermediate 16. This process of ligand exchange seems to be nearly thermoneutral, and the coordination event benefits both reactive partners in a synergic way: azide coordination discloses the β -

nucleophile qualities, and the azide's term gets event more electrophilic, just like vinylidene does. The first C-N bond formation event and the development of a cyclic structure containing a metal occur in **Step C**. When copper (I) is used the catalyst in this stage, we see an increase in the rate of reaction. Ultimately, the desired product 1,4-triazole will develop after structural rearrangement. [87]



Scheme 8. Proposed catalytic cycle for CuAAC “click” reaction. [88]

When copper (II) is utilized without the assistance of a reducing agent 1,2,3-triazole generally seems to develop with yields substantially below expectations. The formation of the reaction product would also be altered, as we would have a mixture of 1,4 and 1,5 regioisomeric compounds. Without the purposeful inclusion of a reducing agent like sodium ascorbate, a study has demonstrated how copper acetate in particular speeds up the CuAAC reaction in organic solvents, especially in alcohols. According to the most widely recognized theory, this reaction involves a homocoupling process in which $\text{Cu}(\text{OAc})_2$ is reduced

using an alcoholic solvent or terminal alkyne, leading to the rapid emergence of the catalytic species Cu(I). [88]

7.5.2 Application of triazoles

The CuAAC “click” reaction holds significant promise in pharmaceutical research due to the biorthogonality and relative inertness of azide and alkyne partners toward biological molecules and aqueous environments [89]. This unique feature allows for the selective labelling and modification of biomolecules without interfering with their natural functions. Consequently, several drugs targeting biomolecules have been synthesized using this “click” chemistry approach, enabling parallel production of various therapeutic agents once a “clickable” derivative of the biomolecule is created [90]. Triazoles and their derivatives, in particular, have garnered considerable interest in recent decades for their diverse biological properties, which include anticancer, antiviral, antimalarial, antioxidant, antileishmanial, antifungal, and antibacterial activities, as well as anticonvulsant effects [91-93]. (Figure 36).

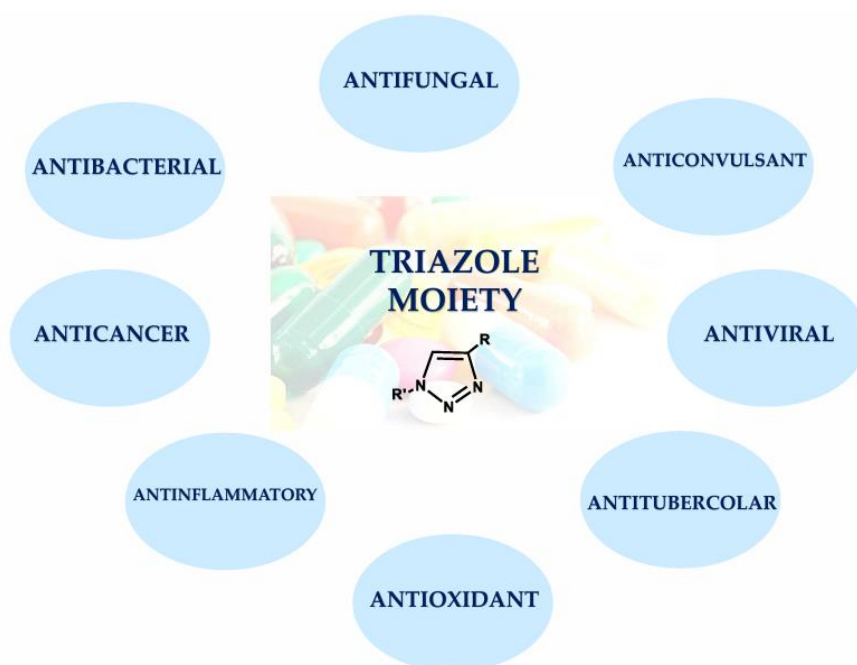
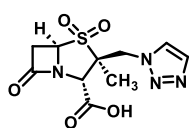


Figure 36. Pharmacological activities of triazoles.

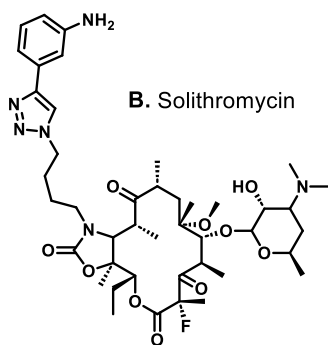
According to recent studies, triazole is thought to be most effective scaffold and a significant isostere of thiopurine, imidazole, benzotriazole and others conjugates in the synthesis of novel drug candidates. [94-96] This structure serves as the primary nucleus of several drugs and exhibits good inhibition of a wide range of enzymes, including β -lactamase, tyrosinase, acetylcholinesterase, carbonic anhydrase and α -glucosidase. [97-98] Nevertheless, there are a few significant drawbacks to click reactions, including the biocompatibility of 1,2,3-triazoles and the safety of copper catalyst in vivo. Moreover, there are several explosive heavy metal azides, which raise severe issues for click synthesis and large-scale pharmaceutical research. Despite this, the CuAAC reaction has proven to be the most effective and optimal tool for medicinal chemistry when it comes to creating new biomolecules or inducing changes in preclinical and clinical tests. [99] Since 1,2,3-triazoles are robust against metabolic degradation and readily connect with biological targets, they serve as biocompatible linkers. Furthermore, triazoles are stable against both basic and acid hydrolysis and have a strong aromatic stabilization. Numerous investigations have been done on the creation of novel anticancer agents with tailored modes of action because cancer is a severe public health issue. CuAAC reactions have been instrumental in development of several anti-cancer drugs, which is why a lot of research has been carried out utilizing the triazole nucleus as a foundation for the synthesis of possible anticancer agents. Mandalapau *et al.* study, which reported the synthesis of conjugate libraries of 1,2,3-triazole based on curcumin and assessed their antitumor activity towards endocrine tumours, is one example of this. [100] Additionally, Osmaniye *et al.* used the MTT experiment to prepare and characterize in vitro investigations of several novel triazoles as anticancer agents against the breast cancer cell line (MCF-7), utilizing the medication Doxorubicin as a positive reference. In docking investigations, interactions were evaluated

and the results showed that the human aromatase enzyme establishes a π - π interaction which is responsible for the inhibitory potential against MCF-7 cells. [101] Triazoles can also be used as antibacterial agents. The increasing prevalence of disease worldwide due to bacterial pathogens resistant to antibiotics is a major concern for human health. Recently, new antibacterial medicines that target novel molecular targets linked to the prevention of bacterial growth have been synthesized using click chemistry. The design, synthesis and in vitro testing of novel hybrid compounds based on triazole-based chalcones, and flavones were demonstrated by Kant *et al.* Twentyfive novel hybrid compounds were synthesized using copper-catalysed click chemistry; some of these compounds had good antibacterial action against *K. Pneumoniae*, *P. Aeruginosa*, *S. Aureus*, *E. Faecalis* and *E. Coli*. [102] In a different study Lal *et al.* have developed several 1,2,3-triazoles analogues based on imine, which have demonstrated a significant potency against *E. Coli* due to the formation of hydrogen bonds with *E. Coli* DNA gyrase. [103] Substantial attempts have been undertaken to create antiviral medications that target specific human viruses, including the coronavirus (CoV), HIV, herpes, hepatitis and influenza. [104] Arnàiz *et al.* utilized CuAAC to create anionic carboxysilane dendrimers, which were then examined for their ability to combat HIV. [105] Because of its excellent selectivity, yields, flexibility and dependability, CuAAC is the recommended technique for dendrimer synthesis. Esters were mixed with functionalized alkynes to create these molecules. These displayed strong anti-viral properties. Zhan *et al* examined in 2020 the antiviral activity of 4-phenyl-1H-1,2,3-triazole phenylaniline derivatives in a different study. They also evaluated the cytotoxicity of these derivatives using TZM-bl cells that were fully infected with the HIV-1 and NL4- virus. According to the antiviral data, most of the compounds exhibited moderate to strong efficacy against HIV-1 virus and NL4-3. [106] click reactions have been thought to be

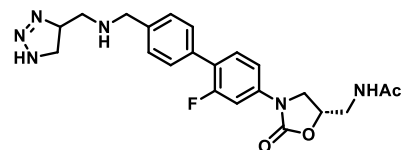
perfect for producing radiopharmaceuticals for positron emission tomography (PET) nuclear imaging in addition to serving as a scaffold for the development of possible novel medications. Applications by using resonance imaging (MRI) and single photon emission computed tomography (SPECT) are extensive in USA. One-pot synthesis of ^{11}C -labelled 1,2,3-triazoles was achieved by Schirmacher *et al.* [107] Currently undergoing testing are several medications based on triazoles, one of which is the antibiotic Radezolid, an oxazolidinone. Melinta Therapeutics is developing an antibiotic intended to treat skin infections and bacteria. [108] Synthesized using cycloaddition processes (3+2), Molidstat (BAY 85-3934) is a novel inhibitor of prolyl hydroxylase that is presently undergoing phase III clinical studies for the treatment of renal anaemia. [109-110] Another anticancer medication produced using click chemistry is carboxyammidotriazole. Although this drug was utilized in clinical studies on patients with solid tumours, it was removed since human trials did not yield positive outcomes. [111] Azide-alkyne cycloaddition is used to create Rufinamide, a derivative of triazoles. Lennox-Gastuats syndrome and other seizure disorders are treated with it as an anticonvulsant. Tazobactam is a triazole-based medication that is derived from penicillanic acid sulfone and is known to block the activity of the bacterial enzyme β -lactamase. [90] All the structures are shown in **Figure 37**.



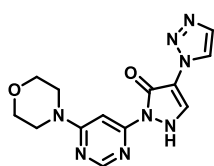
A. Tazobactam



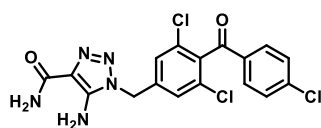
B. Solithromycin



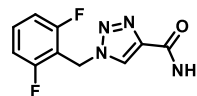
C. Radezolid



D. Molidustat



E. Carboxyamidotriazole



F. Rufinamide

Figure 37. Chemical structures of marketed therapeutics.

7.6 Potential toxicity of copper

Copper (Cu) is an essential trace element present in small amounts across various cells and tissues with the highest concentration in the liver. Cu ions exist in two forms in vivo: reduced copper (Cu^+) and oxidized copper (Cu^{2+}). [112] Since the 1920s, copper supplements have been used to treat anemia in animals, and human cases of copper deficiency have been reported in 1960s. [113-114] Copper acts as a critical cofactor in the structural and catalytic functions of several enzymes, such as lysyl oxidase, cytochrome c oxidase, tyrosinase, dopamine β -hydroxylase, and Cu-Zn superoxide dismutase (Cu, Zn_SOD). [115] These enzymes play essential roles in processes like development, maintenance and growth. The adsorption of copper in human body depends on the chemical form of copper and other food component, with only 30 to 50 percent of ingested copper, primarily Cu^{2+} , being absorbed in the small intestine. [116-118] Copper is carried by the blood, mainly bound to albumin, and is either stored in the liver, eliminated through bile or retained for use in enzymes. However, while copper plays vital physiological roles, its use as a homogeneous catalyst in industrial and chemical processes poses certain risks. When copper is used in homogeneous catalysis, it can remain in the final reaction products. This copper residual is a critical issue in pharmaceutical and food applications due to its potential toxicity. Chronic copper poisoning can cause liver cirrhosis, haemolysis, brain damage and kidney failure. [119] Moreover, copper has been implicated in the pathogenesis of neurodegenerative diseases like Alzheimer's and Wilson's disease, where dysregulated copper metabolism and oxidative stress play a key role. In Alzheimer's disease, for example, copper bound to amyloid plaques catalyses the production of harmful reactive oxygen species (ROS), contributing to neuronal degradation and cognitive decline (**Figure 38**). [120-121] To address

these risks, anchoring copper onto solid supports as a heterogeneous catalyst has become a valuable approach. Unlike homogeneous catalysts, solid-supported copper remains immobilized, significantly limiting the leaching of copper into reaction products, which enhances safety in sensitive applications. Additionally, heterogeneous catalysts are more stable and reusable, offering advantages in reducing contamination and promoting sustainability. Although synthesizing supported copper catalysts can be more complex and costly, their benefits, particularly in terms of reducing health risks and environmental impact, make them an attractive option for various industrial and pharmaceutical processes. [122]

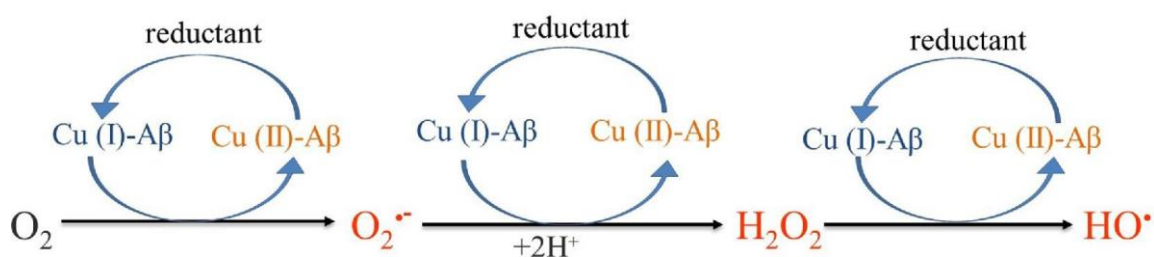


Figure 38. Mechanism of ROS production from a reductant and dioxygen is catalysed by the Cu-Aβ complex. Superoxide anion (O₂^{•-}), hydrogen peroxide (H₂O₂), and the hydroxyl radical (HO[•]) are ROS species produced during the reaction mechanism. [121]

8. Objectives of this thesis in the field of COP

A new covalent organic polymer (COP) featuring amide bonds was designed and synthesized starting from pyridine 2,6-dicarboxylic acid and tetrakis (4-aminophenyl) methane. The polymer was created using the conventional synthetic approach. The decision to employ amide bonds, rather than the more commonly used imine bonds, was based on their superior structural stability. Although imine bonds are prevalent in similar systems, the stability offered by amide linkages made them the preferred choice for a more stable heterogeneous catalyst. The resulting COP was thoroughly characterized both chemically and morphologically (via FT-IR, thermogravimetric analysis, BET, AFM and SEM). Starting from the synthesized COP, the coordination of the system with different metals was tested, among which the coordination with copper (II) acetate was particularly encouraging. Copper has impressive catalytic properties, for this reason it was used to construct a metal-organic heterogeneous catalyst. A solution containing the copper acetate at various concentrations was prepared, and it was allowed to react with the polymer that had already been created, obtaining the final product $\text{Cu}^{2+}\text{@COP}$. It was then examined if Cu^{2+} could be reduced to Cu^+ . To facilitate the reaction between the $\text{Cu}^{2+}\text{@COP}$, an aqueous solution of ascorbic acid, as a reducing agent, was prepared in a concentration of 50 mM. The metal content in this heterogeneous catalyst was quantified in percentages using ICP-MS analysis. In addition, XPS analyses was performed to verify that the reduction of copper from (II) to (I) was successful. Then we provide the characterization from a chemical (FT-IR, Thermogravimetric Analysis, RAMAN) and morphological (AFM, SEM) point of view of the obtained systems. The synthesized metal organocatalyst has been tested in Copper (I)-Catalysed Alkyne-Azide Cycloaddition (CuAAC) “click” reaction.

Specifically, to compare the yields of the compounds produced, reactions were conducted in both homogeneous phase with copper sulphate (as the standard synthetic protocol proposed by Sharpless) and heterogeneous phase with Cu^{2+} @COP and Cu^+ @COP. The use of heterogeneous catalysis was clearly superior to the homogeneous one in particular Cu^+ @COP has proven to be more effective than Cu^{2+} @COP in all the reactions. The product were affected by the steric hindrance in proximity of azides. One of the main advantages that should be highlighted is that aqueous solvents are mostly used both in the copper coordination step to COP and in the CuAAC “click” reaction step, leading to more sustainable chemistry. Furthermore, the triazole products were obtained by crystallization process, bypassing the use of chromatographic columns for purification step.

9. Materials and Methods

9.1 Chemicals and Reagents

All solvents and all reagents used for the synthesis of COP, Cu²⁺@COP, Cu⁺@COP and in the CuAAC “click” reaction were supplied from Merck (Darmstadt, Germany). Pre-coated silica gel F₂₅₄ sheets for TLC from Merck (Darmstadt, Germany) were used for reaction monitoring.

9.2 Instruments

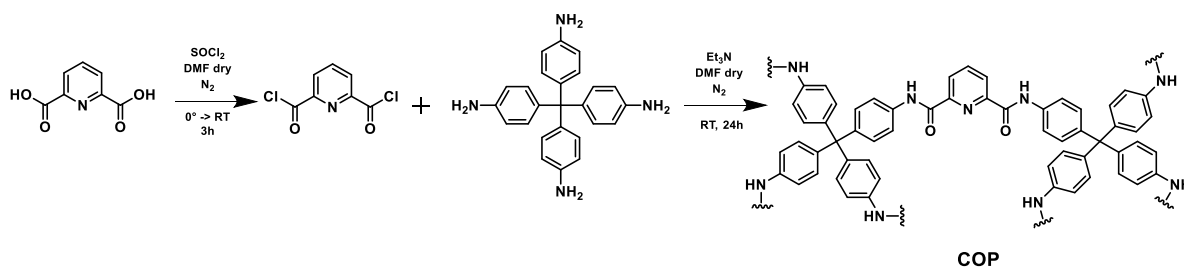
The ¹H- and ¹³C-NMR spectra were obtained with either deuterated chloroform (CDCl₃), deuterated methanol (CD₃OD) and deuterated dimethyl sulfoxide (DMSO) solution using a Bruker spectrometer. ¹H NMR spectra were obtained at 400 MHz, while ¹³C spectra were at 100 MHz ATR-FTIR spectroscopy was performed using a Jasco FT/IR-6800 equipped with an ATR (Attenuated Total Reflectance) accessory having a spectral range of 4000-650 cm⁻¹. Scanning Electron Microscopy (SEM, JEOL JSM-7100), images of the COP, COP@Cu²⁺ and COP@Cu⁺ were taken operating at 5 kV. The solution was drop casted onto a silicon substrate. Nitrogen sorption and desorption measurements were done at 77K using TriStar 3000 from Micrometrics. Carbon black lot 180049/180052 (21.3 m²/g ± 0.75) was used as certified reference material to check the accuracy of the analyser by triplicate. Result (mean of three estimates): 21.9537 m²/g (SD: 0.13575). The degassing temperature for this process reached 100°C and the degassing was set for 24h. The relative pressure (P/P_0) used for the BET determination ranges from 2.69E-5 to 0.990998. Thermogravimetric Analysis was performed on a SDT 650, TA Instrument Waters. The experimental conditions

required alumina crucibles of 90 μL volume, and an atmosphere of dry nitrogen with 50 mL/min flow rate. The treatment of the samples (COP, Cu^{2+} @COP, Cu^+ @COP) includes a ramp rate from 30° to 1500 °C at a rate of 20 °C min^{-1} . PXRD patterns were collected with MiniFlex 600 powder diffractometer equipped with a X-ray generator of 600 W (40 kV-15 mA). PXRD measurements were collected on flocculated samples in ethanol with a step sized of 1.5° 2Θ and a measuring time of 60 seconds per step. The surface topography of COP and Cu^{2+} @COP samples was investigated by Atomic Force Microscopy (AFM) by using the MultiMode 8 AFM microscope (Bruker, Billerica, Massachusetts, USA) equipped with a Nanoscope V controller in Tapping Mode in air. Commercial silicon cantilever RTESPA-150 (rectangular geometry, cantilever resonance frequency 150 kHz and nominal spring constant 6 N/m) with a nominal tip radius of 8 nm was used to analyze properties such as topography and roughness across scan size areas of 1 μm \times 1 μm . Images of 512 \times 512 pixels were collected and elaborated using the Nanoscope Analysis 1.8 software (Bruker, Billerica, MA, USA). The analyses were performed using iCAP 7200 ICP-OES Duo from Thermo Fisher Scientific, USA, in dual view (radial and axial configuration). Acid digestion of the samples has been performed using Ethos UP Microwave Digestion System from Milestone, Italy, equipped with PTFE-TFM SK-15 easy TEMP vessels from Milestone. Samples were transferred into the ICP-OES with the autosampler ASX-560 from Teledyne Cetac Technologies, USA. Standard solutions were prepared using the Certipur® ICP multi-element standard solution XVI (from Sigma-Aldrich) at 100 mg/L in nitric acid. Suprapur® Hydrochloric acid 36% and Suprapur® Nitric acid 69% for the preparation and dilution of the solutions were obtained from Sigma-Aldrich. Ultrapure water (with a resistivity of 18,2 $\text{M}\Omega\text{-cm}$) was obtained using the purification system Direct-Q® 3 UV Millipore, using Biopak® filter by Merck, Germany.

Argon gas 5.0, purity $\geq 99,999\%$ mol, was obtained from Nippon Gases Rivoira. Data were managed and analysed using the software Qtegra ISDS (Intelligent Scientific Data Solution Software) from Thermo Fisher Scientific. Raman spectra were run at room temperature in backscattering geometry with an inVia Renishaw micro-Raman spectrometer equipped with an air-cooled CCD detector and super-Notch filters. An Ar⁺ ion laser ($\lambda_{\text{laser}} = 514 \text{ nm}$) was used, coupled to a Leica DLML microscope with a 20 \times objective. The resolution was 2 cm⁻¹ and spectra were calibrated using the 520.5 cm⁻¹ line of a silicon wafer. Raman spectra were acquired with 1% of power, 10 seconds of spectral acquisition, and 20 scans. Diffuse reflectance UV-Vis spectra were acquired with a Shimadzu UV-2600i spectrometer equipped with an integrating sphere (ISR-2600Plus). Each spectrum was collected in the spectral range between 220-900 nm, with a data interval of 0.1 nm and a slit width of 5 nm. XPS measurements were carried out using an Omicron NanoTechnology Multiprobe MXPS system equipped with a Mg K α ($h\nu = 1253.6 \text{ eV}$) X-ray source, operating the anode at 14 kV and 16 mA. Narrow binding energy regions were acquired using an analyzer pass energy of 20 eV. A take-off angle of 21 $^\circ$ with respect to the sample surface normal was adopted. The experimental spectra were theoretically reconstructed by fitting the secondary electrons background to a Shirley function and the elastic peaks to pseudo-Voigt functions described by a common set of parameters: position, full-width at half-maximum (FWHM), Gaussian-Lorentzian ratio.

9.3 Synthesis of COP

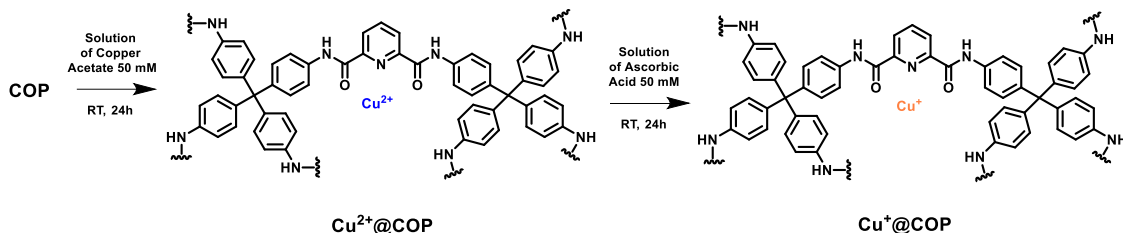
COP was synthesized starting from pyridine-2,6-dicarboxylic acid and tetrakis (4-aminophenyl) methane through conventional procedure as is reported in **Scheme 9**. Pyridine-2,6-dicarboxylic acid (351.39 mg; 2.10 mmol) was dissolved in *N,N*-dimethylformamide (V= 4.0 mL), thionyl chloride (152 μ L; 2.10 mmol; d: 1.64 g/cm³) was then added at zero degrees drop by drop and stirred for three hours at room temperature to promote the acid activation. Then were dissolved in *N,N*-dimethylformamide (V= 2.0 mL), triethylamine (0.44 mL; 3.15 mmol; d: 726 g/cm³) and tetrakis (4-aminophenyl) methane (400 mg; 1.05 mmol). The reaction was left at room temperature under inert atmosphere, due to the presence of nitrogen, for 24 hours under stirring. Then to the reaction, a saturated sodium chloride solution was added to facilitate the precipitation of the COP, which was filtered, washed with distilled water in order to remove the salt and dried at 100 °C.



Scheme 9. Synthetic procedure of COP.

9.4 Synthesis of $\text{Cu}^{2+}@COP$ and $\text{Cu}^+@COP$

Copper complexes constructions were carried out, as it is presented in **Scheme 10**, by adding copper (II) acetate onto COP to obtain $\text{Cu}^{2+}@COP$. A solution 50 mM of copper (II) acetate was added to 100.0 mg of COP and the mixture was left at room temperature for 24 hours under stirring. Then the solid was filtered, washed with distilled water to remove the excess of the copper acetate and dried at 100°C for 5 hours. The synthesis of $\text{Cu}^+@COP$ started from $\text{Cu}^{2+}@COP$ (100.0 mg) which was added into a solution 50 mM of ascorbic acid and the mixture is left at room temperature to let the reduction of copper. Then the solid is filtered and washed with distilled water and dried at 100°C for 5 hours under inert atmosphere due to the presence of nitrogen, to avoid possible oxidation reactions of the metal.



Scheme 10. Synthesis of $\text{Cu}^{2+}@COP$ and its reduction into $\text{Cu}^+@COP$.

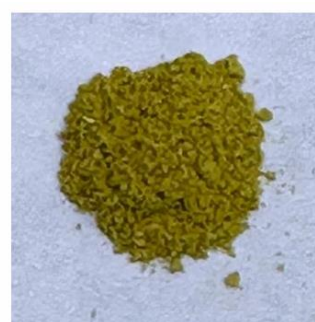
Figure 39 illustrates how the polymer's colour changes depending on the reaction step. Specifically, after the first step, the product has a brownish colour; after coordination with copper acetate, it turns green; and in the final step, which involves ascorbic acid as reductant reagent, the product becomes yellow.



COP



Cu²⁺@COP



Cu⁺@COP

Figure 39. Reaction products obtained: COP, Cu²⁺@COP, Cu⁺@COP.

9.5 Synthesis of 1,2,3-triazole (1-11) through homogeneous phase, $\text{Cu}^{2+}@\text{COP}$, $\text{Cu}^+@\text{COP}$

As shown in **Figure 40**, a library of triazoles (1-11) was synthesized using different azides precursors. Each product obtained was characterized using ^1H -NMR and ^{13}C -NMR.

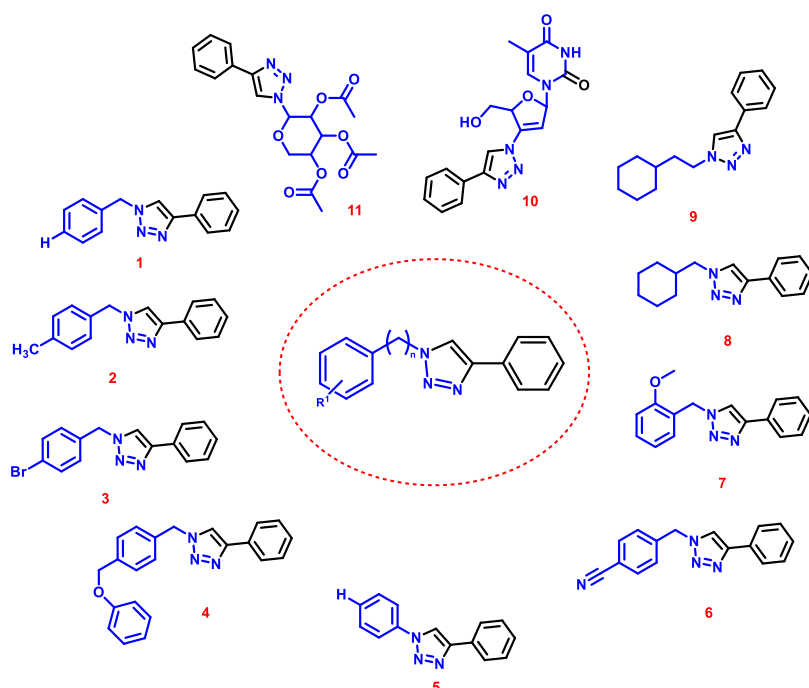


Figure 40. Products of the CuAAC “click” reaction 1-11.

General procedure in homogeneous phase

Triazole compounds were synthesized by the following procedure: a solution of azide precursors (0.45 mmol) was dissolved in $\text{H}_2\text{O}/t\text{-But}$ 2:1 ($V = 2.0$ mL), then copper sulphate (3.59 mg; 0.02 mmol), ascorbic acid and phenylacetylene (55.2 mg; 0.54 mmol; $d: 930$ Kg/m³) were added to the reaction. The reaction was left at 60 °C and its course is controlled by TLC until complete after 24 hours (Mobile

Phase: Hex/EtOAc 2:1). The organic product was then extracted by ethyl acetate (3x20 mL). Finally, the product was dried over anhydrous Na₂SO₄ and concentrated at rotavapor. The final product was purified through a chromatographic column with silica gel. Mobile Phase: AcOEt/n-Hexane: 3:1.

General procedure with Cu²⁺@COP

A solution of azide precursors (0.45 mmol) was dissolved in H₂O/^tBut 2:1 (V= 2.0 mL), then Cu²⁺@COP (5% mol), ascorbic acid (15.85 mg; 0.09 mmol) and phenylacetylene (55.2 mg; 0.54 mmol; d: 930 Kg/m³) were added to the reaction. The reaction was left at 60 °C and its course is controlled by TLC until complete after 24 hours (Mobile Phase: Hex/EtOAc 2:1). The reaction was filtered to remove Cu²⁺@COP. Then the organic product is then extracted by ethyl acetate (3x20 mL). Finally, the product is dried over anhydrous Na₂SO₄ and concentrated at rotavapor. The final product is purified through crystallization in n-hexane to remove the excess of phenylacetylene and to let the formation of a white precipitation which was then filtered.

General procedure with Cu⁺@COP

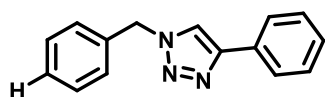
A solution of azide precursors (0.45 mmol) was dissolved in H₂O/^tBut 2:1 (V= 2.0 mL), then Cu⁺@COP (5% mol) and phenylacetylene (55.2 mg; 0.54 mmol; d: 930 Kg/m³) were added to the reaction. The reaction was left at 60 °C and its course is controlled by TLC until complete after 24 hours (Mobile Phase: Hex/EtOAc 2:1). The reaction was, then, filtered to remove the presence of the Cu⁺@COP. Then the organic product was then extracted by ethyl acetate (3x20 mL). Finally, the product was dried over anhydrous Na₂SO₄ and concentrated at rotavapor. The final product was purified through crystallization in n-Hexane to remove the

excess of phenylacetylene and to let the formation of a white precipitation which was then filtered.

General procedure with Cu²⁺@COP without ascorbic acid

A reaction test was performed to determine whether the yields obtained were truly higher than with Cu (I), since examples of CuAAC reactions catalysed by copper acetate without the assistance of a reducing agent are provided in the literature. [136] The following procedure was used: a solution of azide precursors (0.45 mmol) was dissolved in H₂O/*t*But 2:1 (V= 2.0 mL), then Cu²⁺@COP (5% mol) and phenylacetylene (55.2 mg; 0.54 mmol; d: 930 Kg/m³) were added to the reaction. The reaction was left at 60 °C and its course was controlled by TLC until complete after 24 hours (Mobile Phase: Hex/EtOAc 2:1). The reaction was filtered to remove the presence of the Cu²⁺@COP. Then the organic product was then extracted by ethyl acetate (3x20 mL). Finally, the product was dried over anhydrous Na₂SO₄ and concentrated at rotavapor. The final product was purified through crystallization in *n*-hexane to remove the excess of phenylacetylene and to let the formation of a white precipitation which was then filtered.

Synthesis and characterization of 1



This compound was synthesized starting from benzyl azide (59.91 mg; 0.45 mmol) which was dissolved in H₂O/*t*But 2:1 (V= 2.0 mL), then copper sulphate (3.59 mg; 0.02 mmol), ascorbic acid (15.85 mg; 0.09 mmol) and phenylacetylene (55.2 mg; 0.54 mmol; d: 930 Kg/m³) were added to the reaction. For synthesis with

Cu⁺@COP and Cu²⁺@COP, a 5% catalyst was used in moles compared to azide. In the case of the Cu²⁺@COP reaction was performed with ascorbic acid (15.85 mg; 0.09 mmol).

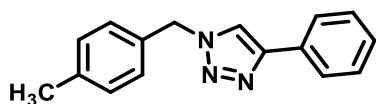
Yield: reported in **Tab. 6**.

Aspect: White solid.

¹H NMR (CD₃OD, 400 MHz, δ, ppm): 5.65 (2H, s, -CH₂-), 7.39 (8H, m, 8 H_{Ar}, J=8Hz), 7.81 (2H, dd, 2 H_{Ar}, J=8Hz), 8.31 (1H, s, 1H_{Triazole}).

¹³C{H}- NMR (MeOD₄, 101 MHz, δ, ppm): 54.25, 119.53, 125.71-134.71, 148.25.

Synthesis and characterization of 2



This compound was synthesized starting from 1-(azidomethyl)-4-methylbenzene (66.23 mg; 0.45 mmol) which was dissolved in H₂O/*t*But 2:1 (V= 2.0 mL), then copper sulphate (3.59 mg; 0.02 mmol), ascorbic acid (15.85 mg; 0.09 mmol) and phenylacetylene (55.2 mg; 0.54 mmol; d: 930 Kg/m³) were added to the reaction. For synthesis with Cu⁺@COP and Cu²⁺@COP, a 5% catalyst was used in moles compared to azide. In the case of the Cu²⁺@COP reaction was performed with ascorbic acid (15.85 mg; 0.09 mmol).

Yield: reported in **Tab. 6**.

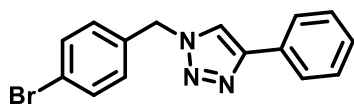
Aspect: White solid.

¹H NMR (CDCl₃, 400 MHz, δ, ppm): 2.38 (3H, s, -CH₃-), 5.56 (2H, s, -CH₂-), 7.33 (7H, m, 7 H_{Ar}, J=8Hz), 7.66 (1H, s, 1H_{Triazole}), 7.81 (2H, d, 2 H_{Ar}, J=8Hz).

¹³C{H}- NMR (CDCl₃, 101 MHz, δ, ppm): 54.11, 119.41, 125.72-131.60, 139.79.

Anal. Calcd for C₁₉H₂₃N₃O₇: C, 56.29; H, 5.72; N, 10.37; O, 27.62.

Synthesis and characterization of 3



This compound was synthesized starting from 1-(azidomethyl)-4-bromobenzene (95.42 mg; 0.45 mmol) which was dissolved in H₂O/*t*But 2:1 (V= 2.0 mL), then copper sulphate (3.59 mg; 0.02 mmol), ascorbic acid (15.85 mg; 0.09 mmol) and phenylacetylene (55.2 mg; 0.54 mmol; d: 930 Kg/m³) were added to the reaction. For synthesis with Cu⁺@COP and Cu²⁺@COP, a 5% catalyst was used in moles compared to azide. In the case of the Cu²⁺@COP reaction was performed with ascorbic acid (15.85 mg; 0.09 mmol).

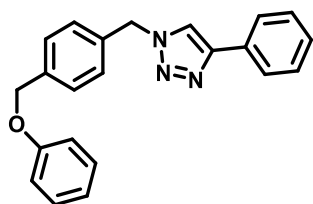
Yield: reported in **Tab. 6**.

Aspect: White solid.

¹H NMR (CDCl₃, 400 MHz, δ, ppm): 5.61 (2H, s, -CH₂-), 7.35 (8H, m, 8 H_{Ar}, J= 8Hz), 7.68 (2H, t, 2 H_{Ar}, J=8Hz), 7.83 (1H, s, 1H_{Triazole}).

¹³C{H}- NMR (CDCl₃, 101 MHz, δ, ppm): 53.57, 122.09-132.36, 133.71.

Synthesis and characterization of 4



This compound was synthesized starting from 1-(azidomethyl)-4-(phenoxy methyl) benzene (107.67 mg; 0.45 mmol) which was dissolved in H₂O/*t*But 2:1 (V= 2.0 mL), then copper sulphate (3.59 mg; 0.02 mmol), ascorbic acid (15.85 mg; 0.09 mmol) and phenylacetylene (55.2 mg; 0.54 mmol; d: 930 Kg/m³) were added to

the reaction. For synthesis with Cu⁺@COP and Cu²⁺@COP, a 5% catalyst was used in moles compared to azide. In the case of the Cu²⁺@COP reaction was performed with ascorbic acid (15.85 mg; 0.09 mmol).

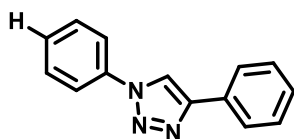
Yield: reported in **Tab. 6**.

Aspect: White solid.

¹H NMR (CDCl₃, 400 MHz, δ, ppm): 5.10 (2H, s, -CH₂-N-), 5.54 (2H, s, -O-CH₂-), 7.01 (2H, d, 2 H_{Ar}, J= 8Hz), 7.41 (10H, m, 10 H_{Ar}, J= 4Hz), 7.66 (1H, s, 1H_{Triazole}), 7.82 (2H, d, 2H_{Ar}, J= 8Hz).

¹³C{H}- NMR (CDCl₃, 101 MHz, δ, ppm): 53.78, 70.11, 115.45, 119.38, 125.72-130.61, 136.63, 148.13, 159.16.

Synthesis and characterization of 5



This compound was synthesized starting from aniline (41.89 mg; 0.45 mmol) which was dissolved in H₂O/^tBut 2:1 (V= 2mL), then copper sulphate (3.59 mg; 0.02 mmol), ascorbic acid (15.85 mg; 0.09 mmol) and phenylacetylene (55.2 mg; 0.54 mmol; d: 930 Kg/m³) were added to the reaction. For synthesis with Cu⁺@COP and Cu²⁺@COP, a 5% catalyst was used in moles compared to azide. In the case of the Cu²⁺@COP reaction was performed with ascorbic acid (15.85 mg; 0.09 mmol).

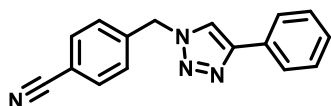
Yield: reported in **Tab. 6**.

Aspect: White solid.

¹H NMR (CDCl₃, 400 MHz, δ, ppm): 7.51 (6H, m, 6H_{Ar}, J=8Hz), 7.83 (2H, d, 2H_{Ar}, J= 8Hz), 7.95 (2H, d, 2H_{Ar}, J= 8Hz), 8.23 (1H, s, 1H_{Triazole}).

$^{13}\text{C}\{\text{H}\}$ - NMR (CDCl_3 , 400 MHz, δ , ppm): 117.63, 120.57, 125.89-130.23, 137.09, 148.43. Anal.

Synthesis and characterization of 6



This compound was synthesized starting from 4-(azidomethyl) benzonitrile (71.17 mg; 0.45 mmol) which was dissolved in $\text{H}_2\text{O}/t\text{But}$ 2:1 ($V= 2.0$ mL), then copper sulphate (3.59 mg; 0.02 mmol), ascorbic acid (15.85 mg; 0.09 mmol) and phenylacetylene (55.2 mg; 0.54 mmol; $d: 930$ Kg/m^3) were added to the reaction. For synthesis with $\text{Cu}^+\text{@COP}$ and $\text{Cu}^{2+}\text{@COP}$, a 5% catalyst was used in moles compared to azide. In the case of the $\text{Cu}^{2+}\text{@COP}$ reaction was performed with ascorbic acid (15.85 mg; 0.09 mmol).

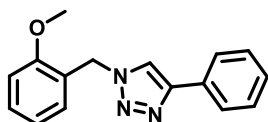
Yield: reported in Tab. 6.

Aspect: White solid.

^1H NMR (CDCl_3 , 400 MHz, δ , ppm): 5.68 (2H, s, $-\text{CH}_2-$), 7.28 (1H, s, $1H_{\text{Triazole}}$), 7.40 (5H, m, $5H_{\text{Ar}}$, $J= 4\text{Hz}$), 7.71 (2H, d, $2H_{\text{Ar}}$, $J= 8\text{Hz}$), 7.84 (2H, d, $2H_{\text{Ar}}$, $J= 8\text{Hz}$).

$^{13}\text{C}\{\text{H}\}$ - NMR (CDCl_3 , 101 MHz, δ , ppm): 54.11, 119.41, 125.72-131.60, 139.92, 148.67.

Synthesis and characterization of 7



This compound was synthesized starting from 1-(azidomethyl)-2-methoxybenzene (73.43 mg; 0.45 mmol) which was dissolved in H₂O/But 2:1 (V= 2.0 mL), then copper sulphate (3.59 mg; 0.02 mmol), ascorbic acid (15.85 mg; 0.09 mmol) and phenylacetylene (55.2 mg; 0.54 mmol; d: 930 Kg/m³) were added to the reaction. For synthesis with Cu⁺@COP and Cu²⁺@COP, a 5% catalyst was used in moles compared to azide. In the case of the Cu²⁺@COP reaction was performed with ascorbic acid (15.85 mg; 0.09 mmol).

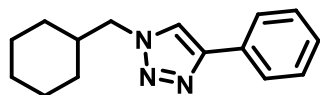
Yield: reported in Tab. 6.

Aspect: White solid.

¹H NMR (CDCl₃, 400 MHz, δ, ppm): 3.91 (3H, s, -CH₃-), 5.62 (2H, s, -CH₂-), 6.98 (2H, m, 2H_{Ar}, J= 4Hz), 7.36 (4H, m, 4H_{Ar}), 7.74 (1H, s, 1H_{Triazole}), 7.83 (2H, d, 2H_{Ar}, J= 8Hz).

¹³C{H}- NMR (CDCl₃, 400 MHz, δ, ppm): 49.28, 55.55, 110.80, 119.83-130.67, 157.19. Anal. Calcd for C₁₆H₁₅N₃O: C, 72.43; H, 5.70; N, 15.84; O, 6.03.

Synthesis and characterization of 8



This compound was synthesized starting from (azidomethyl)cyclohexane (62.64 mg; 0.45 mmol) which was dissolved in H₂O/But 2:1 (V= 2.0 mL), then copper sulphate (3.59 mg; 0.02 mmol), ascorbic acid (15.85 mg; 0.09 mmol) and phenylacetylene (55.2 mg; 0.54 mmol; d: 930 Kg/m³) were added to the reaction. For synthesis with Cu⁺@COP and Cu²⁺@COP, a 5% catalyst was used in moles compared to azide. In the case of the Cu²⁺@COP reaction was performed with ascorbic acid (15.85 mg; 0.09 mmol).

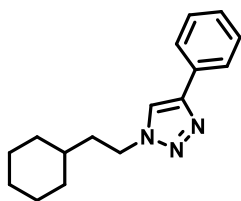
Yield: reported in Tab. 6.

Aspect: White solid.

¹H NMR (CDCl₃, 400 MHz, δ, ppm): 1.12 (1H, m, 1 *H*_{Alifatic}, J= 4Hz), 1.16 (4H, m, 4 *H*_{Alifatic}, J=4Hz), 1.44 (1H, d, 2 *H*_{Alifatic}, J= 4Hz), 1.62 (4H, m, 4 *H*_{Alifatic}, J= 4Hz), 1.70 (1H, m, 1 *H*_{Alifatic}, J= 4Hz), 4.16 (2H, d, -CH₂, J= 8Hz), 7.03 (1H, d, 1*H*_{Ar}, J= 8Hz), 7.17 (1H, d, 1*H*_{Ar}, J= 8Hz), 7.27 (1H, d, 1*H*_{Ar}, J= 8Hz), 7.34 (1H, s, 1*H*_{Triazole}), 7.77 (1H, d, 1*H*_{Ar}, J= 8Hz).

¹³C{H}- NMR (CDCl₃, 101 MHz, δ, ppm):21.19, 54.11, 119.41, 125.72-131.60, 138.79.

Synthesis and characterization of 9



This compound was synthesized starting from (2-azidoethyl) cyclohexane (68.95 mg; 0.45 mmol) which was dissolved in H₂O/But 2:1 (V= 2.0 mL), then copper sulphate (3.59 mg; 0.02 mmol), ascorbic acid (15.85 mg; 0.09 mmol) and phenylacetylene (55.2 mg; 0.54 mmol; d: 930 Kg/m³) were added to the reaction. For synthesis with Cu⁺@COP and Cu²⁺@COP, a 5% catalyst was used in moles compared to azide. In the case of the Cu²⁺@COP reaction was performed with ascorbic acid (15.85 mg; 0.09 mmol).

Yield: reported in **Tab. 6**.

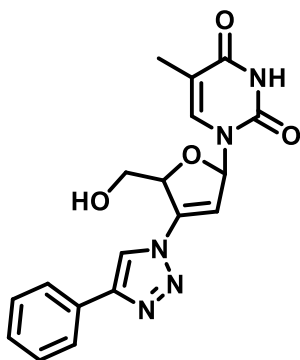
Aspect: White solid.

¹H NMR (CDCl₃, 400 MHz, δ, ppm): 0.82 (2H, m, -CH₂, J= 4Hz), 1.05 (4H, m, 4 *H*_{Alifatic}, J= 8Hz), 1.11 (1H, m, 1 *H*_{Alifatic}, J= 4Hz), 1.51 (6H, m, 6 *H*_{Alifatic}, J= 4Hz), 3.14

(1H, t, -CH₂-, J= 8Hz), 4.28 (1H, t, -CH₂-, J= 8Hz), 7.20 (3H, m, 3 H_{Ar}, J= 8Hz), 7.61 (1H, s, 1 H_{Triazole}), 7.70 (2H, d, 2 H_A, J= 4Hz).

¹³C{H}- NMR (CDCl₃, 101 MHz, δ, ppm): 26.03-26.46, 33.04, 35.02, 36.07, 37.77, 48.33, 49.23, 125.70, 127.66, 128.10, 128.85, 130.75, 133.27-133.34.

Synthesis and characterization of 10



This compound was synthesized starting from 1-(4-azido-5-(hydroxymethyl)-2,5-dihydrofuran-2-yl)-5-methylpyrimidine-2,4-(1H,3H)-dione (119.35 mg; 0.45 mmol) which was dissolved in H₂O/*t*-But 2:1 (V= 2mL), then copper sulphate (3.59 mg; 0.02 mmol), ascorbic acid (15.85 mg; 0.09 mmol) and phenylacetylene (55.2 mg; 0.54 mmol; d: 930 Kg/m³) were added to the reaction. For synthesis with Cu⁺@COP and Cu²⁺@COP, a 5% catalyst was used in moles compared to azide. In the case of the Cu²⁺@COP reaction was performed with ascorbic acid (15.85 mg; 0.09 mmol).

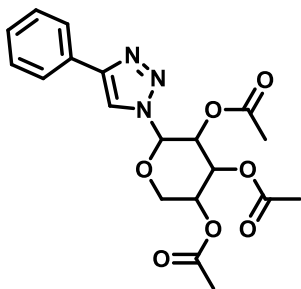
Yield: reported in Tab. 6.

Aspect: White powder.

¹H NMR (DMSO, 400 MHz, δ, ppm): 1.14 (3H, s, -CH₃-), 1.90 (1H, s, 1 H_{Al}), 1.98 (1H, s, 1 H_{Al}), 2.95 (2H, m, 2 H_{Al}, J=8Hz), 4.06 (1H, m, 1H, 1 H_{Al}), 4.45 (1H, s, -OH), 6.15 (1H, s), 7.29 (1H, s, 1 H_{Ar}), 7.37 (1H, t, 1 H_{Ar}, J= 8Hz), 7.40 (1H, s, 1 H_{Ar}), 7.77 (2H, d, 2 H_{Ar}, J= 8Hz), 7.90 (1H, s, -NH-).

$^{13}\text{C}\{\text{H}\}$ - NMR (DMSO, 101 MHz, δ , ppm): 12.57-14.56, 59.84, 61.23, 84.36, 84.91, 110.13, 121.49, 125.64, 125.64, 128.48, 129.43, 131.04, 136.74, 147.04, 150.93, 164.22.

Synthesis and characterization of 11



This compound was synthesized starting from 2-azidotetrahydro-2*H*-pyran-3,4,5-triyl triacetate (135.57 mg; 0.45 mmol) which was dissolved in $\text{H}_2\text{O}/t\text{-But}$ 2:1 ($V=2.0$ mL), then copper sulphate (3.59 mg; 0.02 mmol), ascorbic acid (15.85 mg; 0.09 mmol) and phenylacetylene (55.2 mg; 0.54 mmol; $d: 930$ Kg/m³) were added to the reaction. For synthesis with $\text{Cu}^+\text{@COP}$ and $\text{Cu}^{2+\text{@COP}}$, a 5% catalyst was used in moles compared to azide. In the case of the $\text{Cu}^{2+\text{@COP}}$ reaction was performed with ascorbic acid (15.85 mg; 0.09 mmol).

Yield: reported in **Tab. 6**.

Aspect: White powder.

^1H NMR (CDCl_3 , 400 MHz, δ , ppm): 1.94 (3H, s, $-\text{CH}_3\text{-C=O}$), 2.0 (6H, s, 2 $-\text{CH}_3\text{-C=O}$), 3.71 (1H, m, 1 H_{Triazole} , $J=8\text{Hz}$), 4.36 (2H, s, 1 H_{Al}), 5.04 (1H, t, 1 H_{Al} , $J=4\text{Hz}$), 5.05 (1H, t, 1 H_{Al} , $J=4\text{Hz}$), 5.32 (1H, d, 1 H_{Al} , $J=8\text{Hz}$), 5.60 (1H, m, 1 H_{Al} , $J=8\text{Hz}$), 7.18 (1H, 1 H_{Ar} , $J=8\text{Hz}$), 7.21 (2H, m, 2 H_{Ar} , $J=4\text{Hz}$), 7.28 (2H, m, 2 H_{Ar} , $J=8\text{Hz}$).

$^{13}\text{C}\{\text{H}\}$ - NMR (CDCl_3 , 101 MHz, δ , ppm): 21.24, 55.07, 66.26, 66.54, 67.45, 67.72, 83.21, 84.28, 126.15, 127.46, 128.92, 134.50, 170.88, 171.14.

10. Results and Discussion

The idea of the project is the investigation of a novel COP to be used in heterogeneous CuAAC “click” catalysis. The following steps describe the experimental process: i) creating a stable, insoluble covalent organic polymer in reaction solvents; ii) coordination with copper (II) and then reduction to copper (I); iii) characterization of the solid covalent organic support coordinated with copper (II) and (I) in all stages of synthesis especially in the reduction step in order to investigate about the stability; iv) use of covalent organic support coordinated with copper catalyst proving the potential benefits of using copper (I) directly as opposed to copper (II) and the homogeneous phase.

10.1 Characterization of the COP

To elucidate the crystallinity X-Ray diffraction (pXRD) was performed and indicate an amorphous pattern (**Fig. 41A**). The thermal stability of COP was probed by thermal gravimetric analysis (TGA), shown in **Figure 41C**. The analysis demonstrated no weight loss occurs until 600° C confirming the high thermal stability of COP. Beyond this range, a significant weight loss of 58.8% was observed. The isothermal nitrogen sorption measurement of COP confirms the non-porosity of the system (**Figure 41D**). The data were fitted to the Brunauer-Emmett-Teller (BET) model, it was found that COP had a BET Surface Area of $23.89 \pm 1 \text{ m}^2/\text{g}$. To explore the morphology of COP we performed an analysis by scanning electron microscopy (SEM) and atomic force micrographs (AFM). From the **Figure 41C**, it is possible to highlight the presence of a porous structure in which the COP skeleton is formed by almost fused nanoparticles in

agreement with the compactness of nanoparticles monitored by SEM (**Figure 41F**).

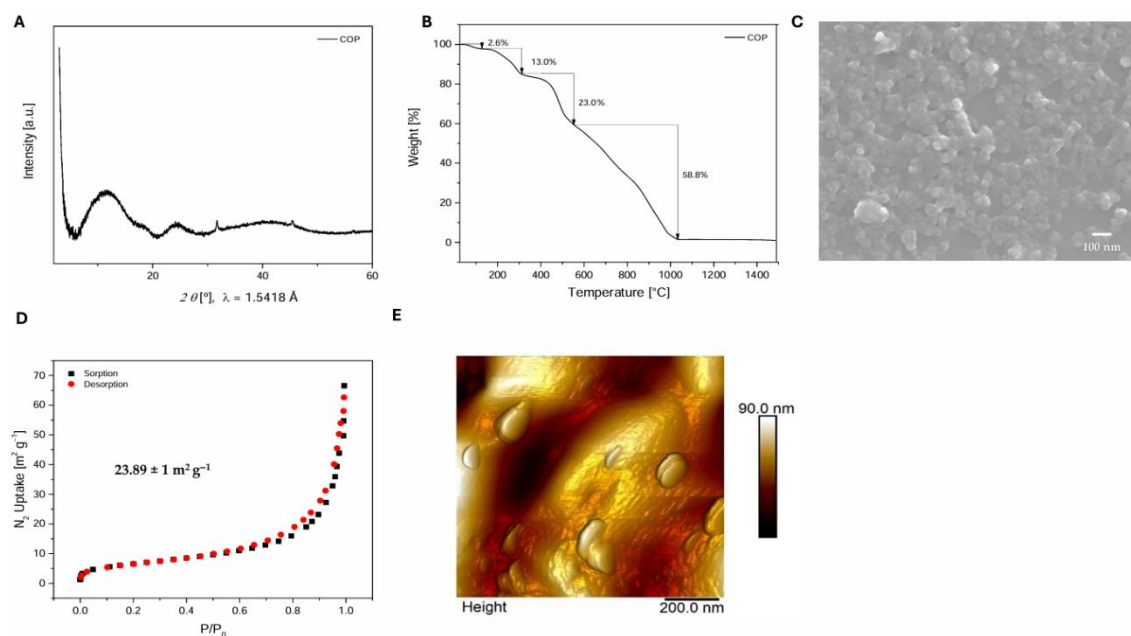


Figure 41. A) pXRD of COP. B) TGA curve of COP. C) SEM image at high magnification of COP nanoparticles agglomerate. D) Nitrogen gas sorption (black square) and desorption (red dots) of COP at 77K. E) Atomic force micrographs of COP.

10.2 Characterization of the Cu²⁺@COP and Cu⁺@COP

Both Cu²⁺@COP and Cu⁺@COP were characterized by a chemical and morphological point of view as is shown in **Figures 42-43**. Through pXRD was confirmed the amorphous pattern of both the polymers. (**Figure 42A**) ICP-MS analysis was also carried out to determine the loading amount of the copper. The loading amount was determined to be 3.0 wt % for the Cu²⁺@COP and 2.5% for the Cu⁺@COP. A thermogravimetric analysis (TGA) was performed, and reported in **Figure 42B**, to examine the chemical and physical characteristics of the final product. From the profile it is possible to demonstrate that no weight loss occurs until 400° C for Cu²⁺@COP, and 450° C for Cu⁺@COP, confirming the high thermal stability of both the systems, indicating that the reduction of the copper doesn't affect too much to thermal stability. Therefore, the incorporation of copper in both the species decreases the thermal stability if we compare these results to the one of the COP.

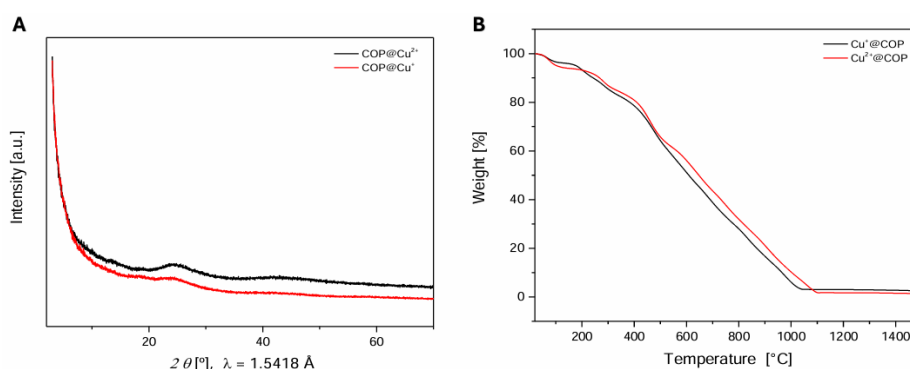


Figure 42. A) X-Ray diffraction measurements of the Cu²⁺@COP (black) and Cu⁺@COP (red). B) Thermogravimetric Analysis of the Cu²⁺@COP (red) and Cu⁺@COP (black).

To investigate how the presence of the copper may alter the morphology of the structure of the COP we studied pictures obtained by scanning electron

microscopy (SEM) and atomic force micrographs (AFM). From the obtained image, reported in **Figure 43A** and **Figure 43B** as well as in **Figure 43C** and **Figure 43D**, it is possible to highlight that the COP skeleton in the presence of both Cu^+ and Cu^{2+} appears grained with easily recognizable aggregated nanoparticles.

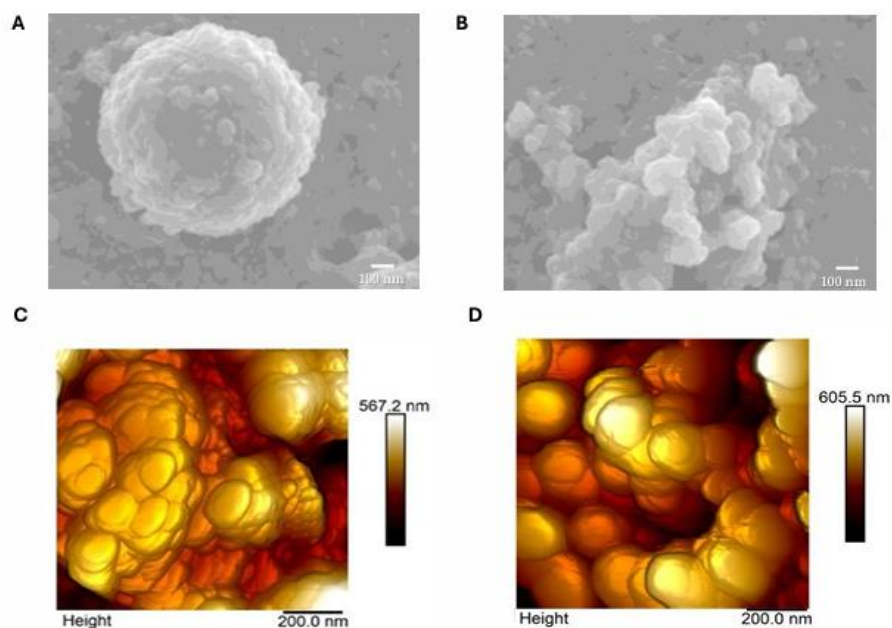


Figure 43. A) SEM image at high magnification of Cu^{2+} @COP nanoparticles agglomerate. B) SEM image at high magnification of Cu^+ @COP nanoparticles agglomerate. C) Atomic force micrographs of Cu^{2+} @COP. D) Atomic force micrographs of Cu^+ @COP.

XPS measurements were conducted, see **Figure 44**, to ascertain the presence of Cu and obtain insights into its oxidation state within the COP samples. Therefore, the large photoionization cross-section region of Cu $2p_{3/2}$ was recorded (see Figure XPS), and a curve-fitting deconvolution procedure was applied in order to extract information on the relevant ionization features. Both samples, Cu^+ @COP and Cu^{2+} @COP (Figure XPS a and b, respectively) display a major component at 934.45 eV binding energy (BE) followed by a two-fold satellite

extending in the range 940-945 eV (all three curves are evidenced in red). In copper compounds, these features are attributed to core-ionized final states, which are screened by charge transfer from the O ligands (component at 934.45 eV) and unscreened (satellite). This latter doublet is split due to core-valence spin coupling, which is typical of d^9 (Cu^{2+}) species. [124] The presence of this feature coupled to the position of the main peak calls for the presence of Cu^{2+} in both samples. In $\text{Cu}^+\text{@COP}$, a lower BE component is also detected (blue filled curve) falling at 932.32 eV. This component displays a BE more typical of d^{10} (Cu^+) compounds, with no associated satellites. [125] Therefore, one could hypothesize that native Cu^+ ions are present within the $\text{Cu}^+\text{@COP}$ framework, but they undergo quick oxidation to Cu^{2+} when the sample is exposed to ambient conditions.

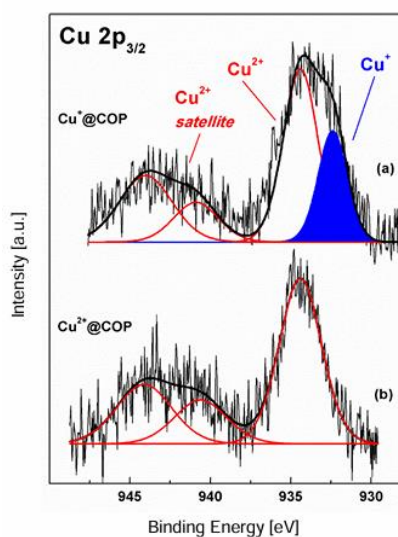


Figure 44. Figure XPS. Cu 2p_{3/2} ionization region of **a)** Cu⁺@COP and **b)** Cu²⁺@COP.

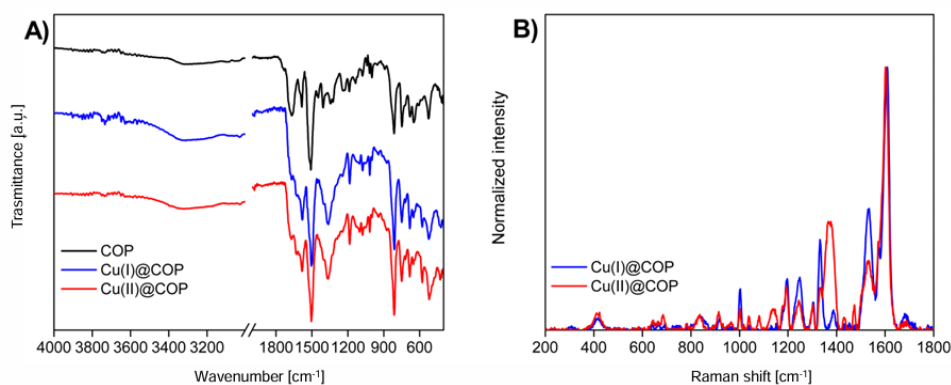


Figure 45. A) Comparison FT-IR spectres of COP (black), Cu⁺@COP (blue) and Cu²⁺@COP (red). B) Raman spectra of COP (black), Cu⁺@COP (blue) and Cu²⁺@COP (red).

The FT-IR spectrum of the ligand COP shown in **Figure 45A** (black line) displays a weak peak localized at $\approx 3320\text{ cm}^{-1}$ due to the free N-H stretching vibrations. The presence of the amide groups is proved by the presence of the amide I band (ν C=O) at $\approx 1665\text{ cm}^{-1}$ and the amide II band at $\approx 1584\text{ cm}^{-1}$, which is relative to the N-H bending vibrations. Moreover, the skeletal vibrations involving the carbon-carbon and carbon-nitrogen stretching vibrations within the rings and those C-N of the aniline-based moieties are observable in the spectral range between $1550\text{--}1300\text{ cm}^{-1}$. Finally, the marked bands centered at ≈ 812 and $\approx 748\text{ cm}^{-1}$ are ascribable to the C-H out-of-plane bending vibrations. In the presence of the metal cations Cu⁺ and Cu²⁺ (**Figure 45A**, blue and red lines), the amide I band shifts becoming a shoulder from ≈ 1665 in the free ligand to 1632 cm^{-1} in the copper-based COP owing to the plausible coordination of the amide oxygen, according to the literature. [126-129] However, a component of the native amide I band remains, probably because not all sites are saturated. Finally, the metal coordination exerted by the nitrogen of both pyridine and aniline derivates affects the infrared features in the spectral range between $1430\text{--}1300\text{ cm}^{-1}$. To obtain additional information on the samples, the Raman spectra have been recorded (**Figure 45B**).

Noteworthy it was impossible to acquire the spectrum of the free ligand owing to its high fluorescence that was partially quenched in the presence of copper ions. In particular, the Raman spectra of the copper-based COP (**Figure 45B**, blue and red lines) display similar features and only spectral differences in terms of relative intensities of some bands regarding the skeletal and C-N vibrations, therefore suggesting a nonidentical coordination of Cu⁺ and Cu²⁺ ions. Furthermore, the spectra, display the characteristic Raman signal of the pyridine centered at ≈ 1004 cm⁻¹ vs. 1007 cm⁻¹ as reported in literature. [130] Finally, in the portion of low energy of the spectra, the medium peak at ≈ 416 cm⁻¹, could be tentatively attributed to the characteristic δ (Cu-O-Cu) bending vibrations. [131] Besides, the other diagnostic Cu-N vibrations are not appreciable possibly due to their low intensity.

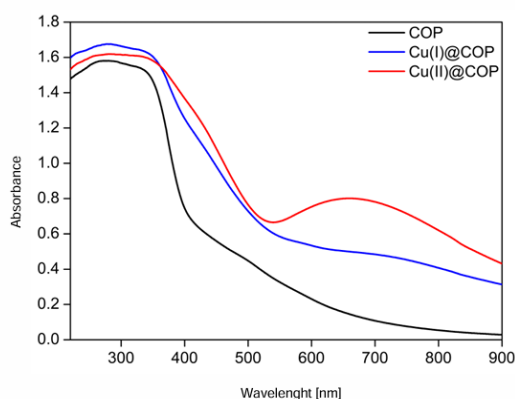


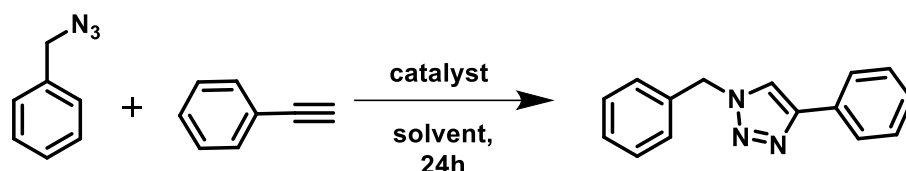
Figure 46. Diffuse reflectance UV-Vis spectra.

The Diffuse reflectance UV-Vis, see **Figure 46**, spectrum of the free ligand displays an intense and broad absorption in the UV region with a maximum localized at 278 nm due to the π - π^* electron transition of the aromatic domains and retained in the copper-based COP. Conversely, in the Cu²⁺@COP there is a band localized at 660 nm relative to d-d electron transitions, which is absent in the compound with the Cu(I) centers even if there is a slight absorption in the

same region, probably because a fraction of Cu (II) is present as a consequence of oxidative phenomena. [132]

10.3 Catalytic application in CuAAC “click” reaction

Covalent organic support coordinated with copper (II) and (I) were tested in CuAAC “click” reactions. First a screening was performed in different temperature conditions, solvent and percentage of catalyst between benzyl azide and phenylacetylene to identify the optimal conditions of reactions in terms of best yield. The first reaction was carried out in homogeneous phase, with copper sulphate as catalyst, in H₂O/*t*-But (2:1) at room temperature, following a synthetic protocol reported in literature and a yield of 10% was confirmed. [123] In these conditions it is possible to observe in **Table 5** as the yield in presence of the heterogeneous catalyst especially with Cu⁺@COP is considerably better than the homogeneous phase. Starting from this, changes were made, and the result is that the optimal synthetic conditions are with H₂O/*t*-But (2:1) at 60 °C with 5% in moles of catalyst.



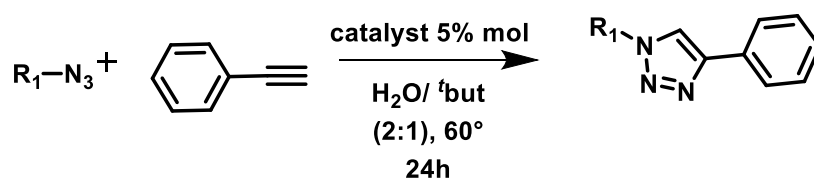
Catalyst	Loading (mol %)	Solvent (v/v)	Temperature (°C)	Yield (%)
Cu ²⁺ @COP	1	ACN	R.T.	36.0
Cu ⁺ @COP	1	ACN	R.T.	23.0
Homogeneous Phase	1	ACN	R.T.	<1
Cu ²⁺ @COP	1	ACN	60.0	65.0
Cu ⁺ @COP	1	ACN	60.0	35.0
Homogeneous Phase	1	ACN	60.0	1.0

Cu ²⁺ @COP	1	Toluene	R.T.	1.0
Cu ⁺ @COP	1	Toluene	R.T.	<1.0
Homogeneous	1	Toluene	R.T.	<1.0
Phase				
Cu ²⁺ @COP	1	Tetrahydrofuran	R.T.	19.0
Cu ⁺ @COP	1	Tetrahydrofuran	R.T.	17.0
Homogeneous	1	Tetrahydrofuran	R.T.	<1.0
Phase				
Cu ²⁺ @COP	1	H ₂ O/ ^t But (2:1)	R.T.	8.5
Cu ⁺ @COP	1	H ₂ O/ ^t But (2:1)	R.T.	35.0
Homogeneous	1	H ₂ O/ ^t But (2:1)	R.T.	10.0
Phase				
Cu ²⁺ @COP	1	H ₂ O/ ^t But (2:1)	R.T.	40.0
Cu ⁺ @COP	1	H ₂ O/ ^t But (2:1)	R.T.	60.0
Homogeneous	1	H ₂ O/ ^t But (2:1)	R.T.	39.0
Phase				
Cu ²⁺ @COP	5	H ₂ O/ ^t But (2:1)	60.0	46.0
Cu ⁺ @COP	5	H ₂ O/ ^t But (2:1)	60.0	95.0
Homogeneous	5	H ₂ O/ ^t But (2:1)	60.0	55.0
Phase				
Cu ²⁺ @COP	1	MeOH	R.T.	45.0
Cu ⁺ @COP	1	MeOH	R.T.	42.0
Homogeneous	1	MeOH	R.T.	39.0
Phase				
Cu ²⁺ @COP	1	H ₂ O/MeOH (1:1)	R.T.	34.0
Cu ⁺ @COP	1	H ₂ O/MeOH (1:1)	R.T.	36.0
Homogeneous	1	H ₂ O/MeOH (1:1)	R.T.	39.0
Phase				
Cu ²⁺ @COP	1	H ₂ O/MeOH (1:1)	60.0	43.0
Cu ⁺ @COP	1	H ₂ O/MeOH (1:1)	60.0	75.0
Homogeneous	1	H ₂ O/MeOH (1:1)	60.0	60.0
Phase				

Cu ²⁺ @COP	1	Neat	R.T.	<1
Cu ⁺ @COP	1	Neat	R.T.	<1
Homogeneous Phase	1	Neat	R.T.	<1

Table 5. Optimization of CuAAC “click” reaction conditions.

Under the optimum reaction conditions, we expanded the CuAAC “click” reactions with other azides and the results are reported in **Table 6**.



Entry	Substrate	Product	Homogeneous Phase (%)	Cu ²⁺ @COP Yield (%)	Cu ⁺ @COP Yield (%)
1	<chem>c1ccc(cc1)CN=[N+]=[N-]</chem>	<chem>c1ccc(cc1)C1=CN=C(N1)Cc2ccc(cc2)</chem>	46.0	55.0	95.0
2	<chem>Cc1ccc(cc1)CN=[N+]=[N-]</chem>	<chem>Cc1ccc(cc1)C1=CN=C(N1)Cc2ccc(cc2)</chem>	51.0	52.0	70.0
3	<chem>Brc1ccc(cc1)CN=[N+]=[N-]</chem>	<chem>Brc1ccc(cc1)C1=CN=C(N1)Cc2ccc(cc2)</chem>	13.5	65.0	85.0
4	<chem>c1ccc(cc1)COc2ccc(cc2)CN=[N+]=[N-]</chem>	<chem>c1ccc(cc1)COc2ccc(cc2)C1=CN=C(N1)Cc3ccc(cc3)</chem>	42.0	57.0	68.0
5	<chem>Nc1ccc(cc1)CN=[N+]=[N-]</chem>	<chem>Nc1ccc(cc1)C1=CN=C(N1)Cc2ccc(cc2)</chem>	38.0	53.0	59.0

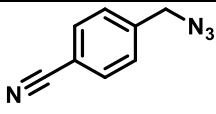
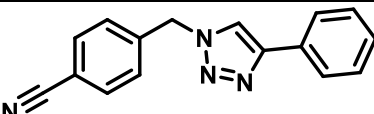
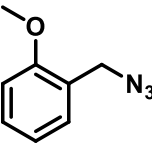
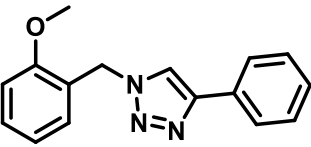
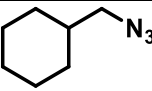
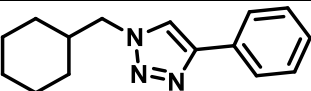
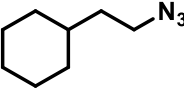
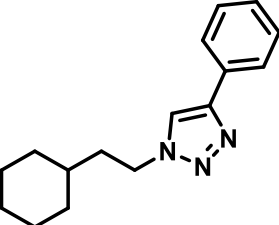
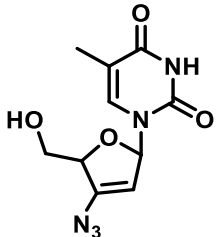
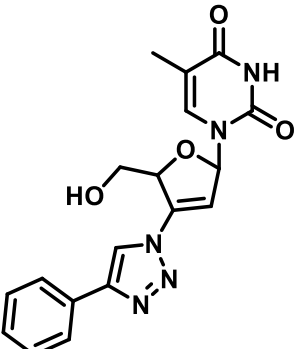
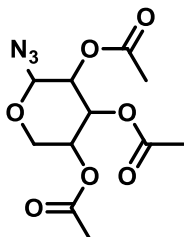
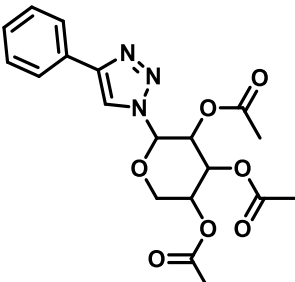
6			58.0	63.0	70.0
7			23.0	25.0	28.0
8			15.0	27.0	58.0
9			76.0	80.0	87.0
10			40.0	44.0	79.0
11			44.0%	45.0%	57.0%

Table 6. Substrate scope of catalyzed CuAAC “click” reactions.

Analysing the values in **Table 6** makes it possible to demonstrate that heterogenous catalysis always favours the formation of products over homogeneous catalysis. In particular, the true yield advantage of using Cu⁺@COP

over $\text{Cu}^{2+}@\text{COP}$ and the homogeneous phase can be understood. This confirms that the metal reduction process, which occurs beforehand rather than in situ, is more stable and effective over an extended period. Based on the collected data, assumptions about how the structure of precursors affects product formation can be made. In fact, if the substituent of the azides precursors are present in *para* position on the aromatic ring, will have a less steric hindrance and an improvement in terms of yield of the resulting formation of the product. In contrast, the formation of the final product occurs even with significantly lower yields if the substituent is present in the *ortho* position of the aromatic ring (**Product 7**). The length of the azides precursor's chain is another structural element that may affect the yield of the product that is synthesized. In fact, if group $-\text{N}_3$ is connected to a methylene group or one of longer length, will have higher yields than when directly linked to the aromatic structure (**Product 5**), nucleoside derivative (**Product 10**) and sugar derivative (**Product 11**).

11. Conclusions and future perspectives

In conclusion, we designed and synthesized a novel covalent organic polymer (COP) based on amide linkages. Although the material is not crystalline, it demonstrates good structural stability and strong coordination capabilities with copper. Our study primarily focused on copper due to its catalytic properties in numerous organic reactions. After characterizing the Cu^{2+} @COP complex, we reduced the metal to form a new system, Cu^+ @COP, and confirmed this reduction through the same characterization techniques, alongside a detailed analysis of the oxidation state of the metal. Our investigation highlights the advantages of the Cu^+ @COP system in comparison to the Cu^{2+} @COP system, particularly in the copper-catalyzed azide-alkyne cycloaddition (CuAAC) "click" reaction in homogeneous phase. Once the optimal synthetic conditions were established, we tested a range of azides with different structural characteristics. In every case, the direct use of Cu (I) led to higher product yields than the in-situ reduction of Cu (II) using ascorbic acid as a reducing agent. A significant achievement of this work is the reduction in the use of harmful organic solvents, both in the synthesis of the metal-organic complex and its application in the CuAAC reaction. Additionally, the insolubility of these polymers in all common reaction solvents allows for a catalytic process in heterogeneous phase, where the catalyst can be easily recovered by simple filtration. The 1,2,3-triazole products can be obtained via straightforward extraction and crystallization, eliminating the need for purification by silica gel chromatography and contributing to greener, more sustainable chemistry. One of our future goals is to convert the amorphous covalent organic polymer into a covalent organic framework (COF), which could exhibit the typical features of these materials, such as porosity, crystallinity, and large surface area. Further work is also needed to improve reaction kinetics. The

amorphous structure arises from rapid amide bond formation, leading to inherent disorder in the final product. Nonetheless, it is plausible that a COF with amide linkages could be obtained by altering the synthetic approach or introducing reaction modulators. Since copper coordination in the current system (COP) is limited to the catalyst's surface, developing a crystalline and porous structure is a critical step that could broaden the range of applications. Indeed, we observed a decrease in product yields with each successive reaction. By creating a more crystalline and porous structure, we expect to increase the copper content within the polymer, minimizing copper loss during filtration and enabling more recycling cycles. This would enhance the sustainability of the overall process.

12. References

- [1] G. N. Lewis. *Chemical Catalog Company* **1996**.
- [2] G. N. Lewis. *Journal of American Society* **1916**, 38, 4, 762-785.
- [3] W. Heitler, F. London, F. Wechselwirkung. *Zeitschrift für Physik* **1927**, 44, 6, 455-472.
- [4] H. Staudinger, H. Uber. *A Source Book in Chemistry 1900-1950* **1920**, 53, 6, 1073-1085.
- [5] H. Frey, T. Johann. *Polymer Chemistry* **2020**, 11, 1, 8-14.
- [6] M. Peplow. *Nature* **2016**, 536, 7616, 266-268.
- [7] T. Skirjanc, D. Shetty, E. Matjaz Valant. *ACS Sensors* **2021**, 6, 4, 1461-1481.
- [8] Q. Wang, D. Astruc. *Chemical Reviews* **2020**, 120, 2, 1438-1511.
- [9] O. L. Hollis. *Analytical Chemistry* **1966**, 38, 2, 309-316.
- [10] J. C. Moore. *Journal of Polymeric Science* **1964**, 2, 2, 835-84326.
- [11] P. Kaur, J. T. Hupp, S. T. Nguyen. *ACS Catalysis* **2011**, 1, 7, 819-835.
- [12] Z. Xiang, D. Cao, L. Dai. *Polymer Chemistry* **2015**, 6, 11, 1885-2152.
- [13] Z. Xiang, X. Zhou, C. Zhou, S. Zhong, X. He, C. Qin, D. Cao. *Journal of Materials Chemistry* **2012**, 22, 22663.
- [14] A. P. Cote, A. Benin, N. W. Ockwig, M. O'Keeffe, A. J. Marzger, O. M. Yaghi. *Science* **2005**, 310, 1166-1170.
- [15] X. Feng, X. Ding, D. Jiang. *Royal Society of Chemistry* **2012**, 41, 6010-6022.
- [16] S. J. Rowan, S. J. Cantrill, G. R. L. Cousins, J. K. M. Sanders, J. F. Stoddart. *Angewandte Chemie International Edition* **2002**, 41, 898-952.
- [17] N.L. Campbell, R. Clowes, L. K. Ritchie, A. Cooper. *Mathematics Chemistry* **2009**, 21, 204-206.
- [18] M. Dogru, A. Sonnauer, A. Gavryushin, P. Knochel, T. Bein. *Chemistry Communications* **2011**, 47, 1707-1709.

- [19] P. Kuhn, M. Antonietti, A. Thomas. *Angewandte Chemie International Edition* **2008**, *47*, 3450-3453.
- [20] M. J. Bojdys, J. Jeromenok, A. Thomas, M. Antonietti. *Advanced Materials* **2010**, *22*, 2202-2205.
- [21] J. W. Colson, A. R. Woll, A. Mukherjee, M. P. Levendorf, E. L. Spitler, V. B. Shields, M. G. Spencer, J. Park, W. R. Dichtel. *Science* **2011**, *332*, 228-231.
- [22] E. L. Spitler, J. W. Colson, F. J. Uribe-Romo, A. R. Woll, M. R. Giovino, A. Saldivar, W. R. Dichtel. *Angewandte Chemie International Edition* **2012**, *51*, 2623-2627.
- [23] E. L. Spitler, B. T. Koo, J. L. Novotney, J. W. Colson, F. J. Uribe-Romo, G. D. Gutierrez, P. Clancy, W. R. Dichtel. *Journal of American Chemical Society* **2011**, *133*, 19416-19421.
- [24] Z. Miao, G. Liu, Y. Cui, Z. Liu, J. Li, F. Han, Y. Liu, X. Sun, X. Gong, Y. Zhai, Y. Zhao, Y. Zeng. *Angewandte Chemie International Edition* **2019**, *58*, 15, 4906-4910.
- [25] G. Ertl. *Angewandte Chemie International Edition* **2009**, *48*, 6600-6606.
- [26] E. Roduner. *Chemical Society Review* **2014**, *43*, 8226-8239.
- [27] B. Cornils, W. A. Herrmann, J.H. Xu, H.W. Zanthoff. *Wiley-VCH, Weinheim* **2000**.
- [28] D. J. Cole-Hamilton. *Science* **2003**, *299*, 5613, 1702-1706.
- [29] J. Villà, A. Warshel. *Journal of Physical Chemistry B* 2001, *105*, 7887-7907.
- [30] D. J. Cole-Hamilton. *Science* **2003**, *299*, 5613, 1702-1706.
- [31] D. E. Koshland. *Proceedings of the National Academy of Sciences of the United States* **1958**, *44*, 98-104.
- [32] M. Heitbaum, F. Glorius, I. Escher. *Angewandte Chemie International Edition* **2006**, *45*, 4732.
- [33] M. Benaglia, A. Puglisi, F. Cozzi. *Chemical Reviews* **2003**, *103*, 3401.
- [34] C. Song, S. Lee. *Chemical Reviews* **2002**, *102*, 3495.

- [35] A. Corma. *Chemical Reviews* **1997**, 97, 2373.
- [36] Q. Fan, Y. Li, ASC Chan. *Chemical Reviews* **2002**, 102, 3385.
- [37] T. E. Kristensen, T. Hansen. *European Journal of Organic Chemistry* **2010**, 3179.
- [38] D. Zhao, J. Feng, Q. Huo, N. Melosh, G. H. Fredrickson, B. F. Chmelka, G. D. Stucky. *Science* **1998**, 279, 548.
- [39] Y. Zhang, L. Zhao, S. S. Lee, J. Y. Ying. *Advanced Synthesis & Catalysis* **2006**, 348, 2027.
- [40] Y. Zhang, L. Zhao, P. K. Patra, J. Y. Ying. *Advanced Synthesis & Catalysis* **2008**, 350, 662.
- [41] D. C. Sherrington. *Journal of Polymeric Science: Part A* **2001**, 39, 2364.
- [42] P. Hodge. *Chemical Society Review* **1997**, 26, 417.
- [43] R. L. Albright. *Polymerization Reaction* **1986**, 4, 155.
- [44] M. X. Tan, Y. Zhang, J. Y. Ying. *Advanced Synthesis Catalysis* **2009**, 351, 1390.
- [45] Y. Zhang, L. Zhao, P. K. Patra, D. Hu, J. Y. Ying. *Nano Today* **2009**, 4, 13.
- [46] D. Yu, Y. Zhang. *Proceedings of the National Academy of Sciences USA* **2010**, 107, 20184.
- [47] S. A. John, P. J. Ollivier, T. E. Mallouk. *Science* 1999, 283, 963.
- [48] A. P. Cote, A. Benin, N. W. Ockwig, M. O'Keeffe, A. J. Matzger, O. M. Yaghi. *Science* 2005, 310, 1166-1170.
- [49] R. W. Tilford, W. R. Gemmill, H. C. Zur Loye, J. J. Lavigne. *Chemical Materials* 2006, 18, 5296.
- [50] S. Wan, J. Guo, J. Kim, H. Ihee, D. Jiang. *Angewandte Chemie International Edition* **2008**, 47, 8826.
- [51] A. Corma, H. Garc, F. X. Llabr i Xamena, *Chemical Reviews* **2010**, 110, 4606.
- [52] N. B. McKeown, P. M. Budd. *Chemical Society Reviews* **2010**, 110, 4606.
- [53] O. K. Farha, Y.-S. Bae, B. G. Hauser, A. M. Spokoyny, R. Q. Snurr, C. A. Mirkin, J. T. Hupp. *Chemical Communication* **2010**, 46, 1056.

- [54] K. Haupt, K. Mosbach. *Chemical Reviews* **2000**, 100, 2495.
- [55] M. E. Davis, A. Katz, W. R. Ahmad. *Chemical Materials* **1996**, 8, 1820.
- [56] J. B. Nagy, P. Bodart, I. Hannus, I. Kiricsi. *Decagen Ltd.* **1998**.
- [57] B. Wichterlova, S. Bedna. *Applied Catalysis* **1991**.
- [58] P. Prokesová, N. Zilkova, S. Mintova, T. Bein, J. Cejka. *Applied Catalysis* **2005**, 281, 85.
- [59] J. Perez-Ramirez, C. H. Christensen, K. Egeblad, J.C. Groen. *Chemical Society Reviews* **2008**, 37, 2530.
- [60] Z. Musilova-Pavlackova, S.I. Zone, J. Cejka. *Sopramolecular Catalysis* **2010**, 53, 273.
- [61] A. K. Cheetham, G. Ferey, T. Loiseau. *Angewandte Chemie International Edition* **1999**, 38, 3268.
- [62] A. Dhakshinamoorthy, M. Alvaro, H. Garcia. *Chemical Communications* **2012**, 48, 11275.
- [63] D. Farrusseng, S. Aguardo, C. Pinel. *Angewandte Chemie International Edition* **2009**, 48, 7502.
- [64] J. Liang, Z. Liang, R. Zou, Y. Zhao. *Angewandte Chemie International Edition* **2019**, 29, 30, 1701139.
- [65] C. Coperet, A. Comas-Vives, M. Conley, D. P. Estes, A. Fedorov, V. Mougel, H. Nage, F. Nunez-Zarur, P. A. Zhizhko. *Chemical Reviews* **2016**, 116, 2, 323-421.
- [66] K. M. Samantaray, V. D'Elia, E. Pump, L. Falivene, M. Hard, S. Ould Chikh, L. Cavallo, J. M. Basset. *Chemical Reviews* **2020**, 120, 2.
- [67] M. P. Conley, V. Mougel, D. V. Peryshkov, W. P. Forrest, D. Gajan, A. Lesage, L. Emsley, C. Coperet, R. R. Schrock. *Journal of American Society* **2013**, 135, 19068-19070.
- [68] M. P. Conley, P. William, V. Mougel, C. Coperet, R. R. Schrock. *Angewandte Chemie International Edition* **2014**, 53, 51, 14221-14224.

- [69] B. G. Bailey, M. Foscatto, C. S. Higman, S. Carolyn, S. C. Giorno, R. V. Jensen, E. FoggDeryn. *Journal of American Society* **2018**, *140*, 22, 6931-6944.
- [70] P. Serna, C. Bruce. *ACS Accounts* **2014**, *47*, 8, 2612-2620.
- [71] S. E. Allen, R. R. Walvoord, R. Padilla-Salinas, E. M. C. Kozlowski. *Chemical Reviews* **2013**, *113*, 8, 6234-6458.
- [72] S. R. Chemler. *Journal of Organic Chemistry* **2015**, *11*, 2252-2253.
- [73] H. C. Kolb, M. G. Finn, K. B. Sharpless. *Angewandte Chemie* **2001**, *113*, 2056-2075.
- [74] V. V. Rostovtsev, L. G. Green, V. V. Fokin, K. B. Sharpless *Angewandte Chemie* **2002**, *114*, 2708-2711.
- [75] G. Franc, A. K. Kakkar. *Journal of European Chemistry* **2009**, *15*, 5630-5639.
- [76] G. Kumaraswamy, K. Ankamma, A. Pitchaiah. *Journal of Organic Chemistry* **2007**, *72*, 9822-9825.
- [77] C. Brikie, F. Rohrbach, A. Gottschalk, G. Mayer, A. Heckel. *Angewandte Chemie* **2012**, *124*, 8572-8604.
- [78] M. A. Tasdelen, Y. Yagci. *Angewandte Chemie* **2013**, *52*, 23, 5930-5938.
- [79] H. C. Kolb, M. G. Finn, K. B. Sharpless *Angewandte Chemie International Edition* **2002**, *67*, 3057-3062.
- [80] R. Huisgen. *Angewandte Chemie International Edition* **1963**, *2*, 565-598.
- [81] L. Zhang, X. Chen, P. Xue, H. H. Y Sun, I. D. Williams, K. B. Sharpless, V. V. Fokin, G. Jia. *Journal of the American Society* **2005**, *127*, 15998-15999.
- [82] B. C. Boren, S. Narayan, L. K. Rasmussen, L. Zhang, H. Zhao, G. Jia, V. V. Fokin. *Journal of the American Society* **2008**, *130*, 8923-8930.
- [83] M. Meldal, C. W. Tornoe. *Chemical Reviews* **2008**, *108*, 2952-3015.
- [84] V. V. Rostovtsev, L. G. Green, V. V. Fokin, K. B. Sharpless. *Angewandte Chemie International Edition* **2002**, *41*, 2596-2599.
- [85] J. E. Hein, V. V. Fokin. *Royal Society of Chemistry* **2010**, *39*, 1302-13015.

- [86] J. Dandriyal, R. Singla, M. Kumar, V. Jaitak. *Journal of Medicinal Chemistry* **2016**, 119, 141-168.
- [87] G. C. Kuang, E. A. Michaels, T. Simmons, R. J. Clark, L. Zhu. *Journal of Organic Chemistry* **2010**, 75,19.
- [88] J. Kaur, M. Saxena, N. Rishi. *Bioconjugate Chemistry* **2021**, 32, 8, 1455-1471.
- [89] Winge, R. K. Mehra. *International review of experimental pathology* **1990**, 31, 47-83.
- [90] C. Ureau, P. Dorlet. *Coordination Chemistry Reviews* **2012**, 256, 2175-2187.
- [91] S. K. Singh, V. Balendra, A. A. Obaid, J. Esposto, M. A. Tikhonova, N. K. Gautam, B. Poeggeler. *Metallomics* **2022**, 14, 6.
- [92] P. S. Donnelly, Z. Xiao, A. G. Wedd. *Bioinorganic chemistry/ Biocatalysis and biotransformation* **2007**, 11, 2, 128-133.
- [93] M. Olivares, R. Uauy. *The American Journal of Clinical Nutrition* **1996**, 63, 5, 791S-796S.
- [94] B. Liu, C. Chen, Y. Zhang, X. Liu, W. Chen. *Organometallics* **2013**, 32, 19.
- [95] G. C. Kuang, E. A. Michaels, T. Simmons, R. J. Clark, L. Zhu. *Journal of Organic Chemistry* **2010**, 75,19.
- [96] C. Bunders, J. Cavanagh, C. Melander. *Organic Biomolecular Chemistry* **2011**, 9, 5476-5481.
- [97] W. M. Eldehna, A. Nocentini, Z. M. Elsayed, T. Al-Warhi, N. Aljaeed, O. J. Alotaibi, C. T. Supuran. *ACS Medicinal Chemistry Letters* **2020**, 11, 1022-1027.
- [98] F. Ran, Y. Liu, S. Yu, K. Guo, W. Tang, X. Chen, G. Zhao. *Bioorganic Chemistry* **2020**, 94, 103367.
- [99] C. A. Kluba, T. L. Mindt. *Molecules* **2013**, 18, 3206-3226.
- [100] D. Osmaniye, B. N. Saglik, S. Levent, S. Ilgin, Y. Ozkay, Z. A. Kaplancikli. *Journal of Molecular Structure* **2021**, 1246, 131198.

- [101] D. Mandalapu, K. Saini, S. Gupta, V. Sharma, M. M. Yaseen, S. Chaturvedi, V. Bala, S. Thakur, J. P. Maikhuri, P. Jagdamba, M. Wahajuddin, R. Konwar, G. Gupta, V. L. Sharma. *Bioorganic & Medicinal Letters* **2016**, 26, 17, 4223.
- [102] R. Kant, D. Kumar, D. Agarwal, R. Devi, R. Tilak. *European Journal of Medicinal Chemistry* **2016**, 113, 34-49.
- [103] A. Kumar, K. Lal, N. Poonia, A. Kumar. *Research on Chemical Intermediates* **2022**, 48, 2933-2948.
- [104] T. Ouyang, X. Liu, H. Ouyang, L. Ren. *Virus Research* **2018**, 256, 21-28.
- [105] E. Arnaiz, E. Vacas-Cordoba, M. Galan, M. Pion, R. Gomez, M. A. Munoz-Fernandez, F. J. Mata. *Journal of Polymer Science Part A* **2014**, 52, 8, 1099-1112.
- [106] L. Sun, T. Huang, A. Dick, M. E. Meuser, W. A. Zalloum, C. H. Chen, X-Ding, P. Gao, S. Cocklin, K. H. Lee, P. Zhan, X. Liu. *European Journal of Medical Chemistry* **2020**, 190, 112085.
- [107] R. Schirmacher, Y. Lakhrissi, D. Jolly, J. Goodstein, P. Lucas, E. Schirmacher. *Tetrahedron Letters* **2008**, 49, 4824-4827.
- [108] J. Zhou, A. Bhattacharjee, S. Chen, Y. Duffy, E. Farmer, J. Goldberg, R. Hanselmann, J. A. Ippolito, R. Lou. *Bioorganic Medicinal Chemistry* **2008**, 18, 6179-6183.
- [109] B. Rickborn. *Organic Reaction* **1998**, 1-393.
- [110] L. Fisera, D. Pavlovic. *Chemical Communications* **1984**, 49, 1990-2000.
- [111] A. Ashto. *Scholarly Editions* **2012**, 3937.
- [112] M. C. Linder, M. Hazegh-Azam. *Journal of the American Clinical Nutrition* **1996**, 63, 7975-8115.
- [113] E. B. Hart, J. Steenbock, J. Waddell, C. A. Elvehjem. *Journal of Biological Chemistry* **1928**, 77, 797-812.
- [114] A. Cordano, J. Baertl, G. G. Graham. *Pediatrics* **1964**, 34, 324-336.

- [115] R. Uauy, M. Olivares, M. Gonzalez. *American Journal of Clinical nutrition* **1998**, 67, 269-275.
- [116] S. H. Sandstead. *Journal of American of Clinical Nutrition* **1995**, 61, 6215.
- [117] D. G. Barceloux. *Journal of Clinical Toxicology* **1999**, 37, 217-237.
- [118] J. R. Turnlund, W. R. Keyes, G. L. Peiffer, K. C. Scott. *American Journal of the Clinical Nutrition* **1998**, 67, 1219-1225.
- [119] R. Uauy, M. Olivares, M. Gonzalez. *American Journal of the Clinical Nutrition* **1998**, 67, 952S-959S.
- [120] Winge, R. K. Mehra. *International review of experimental pathology* **1990**, 31, 47-83.
- [121] W. J. Klein, E. N. Metz, A. R. Prezzo. *Archives of Internal Medicine* **1972**, 129, 578-582.
- [122] D. Beshgetoor, M. Hambidge. *American Journal of Clinical Nutrient* **1998**, 67, 1017S-1021S.
- [123] B. Liu, C. Chen, Y. Zhang, X. Liu, W. Chen. *Organometallics* **2013**, 32, 19.
- [124] J. Ghijsen, L. H. Tjeng, J. van Elp, H. Eskes, J. Westerink, G. Sawatzky. *Physical Review B* **1988**, 38, 16.
- [125] T. Schedel-Niedrig, T. Neisius, I. Böttger, E. Kitzelmann, G. Weinberg, D. Demuth, R. Schlögl. *Physical Chemistry Chemical Physics* **2000**, 2, 2407-1417.
- [126] B. P. Hay, R. D. Hancock. *Coordination Chemistry Reviews* **2001**, 212, 1, 61-78.
- [127] L. A. Clapp, C. J. Siddons, D. G. VanDerveer, J. H. Reibenspies, S. B. Jones, R. D. Hancock. *Dalton Transactions* **2006**, 2001-2007.
- [128] H. Maumela, R. D. Hancock, L. Carlton, J. H. Reibenspies, K. P. Wainwright. *Journal of the American Chemical Society* **2005**, 117, 6698-6707.
- [129] S. Afaq, M. U. Akram, W. Mahmood, A. Malik, M. Ismail, A. Ghafoor, M. Ibrahim, M. un-Nisa, M. N. Ashiq, F. Verpoort, A. H. Chughtai. *ACS Omega* **2023**, 8, 6638-6649.

- [130] A. Mühlig, D. Cialla-May, J. Popp. *The Journal of Physical Chemistry C* **2017**, *121*, 4, 2323-2332.
- [131] M. Malik, A. Switlicka, A. Bienko, U. K. Komarnicka, D. C. Bienko, S. Koziel, A. Kyziot, T. Mazur, B. Machura. *RSC Advances* **2022**, *12*, 27648.
- [132] L. V. Menon, E. Manoj. *Journal of Inorganic Biochemistry* **2024**, *255*, 112538.

Part C

13. Introduction to Metal Organic Frameworks (MOFs)

Over the past 30 years, extensive research has been conducted in the literature on open-framework materials, with numerous examples describing the controlled design of porous solids possessing specific physico-chemical properties. [1] These materials include Metal Organic Frameworks (MOFs), also known as porous coordination polymers (PCPs), which are an emerging class of porous crystalline metal-organic solids. MOFs exhibit high crystallinity, porosity and large surface area, and are constructed from metal-containing nodes (also known as secondary building units, or SBUs) and organic linkers and can be obtained using different synthetic approaches as reported in **Figure 47**. [2]

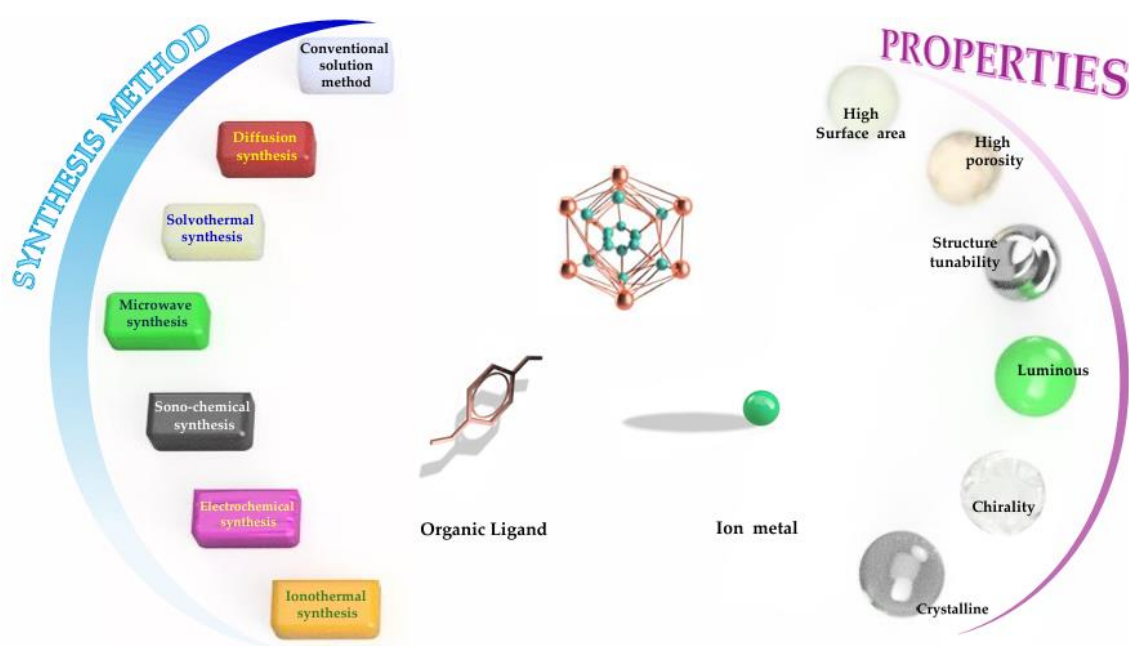


Figure 47. Schematic illustration showing various synthetic approaches for generating MOFs and some specific properties that can be achieved with these artificial functional materials.

Coordination bonds between organic ligands and metal ions can create a network with a specific architecture, by controlling features such as the coordination modes of the inorganic metal ions (or clusters) and the geometries of organic linkers. [3-4] Organic linkers, also known as organic multi-tooth binders, are often composed of carboxylates, azoles, nitriles, and other similar compounds. Additionally, binders can be created and altered through organic synthesis to fit the needs of nodes within the target network. The characteristics of metal nodes and binders, such as their redox active nature, and other physico-chemical attributes of the final network, such as porosity, pore size, and/or pore surface area, typically determine the application of target material. Predicting the network structure is possible if the network node is properly specified. [5-6] Typically, the metal centres inside the MOF structure are composed of metal-azolate or metal-carboxylate clusters. [7-8] However, the influence of the solvent during MOF synthesis, as well as the reaction conditions such as temperature, reaction time, and or pressure among others, also allow for the creation of over 100 different topologies, [9] including two-dimensional (2D) and three-dimensional (3D) structures. Indeed, host and/or solvate molecules can also occupy the pores of the final structure, which is sometimes crucial for the stability of the final crystal. Other types of interactions, such as hydrogen bonds, metal-metal and π - π interactions, may also occur, contributing to the stability of MOF crystals. [10] MOFs are also classified based on the variability of their pore sizes. When the pore size is less than 20 Å, the MOFs crystals are regarded as a microporous. Pore sizes between 20 and 500 Å, are considered mesoporous, and pores larger than 500 Å are classified as macroporous. Most mesoporous and macroporous structures have an amorphous nature. However, there are examples in the literature where large SBU, combined with stiff and long polycarboxylate ligands, have been used to create mesoporous and macroporous

MOFs. [11-12] In the last decades, MOF crystals and films have been considered for different applications, including thin-film electronic devices for sensing, as membrane materials catalyst, drug delivery agents and/or for electrochemical applications. [13] The main advantage of MOFs compared to other porous crystalline materials, such as zeolites, lies in their tuneable structure and functionality. [14-15] As indicated earlier, MOFs offer greater flexibility in design due to the wide variety of metal nodes and organic linkers that can be used. This allows for precise control over pore size, shape, and chemical environment, enabling the creation of materials tailored for specific applications. In sharp contrast, the topology of zeolites is based on a finite number of secondary structure elements, as they are composed of tetrahedral fragments. [16-17] Many structural properties of MOFs are also shared with Covalent Organic Frameworks (COFs), a different class of porous crystalline materials formed through covalent bonds rather than from ionic interactions. These shared properties include high surface area, tuneable pore sizes, and the ability to incorporate a wide variety of functional groups in the crystal structure. COFs also exhibit remarkable stability and versatility, making them also suitable for a wide number of applications in gas storage, separation, catalysis, and drug delivery. From the standpoint of chemical reactivity, the controlled generation of COFs is more challenging than that of MOFs. This is because the number of reactions available to bind and unbind the molecular building blocks to form a COF crystalline structure is very limited compared to the variety of ionic interactions that can be utilized to generate MOF crystals. For example, most stable COFs described to date are based on imine condensation reactions. Additionally, the covalent bonds in COFs require more stringent reaction conditions and precise control over the synthesis process to achieve the desired crystalline structure.

Despite these challenges, COFs offer unique advantages, such as enhanced chemical stability. [18]

13.1 Synthetic Approaches

The synthesis of MOFs is influenced by numerous variables, such as reaction time, temperature, solvent composition, organic ligands, and metal ions, counter-ion presence and crystallization kinetics, which promote crystal nucleation and growth. In most cases, MOF synthesis is performed in a liquid phase by mixing solutions of organic ligand and metal salt. When selecting synthetic conditions, it is crucial to consider the solvent's reactivity and redox potential. These factors are also crucial in figuring out the thermodynamics and activation energy of each reaction. Although growing individual crystals proved to be challenging, solid state synthesis techniques have been applied in certain cases. MOF crystals have frequently been grown by slowly evaporating the reaction solution. Below, we present various synthetic methods employed in the synthesis of MOFs:

Hydrothermal (HT)/ Solvothermal synthesis

Using the hydrothermal synthesis approach, [19] crystalline materials are produced at temperatures ranging from 80° to 220° C from aqueous solutions. This process is carried out in hermetically sealed stainless-steel autoclaves, where autogenous pressure develops. This synthetic approach usually results in high-quality crystalline materials due to the controlled temperature and pressure conditions, which promote effective nucleation and growth of the crystals. The hydrothermal approach is advantageous during MOFs synthesis for two main reasons: firstly, high temperatures can enhance the solubility of the precursors in the reaction medium; secondly, it can rapidly initiate the nucleation process. [20-21] This approach is appropriately employed for materials that have a vapor pressure close to their melting points. The main disadvantage of this method is

the long operating time (can be 3-4 days) and the practically impossible observation of crystal growth. In the case of a solvent other than water, for example organic solvents or ionic liquids, the processes are called solvothermal or ionothermic, respectively. [22-24]

Microwave and ultrasound assisted synthesis

Similar to traditional hydrothermal and solvothermal synthesis, microwave-assisted synthesis is used for the generation of MOFs. [25-26] This method offers several advantages, including enhanced phase and morphological control, reduced crystallization timeframes, and improved particle size distribution through the use of microwave irradiation (MW). The microwave-assisted method was first applied to synthesize MIL-100(Fe) in 2012, and the reaction time was reduced from several days to 6 minutes. MIL-100 (Fe), composed of trimesic acid as the organic ligand and ferrous chloride as a metal node, was exposed to 1600 Watts of irradiation and a temperature of 130° C, for six minutes. This synthesis marks the first instance of MOF being created using microwave irradiation approach. [27] The results obtain during the microwave synthesis indicate that the yield and crystal sizes of the resulting MOF crystals are nearly identical to those achieved by using a hydrothermal approach. The fundamental principle of microwave-assisted synthesis is the interaction of electromagnetic radiation with electric charges, which can include solid ions and electrons or polar molecules in the solvent solution. The electrical resistance of the solid causes an electric current to flow through it. [28] Due to the molecule's increased kinetic energy in the liquid phase because of temperature rise, there are more collisions between polar molecules when an electromagnetic field is applied at a higher frequency. This method has also been used to synthesize both MIL-101 (Cr), which is formed by

terephthalic acid as an organic ligand and chromium (III) nitrate as a metal ion [29]; and MIL-5, which is composed of ethylenediphosphonic acid as organic ligand and ammonium metavanadate as metallic ion [30]. Ionic liquids are an excellent choice for this synthetic approach due to their unique properties of polarizability and ionic conductivity, which make them effective microwave adsorbent agents in addition to traditional solvents. [31] An additional simple, effective, affordable and eco-friendly technique for synthesizing MOF with smooth surfaces under ultrasonic irradiation is the ultrasonic/sonochemical method. Sonochemistry studies how strong ultrasonic irradiation (20 kHz-10 MHz) alters the chemical and physical characteristics of molecules. [32] The process of creating organic metal-coordinating polymers with nanoscale size follows a bottom-up strategy. In fact, when ultrasonic radiation directly interacts with molecules, no chemical reaction may occur; on the other hand, when ultrasound and liquid are joined, an alternating pattern of pressures arises. The solvent is generating tiny bubbles, because of this pressure change. These bubbles then expand and burst; this entire process is known as cavitation. In a few microseconds, [33] hot patches surround the liquid, which is at a temperature of roughly 5000° C and a pressure of roughly 500 atm, during the cavitation process. MOF-5, MIL-53 (Fe) and MOF-177 are some examples of MOF crystals synthesized through this ultrasound approach. [34] Respectively, MOF-5 is composed of terephthalic acid as organic ligand and zinc nitrate as metal ion; MIL-53 (Fe) is formed by trimesic acid as organic ligand and ferric chloride as metal ion, while MIL-177 is designed by 4,4',4''-benzene-1,3,5-triyl-tribenzoic acid as organic ligand and zinc nitrate hexahydrate as metal ion. [35-36]

Electrochemical Approaches

Electrochemical synthesis (EC) provides an alternative approach for the synthesis and design of MOFs, offering a straightforward, manageable, and well-controlled procedure. EC allows for precise control over reaction conditions, such as voltage and current, which can lead to better reproducibility and scalability. Additionally, EC can often be conducted at room temperature and pressure, making it more energy-efficient and environmentally friendly compared to traditional methods. Additionally, in some cases, EC does not need to use any counterions from metal salts like nitrate, perchlorate, or chloride to generate a MOF crystal. [37] For example, Cu-MOF is the first MOF structure to be synthesized electrochemically, using tricarboxylate benzene at the cathode and copper plates as the anode. [38]

Mechanochemical Approaches

One of the first considerations when talking about sustainable chemistry is the avoidance of organic solvents as they have numerous environmental impacts. Three key advantages of the synthesis of MOFs using mechanochemical methods are the elimination of organic solvents, the short reaction time (ranging from 10 to 60 minutes) and the ability to achieve quantifiable yields. Through the mechanochemical process, which includes the grinding phase, the correct orientation of the intramolecular interactions is favoured, aimed at the formation of the coordination complex. [39-41] By using affordable metal precursors like oxides or carbonates, instead of nitrates and metal chlorides, the mechano-synthesis pathway helps to reduce byproduct waste. This synthetic approach, or a prolonged grinding process, has produced several MOFs, such as the MIL-88 B (Fe), which is composed of terephthalic acid as organic ligand and iron (III)

chloride hexahydrate as metal ion. Therefore, MIL-88B (Fe) exhibits high yield, crystallinity, thermal stability, hydrophilicity and flexibility.

Slow evaporation and diffusion approaches

This is a synthetic strategy that is performed at room temperature and does not require energy effort. During the slow evaporation process, reagent solutions are mixed and allowed to evaporate slowly, resulting in crystal formation when a critical concentration is reached. In diffusion approaches, the crystallization process is often initiated by placing solutions containing MOF precursors above or below solvents in which the precursors are insoluble. As the MOF precursors slowly diffuse into the liquid phase where their solubility is reduced crystallization is triggered. Sometimes, a third solvent layer is introduced between the two, further slowing the diffusion process. Gels are often used in these crystallization processes to slow down the diffusion of both precursors and non-solvents. [42-43]

13.2 Green approaches for the synthesis of MOFs

Green chemistry is based on 12 principles that represent the guidelines for energy efficiency, construction of innovative materials, use of safer solvents and reagents, therefore less toxic, and disposal of biodegradable waste and toxic byproducts. In recent decades, one of the goals has been to promote sustainable synthesis models for the synthesis of MOFs. To do so, it is necessary to carry out preliminary assessments that include that precursors must be mostly biocompatible, provide low energy input, a safe reaction environment consisting mostly of aqueous solvents. [44-46] The choice of solvent plays a crucial role in the synthesis of MOFs, as was previously described. The solvent can act as directing agents in the structure or participate in the coordination with metal ions. [47] Organic solvents such as dimethylformamide (DMF) and *N,N*-diethylformamide (DEF) are frequently used in the conventional synthesis of MOF. [48-49] These solvents are particularly attractive for reactions in non-aqueous media due to their well-defined acid-base chemistry, which significantly influence the interactions with the corresponding solutes. [50] Because of their low evaporation rates, these solvent's high boiling temperatures further extend the time that reaction media are available. [51] Nevertheless, when these solvents are heated or burned, a significant number of hazardous amines may be produced. [52] The use of green procedures is not always advantageous from an economic point of view, even if it makes chemical reactions that would otherwise be impractical much safer. [53-54] The environmental impact of a solvent is assessed based on factors such as its biodegradability, ease of extraction from natural and renewable resources and its impact on health. [55] The toxicological risk of a solvent could be reduced if it was produced from recyclable waste. [56] One of the main limitations of MOF synthesis in aqueous media is the poor solubility of

the precursors, unlike in organic solvents. To enhance solubilization, it is useful to start from a careful structural analysis of the organic linkers and metal salts. Additionally, incorporating molecules that present hydrophobic organic groups (such as alkylphosphonic acids and organosilicon polymers) or modulators (polyvinylpyrrolidone and formic acid) into the reaction the environment can facilitate the solubility of the precursors, and hence, increase the probability of crystal growth. As in the case of organic solvents, also for aqueous ones, sometimes the products obtained can present non-optimal characteristics in terms of crystallinity, and/or poor stability of the final product. [57-59] Since research today is mainly aimed at promoting synthetic processes that can be directed towards a more sustainable chemistry, the use of aqueous solvents represents one of the primary objectives. A recent work proposes the use of alkaline-based salts of organic linkers, in particular those based on carboxylates; this determines an increase in their solubility in water, otherwise impossible for common organic precursors. On the basis of this strategy the following compounds have been synthesized: CAU-22 (Zr) [60], MIL-9 (Ti) [61] and MOF-74 (Zn) [58]. Respectively CAU-22 is composed of 4,4'-biphenyldicarboxylic acid (BPDC) as organic ligand and zirconium chloride as metal ion; MIL-9 (Ti) is formed by terephthalic acid as organic ligand and titanium isopropoxide as metal ion; finally, MOF-74 (Zn) is made up of 2,5-dihydroxybenzene-1,4-dicarboxylic acid as organic ligand and zinc nitrate as metal ion. A further intriguing choice for an eco-friendly reaction medium is supercritical liquids. Supercritical carbon dioxide ($s\text{CO}_2$) and water show great promise for the synthesis of MOFs. [62] Therefore, it can be concluded that, thanks to their tuneable properties (polarity, viscosity, surface tension, phase, etc.) under appropriate synthesis conditions, MOFs can be obtained through eco-sustainable synthesis procedures. [63-64] Beyond a critical threshold, increases in temperature and pressure alter the

properties of water, including its polarity and hydrogen bonding. For example, high temperature water (HTW) exhibits a density, ionization constant similar to those of non-polar solvents. Above a critical threshold, increases in temperature and pressure alter the properties of water, including its polarity and hydrogen bonding. Therefore, under conditions of high temperatures and pressures, the corrosion process, especially of the organic linkers became intense. Consequently, in some situations, the synthesis of MOF may also restrict the use of HTW and supercritical water as solvents. Because of its unique chemical characteristics, $s\text{CO}_2$ is a promising solvent for a variety of uses, including extraction, polymerization, biomedicine, catalytic reactions, and synthetic approaches. It also makes it simple to dissolve organic compounds that are insoluble in water. [65-66] Although supercritical fluid was initially used only to clear the pores of trapped solvents after the MOF synthesis, its effectiveness has been demonstrated in designing innovative and sustainable methods for generating MOFs. [67] By using $s\text{CO}_2$, two-dimensional and three-dimensional crystalline coordination structures were obtained. [68] Portoles-Gil *et al.* [69] have extended this green synthesis approach to the construction of a different 2D MOF based on transition metals (Cu^{2+} or Zn^{2+}), in which a small amount of *t*-butyl pyridine has been added to increase the solubility of $s\text{CO}_2$. Specifically, a 1D copper coordination complex was developed using the two bipyridyl ligands in $s\text{CO}_2$. There are new alternatives to hazardous solvents, such as ionic liquids (IL). An IL is a liquid at or below 100 °C that is made up of cations and organic/inorganic anions. Tetrachloroaluminate, triphlate, hexafluorophosphate, ammonium/quaternary phosphonium, imidazolium or pyridinium are examples of related anionic species, whereas the positively charged cation component could be a metal such as sodium. [70-71] ILs are defined as compounds with a melting point lower than that of water. ILs have

proven to be promising candidates for achieving environmentally friendly chemical reactions and are considered sustainable solvents. Because of their low volatility, vapour pressure and low flammability, ILs have recently garnered increased attention as green solvents. Another significant aspect of ionic liquids is the vast array of ion combinations available. In order to guide the MOF precursors and modify the porous structures, ILs can thus be characterized as “design solvents” that can function as structure coordinating agents. [72] ILs offer several unique qualities, including the ability to solubilize both organic and inorganic substances with extraordinarily high stability, low volatility, and recyclable nature, which allows for the synthesis of a wide range of MOFs. In addition, the synthesis of MOFs with a net charge can be due to the large concentration of charged ions in ILs. It is possible to carry out the IL-based MOF synthesis method at both ambient and ionothermal temperatures, especially the former case has provided promising results. It has recently been suggested to employ biocompatible ILs as deprotonation agents rather than hazardous amines to create high-quality green MOFs. [73-74] Lastly, a combination of ILs and sCO₂ has been suggested for the rapid synthesis of MOFs at room temperature. This mixture can help ILs become less viscous, allowing mass transfer to occur at lower temperatures and over shorter period of time. [73] A valid alternative that represents a natural, renewable and economical source is biomass. Molecules harvested from biomass, such as amino acids, peptides, bases and polysaccharides, can be used as linkers to replace traditional organic molecules with higher toxicity. Therefore, the combination of biomass and MOFs represents a sustainable and low-cost strategy for the preparation of advanced functional materials such as BioMOFs, with excellent performance. [76] Glycerol and its byproducts are examples of bioderived solvents. These polar, non-flammable molecules are biodegradable, have low toxicity, high boiling points and low

vapour pressure. Due to its low dielectric constant, glycerol also permits acoustic cavitation and the dissolution of several organic and inorganic salts as well as a range of a transition metal ion complexes. Thus, glycerol can facilitate more effective mass transfer and heating in support of reaction kinetics. Glycerol's high boiling point of 290 °C facilitates the induction of processes without solvent loss, such as through spontaneous vaporization. Glycerol is an attractive solvent for a variety of chemical transformations and offers an alternative method for the environmentally friendly and sustainable manufacturing of desired goods due to its low cost, recyclability, nontoxic nature, and biodegradability. [77-79] However, it is difficult to apply green solvents to all kinds of chemical reactions. The physiochemical features of acidity (ability to give H bonds), basicity (ability to take H bonds), polarity, and polarizability are all offered differently by each solvent. Reaction rate, product selectivity, and the number of synthesis steps can all be significantly impacted by the solvent. [80-81]

13.2.1 Metal precursors and organic linkers for the synthesis of sustainable MOFs

It is important to consider the environmental impacts of the counter ions accompanying the metal ions during the synthesis of MOFs, as they can produce toxic by-products that may harm both persons and ecosystems. For the synthesis of MOFs, the ideal precursors are salts of nitrates, perchlorates, chlorides, acetates, carbonates, hydroxides and oxides due to their high solubility and the formation of water as by-products of reaction. Sulphate-based metal salts, which are generally soluble in water, can be used as models to create sustainable MOFs. Using water as a solvent, trimesic acid and aluminium sulphate as a starting material, CAU-10 was synthesized using this approach. Nonetheless, the porosity, stiffness, and crystal structure of the sulphate anions can be impacted by strong interfacial interactions that occur inside the framework topology. [82-83] Currently, the most affordable, safe, and sustainable metal salts that offer environmentally friendly anions for MOF synthesis are metal hydroxides, acetate and oxides. Since Fe (II) and Zn (II) are found naturally in the human body, it has been determined that they are the least dangerous transition metals. It is crucial to take the organic linker's toxicity into account in addition to the metal ion component. Due to their coordination reactivity with metal nodes, polycarboxylic acids (such as terephthalic and trimesic acid) are the most widely used and traditional linkers available for the synthesis of MOFs. Because of their petrochemical nature, using these organic linkers frequently leads to the development of hazardous by-products. Initially, the synthesis of MOFs involved the use of protonated linkers, such as imidazoles or carboxylic acids, which resulted in a stream of hazardous by-products. Reductions in releases of these toxic chemicals can be achieved by using linkers in their anionic

forms (such as sodium salts). [84] For the synthesis of sustainable MOFs, linkers such as amino acids, nitrogenous bases, peptides, cyclodextrins, and saccharides have been employed. These bioactive compounds have reactive chemical groups that readily mix and coordinate with different metals ions to form BioMOFs. The synthesis of BioMOFs is becoming more and more popular due to their structural diversity, biocompatibility, natural abundance, and compatibility with biological systems. Despite these benefits, the inherent poor symmetry and considerable flexibility of the biomolecules used for their synthesis make it difficult to produce high-quality biocrystals. [85] One of the most often utilized biomolecules in the development of BioMOFs is nitrogen bases. Numerous solitary pairs of nitrogen and oxygen atoms in these heterocyclic molecules are available for coordination with metal ions. Purines, like adenine, are better suited for interacting with substances other than pyrimidines because they have more heteroatoms and hydrogen-bonding groups than the other type of nitrogenous base. [86-88] The presence of carboxylate and amino functional groups in proteins, peptides and other biomolecules such as amino acids make them suitable ligands for the synthesis of BioMOFs. Combining amino and carboxylic functional groups facilitates the creation of distinctive extended network structures. [89] The saccharides have been proposed as chiral building blocks for the synthesis of MOFs as additional biocompatible organic ligands. Among these, cyclodextrins are a type of oligosaccharides characterized by hydrophilic outer edges and a hydrophobic central cavity. They come in various forms, such as α -cyclodextrin, β -cyclodextrin, η -cyclodextrin, each differing in the number of glucose units they contain. Biopolymers, which include cellulose, lignin, chitin and others, represent another category of sustainable organic linkers. [90] These are the most abundant and renewable carbon sources, which possess many functional groups responsible for the design of a wide range of compounds. Among them the most

important are represented by glucose, 5-hydroxymethylfurfural (HMF), levulinic acid, formic acid, lactic acid, glucuronic acid and acetic acid [81] which represent the precursors of MIL-101, MIL-47, MIL-53, Zr-CAU-28 and Ce-CAU-28. [91-94] Respectively, MIL-47 consists of terephthalic acid as the organic ligand and vanadyl sulphate as the metal node; Zr-CAU-28 consists of 2-aminoterephthalic acid as the organic ligand and zirconium chloride as the metal node; finally, Ce-CAU-28 shares the same organic ligand as Zr-CAU-28 but features cerium nitrate as the metal ion.

13.3 Using a micellar approach as a novel sustainable MOF synthesis strategy

As mentioned above, traditional methods for synthesizing COFs and MOFs often require the use of high temperatures, which combined with the poor solubility of their precursors, can hinder adequate control over the size of the crystalline domains and the morphology of the resulting products, thereby limiting the processability of COFs and MOFs. [95] In 2017, Dichtel *et al.* developed a synthetic protocol for preparing stable COF particles, allowing the size to be modulated between forty and hundreds of nanometres. [96] This work represents a significant breakthrough in reducing the size of COF crystals, thereby, converting them into processable materials. By obtaining materials on a nanometric scale, significant advantages can be realized. For example, the nanometre size of COF crystals is particularly interesting for applications in biomedicine, such as drug delivery agents. Additionally, their nanoscale sizes can enhance their processability via printing technique. [97] However, Ditchel's group reported the formation of boron-based COFs at the nanoscale, but these COFs are not as stable as imine-based COFs. Therefore, it is crucial to develop a methodology to produce nanoscale imine-based COFs for biomedical applications. [98-99] To overcome this limitation, Franco *et al.* have developed an efficient one-pot synthesis to generate stable and homogeneous colloidal solutions of imine-based COF nanoparticles (ca. 20 nm in diameter) in water. [100] A micellar catanionic system was developed, supported by the presence of acetic acid as a reaction catalyst. Therefore, in the reaction environment there is an anionic surfactant, sodium dodecyl sulphate (SDS), and cationic one, cetyltrimethylammonium bromide (CTAB), in a ratio of 3:97, respectively; this precise ratio ensures the formation of small micelles, unlike what would happen

if only an anionic surfactant were used. [101-102] The use of this approach involves confined volumes within which the solubilization of the precursors, 1,3,5-tris-(4-aminophenyl) benzene (TAPB) and 1,3,5-triformylbenzene (BTCA) respectively, occurs. Note that TAPB and BTCA are insoluble at room temperature in water. Through various techniques such as DLS, SAXS, SEM and TEM, the obtaining of stable imine-based nanoparticles with a diameter of less than 20 nm at room temperature and atmospheric pressure was confirmed. Micelles represent colloidal aggregates that form when the concentration of surfactant reaches a certain critical level, called critical micellar concentration. These have a different shape: spherical, cylindrical, lamellar and discoidal. They are made up of hydrophobic portion facing inwards in aqueous media and hydrophilic portion facing outwards. Therefore, they are considered as amphiphilic molecules capable of dissolving organic precursors in water, leading to the production of a pseudo-phase that can facilitate chemical reactions of monomers with a hydrophobic nature in water. Various surfactants are used including DTAB, CTAB, CTAHS and SDS. Furthermore, commercially available amphiphilic block copolymers, such as poly (ethylene oxide), Pluronic-poly (propylene oxide), poly(ethylene oxide), or PEO-PPO-PEO as P123 and F127, are examples of non-ionic surfactants that have been widely used as soft models in recent decades to produce materials with large pore sizes and variable pore structures. In the same study, Franco *et al.* also demonstrated the versatility of their approach, by synthesizing another imine-based COF, Tz-COF, via the reaction between 2,4,6-tris(4-aminophenyl)-1,3,5-triazine (Tz) and BTCA; as well as a MOF, specifically MIL-100 (Fe). The limit of MIL-100 (Fe) is mainly due to the difficult crystallization conditions, but thanks to the use of their method Franco *et al.* could generate particles with a diameter of around 20 nm, which represents the smallest size reported for this biodegradable and non-toxic MOF.

A further study that uses the cationic model is the one that leads to the synthesis of COF-300 in which terephthalic acid and tetrakis (4-aminophenyl) methane are the precursors. [103] Another example is the use of reverse micelles which are powerful methods that can also be used for the synthesis of MOFs under milder and more controllable conditions. [104] This approach has been used for example for the synthesis of ZIF-8 nanocrystals, constituted of imidazole as organic ligand and zinc nitrate as metal ion. Precise control of the size of ZIF-8 nanocrystals was achieved by adjusting the concentration of precursors, the reaction temperature, the volume of water and the type of surfactants. [105] The same approach has also been used for the synthesis of Eu-MOF, which is formed by terephthalic acid as organic ligand and europium nitrate as metal ion. [104]

13.4 Applications

The versatility of MOFs and COFs has driven significant advancements in exploiting their unique properties across various application fields, including gas separation and storage, vapor adsorption, catalysis, chemical sensing, biomedical applications and ion conductors as shown in **Figure 48**. [106-107] MOFs and COFs stand out from other materials due to their high porosity, stability and tuneable pore sizes and chemistries. [108-109] The first method to selectively adsorb a certain type of gas molecule from a gas mixture is to modify the porosity and consequently the chemical composition of the structure.

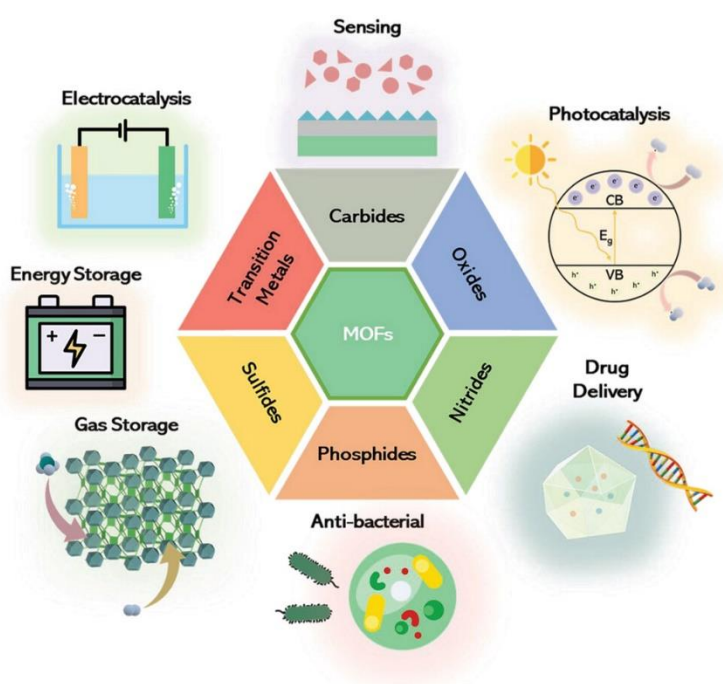


Figure 48. Illustration showing different families of MOFs and their potential applications. [110]

Nonetheless, the pore structures of MOFs and the sizes of gas molecules are typically very similar. Consequently, in order to increase affinity for a particular

adsorbate, MOFs must have additional requirements that may depend on the type of linker or metal ion used during their synthesis. For example, the presence of crystalline structures with open metal sites (OMS) can increase the adsorption affinity for gases molecules. [111] For a range of fuel cell applications, hydrogen is regarded as a superior alternative energy source. For this reason, a lot of effort has been devoted to its storage. [112] Regarding hydrogen adsorption, this is often limited by the poor interaction capacity with the adsorbent surfaces, but it can be improved when considering MOFs with large surface area and tuneable pore structure. To improve this interaction, the MOF must have pore size with a diameter comparable to a hydrogen molecule (2.89 Å). In addition, the MOF's pore volume and surface area grow in proportion to the gravimetric adsorption of high-pressure hydrogen. [113] Comprehensive research has demonstrated that the ability of MOFs to absorb and transport volumetric methane is significantly influenced by the electrostatic and van der Waals interactions between MOFs and CH₄, as well as the framework's flexibility. The adsorption of this gas occurs mainly in the areas of the MOFs that have a high density of OMS, among which it is possible to consider M-MOF 74 (M= Mg, Mn, Co, Ni, Zn). [114] Another goal is to design suitable MOFs and COFs structures that can absorb and capture CO₂. [115] The design of MOFs and COFs as adsorbent for CO₂ collection has been extensively investigated. Significant research efforts have focused on developing MOFs, such as MOF-177 and Mg-MOF-74 that can effectively capture CO₂. [116] The use of highly selective porous materials like MOFs and COFs is necessary for the selective adsorption of hazardous gases produced in various industrial processes. It is known that hazardous CO from binary mixtures is more challenging to capture than the easily polarized CO₂. Nevertheless, a number of technologies have demonstrated potential in eliminating harmful gases. These include MIL-53(Al)-TDC, designed by 2,5-dicarboxylic acid as organic ligand and

aluminium nitrate as metal ion; that could remove sulphur dioxide from the air [117]; UiO-66-COOH, composed of terephthalic acid as organic ligand and zirconium chloride as metal node, which could remove ammonia from the air [118]; and MFM-520 formed by 2,6-naphthalenedicarboxylic acid as organic ligand and zinc nitrate as metal node, which absorbs nitrogen oxide [119]. Indeed, MOFs have further been used in the field of catalysis; in particular, they are frequently employed as heterogeneous catalysts in the form of pure solids. If there are open coordination sites accessible, using their metal nodes is the most straightforward method. Catalytic sites can also be created using organic linkers. Because of their adjustable pore structure, MOFs are frequently employed as hosts for encasing extra catalytic sites, such as metal nanoparticles or enzymes, in addition to their possible inherent catalytic activity. Certain MOFs can serve as precursors for the single-pass synthesis of highly loaded and uniformly dispersed supported nanoparticles-based catalysts when they go through regulated heat degradation. These materials also open up opportunities for electrochemistry and photochemistry, alongside thermal catalysis. Despite having a high metal concentration, MOFs have not always been straightforward to apply in catalysis. Their susceptibility to moisture, instability to heat and chemicals, and potential metal blockage by organic linkers could hinder their use in catalysis. MOFs perform a variety of roles in catalysis; in particular, $\text{Cu}_3(\text{BTC})_2$ has been found to be a highly selective Lewis acid catalyst for terpene derivative isomerization. [120] Bimetallic MOFs are another class of catalyst that functions as a Lewis acid. As an example, MIL-100 ($\text{Fe}^{(III)}$, $\text{Ni}^{(II)}$) contains varying proportions of $\text{Ni}^{(II)}$, which has led to the creation of products with good activity in various organic reactions. Currently, bimetallic MOFs can be constructed with the different ratio of metals. [121-122] Additionally, these bimetallic MOFs are also employed as photocatalysts in a range of reactions, from UV-driven dye

oxidation to hydrogen and oxygen evolution reactions, but this area of research is still in its early stage. [123] Moreover, due to their high porosity, bimetallic MOFs are also employed in the drug delivery. In fact, a high drug load capacity is a characteristic that drug carriers typically seek. With MIL-100 (Cr) and MIL-101 (Cr), the first application of very porous lattice structures as drug carriers has been shown. [124] These two demonstrated good loading capacities, however the chromium toxicity represents clear limiting factor. Because of this, attempts have been made to swap out this metal and exchange it with more biocompatible ones. These include MIL-53, MIL-88A, MIL-88B, MIL-89, MIL-100 and MIL-101-NH₂, which have been utilized as better tolerated substitutes with integrated drug delivery capabilities for both drug administration and contrast enhancement in MRI. MIL-88A is composed of terephthalic acid as organic ligand and iron (III) chloride as metal ion; MIL-89 is formed by trimesic acid as organic ligand and aluminium nitrate as metal ion; MIL-101-NH₂ is synthesized using 2-amino terephthalic acid as the organic ligand and chromium (III) nitrate as the metal ion. These systems therefore have high drug loading capacities, furthermore, thanks to their structure together with any external stimuli, it is possible to release the encapsulated drugs in a controlled and variable manner. [125] Given their broad range of applications, COFs and MOFs can also be used to create sensitive and selective chemical sensors. They share the same properties that make them ideal candidates for adsorption and separation applications. This is possible by virtue of their internal surface area, tuneable pores and microporous structure, which allow high adsorption even at low concentrations. MOFs are employed in electromechanical, chemoresistive, optical and electrochemical sensors. Over the past twenty years, reticular structures have shown themselves to be very good options for various devices that need a mix of ion and electron conductivity, such as fuel cells, batteries, and supercapacitors. [126-128] Since not

all MOFs are good conductors, several studies have been conducted to improve this property through “through-bond” and “through-space” strategies. In the case of the first approach, charge transfer occurs through orbital overlap between metal nodes and organic linkers and by integrating a metal-organic linker inside a MOF. The “through-space” strategy is based on increasing the conductivity through weak interactions that develop inside MOFs, for example donor-acceptor interactions between metal ions and ligands, or by introducing guest molecules into the pores. Another aspect that can improve the conductivity of MOFs is the functionalization of linkers that contain electron-withdrawing or electron-donating groups. [129] Electronic conductivity critically depends on the concentration of free carriers. A common approach used to increase the concentration of free carriers, which are ubiquitous in materials such as organic conductors and metal oxides, is through the oxidation or sub-stoichiometric reduction of redox-active elements. Ionic conductors can also be based on MOFs. Ionic conductors are materials that conduct electric current primarily or entirely through the movement of ions rather than electrons or holes, although ionic conductivity often coexists with electronic conductivity. In the context of ionic conductors, MOFs typically focus on the transport of cations. The most important cations in this context are Li^+ , Na^+ , Mg^{2+} , Zn^{2+} , and Al^{3+} . [125]

13.5 Cu-CAT-1

MOFs have been produced using molecules that mimic the chelating ability of certain organic units found in biological systems. Recently, molecules such as 1,2,4,5-tetrahydroxybenzene or 1,4-dihydroxybenzoquinone, along with some other homologues, have been incorporated in MOF structures. For example, a highly conjugated tricatecholated linker, such as 2,3,6,7,10,11-hexahydroxytriphenylene (HHTP), has been used to generate MOF crystals with different metals, including copper, nickel and/or cobalt. Due to this broad coordination ability with different metals, these systems are generally referred to "M-CAT"., where "M" denotes the metal used during the synthesis of the MOF. Typically, two equivalents of the corresponding metal (II) acetate are combined with one equivalent of HHTP to synthesize the respective M-CAT MOFs. CATs were prepared by combining 1 equivalent of HHTP with 2 equivalents of the respective hydrated metal (II) acetate in an aqueous solution and heating at 85 °C for 24 h to obtain needle-like crystals. [130] Cu-CAT 1 shows good conductivity properties due to the effective orbital overlap between copper and the organic ligand, the calculated value of which is 0.18–0.21 S/cm, which is more than 1 order of magnitude higher than a previously reported value for an iodine-loaded MOF. In addition, preliminary electrochemical measurements of Cu-CAT-1 were also performed using different nonaqueous electrolytes. Cyclic voltammetry measurements reveal that there are several reversible redox peaks, indicating that Cu-CAT-1 can be used as an electrochemical energy storage material. For this reason, numerous experiments have been conducted using Cu-CAT-1 as an electrode material for solid-state supercapacitors. [131] In particular, the study by Xu *et al.* used conductive Cu-CAT-1 nanowires (NWA) as the only high-performance solid-state supercapacitor electrode that could achieve a very high

normalized surface capacitance of $22 \mu\text{F cm}^2$. Furthermore, a parallel investigation was conducted to evaluate the conductivity qualities of Cu-CAT-1 compared with those of other MOFs including MIL-100, MIL-101, ZIF-8, ZIF-67, and UiO-66. From this list of MOFs, ZIF-67 has the highest capacitance with a value of 0.133 F/g which is 260 times lower than that achieved with Cu-CAT-1 powders. This result suggests that the reason for the poor capacitances of MIL-100, MIL-101, ZIF-8 and UiO-66 is their low conductivity, which significantly limits the electron transport on the framework and the diffusion of ions inside the pores. [132]

13.6 Mn-BTC

Mn-BTC represents a MOF in which trimesic acid (BTC) is used as the organic ligand and manganese as the metal ion. According to the traditional synthesis procedure, polyvinylpyrrolidone (PVP) is added to these two precursors as an additive, the reaction is left for 24 hours at room temperature to obtain a white solid. [133-134] Among transition metal MOFs, manganese-based MOFs are particularly significant due to their wide voltage window, low cost, and environmental friendliness. Additionally, manganese is also widely used as an active compound in supercapacitors, where it contributes to high energy density and excellent cycling stability. As an alternative to trimesic acid present in Mn-BTC, terephthalic acid (BDC) can be also used as the organic binder. [135] When comparing Mn-BTC and Mn-BDC in terms of best anodic performance, the former is better than the latter. [136] The poor conductivity and instability of these manganese-based MOFs can result in their rapid degradation, and hence, lead to poor electrochemical stability and low conductivity values. Several studies have shown that an increase in conductivity can be achieved by improving orbital interaction in the structure, and by favouring the synthesis of these MOFs on conductive substrates, which that can accelerate the migration of ions and further improve the electrical conductivity. Another valid alternative is to create a composite combining these manganese-based MOFs with conductive materials such as activated carbon or carbon nanotubes. [137]

14. Objectives of this thesis in the MOFs field

In this chapter, we develop and optimize various synthetic protocols to control the crystallization of both conductive and non-conductive MOFs at the nanoscale. These protocols are tailored for the application of the nanoscale MOF crystals in diverse applications, ranging from supercapacitors to drug delivery systems. The nanoscale size of the investigated MOFs not only facilitates better processing for the generation of electrodes in supercapacitor applications but also can enable the creation of innovative nanoscale drug delivery agents. For the synthesis of nanoscale MOFs, we further explored the micellar approach reported by Franco *et al.* [100] Our initial focus was on synthesizing Cu-CAT-1. A synthetic protocol was developed using a cationic surfactant, such as CTAB, which dissolved in water to obtain a 0.1 M solution. This solution was then used to solubilize the precursors of Cu-CAT-1, specifically HHTP and copper acetate monohydrate. The reaction was left at 37 °C for 24 h. The resultant product of the reaction was characterized from a chemical and morphological point of view, and the collected data were cross-referenced with published literature to confirm that the structure obtained was Cu-CAT-1. In addition to having a microporous structure with a good surface area, the resulting Cu-CAT-1 also exhibit a XRD pattern comparable to those reported in the literature. A solvothermal synthesis approach is reported in literature that involves a variation of the reaction conditions; in fact, in this case, compared to the micellar approach, the reaction is carried out at 85 °C for 12 hours. The Cu-CAT-1 synthesized using our synthetic approach exhibits a distinct morphological structure compared to the Cu-CAT-1 synthesized employing conventional methods. Specifically, our procedure yields Cu-CAT-1 nanoparticles with an average diameter between 40

and 50 nm, whereas the conventional synthetic methods procedure large fibres, in the micrometre range. This synthetic approach is therefore advantageous for multiple reasons; firstly, the micellar approach uses aqueous solvents, and the reaction can be processed at room temperature and atmospheric pressure; secondly, there is a variation in morphology and a reduction in size even if the typical characteristics of the MOFs remain unchanged (crystallinity, porosity...), which can be advantageous, particularly for processing. The reaction kinetics were also examined by stopping the reactions at various times and measuring the crystallinity of the isolated material at each specific time point. It was observed that a crystalline structure formed within an hour after the reaction started, although there were some morphological differences in the material produced compared to the MOF nanoparticles obtained using 24-hour protocol. We are currently studying the electrochemical properties of Cu-CAT-1 nanoparticles. We plan to integrate Cu-CAT-1 nanoparticles into electrodes using liquid-based deposition methods (e.g., drop casting) to study their performance as supercapacitors, leveraging their high processability due to their nanoscale size. It is important to note that Cu-CAT-1 microcrystalline powder obtained through conventional synthetic approaches will be more challenging to integrate into a supercapacitor electrode using liquid-based deposition methods. We have also synthesized other MOFs using the micellar approach. For instance, we have developed a manganese-based MOF, leveraging the frequent use of manganese in supercapacitor applications. Manganese is favoured in these applications due to its excellent electrochemical properties, such as high specific capacitance and good cyclic stability. This makes manganese-based MOFs particularly suitable for enhancing the performance of supercapacitors. Therefore, a micellar approach was developed and optimized to obtain Mn-BTC at the nanoscale. A catanionic model consisting of SDS and CTAB in a 97:3 ratio was developed and

optimized. SDS and CTAB can generate micelles in aqueous solution, which ensure the solubilization of the Mn-BTC precursors in water and allow the reaction to occur in a confined space to obtain the nanoscale crystals. The reaction is left at 30 °C for 48 hours; as in the case of Cu-CAT-1, also for Mn-BTC the reaction is conducted, at room temperature and atmospheric pressure. The final product was characterized in terms of its chemical and morphological properties and compared with the findings reported in the literature. When compared to the traditional solvothermal method, it is evident that synthesizing the MOF within a confined space (i.e. the micelle) leads to significant morphological variations. Specifically, the traditional method produces a fibrous structure whereas our micellar approach yields nanoparticles with a diameter of approximately 100 nm. We are currently studying the electrochemical properties of Cu-CAT-1 and Mn-BTC nanoparticles. We plan to compare our data with those obtained using traditional synthetic approaches to identify any differences in electrochemical performance when used as electrodes for supercapacitor applications. Once these studies are completed, if they will prove promising, we will consider the coupling of the two systems to build asymmetric supercapacitors.

15. Materials and Methods

15.1 Chemical and reagents

2,3,6,7,10,11-hexahydroxytriphenylene, hexadecyltrimethylammonium bromide were supplied from ThermoFisher Scientific. Manganese chloride, copper acetate monohydrate, trimesic acid, sodium dodecyl sulphate, sodium hydroxide, methanol and absolute ethanol were purchased from Merck (Darmstadt, Germany). Aqueous solutions were prepared with Milli-Q water.

15.2 Instruments

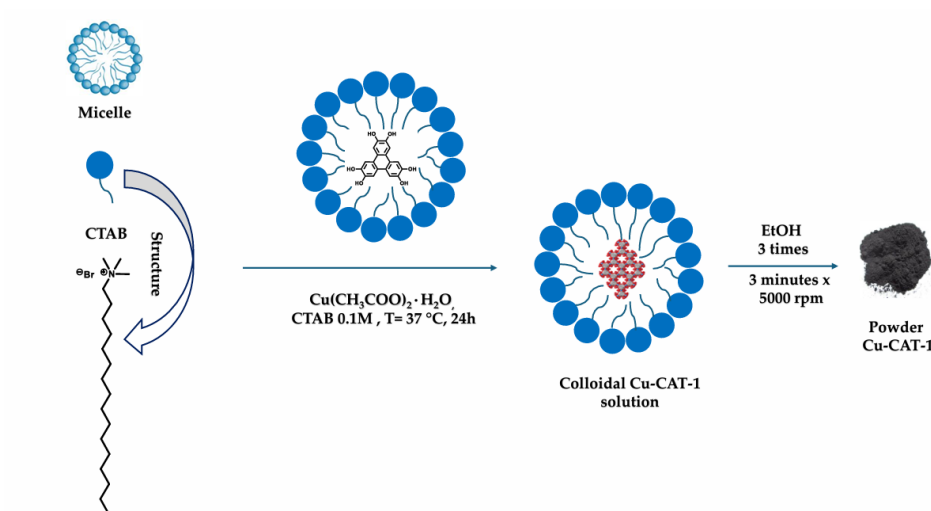
PXRD patterns were collected with PANalytical X'Pert PRO MPD Θ/Θ powder diffractometer of 240 millimetre of radius (CuK α radiation= 1.5418 Å) equipped with a PIXcel detector in a configuration of convergent beam with a focalizing mirror and a transmission geometry with a flat sample sandwiched between low absorbing films (polyester mylar of 3.6 microns of thickness). PXRD measurements were collected on flocculated samples in ethanol with a step sized of $0.0263^\circ 2\Theta$ and a measuring time of 300 seconds per step. Dynamic Light Scattering measurement were performed using a VASCO KIN Particle Size Analyzer from Cordouan Technologies. Measurements of the micellar colloidal precursors solution in water were collected for 60 seconds in a quartz cuvette. The cumulant algorithm was applied to extract the hydrodynamic diameter by means of the Stokes-Einstein equation. X- ray diffraction measurements were performed at XALOC-BL 13 beamline at Alba synchrotron (Bellaterra, Barcelona, Spain), using a photon energy of 15 keV. The flocculated powder in ethanol solution was sealed in a glass capillary. The 2D Debye-Scherrer diffraction rings

from powder measurements were collected on a PILATUS 6M DECTRIS detector and integrated using the Dioptas software package. Nitrogen sorption and desorption measurements were done at 77K using TriStar 3000 from Micrometrics. Carbon black lot 180049/180052 ($21.3 \text{ m}^2/\text{g} \pm 0.75$) was used as certified reference material to check the accuracy of the analyser by triplicate. Result (mean of three estimates): $21.9537 \text{ m}^2/\text{g}$ (SD: 0.13575). The degassing temperature for the analysis of Cu-CAT 1 after 24h of synthesis reached 100°C and the degassing period was set for 20 hours. The relative pressure (P/P_0) used for the BET determination ranges from 3.2899 E^{-5} to 0.9952 (Cu-CAT 1 24h). The degassing temperature for the analysis of Cu-CAT 1 after 1h of synthesis reached 150°C and the degassing period was set for 4h. The relative pressure (P/P_0) used for the BET determination ranges from 3.3122 E^{-5} to 0.9950 (Cu-CAT 1 1h). The degassing temperature for the analysis of Mn-BTC reached 300°C and the degassing period was set for 20h. The relative pressure (P/P_0) used for the BET determination ranges from 2.1618 E^{-5} to 0.9911 (Mn-BTC). Thermogravimetric Analysis (TGA) was performed on a Mettler-Toledo TGA-851 thermobalance. The experimental conditions required $70 \mu\text{L}$ volume alumina crucibles and a dry nitrogen atmosphere with a flow rate of $50 \text{ mL}/\text{min}$. A $10^\circ \text{ C min}^{-1}$ ramp rate was used from 30° C to 800° C . Scanning Electron Microscopy (SEM, JEOL JSM-7100), images of the Cu-CAT 1 and Mn-BTC were taken at 5 kV. The colloidal suspension was drop casted onto a silicon wafer and lightly washed with ethanol to remove the surfactant. After drying at ambient conditions, the samples were sputtered with carbon. An energy-dispersive X-ray (EDX) detector was used for elemental mapping analysis, operating at 10 kV. Scanning Transmission Electron Microscopy (STEM) analysis was carried out in an X-Field Emission Gun (X-FEG) Titan FEI microscope operated at 300 kV. The microscope was equipped with a monochromator, a spherical aberration corrector for the electron probe, which

was aligned using a gold standard sample prior the experiments, assuring a potential spatial resolution of 0.8 Å. Data collection was performed using a low angle annular dark field detector (LAADF). The XPS experiments were carried out in ESFOSCAN, an equipment based on the PHI VersaProbe 4 instrument from Physical Electronics (ULVAC-PHI). Measurements have been done with a monochromatic focused X-ray source (Aluminium Kalfa line of 1486.6 eV) calibrated using the 3d5/2 line of Ag with a full width at half maximum (FWHM) of 0.6 eV. The area analysed was a circle of 100 microns in diameter, and the resolution selected for the spectra was 224 eV Pass Energy and 0.8 eV/step for the general spectra and 27 eV Pass Energy and 0.1 eV/ step for high resolution spectra of the selected elements. The analysis and fitting of the spectra were made with Multipack program. A combination of a low-energy electron gun (less than 10 eV) and a low-energy Argon ion gun (less than 5 eV) was used to discharge the powders when necessary. All measurements were performed in an ultra-high vacuum (UHV) chamber at a pressure between 5×10^{-10} and 5×10^{-9} Torr. Diffuse Reflectance Infrared Fourier Transform Spectroscopy (DRIFT-FTIR) was performed using a Nicolet 5700 equipped with a DRIFT accessory having a spectral range of 4000-400 cm^{-1} . In order to use this approach, the sample must be prepared by combining it with the proper quantity of KBr (matrix transparent to IR light). After the sample is ready, it is put in a micro or macro cup and exposed to infrared radiation. As IR light interacts with the particles and reflects off them, it permeates the sample. This dispersed energy is directed by the mirror at the output toward the spectrometer's detector, which produces the interferogram.

15.3 Synthesis of Cu-CAT-1 nanoparticles

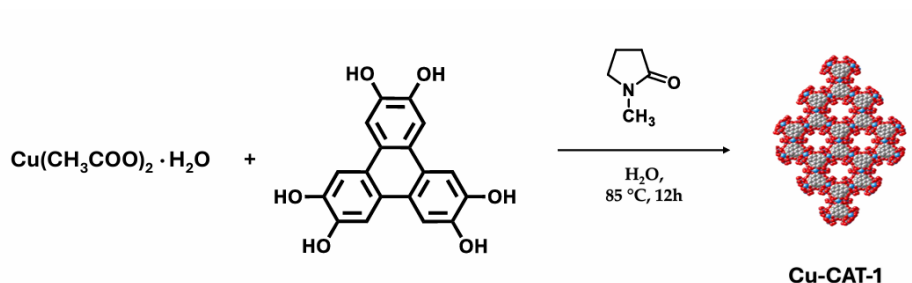
In a typical reaction a 0.1 M aqueous solution of hexadecyltrimethylammonium bromide (CTAB) was prepared. Several reactions were carried out by varying the ratio of the precursors' equivalents before obtaining the optimal synthetic conditions. Specifically, 1.0 mL of 0.1M CTAB aqueous solution was used to solubilize copper acetate monohydrate (34.0 mg; 0.15 mmol) under sonication and 0.5 mL of methanol was used to solubilize HHTP (25.0 mg; 0.077 mmol) under sonication. Following the solubilization of the precursors, 50.0 mL of the 0.1M CTAB aqueous solution is mixed with the HHTP solution. The copper acetate solution is then added drop by drop. The black final solution was left at 37° C for 24 hours, resulting in the isolation of a dark powder, as illustrated in Scheme 11.



Scheme 11. Illustration of the micellar approach used to synthesize nanoscaled Cu-CAT-1 particles and a picture of the final powder obtained.

Experiments were conducted at various reaction times, including 15 minutes, 1 hours or 2 hours to evaluate the crystallinity of the final product isolated at each

reaction time. After 24 hours, 50.0 mL of absolute ethanol is then added to the reaction solution, which allows the micelles that were responsible for the formation of Cu-CAT-1 to burst. This produces a black precipitate that must be thoroughly centrifuged three times (3 minutes x 5000 rpm) to remove the surfactant. Additionally, the synthesis of Cu-CAT-1 was carried out using a conventional solvothermal method, as previously reported in literature [138] and illustrated in **Scheme 12**, to assess the product characterization and facilitate a comparison.



Scheme 12. Scheme showing the synthetic approach used to synthesize Cu-CAT-1 through a conventional method.

Specifically, 3.33 mL of deionized water is used to solubilize copper acetate monohydrate (25.0 mg; 0.077 mmol) and HHTP (16.78 mg; 0.092 mmol), then *N*-methyl pyrrolidone (339.9 mg; 3.42 mmol; $d=1.03\text{ g/cm}^3$) is added. After a few minutes of sonication, the entire solution is heated to $85\text{ }^\circ\text{C}$ for 12 hours. After the reaction has cooled to room temperature, the product was washed 3 times using distilled water and 3 times using acetone. Finally, the product was dried at $60\text{ }^\circ\text{C}$ to produce a black powder.

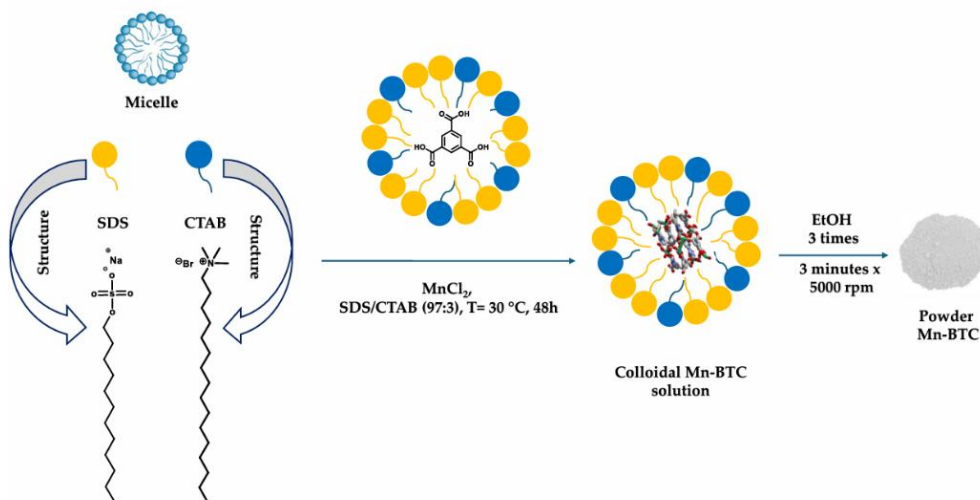
15.4 Synthesis of Mn-BTC nanoparticles

For the synthesis of Mn-BTC nanoparticles a catanionic mixture was prepared by mixing the cationic surfactant hexadecyltrimethylammonium bromide (CTAB) and sodium dodecyl sulphate anionic (SDS) in an SDS/CTAB ratio of 97:3. The ratio has been optimized to promote the formation of micellar assemblies with lower curvature, thus facilitating the colloidal stabilization of MOF precursors, namely trimesic acid and manganese chloride. Two distinct solutions have been prepared:

Solution A: Sodium hydroxide (40.2 mg; 1.00 mmol) is solubilized in 61.0 mL of a solution of 0.1M SDS aqueous solution; then trimesic acid is added (70.47 mg; 0.33 mmol) and only once the complete solubilization has occurred, 2.0 mL of a 0.1 M CTAB aqueous solution are added.

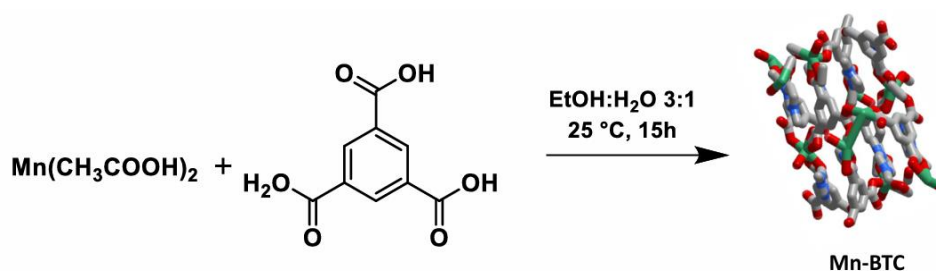
Solution B: Manganese chloride (63.29 mg; 0.39 mmol) is solubilized in 42.0 mL of a solution of 0.1M SDS aqueous solution and only once the complete solubilization is achieved 1.0 mL of a solution of 0.1 M CTAB aqueous solution is added.

Finally, solution A is then added to solution B drop-by-drop under stirring and the final solution is left at 30 °C for 48 hours as it is illustrated in **Scheme 13**.



Scheme 13. Illustration of the micellar approach used to synthesize nanoscaled Mn-BTC particles and a picture of the final powder obtained.

After 48 hours a volume of 103.0 mL of absolute ethanol is added to the reaction, which allows the micelles that were responsible for the formation of Mn-BTC to burst. This produces a white precipitate that must be thoroughly centrifuged three times (3 minutes x 5000 rpm) to remove the surfactants. Additionally, the synthesis of Mn-BTC was carried out using a conventional solvothermal method, as described in literature [139] and illustrated in **Scheme 14**. The synthesis of Mn-BTC crystals using the reported solvothermal method enabled us to easily compare the physicochemical properties of our reaction product with those of the reported one.



Scheme 14. Scheme showing the synthetic approach used to synthesize Mn-BTC through a solvothermal method.

Specifically, 50.0 mL of deionized water is used to solubilize manganese acetate (1230.0 mg; 5.0 mmol), while trimesic acid (3320.0 mg; 15.0 mmol) was dissolved in 150.0 mL of ethanol. Then the two different solutions were mixed, and the final reaction was stirred at 25° C for 15h. After the reaction product was recovered by centrifugation and washed with ethanol three times, a white powder was collected and dried at 60°C for 12 hours.

16. Results and Discussion

16.1 Characterization of Cu-CAT-1 nanoparticles

To elucidate the crystallinity of the Cu-CAT-1, powder X-Ray diffraction (pXRD) was performed. The results indicate that the powder obtained from our micellar synthetic method presents clear diffraction peaks, as shown in **Figure 49A**. Furthermore, a kinetic evaluation of the crystallinity of the reaction at different reaction times was made. Considering that a complete reaction occurs 24 hours after its initiation, the reaction was stopped at different times (fifteen minutes, an hour and two hours) to study the formation of crystals over time. As demonstrated by **Figure 49C**, there is clear evidence of crystallinity in the reaction product as early as 15 minutes, which becomes more pronounced after 1 hour and 2 hours. Consequently, a deeper chemical and morphological characterisation of Cu-CAT-1 after an hour was carried out. The chemical stability of Cu-CAT-1 was examined by suspending the sample in *N,N*-dimethylformamide, acetone and water for 24 hours (**Figure 49B**). The powder X-ray diffraction patterns collected for each sample confirmed the retention of the crystallinity in the nanoscaled Cu-CAT-1 samples.

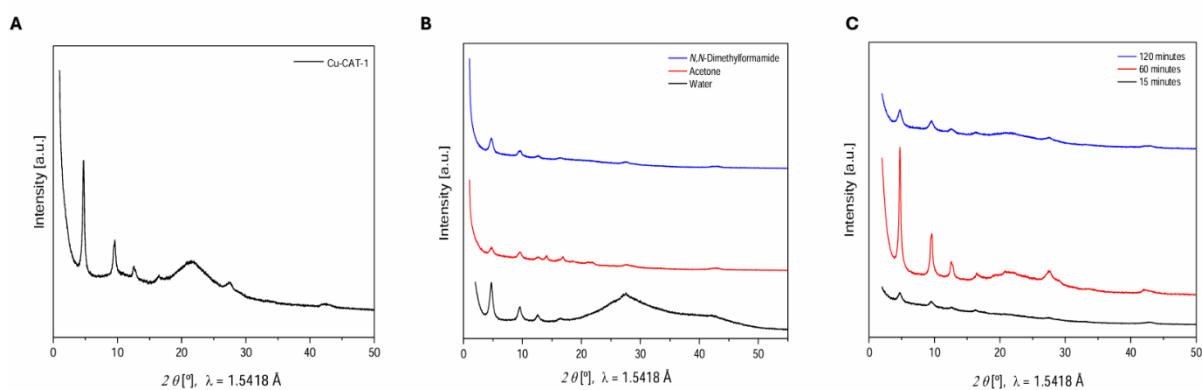


Figure 49. **A)** pXRD of Cu-CAT-1 of 24 hours. **B)** Comparison between pXRD of Cu-CAT-1 after 15 minutes (black), 60 minutes (red) and 120 minutes (blue). **C)** Comparison between pXRD of Cu-CAT-1 after immersing for 24 hours in different solvent: water (black), acetone (red), *N,N*-dimethylformamide (blue).

By modifying the previously described synthetic protocol, we synthesized a product with a significantly different crystallinity, as illustrate in **Figure 50A**. This was achieved by setting up a cationic system with the presence of both CTAB and SDS in different proportions and carrying out the same post-synthetic processing of the reaction product. Comparison of the two pXRD patterns, revealed the existence of contaminants that altered the XRD pattern when SDS was added to the reaction media. We increased the number of ethanol washes to try to eliminate all the surfactants. The FT-IR spectra from the spectra of the Cu-CAT-1 in presence of SDS differs greatly from the spectra of the Cu-CAT-1 with only the CTAB, as illustrate in **Figure 50B**.

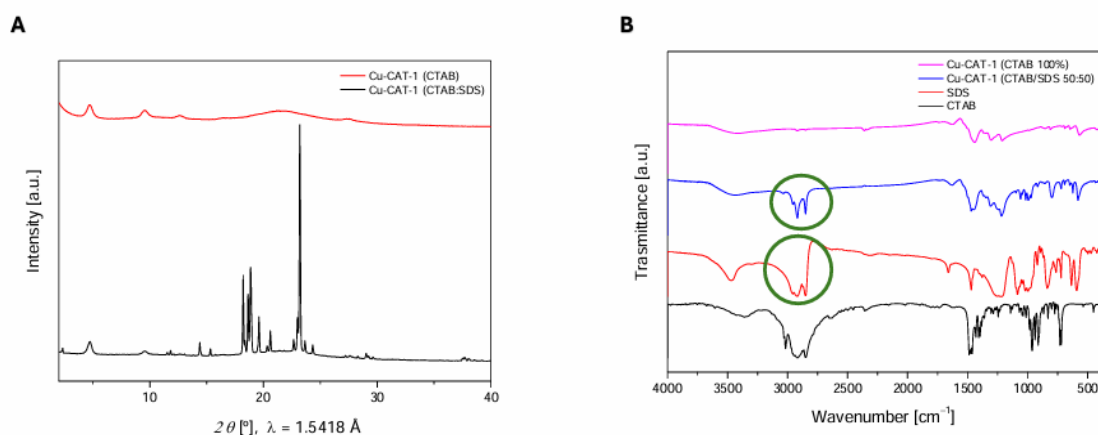


Figure 50. **A)** Comparison between pXRD of Cu-CAT-1 synthesized only with CTAB (black) and pXRD of Cu-CAT-1 synthesized with a CTAB and SDS mixture (red). **B)** Comparison between different FT-IR spectra of Cu-CAT-1 synthesized only with CTAB (purple) and Cu-CAT-1 synthesized with the mixture of CTAB and SDS (blue). FT-IR

profiles of the surfactants SDS (red) and CTAB (black) highlighting how SDS signals are also present in Cu-CAT-1 where anionic surfactant is employed during the synthesis.

Synchrotron X-Ray diffraction studies were performed to confirm that the product obtained after 24 hours is indeed Cu-CAT-1 (**Figure 51**). The obtained diffraction data was obtained using the Pawley refinement technique, with reference to the provided structural model. [140-141] The XRD pattern obtained from the Cu-CAT-1 nanoparticles can be clearly attributed to the diffraction pattern of Cu-CAT-1, which has peaks at 2Θ ($\lambda = 0.827 \text{ \AA}$) = 2.5° , 5.0° , 6.6° , 8.8° .

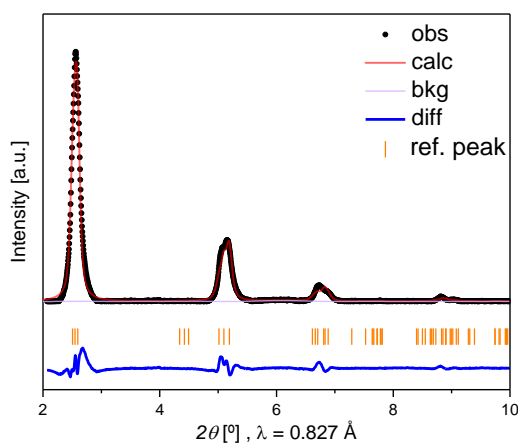
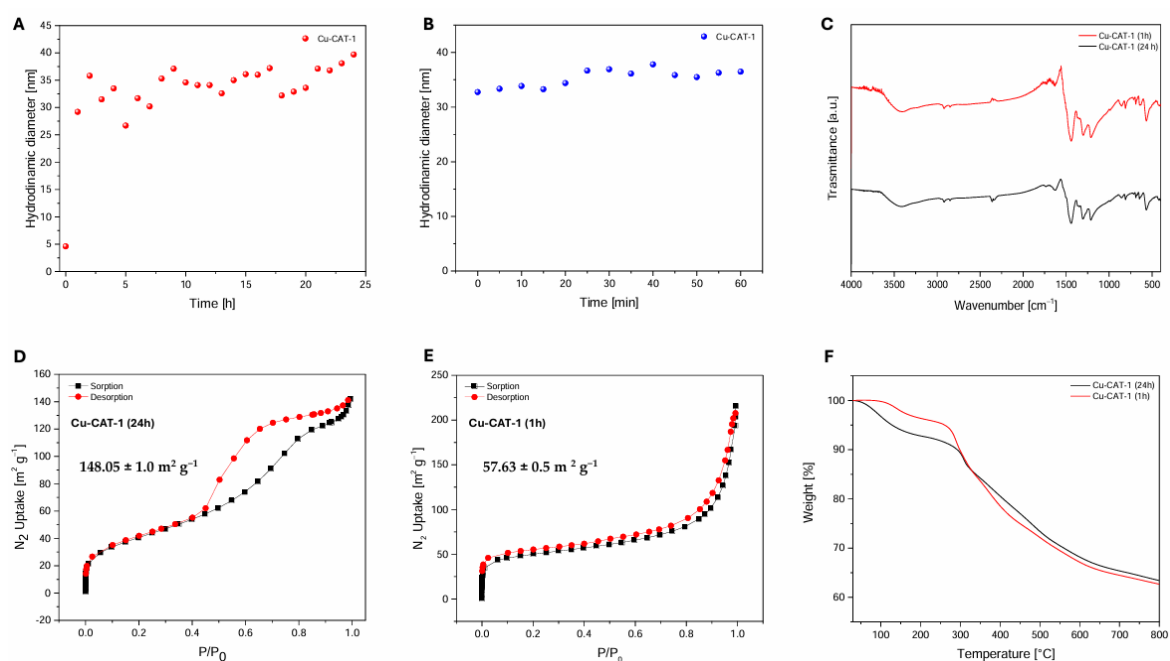


Figure 51. Pawley refinement of synchrotron X-ray diffraction measurements of the flocculated nanoparticles. The observed measurement (black) matches well with the calculated data (red). The background (purple), the reference peaks (orange), and the difference between the observed and the calculated data (blue) are also depicted in the graph. The refinement resulted in a R_w value of 182.29. The observed unit-cell parameters ($I4_1/a$) were $a = 21.46 \text{ \AA}$, $b = 21.10 \text{ \AA}$, $c = 6.50 \text{ \AA}$, which are very close to the theoretical cell values $a = 21.91 \text{ \AA}$, $b = 21.87 \text{ \AA}$, $c = 6.55 \text{ \AA}$.

To elucidate the processes underlying the formation of Cu-CAT-1 nanoparticles in the cationic micellar medium, a time-lapse dynamic light scattering (DLS)

experiment was performed. DLS indicated that the mean hydrodynamic diameter of Cu-CAT-1 nanoparticles stabilized at approximately 36.0 nm after 1 hour from the start of the reaction (**Figure 52A, 52B**). To further investigate the morphology of Cu-CAT-1, we conducted a scanning electron microscopy (SEM) analysis on the flocculated and dried samples at 1h and 24h after the reaction began. After 1 hour of reaction, we observed the formation of Cu-CAT-1 nanoparticles with an irregular and undefined structure, likely because the reagents had not yet fully reacted (**Figure 52I**). On the contrary, after 24 hours, it is possible to identify a well-defined nanoparticle structure with a diameter approximately between 60 nm and 70 nm. Therefore, the morphology of the resulting aggregates is influenced by the variation of the reaction time (**Figure 52J**).



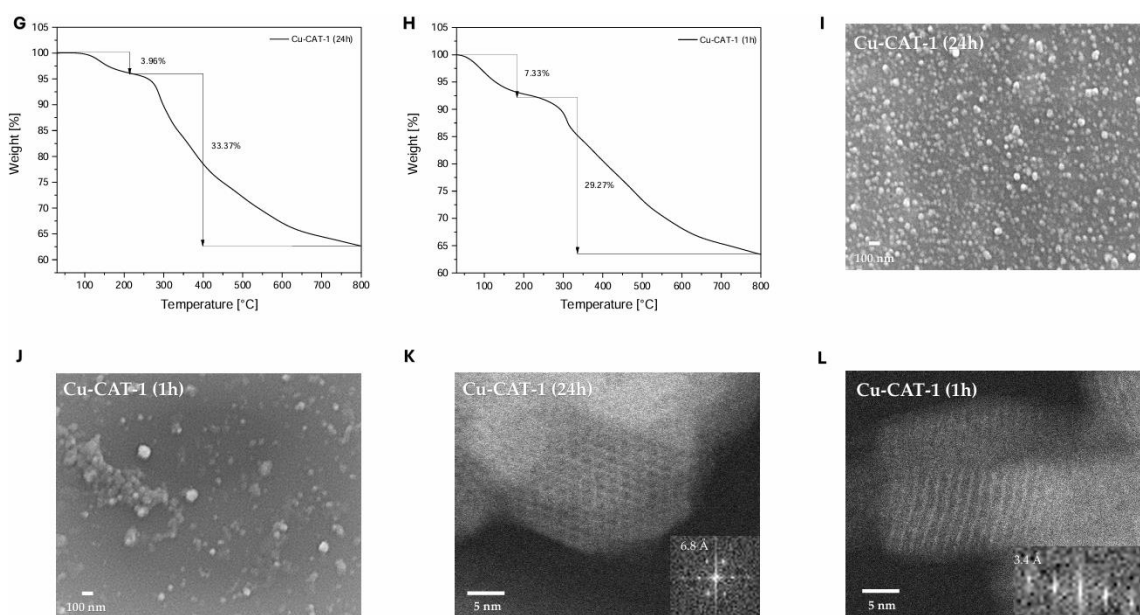


Figure 52. **A)** DLS kinetic profile of Cu-CAT-1 growth measured over 24 hours. **B)** DLS kinetic profile of Cu-CAT-1 growth measured over 1 hour. **C)** Comparison between DRIFT FT-IR spectres of Cu-CAT-1 24 hours (blue) and Cu-CAT-1 of 1 hour (red). **D, E)** Nitrogen gas sorption (black squares) and desorption (red dots) of Cu-CAT-1 measured at 77K after 24 hours and 1 hour, respectively, at 77 K. **F)** Comparison of TGA measurements profiles of Cu-CAT-1 24 hours (black) and Cu-CAT-1 hour (red). **G)** TGA curve of Cu-CAT-1 24 hours. **H)** TGA curve of Cu-CAT-1 of 1 hour. **I)** SEM image at high magnification of Cu-CAT-1 24-hours nanoparticles with a diameter of 60 nm and obtained at 24 hours. **J)** SEM image at high magnification of Cu-CAT-1 of 1-hour nanoparticles with a diameter of 60 nm. **K)** STEM images of Cu-CAT-1 at 24 hours with 60 nm diameter and magnified HR-TEM image of the defined area with measured d -spacing of 6.8 Å. **L)** STEM images of Cu-CAT-1 at 24-hours with 60 nm diameter and magnified HR-TEM image of the defined area with measured d -spacing of 3.4 Å.

Scanning transmission electron microscopy (STEM) studies further validated the observations made by SEM, synchrotron X-ray diffraction, and/or pXRD analysis. STEM images clearly show the formation of spherical nanoparticles after 24 h of reaction with diameters of approximately 60–70 nm, while a less

regular morphology is observed after 1 hour of reaction. The inserts of **Figures 52K 52L** present high resolution (HR) STEM and FFT images, revealing a regular crystalline structure with a d -spacing of 6.8 Å for Cu-CAT-1 nanoparticles after 24 hours (**Figure 52K**) and less defined fringes with a d -spacing of 3.4 Å after 1 hour of reaction (**Figure 52L**). To investigate whether these morphological variations translate into distinct physical-chemical properties, thermogravimetric analyses (TGA) and isothermal nitrogen sorption measurements were performed. Comparing the two thermogravimetric profiles reported in **Figure 52F** it is possible to highlight that the trend of the curve is nearly similar. In fact, both products exhibit good thermal stability up to a temperature between 200° C and 300° C. Beyond this range, a weight loss of 33.37% is observed for Cu-CAT-1 after 24 hours of reaction, and 29.27% for the Cu-CAT-1 after 1 hour of reaction (see **Figure 52G and 52H**). The isothermal nitrogen sorption measurement of Cu-CAT-1 nanoparticles after 24 hours of reaction confirms the porosity of the system (**Figure 52D**). The results were fitted to the Brunauer-Emmet-Teller (BET) model, indicating that the Cu-CAT-1 present a microporous structure with a BET surface area of $148.05 \pm 1.0 \text{ m}^2 \text{ g}^{-1}$. However, it is evident that the Cu-CAT-1 analysed after 1 h of reaction shows a lower porosity ($57.63 \pm 0.5 \text{ m}^2 \text{ g}^{-1}$) which is also confirmed by the results of the other analyses performed (**Figure 52E**). Furthermore, diffuse reflectance Fourier-transform mid-infrared spectroscopy was also used to confirm the chemical composition of Cu-CAT-1 (**Figure 52C**). The observation of the characteristic peaks indicating the binding coordination between copper ions and the HHTP ligand (Cu-O) and copper and water molecules is indicated by the presence of the peaks at 568 and 630 cm^{-1} present in both 24-hours and 1-hour Cu-CAT-1 samples. Furthermore, a high-resolution XPS study was conducted to confirm the oxidation state of copper in the final structure of Cu-CAT-1. **Figure 53**

presents the high-resolution XPS profiles recorded for copper. The Cu 2p_{3/2} orbit shows an asymmetric peak, consisting of a source peak at 934.63 eV and a satellite peak at 943.33 eV. The Cu 2p_{1/2} orbit shows a peak at 954.6 eV, with a spin energy difference of -20.0 eV, which are consistent with an oxidation state of (II) of the copper ions in the MOF.

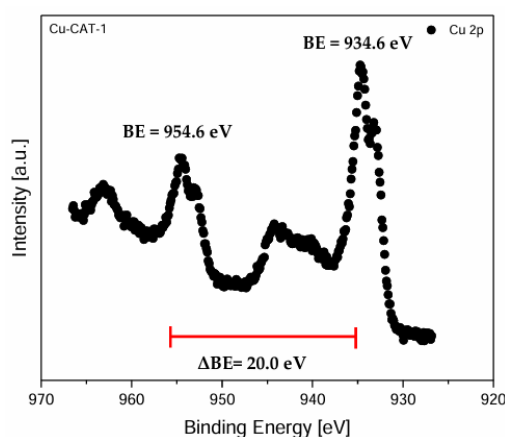


Figure 53. High-resolution XPS spectra recorded for Cu 2p_{3/2} and Cu 2p_{1/2}.

Figure 54 presents the characterization data for Cu-CAT-1 samples prepared using the conventional approach. The X-ray diffraction pattern for Cu-CAT-1, synthesized using the conventional synthetic method, was obtained and compared with the pattern measured from the Cu-CAT-1 nanoparticles generated via the micellar approach (**Figure 54A**). From the comparison it is possible to see how the two-diffraction pattern coincide perfectly highlighting that they present the same crystalline structure. The thermal stability of Cu-CAT-1 was probed by thermal gravimetric analysis (TGA), as shown in **Figure 54C**. The analysis demonstrated no weight loss between 200 °C and 300 °C. Beyond this range, a significant weight loss of 41.73% was observed. The isothermal nitrogen sorption measurement of Cu-CAT-1 samples produce via conventional methods confirms the porosity of the system (**Figure 54B**). The results were fitted

to the Brunauer-Emmet-Teller (BET) model, indicating a Cu-CAT-1 obtained via conventional methods presents microporous structure with a BET surface area of $180.0 \pm 1.0 \text{ m}^2 \text{ g}^{-1}$. To explore the morphology of Cu-CAT-1 obtained by conventional synthesis, we used scanning electron microscopy (SEM). The image in **Figure 54D** shows that the Cu-CAT-1 synthesized via conventional method consists of rods that are several micrometres long. Therefore, comparing it with what was obtained by applying the micellar approach it is possible to see how there is a huge variation in the morphology and size of the final product. Furthermore, diffuse reflectance Fourier-transform mid-infrared spectroscopy was also used to analyse the chemical composition of Cu-CAT-1 (**Figure 54E**). Also, in this case the characteristic band indicating the coordination bond between the copper ions and the HHTP ligand (Cu-O) can be observed. Additionally, the coordination between the copper and water molecules is indicated by the peaks at 568 and 630 cm^{-1} .

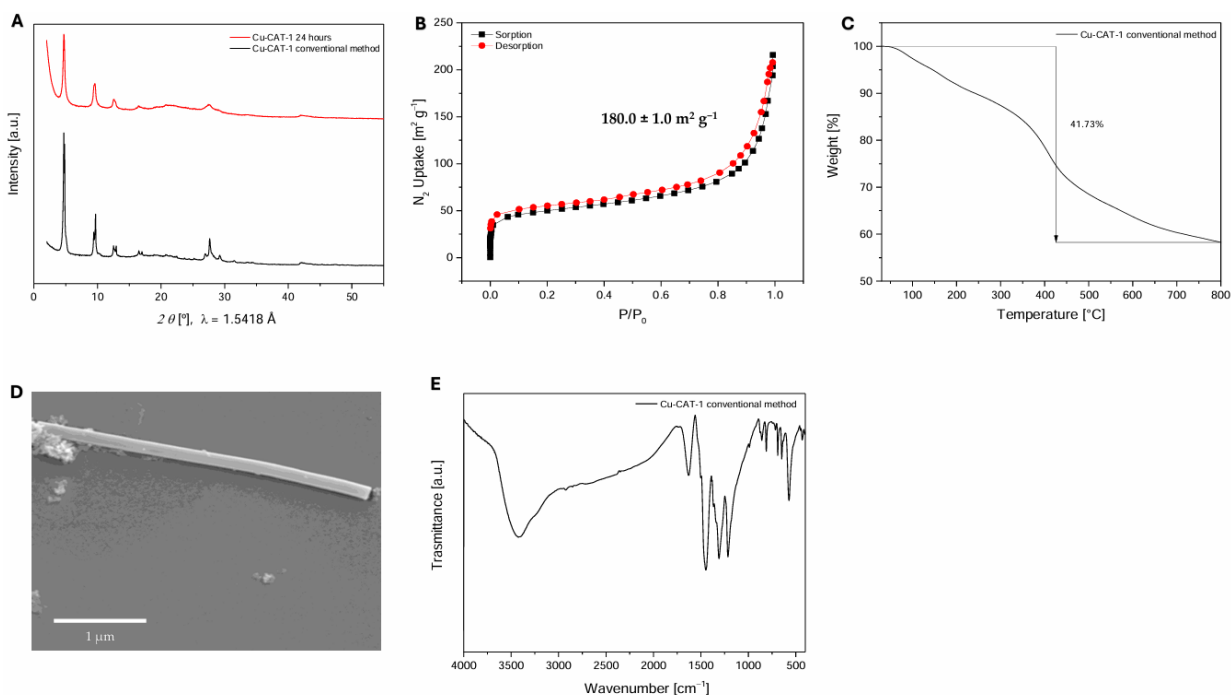


Figure 54. **A)** Comparison between pXRD of Cu-CAT-1 synthesized with conventional methods (black) and 24 hours Cu-CAT-1 nanoparticles (red). **B)** Nitrogen gas sorption (black square) and desorption (red dots) of Cu-CAT-1 synthesized with conventional method measured at 77K. **C)** TGA curve of Cu-CAT-1 synthesized with conventional method. **D)** SEM image at high magnification of Cu-CAT-1 showing rod of several microns; **E)** DRIFT-FT IR spectra of Cu-CAT-1.

16.2 Characterization of Mn-BTC nanoparticles

To elucidate the crystallinity of the structure, powder X-Ray diffraction (pXRD) was performed. The results indicate that the powder obtained from our micellar synthetic method presents clear diffraction peaks, as shown in **Figure 55B**. The peaks at 10.33° and 20.86° are characteristic of the Mn-BTC crystals as reported in the literature, a result that suggests the successful formation of Mn-BTC. [142-143] The progressive growth during the reaction time of Mn-BTC inside the micelles was examined by DLS. A kinetic study was conducted to monitor the progressive increase in the hydrodynamic diameter of Mn-BTC nanoparticles. The diameter stabilized at approximately 142.0 nm after about 10 hours, as shown in **Figure 55A**. To measure the evolution of the reaction at each time point, a 3.0 mL aliquot of the reaction mixture was taken at specified intervals. A thermogravimetric analysis (TGA) was performed to examine the chemical and physical characteristics of the final product after 48 hours of reaction. From the profile, reported in **Figure 55D**, it is possible to demonstrate that no weight loss occurs until 200°C , confirming the high thermal stability of Mn-BTC. At higher temperatures it is possible to highlight a weight loss equal to 44.07%. To explore the morphology of Mn-BTC we performed an analysis by scanning electron microscopy (SEM). The image, in **Figure 55E**, shows that the morphology of the final product of the reaction corresponds to nanoparticles with an approximate diameter of 100 nm. Comparing the acquired image with literature's reports, the Mn-BTC synthesized through conventional approaches exhibit a rod-like morphology with dimensions of several microns. This demonstrates that the shape of the final powder is influenced by the synthetic approach employed. The observations obtained from SEM analysis have been further corroborated by scanning transmission electron microscopy (STEM) investigations. STEM images

clearly show the formation of spherical nanoparticles after 48 h of reaction with diameters of approximately 100 nm. The inserts of **Figures 55G** present high resolution (HR) STEM and FFT images, revealing a regular crystalline structure with a d -spacing of 1.72 Å for Mn-BTC nanoparticles.

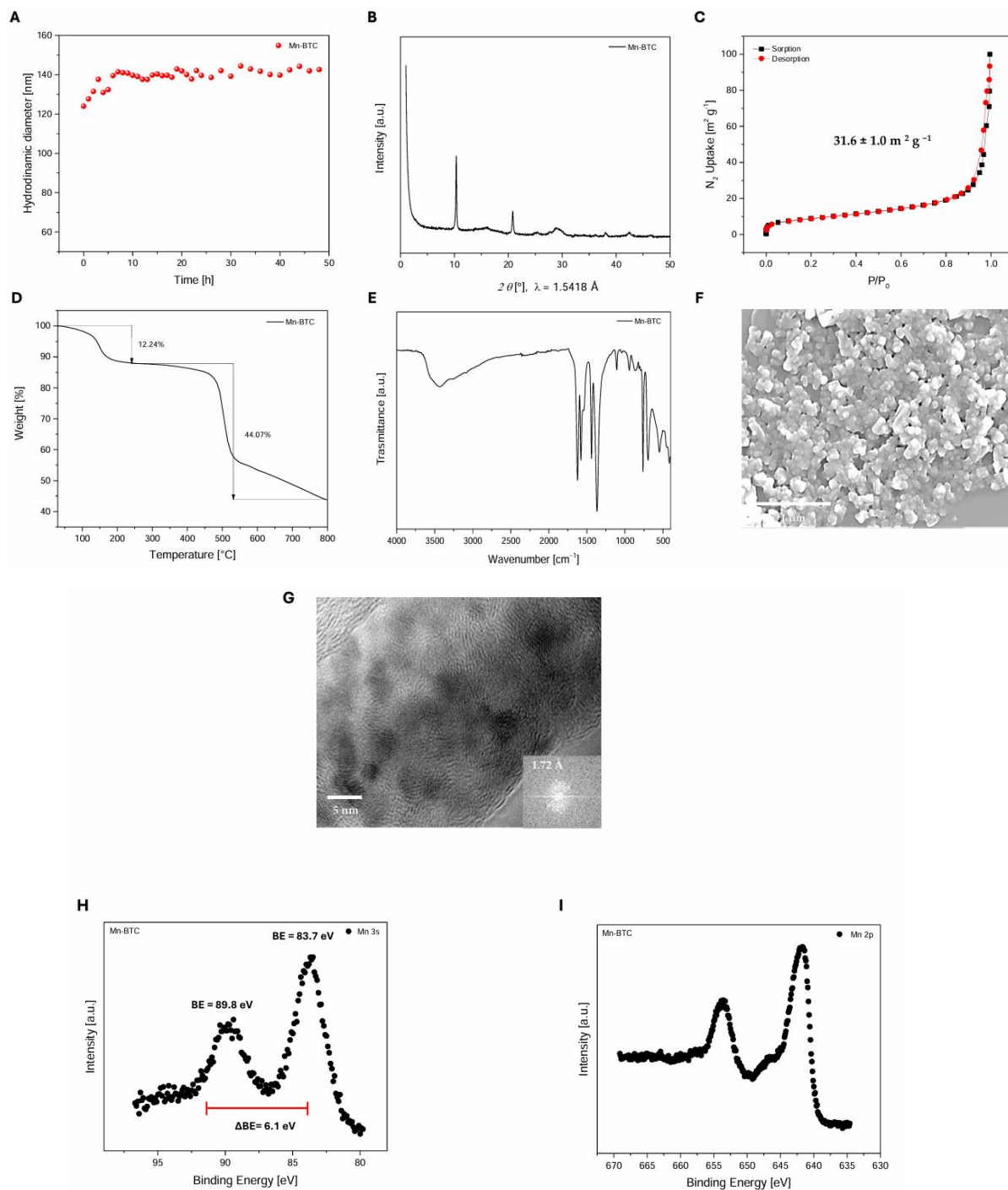


Figure 55. A) DLS kinetic profile of the Mn-BTC growth measured over 48 hours. B) pXRD profile of Mn-BTC. C) Nitrogen gas sorption (black square) and desorption (red dots) of Mn-BTC at 77K. D) TGA curve of Mn-BTC. E) DRIFT-FT IR spectra of Mn-BTC. F) SEM image at high magnification of Mn-BTC nanoparticles with a diameter of approximately 100 nm. G) STEM image of Mn-BTC and magnified HR-TEM image of the defined area with measured d -spacing of 1.72 Å. High-resolution XPS spectral profiles recorded for H) Mn 3s I) Mn 2p_{1/2} and 2p_{3/2}.

The isothermal nitrogen sorption measurement of Mn-BTC nanoparticles confirms the non-porosity of the system (**Figure 55C**). The data were fitted to the Brunauer-Emmett-Teller (BET) model, it was found that Mn-BTC had a BET surface area of $31.6 \pm 1.0 \text{ m}^2 \text{ g}^{-1}$. According to literature, the value of the surface area of this MOF depends on the pre-activation temperature of the sample. [144] In fact, the higher the temperature, the greater the surface value, therefore we performed two tests: the first by pre-activating the Mn-BTC at 120° C for the whole night, the data obtained fitted to the Brunauer-Emmett-Teller (BET) model provided a BET surface value equal to $25.0 \pm 1.0 \text{ m}^2 \text{ g}^{-1}$. With a pre-activation of the sample at a temperature of 300 °C degrees during the night the data obtained and fitted to the Brunauer-Emmett-Teller (BET) model showed an increase in the surface area value equal to $31.6 \pm 1.0 \text{ m}^2 \text{ g}^{-1}$. Furthermore, diffuse reflectance Fourier-transform mid-infrared spectroscopy was also used to confirm the chemical composition of Mn-BTC (**Figure 55E**). The observation of the characteristic peaks indicating the binding coordination between manganese ions and the trimesic acid which is indicated by the presence of the peaks at 1629 and 1579 cm^{-1} . Finally, an XPS study was carried out to confirm the state of oxidation of manganese in the final structure of Mn-BTC. **Figure 55H** and **55I** present the high-resolution XPS profiles recorded for manganese. The Mn 2p_{3/2} peak is centred at 641.7 eV. Additionally, the presence of a satellite, a unique

feature of manganese with an oxidation state (II), is evident. To confirm this oxidation state, we analysed high-resolution of Mn 3s peak that falls at 89.8 eV and 83.7 eV with a spin energy difference of 6.1 eV, which is consistent with manganese in the oxidation state (II). These results clearly indicate that after 48 hours of reaction, manganese in the Mn-BTC nanoparticles is present in the (II) oxidation state.

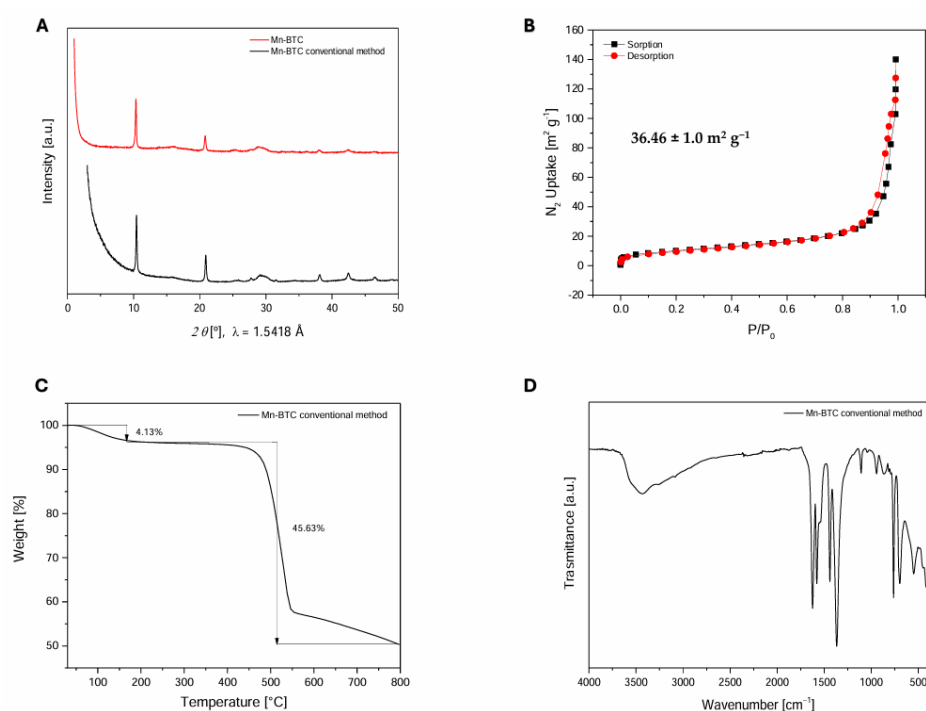


Figure 56. A) Comparison between pXRD of Mn-BTC synthesized with conventional methods (black) and 48 hours Mn-BTC nanoparticles (red). B) Nitrogen gas sorption (black square) and desorption (red dots) of Mn-BTC synthesized with conventional method measured at 77K. C) TGA curve of Mn-BTC synthesized with conventional method. D) DRIFT-FT IR spectra of Mn-BTC.

The data obtained from the characterization of Mn-BTC synthesized using conventional synthetic approaches is presented in **Figure 56**. X-ray diffraction for Mn-BTC obtained by a conventional synthetic approach was obtained and

compared with what was measured from the powder obtained via the micellar approach (**Figure 56A**). From the comparison it is possible to see how the two XRD patterns coincide perfectly highlighting that they are the same crystalline structure. The thermal stability of Mn-BTC was confirmed through thermal gravimetric analysis (TGA), as shown in **Figure 56C**. The analysis revealed no significant weight loss up to 200 °C. Beyond this temperature, a notable weight loss of 45.63% was observed. The isothermal nitrogen sorption measurement of Mn-BTC confirms the non-porosity of the system (**Figure 56B**). The results were fitted to the Brunauer-Emmet-Teller (BET) model, indicating a mesoporous material with a surface area of $36.46 \pm 1.0 \text{ m}^2 \text{ g}^{-1}$. Furthermore, diffuse reflectance Fourier-transform mid-infrared spectroscopy was also used to confirm the chemical composition of Mn-BTC (**Figure 56D**). Also, in this case it is possible to observe the characteristic band indicating the coordination of the bond between the manganese ions and the trimesic acid indicated by the presence of the peaks at 1629 and 1579 cm^{-1} .

16.3 Preparation of the substrate for electrochemical studies

Cu-CAT-1 and Mn-BTC crystals exhibit good electrochemical properties when synthesized using conventional approaches [129, 135]. In this project, we aim to investigate how changes in size and shape impact the electrochemical properties of these MOFs when synthesized through the micellar approach. A reduction in size can not only facilitate their processing but also potentially enhance their surface area, leading to improved electrochemical performance. Additionally, the morphology change could influence the material's conductivity and stability, offering new insights into the optimization of, for example, MOF-based supercapacitors. To prepare the substrates on which to perform the electrochemical measurements, solutions with progressively higher concentrations of Mn-BTC and Cu-CAT-1 nanoparticles were prepared. In parallel, a mixture consisting of 900.0 mg of activated carbon (CA) and 45.0 mg of carbon nanotube (CNT) was prepared, which were solubilized in 3.0 mL of deionized water and heated to 90 °C for a few minutes. The resulting product was treated with a mortar and pestle to remove any lumps, then 0.5 mL of the MOF we were interested in performing the electrochemical studies was added. The entire solution was heated for a few seconds in the microwave and then polyvinyl alcohol (PVA) was added as a binder. The mixture formed by CA/CNT/MOF was left under stirring for two hours at 50 °C in order to obtain a uniform solution which was finally deposited on an aluminium film and the solvent was left to evaporate, obtaining a substrate on which a uniform film made of CA/CNT/MOF is present (**Figure 57**). The obtained substrates were irradiated with the laser light. Mn-BTC was irradiated with a laser light of 80% power at a

wavelength of 700 nm, while in the case of Cu-CAT-1 the same treatment took place with a laser light of 90% power at a wavelength of 800 nm.

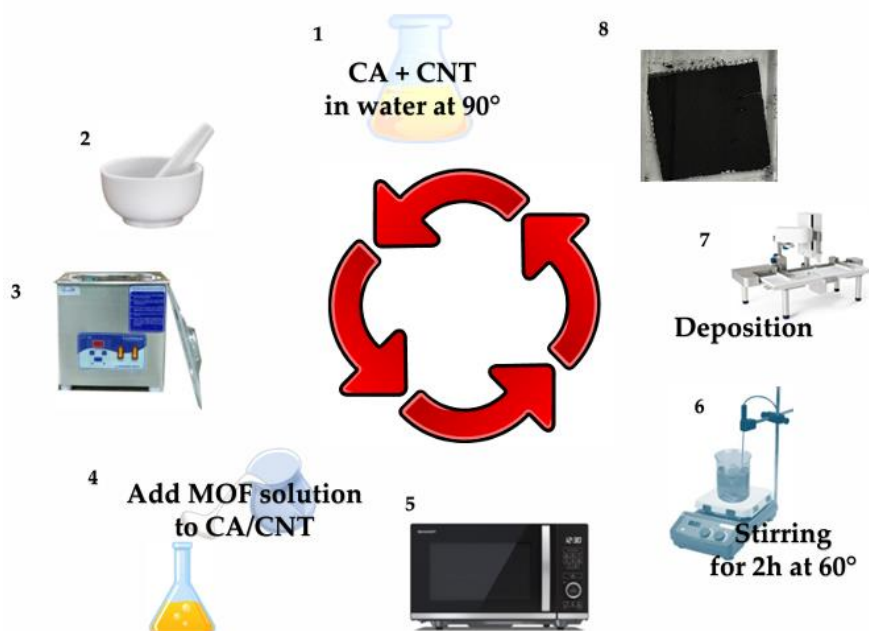


Figure 57. Schematic illustration showing the different steps followed during the synthesis of the electrodes used in supercapacitor applications.

To detect any changes in the oxidation state of these metals present on the substrates, after irradiation with laser light, high-resolution XPS analyses were conducted. **Figure 58A** presents the high-resolution XPS spectra recorded for copper. The Cu $2p_{3/2}$ orbit shows an asymmetric peak, consisting of a source peak at 934.10 eV and a satellite peak at 942.03 eV. The Cu $2p_{1/2}$ orbit shows a peak at 954.1 eV, with a spin energy separation of -19.8 eV, which is consistent with an oxidation state of (II) of the copper ions in the MOF. These results confirm that there was no variation between the oxidation state of copper of the Cu-CAT-1 in the powder versus the film. **Figures 58B** and **58C** present the high-resolution XPS spectra recorded for manganese. Mn $2p_{3/2}$ peak is centred at 641.4 eV which

is consistent with an oxidation state of (III) of the manganese. To confirm the oxidation state, we furthermore analysed high-resolution of Mn 3s peak that falls at 89.3 eV and 83.9 eV with a spin energy difference of 5.4 eV which is consistent with an oxidation state of (III) of the manganese. Therefore, these results indicate that following the construction of Mn-BTC based films, a variation in the oxidation state was noted, in fact the metal oxidizes from (II) to (III).

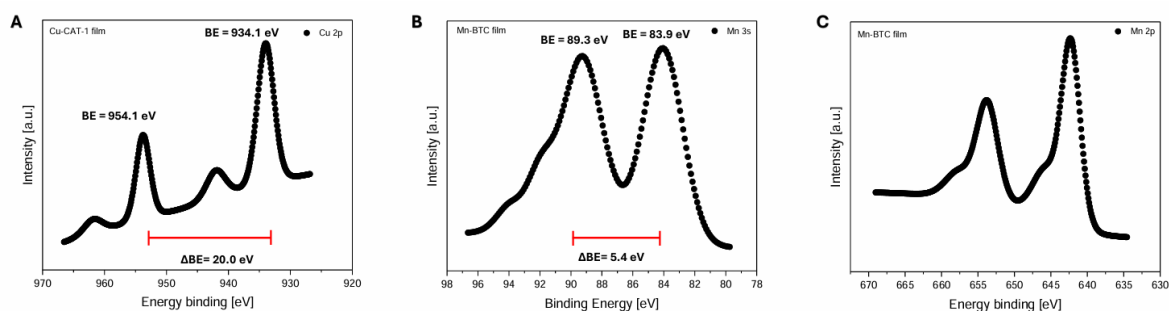


Figure 58. A) High-resolution XPS spectral profiles recorded for Cu-CAT-1 substrate Cu 2p_{1/2} and 2p_{3/2}. High-resolution XPS spectral profiles recorded for Mn-BTC substrate B), and Mn 2p_{1/2} and 2p_{3/2}, C) Mn 3s.

In this second part of the work, we will introduce iron-based MOFs, which are well-documented in the literature for their excellent properties as potential drug-carriers. Additionally, we will discuss, bimetallic MOFs, particularly those composed of biocompatible metals. Our interest in these types of MOFs aligns with the project's objective of exploring innovative drug delivery systems.

17. Iron based MOFs

A notable class of MOFs described in the literature utilize iron-based metal ions combined with organic ligands to form highly organized three-dimensional structures. These MOFs exhibit all of the previously discussed features and are of considerable interest due to their potential applications in various fields, including drug delivery, gas storage, catalysis, and gas separation. Well-known iron-based MOFs include MIL-100 Fe, MIL-88, MIL-53, Fe-BTC, and PCN-250. These compounds are composed of organic ligands with relatively simple structure, consisting of an aromatic ring substituted with several functional groups. Among the mentioned examples, only PCN-250 has an organic ligand with polyaromatic structure, it is synthesized using 3,3',5,5'-azobenzene tetracarboxylic acid and iron nitrate as metal ion. Iron-based MOFs can also include organic linkers with a more complex structure such as porphyrins. This possibility also facilitates the creation of organized structures that can have intermediate porosity depending on the structure of the porphyrin used. Regarding their chemical structure, porphyrins have a hydrophobic chemical structure consisting of an aromatic heterocyclic ring and a hydrophilic portion mainly due to the presence of peripheral functional groups present on the central core. These structures combined with high-valent metals allow the formation of chemically stable structures. MIL-141, which is composed of tetrakis (4-

carboxyphenyl) porphyrin as organic ligand and iron (III) chloride as metal ion, is an example of this type of MOF structures. [145] This example highlights the adaptability of iron-based MOFs and demonstrate how their structural design and ligand selection can be tailored for certain applications. Among the various applications of this class of materials, their use in catalysis is relevant. This is facilitated, by the presence of abundant active sites of unsaturated metals (CUS), such as Lewis's acid sites (LAS), and by their ease of separation and recovery from the reaction environment. In particular, the "MIL" series of iron-based MOFs (such as MIL-47, MIL-53, MIL-88, MIL-100, MIL-101) are employed as Lewis's acid catalysts. [146] Yu *et al.* for example used these Fe-MOFs as Lewis acid catalysts in ozonation reactions. [147] Furthermore, Fe-MOFs can also be employed as redox catalysts mainly involving the oxidation of alcohols, alkanes and olefins. [148] Furthermore, they can be employed as photocatalysts, it is possible to tune these materials by pre-designing or modifying the structure in order to possess photoactive sites for photocatalysis. Compared with other MOFs (such as those based on Ti^{4+} , Zr^{4+} , Zn^{2+} and Cu^{2+}), Fe-MOFs have a good response to visible light. The introduction of amine functional groups into photosensitive Fe-MOFs increases their absorption in the visible light region. [149] In addition to their use as catalysts, they can be used in gas storage; in fact, due to their high porosity and large surface areas, they are considered effective adsorbent materials for gases such as hydrogen, methane and carbon dioxide. [150] Finally, their application in the biological field is particularly significant. Fe-MOFs are non-toxic and biocompatible, which makes them safe for use in medical applications. Additionally, they exhibit great stability, enhancing their effectiveness in drug absorption and delivery. [151] These properties make Fe-MOFs highly suitable for targeted drug delivery systems, where precise and controlled release of therapeutic agents is crucial. Their ability to be easily

functionalized further broadens their potential in various biomedical applications, including imaging and diagnostics.

17.1 MIL-100 (Fe): synthesis, characterization and application in drug delivery

Feréy *et al.* first synthesized MIL-101 consisting of trichromic oxide as a ion metal and terephthalic acid as an organic binder, the acronym MIL used for this material refers to “Materials of the Institute Lavoisier”.[152] MILs consist of several types of organic linkers that can interact with other trivalent metal units, among which we find MIL-100 that can coordinate to several metals such as Fe, Sc, Al and V. Mesoporous iron(III) carboxylate, or MIL-100(Fe), has been the most widely studied MIL in recent years. Horcajada *et al.* first developed the synthesis of MIL-100(Fe) using a conventional synthetic approach through a Teflon-lined autoclave, employing one equivalent of iron (II) chloride as the metal ion, 0.66 equivalents of trimesic acid as the organic linker, 2 equivalents of hydrofluoric acid and 1.2 equivalents of nitric acid. The reaction was left for six days at 150° C and then brought to room temperature where washes with deionized water were performed, and an orange solid was obtained. [153-155] This work served as the initial step for developing and optimizing strategies for synthesizing MIL-100(Fe), including hydrothermal or microwave approaches. There is also another way to obtain MIL-100(Fe). For example, mechanochemical milling can be used to make it without the aid of HF or other solvents. MIL-100(Fe), like all MOFs, owes its stability to several factors that may depend on the reaction conditions, especially temperature, pH, and solvents. Furthermore, MIL-100(Fe) has a zeta potential value (ζ) which is a crucial stability parameter of the structure. ζ corresponds to the electrostatic repulsion force between neighbouring particles in a dispersion that have identical charges. Due to the resistance to aggregation, a high potential (positive or negative) is electrically stable. The ζ value of MIL-100 Fe, tested under neutral or slightly acidic conditions is typically between -10

and -40 mV. Based on this zeta potential value, MIL-100 (Fe) has a negative surface charge, which can affect its colloidal stability and interactions with other molecules or surfaces. The more negative the zeta potential value, the greater the electrostatic repulsion which has the effect of stabilizing any dispersion. [156]

Thanks to its large surface area (SBET $\sim 2000 \text{ m}^2 \text{ g}^{-1}$, $V_p \sim 1.2 \text{ cm}^3 \text{ g}^{-1}$), high porosity, stable and regular structure even in water and physiological environment, MIL-100 (Fe) has been widely studied for drug delivery applications. In fact, this structure allows to load large amounts of drugs (hydrophilic, hydrophobic or amphiphilic) and to control the release kinetics. It is obvious that, in addition to its excellent structural qualities, it should be taken into account that several preliminary studies have been carried out to evaluate the degree of cytotoxicity and tolerance, which have provided optimal results that make it suitable for use in therapeutic formulations. To load drugs into MOFs, there are 3 different approaches. The first is the direct encapsulation method and involves the existence of interactions, which can be covalent or non-covalent, between the pores of the MOF and the drugs. The second is the directed assembly approach that uses specific molecules or prodrugs that directly participate in the formation of the MOF structure by creating coordination bonds. The third approach is the post-synthesis technique that involves the insertion of drugs onto the outer surface of the MOF after its synthesis has taken place. According to recent research, drugs are encapsulated in MIL-100 (Fe) through a two-step encapsulation process that includes mechanochemically assisted encapsulation, impregnation and high-pressure methods. To ensure that the drug is successfully encapsulated in the porous matrix during the impregnation process, several parameters should be considered, such as drug concentration, solvent selection, drug solution temperature, agitation, hydrophobic/hydrophilic balance, etc. The type of solvent used during the impregnation process can affect

the drug encapsulation rate. MIL-100 (Fe) has Lewis sites with unsaturated Fe (III), favouring the formation of a coordination adduct with polar solvent molecules. The physicochemical properties of MOFs, especially the pore size and structural size of the drug, determine how well the drug is encapsulated using the impregnation process. There is a non-covalent interaction, such as π - π stacking, between the hydrophobic (organic linker) and hydrophilic (metal ions) moieties that support the encapsulation of drugs inside the porous structure. MIL-100 (Fe) has a strong binding site for guest molecules (called CUS) inside its structure that facilitates the entry of drugs, regardless of their structure, into the porous matrix even in the absence of solvent. With the help of solvents, drugs are encapsulated inside MOFs using strategies involving high pressure. [157] In contrast, without the use of solvents, drugs are encapsulated inside the porous structure via a mechanochemical approach. Further studies on the kinetics of drug release from MIL-100 (Fe) have been conducted, simulating physiological conditions of pH and temperature. Specifically, it was seen that there are two release phases: in the first phase, the molecules that are released are the more superficial ones that interact with MIL-100 (Fe) in a milder way, this phase has zero-order kinetics; in the second phase, the release of the more internal drug molecules occurs, that is, those that interact with the MOF in a stronger way and that lead to a slow collapse of the porous structure. [158-159]. In addition to its application in drug release, MIL-100 (Fe) is also used in catalysis, photocatalysis and water purification. [160-162]

17.2 MIL-53 (Fe): synthesis, characterization and application in drug delivery

MIL-53(Fe) is an iron-based MOF with a flexible structure, good stability, and low toxicity. [155-157] Due to its simplicity, the solvothermal approach is the most described synthetic method for this MOF. There are several synthesis approaches such as microwave-assisted, electrochemical and solvothermal. [163] Ferric (III) chloride is the metal node and terephthalic acid is the organic linker in MIL-53(Fe). The standard protocol described by Millange *et al.* was followed in the preparation of MIL-53(Fe). Equimolar amounts of HF, terephthalic acid, and iron chloride were combined in the solvent *N,N* dimethylformamide. After being moved to a Teflon-lined stainless-steel autoclave, the precursor solution was heated at 150 °C for three days. Subsequently, DMF was removed from the pores and the solution was washed with methanol and water and dried. The characterization of this material revealed that MIL-53(Fe) possesses a very small residual surface area and is microporous, with a pore diameter of 2 nm or less. Therefore, drugs that could be included in MIL-53(Fe) are limited, such as ibuprofen. [164] On the contrary, drugs that have a larger size require a mesoporous structure, with a pore diameter between 2 and 50 nm, to be included effectively, for this reason systems such as MIL-100(Fe) and MIL-101(Fe) are more appropriate. A study showed that only 16% and 7% of stavudine and progesterone were successfully incorporated into MIL-53 (Fe), respectively. In contrast, 80% of the administered paracetamol was seen to be released very rapidly, suggesting that 20% of the total payload was successfully incorporated into the pores. Obviously, even in this case it is always important to keep in mind the host-guest interactions that are established and that are also responsible for the release kinetics. Considering the release kinetics of paracetamol, it is possible

to note that if it is included in a microporous structure its complete release will occur after 6 days; on the contrary if it will be included in a mesoporous structure, such as MIL-100 (Fe), we would have a greater loading capacity of the drug, but shorter release times that can reach a maximum of 5 days for paracetamol. In conclusion, the primary advantage of using MIL-53 (Fe) as a drug carrier lies in its slow drug release, whereas MIL-100 (Fe) excels in its high loading capacity. These differences are attributed to their distinct crystal structure. [165] Among the different drugs that can be included in MIL-53 (Fe) we also find those used in cancer treatment, for example, doxorubicin [166], 5-fluorouracil [167] and oridonin [168]. In addition to being used as a potential drug carrier, MIL-53 (Fe) has shown also good photocatalytic properties. [169-170]

17.3 Doping of MOFs with second metals

Recent, studies on bimetallic organic frameworks have demonstrated that they possess additional functionalities compared to their monometallic counterparts. These bimetallic frameworks can exhibit modified architectures and characteristics compared to their monometallic counterparts. The metal used to dope the system is often added during the regular MOF synthesis process. Its equivalents can vary, so it could be equimolar, in excess, or less than the MOF's primary constituent metal. Bimetallic iron-copper MOFs have for example been fabricated as an efficient Fenton-type catalyst for the degradation of sulfamethazine. In fact, the doping with copper, as a second metal, created unique properties such as an improved the catalytic activity. [171] Among various MOFs, MIL-100 (Fe) is frequently doped with secondary metals, such as copper and cerium to enhance its properties. For example, this doping can significantly influence water adsorption performance. A recent study demonstrated the synthesis of cerium-doped MIL-100 (Fe) using a solvothermal approach. The inclusion of cerium notably increased the concentration of certain ions in water, particularly phosphate ions, compared to the corresponding MOF in which only iron is present in the structure. [172] The doping of MIL-100 (Fe) with cobalt represents a further example of synthesis of bimetallic systems. In this case the presence of cobalt, as a secondary metal, primarily results in an increase of the BET surface area of the entire system, respecting the monometallic, which is used to support ammonium sulphate in the esterification reactions of acids. In particular, the esterification reaction of oleic acid and methanol was studied using a catalytic support with the monometallic system formed only by MIL-100 (Fe) and the corresponding bimetallic system formed by iron and cobalt. What is evident is a higher yield of the product of the esterification reaction,

thanks to the greater presence of ammonium sulphate present on the bimetallic support, by virtue of the increase in its surface area, compared to the monometallic. [173] Titanium and aluminium can also be used in the doping of MIL-100 (Fe) and have the effect of promoting an increase in the mesoporosity of the system, which can represent an advantage especially in the use of these systems as drug-carriers. [174] The doping of MOFs with secondary metals does not always have positive effects on the structure and in the application field, indeed sometimes it can represent an obstacle or decrease the performance of a material. For example, MIL-53 (Fe) can be doped with metal cations such as lithium, sodium and potassium, this has the effect of influencing the photocatalytic properties of the entire system. Photocatalysis is influenced by factors such as the variation of electronic conductivity and the modification of the total surface area of the material. In the presence of these cations as secondary metals of MIL-53(Fe), the photodegradation efficiency of the system was analysed and it was found to be decreased compared to the corresponding monometallic system. [175] In conclusion, doping MOFs with secondary metals results in the variation of some characteristics of the system, which in most cases has a positive impact from the application point of view. For biomedical applications, it would be highly advantageous to generate MIL-100(Fe) and MIL-53(Fe) nanoparticles using biocompatible synthetic procedures, such as the micellar approach. Studying their biocompatibility and comparing it with the conventional microcrystalline powder typically obtained via standard synthetic methods would provide valuable insights into the potential of these materials in biotechnological applications. Furthermore, it would be of great interest to investigate whether the functionality of MIL-100(Fe) and MIL-53(Fe) nanoparticles can be improved by creating bimetallic nanoparticle structures through the incorporation of another biocompatible metal ion, such as

magnesium. For biomedical applications, it would be highly beneficial to generate MIL-100(Fe) and MIL-53(Fe) nanoparticles using biocompatible synthetic procedures, such as the micellar approach. Studying their biocompatibility and comparing it to the conventional microcrystalline powder typically obtained through standard synthetic methods would provide valuable insights on the potential of these materials in biotechnology applications. Additionally, it would be of great interest to investigate whether the functionality of MIL-100(Fe) and MIL-53(Fe) nanoparticles can be enhanced by creating bimetallic nanoparticle structures through the incorporation of another biocompatible metal ion, such as magnesium.

18. Materials and Methods

18.1 Chemical and reagents

Magnesium chloride anhydrous 99% and hexadecyltrimethylammonium bromide were supplied from ThermoFisher Scientific. Terephthalic acid, trimesic acid, iron (II) chloride tetrahydrate, iron (III) chloride hexahydrate, sodium dodecyl sulphate, trimesic acid, sodium hydroxide and absolute ethanol were supplied from Merck (Darmstadt, Germany). Aqueous solutions were prepared with Milli-Q water.

18.2 Instruments

See Paragraph 3.2.

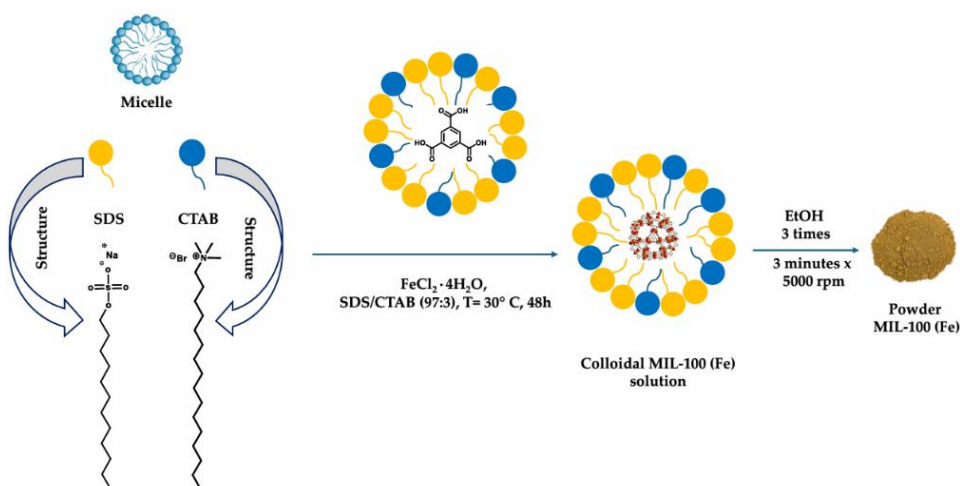
18.3 Synthesis of MIL-100 (Fe) nanoparticles

For the synthesis of this MOF a cationic system was prepared by mixing the cationic surfactant hexadecyltrimethylammonium bromide (CTAB) and sodium dodecyl sulphate (SDS) in an SDS/CTAB ratio of 97:3. The ratio has been optimized to promote the formation of micellar assemblies with lower curvature, thus facilitating the colloidal stabilization of MOF precursors, namely trimesic acid and iron (II) chloride tetrahydrate. Two distinct solutions have been prepared:

Solution A: Sodium hydroxide (40.2 mg; 1.00 mmol) is solubilized in 61.0 mL of a solution of SDS 0.1M; then trimesic acid is added (70.47 mg; 0.33 mmol) and only once the complete solubilization has occurred, 2.0 mL of a solution CTAB 0.1M are added.

Solution B: Iron (II) chloride tetrahydrate (100.0 mg; 0.50 mmol) is solubilized in 42.0 mL of a solution of SDS 0.1M and only once the complete solubilization is achieved is added 1.0 mL of a solution of CTAB 0.1 M.

Finally, solution A is then added to solution B drop-by-drop under stirring and the final solution is left at 30 °C for 48 hours, as illustrated in **Scheme 15**.



Scheme 15. Illustration of the micellar approach used to synthesize nanoscaled MIL-100 (Fe) particles and a picture of the final powder obtained.

After 48 hours 103.0 mL of absolute ethanol is added to the reaction, which allows the micelles that were responsible for the formation of MIL-100 (Fe) nanoparticles to burst. This produces a brown precipitate that must be thoroughly centrifuged three times (3 minutes x 5000 rpm) to eliminate the surfactants.

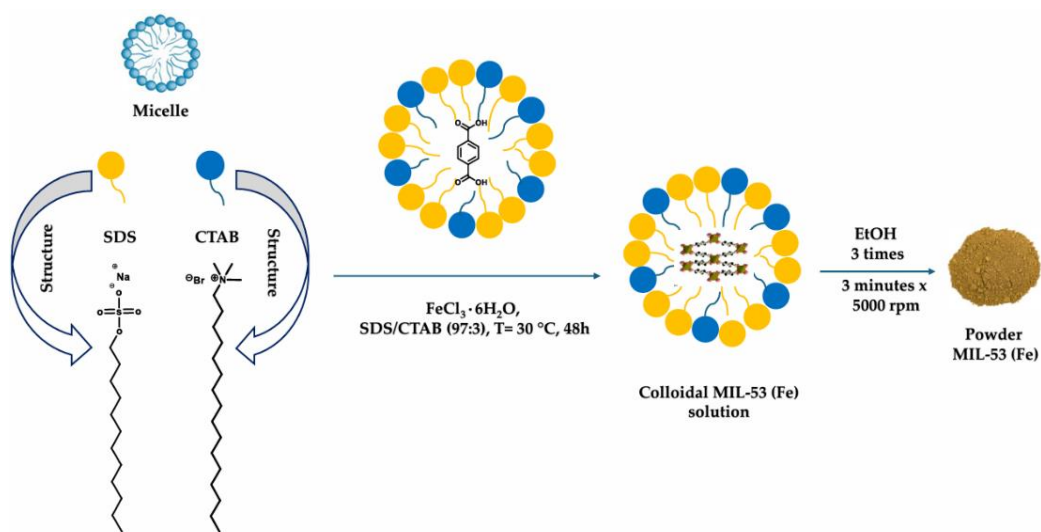
18.4 Synthesis of MIL-53 (Fe) nanoparticles

For the synthesis of this MOF, a cationic system was prepared by mixing CTAB and SDS in 3:97 ratio. The ratio has been optimized to promote the formation of micellar assemblies with lower curvature, thus facilitating the colloidal stabilization of MOF precursors, namely terephthalic acid and iron (III) chloride hexahydrate. Two distinct solutions have been prepared:

Solution A: Sodium hydroxide (40.2 mg; 1.00 mmol) is solubilized in 61.0 mL of a solution of SDS 0.1M; then terephthalic acid is added (55.71 mg; 0.33 mmol) and only once the complete solubilization has occurred, 2.0 mL of a solution CTAB 0.1M are added.

Solution B: Iron (III) chloride hexahydrate (135.97 mg; 0.50 mmol) is solubilized in 42.0 mL of a solution of SDS 0.1M, only once the complete solubilization is achieved 1.0 mL of a solution of CTAB 0.1 M is added.

Finally, solution A is then added to solution B drop-by-drop under stirring and the final solution is left at 30 °C for 48 hours, as illustrated in **Scheme 16**.



Scheme 16. Illustration of the micellar approach used to synthesize nanoscaled MIL-53 (Fe) particles and a picture of the final powder obtained.

After 48 hours 103.0 mL of absolute ethanol is added to the reaction, which allows the micelles that were responsible for the formation of MIL-53 (Fe) to burst. This produces a brown precipitate that must be thoroughly centrifuged three times (3 minutes x 5000 rpm) to eliminate the surfactants.

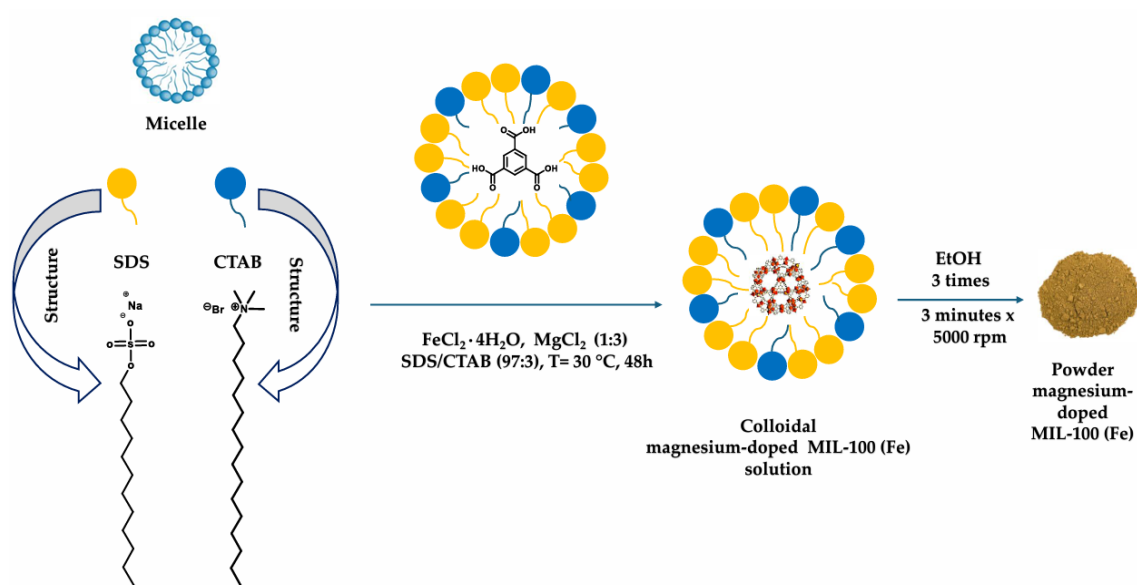
18.5 Synthesis of magnesium-doped MIL-100 (Fe) nanoparticles

For the synthesis of this MOF, a cationic system was prepared by mixing CTAB and SDS in 3:97 ratio. The ratio has been optimized to promote the formation of micellar assemblies with lower curvature, thus facilitating the colloidal stabilization of MOF precursors, namely trimesic acid and iron (II) chloride tetrahydrate. Two distinct solutions have been prepared:

Solution A: Sodium hydroxide (40.2 mg; 1.00 mmol) is solubilized in 61.0 mL of a solution of SDS 0.1M; then trimesic acid is added (70.47 mg; 0.33 mmol) and only once the complete solubilization has occurred, 2.0 mL of a solution CTAB 0.1M are added.

Solution B: Iron (II) chloride tetrahydrate (100.0 mg; 0.50 mmol) and magnesium chloride (142.81 mg; 1.50 mmol) are solubilized in 42.0 mL of a solution of SDS 0.1M and only once the complete solubilization is achieved 1.0 mL of a solution of CTAB 0.1 M is added.

Finally, solution A is then added to solution B drop-by-drop under agitation and the final solution is left at 30 °C for 48 hours, as illustrated in **Scheme 17**.



Scheme 17. Illustration of the micellar approach used to synthesize nanoscaled magnesium-doped MIL-100 (Fe) particles and a picture of the final powder obtained.

After 48 hours, 103.0 mL of absolute ethanol is added to the reaction, which allows the micelles that were responsible for the formation of magnesium-doped MIL-100 (Fe) to burst. This produces a brown precipitate that must be thoroughly centrifuged three times (3 minutes x 5000 rpm) to eliminate the surfactants.

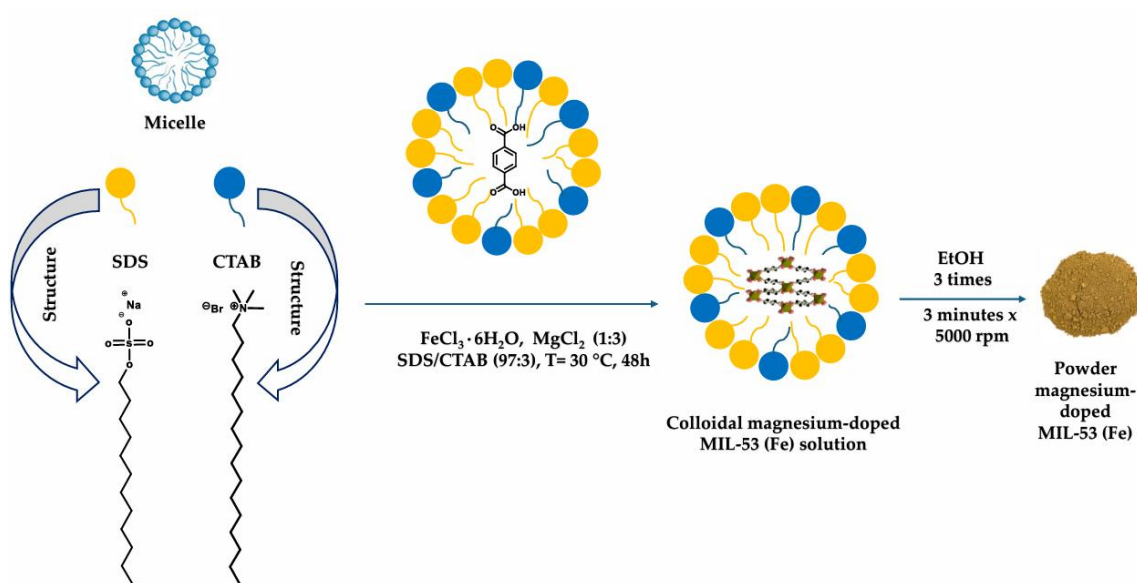
18.6 Synthesis of magnesium-doped MIL-53 (Fe) nanoparticles

For the synthesis of this MOF, a cationic system was prepared by mixing CTAB and SDS 3:97 ratio. The ratio has been optimized to promote the formation of micellar assemblies with lower curvature, thus facilitating the colloidal stabilization of MOF precursors, namely terephthalic acid and iron (III) chloride hexahydrate. Two distinct solutions have been prepared:

Solution A: Sodium hydroxide (40.2 mg; 1.00 mmol) is solubilized in 61.0 mL of a solution of SDS 0.1M; then terephthalic acid (55.71 mg; 0.33 mmol) is added and only once the complete solubilization has occurred, 2 mL of a solution CTAB 0.1M is added.

Solution B: Iron (II) chloride hexahydrate (135.97 mg; 0.50 mmol) and magnesium chloride (142.81 mg; 1.50 mmol) are solubilized in 42 mL of a solution of SDS 0.1M, only once the complete solubilization is achieved 1 mL of a solution of CTAB 0.1 M is added.

Finally, solution A is then added to solution B drop-by-drop under agitation and the final solution is left at 30 °C for 48 hours, as illustrated in **Scheme 18**.



Scheme 18. Illustration of the micellar approach used to synthesize nanoscaled magnesium-doped MIL-53 (Fe) particles and a picture of the final powder obtained.

After 48 hours 103.0 mL of absolute ethanol is added to the reaction, which allows the micelles that were responsible for the formation of magnesium-doped MIL-53 (Fe) to burst. This produces a brown precipitate that must be thoroughly centrifuged three times (3 minutes x 5000 rpm) to eliminate the surfactants.

19. Results and Discussion

At this stage of the thesis, we wanted to investigate whether it is possible to provide an experimental procedure not only to control the synthesis of MIL-100 (Fe) and MIL-53 (Fe) at the nanoscale, but also to obtain corresponding bimetallic systems by incorporating magnesium. First, the synthesis process to obtain MIL-100 (Fe) and MIL-53 (Fe) at the nanoscale was developed and optimized, these systems were characterized and compared with what is already known in the literature. Subsequently, we developed and optimized a synthetic method for the controlled doping of MIL-100 (Fe) and MIL-53 (Fe) nanoparticles with magnesium. Currently, studies are underway to evaluate the biocompatibility and/or toxicity of these materials to different cell lines, and to determine whether and how the presence of magnesium influences these properties.

19.1 Characterization of MIL-100 (Fe) nanoparticles

The X-ray diffraction pattern of MIL-100 (Fe) nanoparticles obtained through micellar approach were obtained and compared with the diffraction pattern reported in the literature (**Figure 59A**). The comparison shows that the two pattern coincide perfectly, indicating that they share the same crystalline structure. To elucidate the process underlying the formation of MIL-100 (Fe) nanoparticles in the cationic micellar medium, a time-lapse DLS experiment was performed (**Figure 59B**). The DLS data indicated that the mean hydrodynamic diameter of MIL-100 (Fe) nanoparticles progressively increases during the first 10 hours of reaction, subsequently reaching a steady state of around 35.0 nm. The thermal stability of MIL-100 (Fe) was probed by thermal gravimetric analysis (TGA), shown in **Figure 59D**, which demonstrate that no

weight loss occurs between 200° C and 300° C. Beyond this temperature a weight loss of 35.57% is observed. The isothermal nitrogen sorption measurement of MIL-100 (Fe) nanoparticles confirms the porosity of the system (**Figure 59C**). The results were fitted to the Brunauer-Emmet-Teller (BET) model, indicating a mesoporous material with a BET surface area of $1034.16 \pm 1.00 \text{ m}^2 \text{ g}^{-1}$. To explore the morphology of MIL-100 (Fe), we conducted scanning electron microscopy (SEM) measurement. From the obtained image, reported in **Figure 59E**, it is possible to see that the morphology of the final product of the reaction corresponds to nanoparticles with a diameter of approximately 100 nm. The observation obtained from SEM analysis have been further corroborated by scanning transmission electron microscopy (STEM) investigations. STEM images clearly show the formation of spherical nanoparticles after 48 hours of reaction with diameter of approximately 100 nm. The inserts of **Figure 59F** present high resolution (HR) STEM and FFT images, revealing a regular crystalline structure with a *d*-spacing of 2.79 Å for MIL-100 (Fe). By comparing the results obtained using the micellar approach with those reported in the literature, it is evident that the traditional solvothermal synthesis produces MIL-100(Fe) crystals of several microns in size. [176-177]

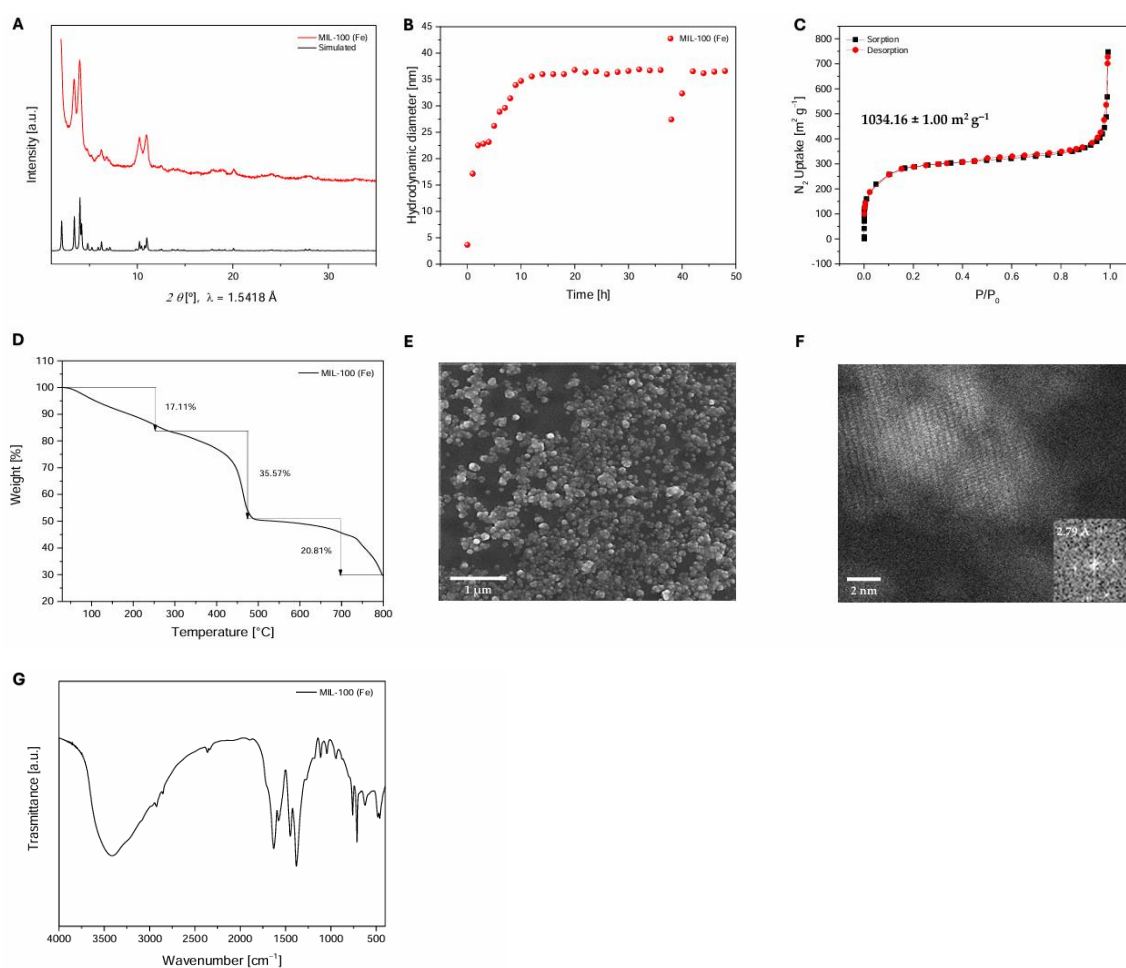


Figure 59. **A)** Comparison between pXRD simulated MIL-100 (Fe) (black) and pXRD 48 hours MIL-100 (Fe) nanoparticles (red). **B)** DLS kinetic profile of the MIL-100 (Fe) growth measured over 48 hours. **C)** Nitrogen gas sorption (black square) and desorption (red dots) of MIL-100 (Fe) measured at 77K. **D)** TGA curve of MIL-100 (Fe). **E)** SEM image at high magnification of MIL-100 (Fe) nanoparticles with a diameter of approximately 100 nm showing nanoparticles. **F)** STEM image of MIL-100 (Fe) and magnified HR-TEM image of the defined area with measured d -spacing of 2.79 Å. **G)** DRIFT-FT IR spectra of MIL-100 (Fe).

Furthermore, diffuse reflectance Fourier-transform mid-infrared spectroscopy was also used to confirm the chemical composition of MIL-100 (Fe), see **Figure 59G**. The broad peak around 3000 cm^{-1} is attributed to the -OH of carboxylate

groups that are not coordinated to the metal centre, possibly due to incomplete deprotonation of some carboxyl groups, or it can be assigned to free or bound water present in the structure. The coordination between iron and oxygen is shown by peaks falling in the range between 650 cm^{-1} , 622 cm^{-1} , 482 cm^{-1} and 460 cm^{-1} and 400 cm^{-1} . If we compared the FT-IR values that we obtained with those reported in the literature confirm that the obtained spectra correspond to that of MIL-100 (Fe). [178] Finally, a measurement of MIL-100 (Fe) ζ was performed. Starting from a solution of MOF in water at a known concentration of 1 mg/mL , a 10-fold dilution was performed, and the potential value was measured, which gave a value of -46 mV . The same measurement was performed on a solution of MOF in PBS at the same concentration and dilution factor, giving a value of -3 mV . Different values for MIL-100 (Fe) Z potential are reported in the literature, generally between -20 and -40 mV , but sometimes they can deviate from this range depending on pH or ionic strength variations. [179] The synthesis of MIL-100 (Fe) was evaluated applying the same synthetic approach, but with a different metal precursor's oxidation state. By varying the metal precursor in the synthesis of MIL-100 (Fe), we noted a variation in the properties of the final product. If ferric (III) chloride hexahydrate were used instead of ferrous (II) chloride tetrahydrate, we would obtain a final product with a different structure. In fact, by comparing the crystalline profile in the latter case with respect to the MIL-100 (Fe) obtained with iron (II), **Figure 60A**, we can note that not all peaks coincide and that they are less defined. Furthermore, a DLS measurement was performed on the reaction mixture, reported in **Figure 60B**, which showed a progressive increase in the hydrodynamic diameter over 48 hours without ever reaching a plateau, as occurs in the case of using MIL-100 (Fe) using the iron (II) precursor.

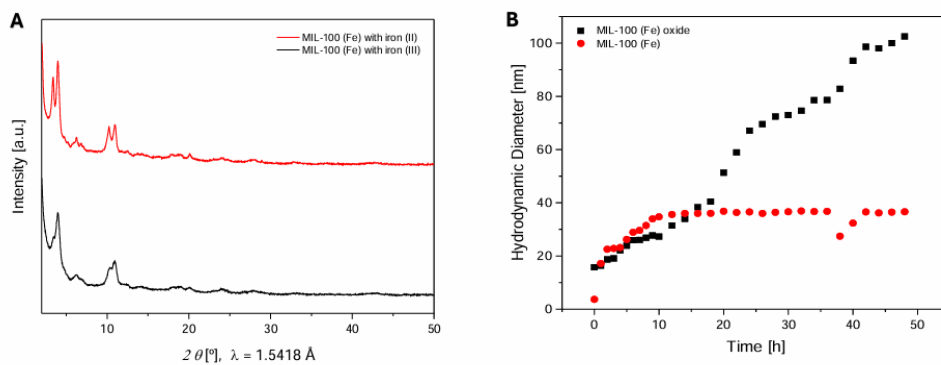


Figure 60. **A)** Comparison between the pXRD of MIL-100 (Fe) synthesized with iron (II) (red) and pXRD of iron (III) (black). **B)** Comparison of the DLS kinetic profiles of MIL-100 (Fe) generated with iron (II) (red) and with MIL-100 with iron (III) (black).

19.2 Characterization of magnesium-doped MIL-100 (Fe) nanoparticles

To synthesize the magnesium-doped MIL-100 (Fe), a synthetic protocol was developed and optimized. Several experiments were conducted, varying the ratio of equivalents between iron and magnesium. In particular, we started from a condition of 1:1 equivalence between the two metals, to then increase the number of equivalents of magnesium bringing it to 1:3 and 1:10 respectively. In conditions of 1:1 and 1:3, a stable product was obtained that did not present significant variations compared to MIL-100 (Fe); while increasing the ratio up to 1:10, it was noted that the product obtained showed a significantly lower stability. Using techniques such as XPS, SEM-EDX and TEM-EDX, we were able to confirm the presence of magnesium within the samples obtained using the 1:3 ratio. From the comparison between the X-ray diffraction profile obtained from MIL-100 (Fe) and the corresponding magnesium-doped system, reported in **Figure 61A**, no differences in terms of crystalline peaks were highlighted. The same is true from the comparison between diffuse reflectance Fourier-transform mid-infrared spectroscopy of the two systems reported in **Figure 61B**, where no signal shifts due to the presence of magnesium are evident, compared to the system where only iron is present. The isothermal nitrogen sorption measurement of magnesium-doped MIL-100 (Fe) confirms the mesoporosity of the system (**Figure 61C**). The data were fitted to the Brunauer-Emmett-Teller (BET) model, it was found that magnesium-doped MIL-100 (Fe) has a BET surface area of $1016.70 \pm 1.00 \text{ m}^2/\text{g}^{-1}$. A thermogravimetric analysis (TGA) was performed to examine the chemical and physical characteristics of the final product. From the TGA data obtained and shown in **Figure 61D**, it is possible to demonstrate that beyond 200°C there is a weight loss of 28.84%, confirming the high thermal

stability of magnesium-doped MIL-100 (Fe). To explore the morphology of magnesium-doped MIL-100 (Fe), we performed an analysis by scanning electron microscopy (SEM). As shown in **Figure 61E**, it is possible to see that the morphology of the obtained product corresponds to nanoparticles with a diameter of approximately 100 nm. The observation obtained from SEM analysis has been further corroborated by scanning transmission electron microscopy (STEM) investigations. STEM images clearly show the formation of spherical nanoparticles after 48 hours of the start of the reaction with a diameter of approximately 100 nm. The inserts of **Figure 61F** present high resolution (HR) STEM and FFT images, revealing a regular crystalline structure with a d -spacing of 2.12 Å. From the results of all these chemical and morphological analyses it is possible to highlight how the presence of magnesium does not significantly influence the structure of the system compared to the monometallic MIL-100 (Fe).

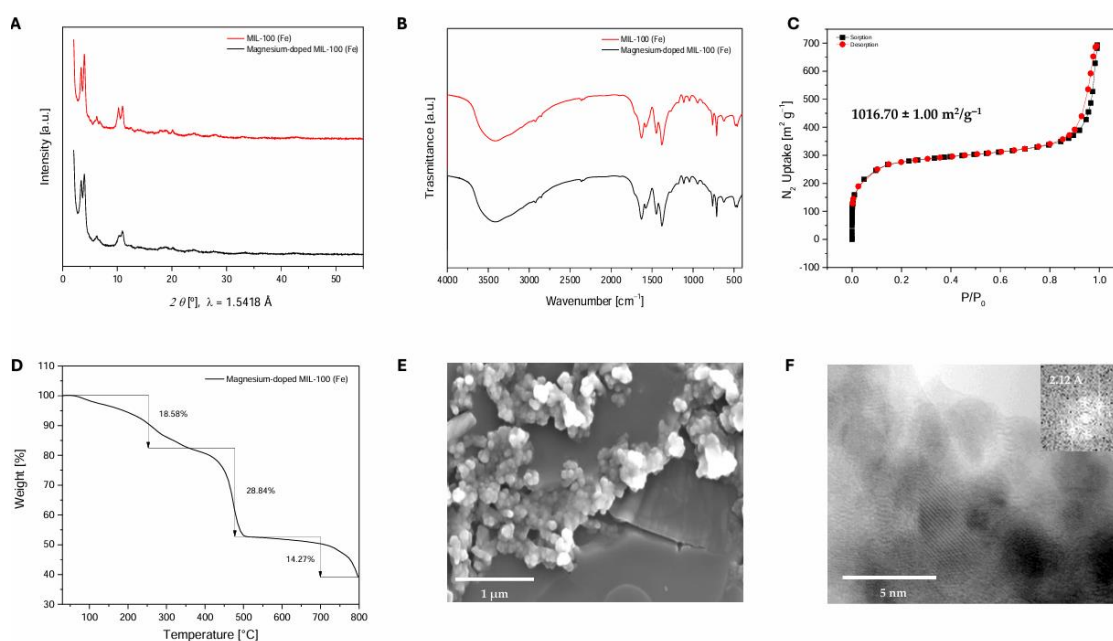
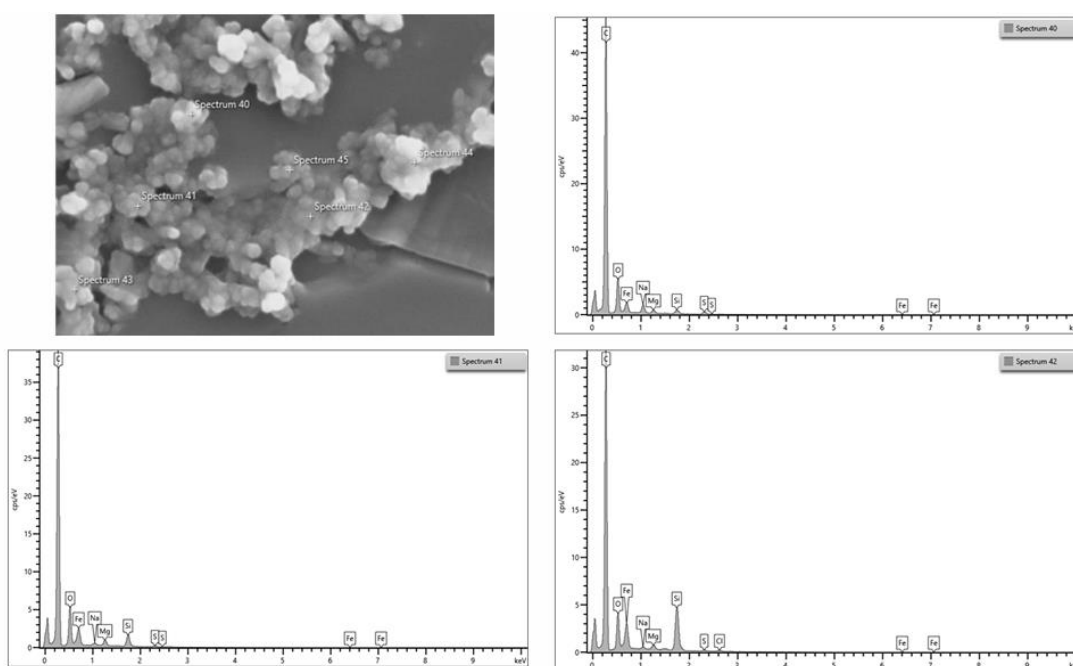


Figure 61. **A)** Comparison between the pXRD of MIL-100 (Fe) (red) and magnesium-doped MIL-100 (Fe) (black). **B)** Comparison of the DRIFT-FT-IR spectra of the MIL-100 (Fe) (red) with magnesium-doped MIL-100 (Fe) nanoparticles (black). **C)** Nitrogen gas

sorption (black square) and desorption (red dots) of magnesium-doped MIL-100 (Fe) at 77K. **D**) TGA curve of magnesium-doped MIL-100 (Fe). **E** SEM image at high magnification of magnesium-doped MIL-100 (Fe) showing nanoparticles with a diameter of approximately 100 nm. **F**) STEM image of magnesium-doped MIL-100 (Fe) and magnified HR-TEM image of the defined area with measured d -spacing of 2.12 Å.

The morphology and element composition of the magnesium-doped MIL-100(Fe) nanoparticles were characterized using SEM-EDX as shown in **Figure 62**. The spectra in **Figure 62** confirms the presence of carbon, oxygen, iron and magnesium in the magnesium-doped MIL-100 (Fe) nanoparticles.



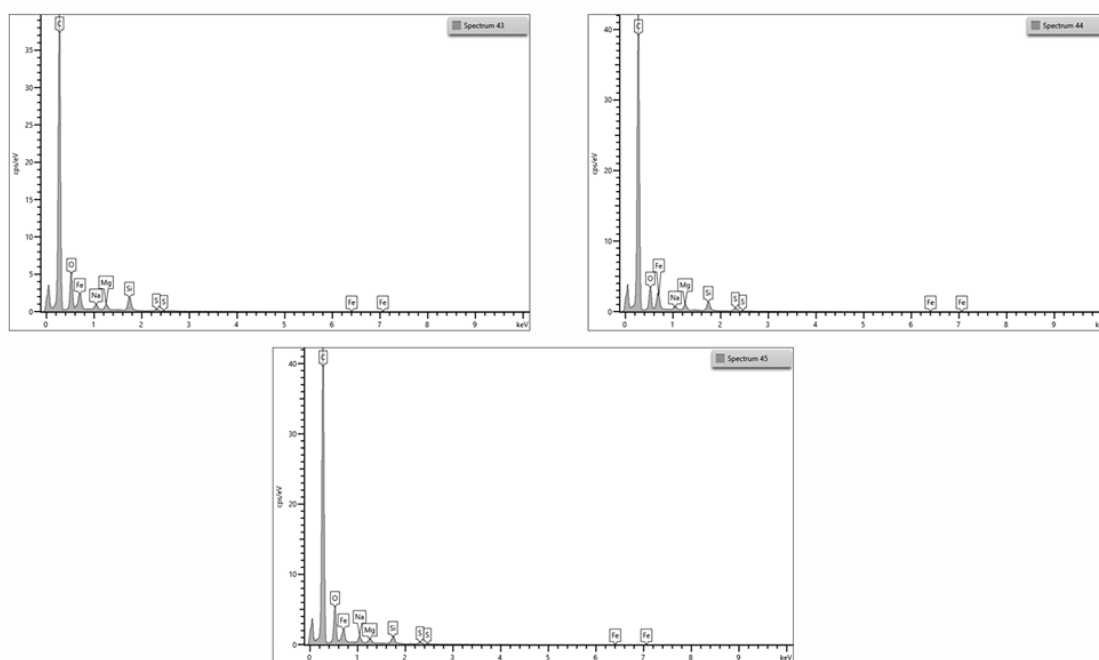


Figure 62. SEM image of the sample where SEM-EDX analysis was performed. The image shows magnesium-doped MIL-100 (Fe) nanoparticles. As shown in the SEM image, five random spots were measured, revealing the presence of carbon, oxygen, iron and magnesium.

Furthermore, a high-resolution XPS study was conducted to confirm the oxidation state of iron and the presence of magnesium in the final magnesium-doped MIL-100 (Fe) nanoparticles. **Figure 63A** presents the high-resolution XPS profiles recorded for iron. The Fe 2p_{3/2} orbit show an asymmetric peak, consisting of a source peak at 710.8 eV, which is consistent with the value reported in the literature corresponding to iron (III) oxide. **Figure 63B** presents the high-resolution XPS profiles recorded for magnesium. The Mg 1s spectral profile revealed the presence of a peak at 1304.0 eV, which correspond exactly to the value reported in the literature.

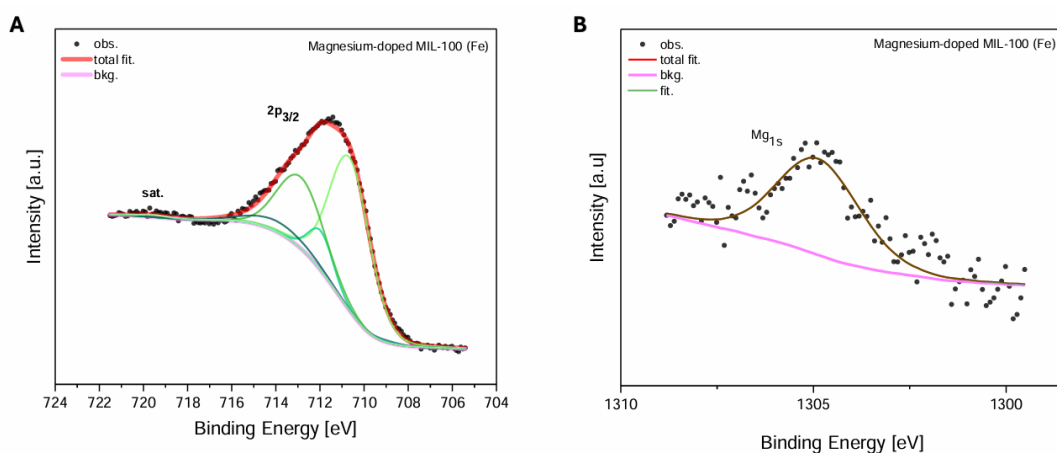


Figure 63. High-resolution XPS spectral profiles recorded for **A)** Fe $2p_{3/2}$ and **B)** Mg $1s$.

Finally, a TEM-EDX analysis was performed to further confirm the presence of magnesium in the system, see **Figure 64**. Energy dispersive X-ray spectroscopy (EDX) reveals the distribution of elements constituting the magnesium-doped MIL-100 (Fe) nanoparticles and confirming the presence of carbon, oxygen, iron and magnesium.

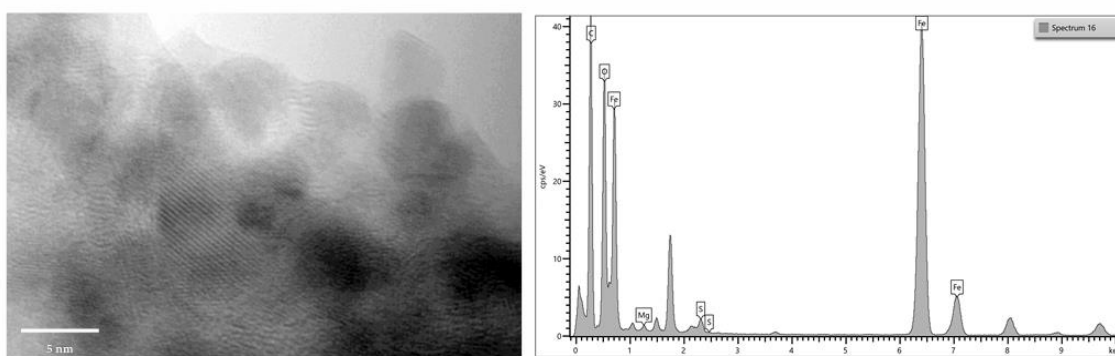


Figure 64. TEM-EDX images magnesium-doped MIL-100 (Fe) nanoparticles indicating their composition which includes carbon, oxygen, iron and magnesium.

19.3 Characterization of MIL-53 (Fe) nanoparticles

We measured X-ray diffraction of MIL-53 (Fe) nanoparticles obtained through the micellar approach and we compared it with the simulated one reported in the literature. [161] As shown in **Figure 65A**, the comparison highlights that the peaks do not coincide. Therefore, the product obtained does not appear to be MIL-53 (Fe). To elucidate the processes underlying the formation of MIL-53 (Fe) nanoparticles in the micellar medium, a time-laps DLS experiment was performed as reported in **Figure 65B**. DLS indicated that the mean hydrodynamic diameter of MIL-53(Fe) increases during the first hours of reaction and then reached a steady state at around 56.0 nm. The isothermal nitrogen sorption measurement of MIL-53 (Fe) nanoparticles confirms the porosity of the system. However, analysis of the graph shown in **Figure 65C** reveals that the curve's trend is not regular, probably due to structural defects. The data were fitted to the Brunauer-Emmett-Teller (BET) model, it was found that MIL-53 (Fe) nanoparticles had a BET surface area of $508.95 \pm 19.32 \text{ m}^2 \text{ g}^{-1}$. The thermal stability of MIL-53 (Fe) was tested employing thermal gravimetric analysis (TGA), shown in **Figure 65D**, which demonstrate that the MIL-53 (Fe) nanoparticles have good thermal stability up to 200° C. At higher temperatures there is in fact a significant weight loss equal to 36.07%. To explore the morphology of MIL-53 (Fe) we performed a scanning electron microscopy (SEM) analysis. As shown in **Figure 65E** it is possible to see that the morphology of the obtained product corresponds to nanoparticles with a diameter of approximately 100 nm. The observation obtained from SEM analysis have been further corroborated by scanning transmission electron microscopy (STEM) measurements. STEM images show a spherical-like shape, although it is not perfectly regular. The inserts of **Figure 65F** reveals the presence of crystalline fringes inside the structure with a *d*-spacing of

2.59Å. Furthermore, diffuse reflectance Fourier transform mid-infrared spectroscopy was also used to confirm the presence of the characteristic bands indicating the binding between iron and terephthalic acid is indicated by the presence of the peaks falling in the range between 400 and 650 cm^{-1} , specifically at 622, 482 and 460 cm^{-1} (Figure 65G).

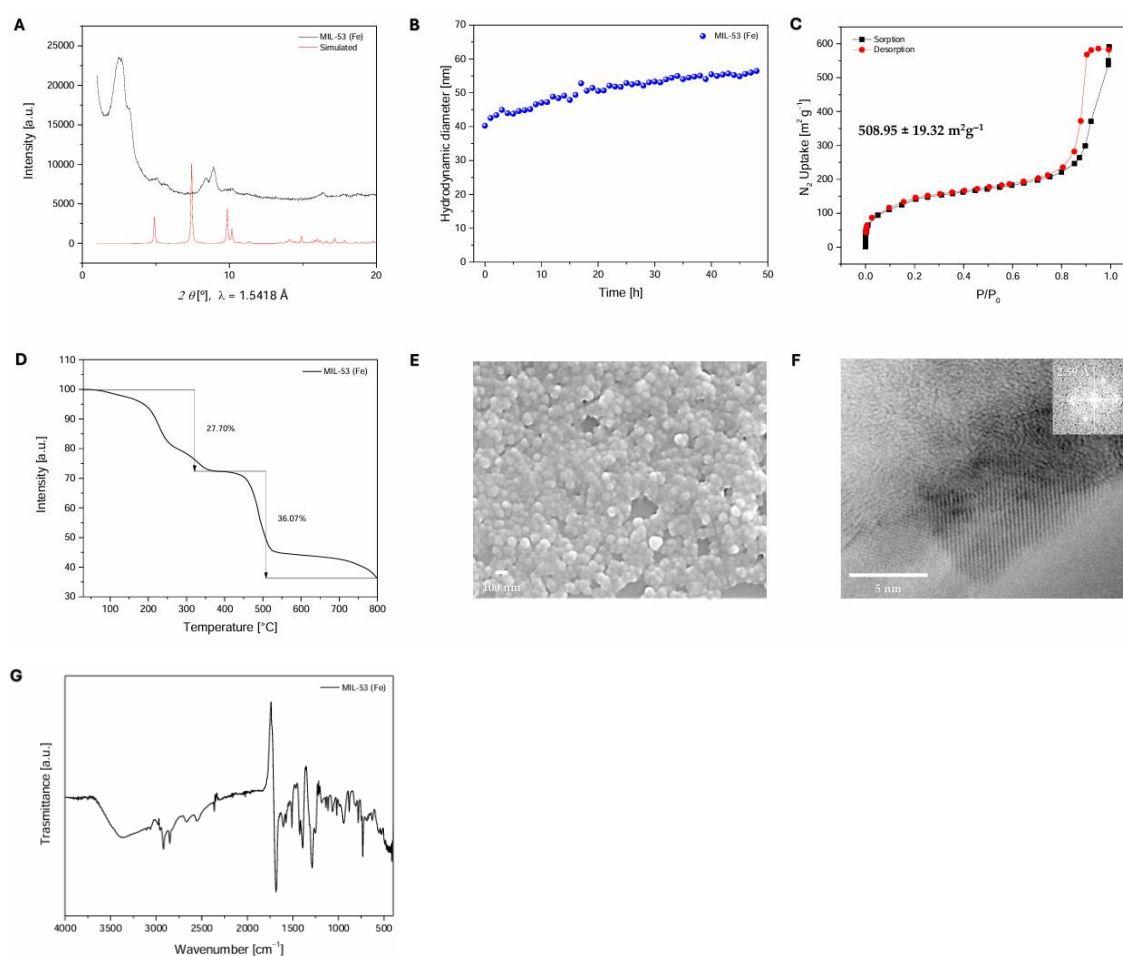


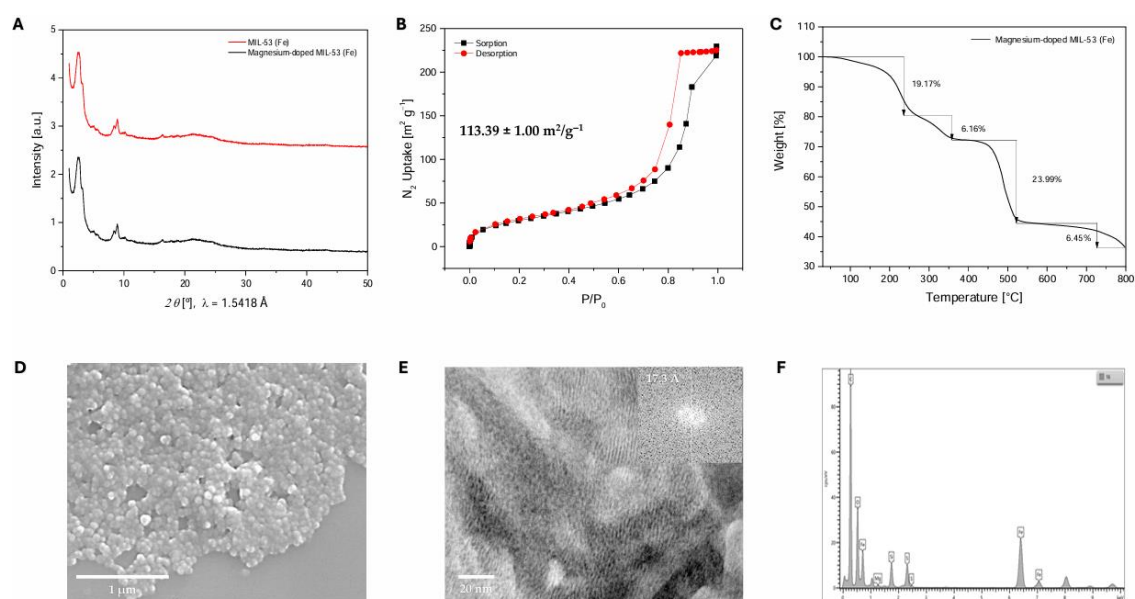
Figure 65. A) Comparison between pXRD of MIL-53 (Fe) (black) and the simulated (red). B) DLS kinetic profile of MIL-53 (Fe) growth measured over 48 hours. C) Nitrogen gas sorption (black square) and desorption (red dots) of MIL-53 (Fe) measured at 77K. D) TGA curve of MIL-53 (Fe). E) SEM image at high magnification of MIL-53 (Fe) nanoparticles with a diameter of approximately 100 nm. F) STEM image of MIL-53 (Fe)

and magnified HR-TEM image of the defined area with measured d -spacing of 2.59 Å;
G) DRIFT-FT-IR spectra of the MIL-53 (Fe).

19.4 Characterization of magnesium-doped MIL-53 (Fe) nanoparticles

For the synthesis of magnesium-doped MIL-53 (Fe) nanoparticles, the same optimized synthetic protocol described in **Section 18.5** is applied. Using techniques such as XPS and TEM-EDX, we were able to confirm the presence of magnesium within the magnesium-doped MIL-53 (Fe) nanoparticles, which were also synthesized using a 1:3 ratio of Fe to Mg. From the comparison between the X-ray diffraction profile obtained from MIL-53 (Fe) and the corresponding magnesium-doped system, no differences in terms of crystalline peaks are highlighted (see **Figure 66A**). The isothermal nitrogen sorption measurement of magnesium-doped MIL-53 (Fe) nanoparticles confirms the mesoporosity of the system. However, analysis of the graph reported in **Figure 66B** reveals an irregular curve trend, likely due to defects present in the structure. The data were fitted to the Brunauer-Emmett-Teller (BET) model, it was found that magnesium-doped MIL-53 (Fe) nanoparticles has a BET surface area of $113.39 \pm 1.00 \text{ m}^2/\text{g}^{-1}$. A thermogravimetric analysis (TGA) was performed to examine the chemical and physical characteristics of the final product. From the TGA data, reported in **Figure 66C**, it is possible to demonstrate that beyond 200°C there is a weight loss of 23.99%, confirming the high thermal stability of magnesium-doped MIL-53 (Fe) nanoparticles. To explore the morphology of magnesium-doped MIL-53 (Fe) nanoparticles we performed an analysis by scanning electron microscopy (SEM), see **Figure 66D**. From the obtained data, it is possible to see that the morphology of magnesium-doped MIL-53 (Fe) powder corresponds to nanoparticles with a diameter of approximately 100 nm. The observation obtained from SEM analysis have been further corroborated by scanning transmission electron microscopy (STEM) investigations. STEM images clearly

show the formation of spherical nanoparticles 48 hours after the start of the reactions, where the nanoparticle's diameters were approximately 100 nm. The inserts of **Figure 66E** present high resolution (HR) STEM and FFT images, revealing a regular crystalline structure with a *d*-spacing of 17.3 Å. From the results of all these chemical-morphological analyses it is possible to highlight how the presence of magnesium does not significantly influence the structure of the system compared to the monometallic MIL-53 (Fe) nanoparticles. Therefore, a TEM-EDX analysis was performed to further confirm the presence of magnesium in the system. Energy dispersive X-ray spectroscopy (EDX), as shown **Figure 66F**, reveals the chemical composition within the magnesium-doped MIL-53 (Fe) nanoparticles confirming the presence of carbon, oxygen, iron and magnesium.



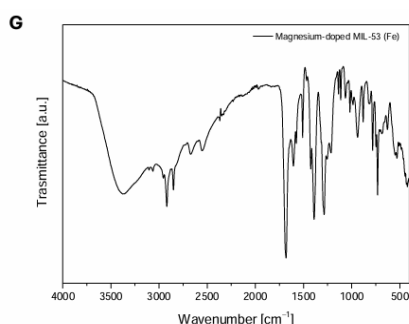


Figure 66. **A)** Comparison between pXRD of magnesium-doped MIL-53 (Fe) nanoparticles (black) and MIL-53 (Fe) (red). **B)** Nitrogen gas sorption (black squares) and desorption (red dots) of magnesium-doped MIL-53 (Fe) at 77K. **C)** TGA curve magnesium-doped MIL-53 (Fe). **D)** SEM image at high magnification of magnesium-doped MIL-53 (Fe) nanoparticles with a diameter of approximately 100 nm. **E)** STEM image of magnesium-doped MIL-53 (Fe) and magnified HR-TEM image of the defined area with measured d -spacing of 17.3 Å. **F)** TEM-EDX spectrum of magnesium-doped MIL-53 (Fe) nanoparticles indicating their composition which includes carbon, oxygen, iron and magnesium. **G)** DRIFT-FT-IR spectra of the magnesium-doped MIL-53 (Fe).

Furthermore, diffuse reflectance Fourier-transform mid-infrared spectroscopy was also used to confirm the presence of the functional groups (**Figure 66G**). The observation of the characteristic peaks indicating the binding coordination between iron and terephthalic acid is indicated by the presence of the peaks falling in the range between 400 and 650, specifically at 622, 482 and 460 cm^{-1} .

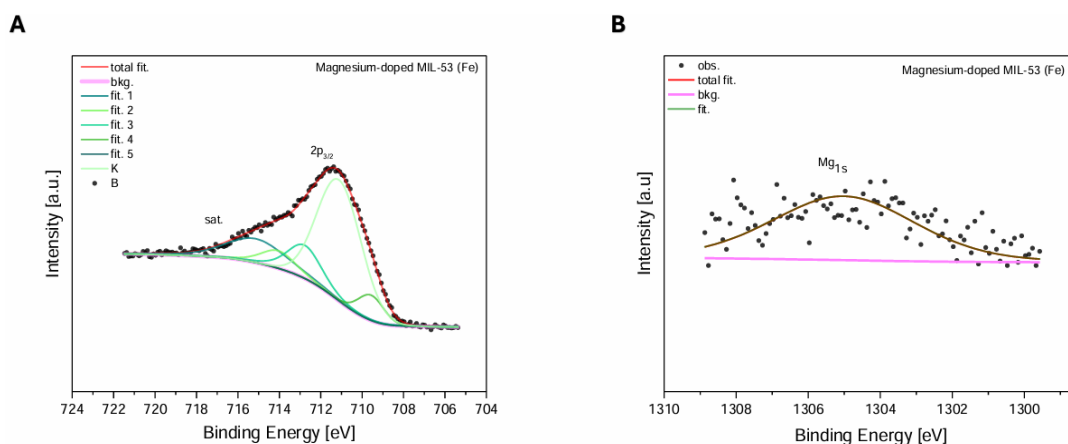


Figure 67. High-resolution XPS spectral profiles recorded for **A)** Fe $2p_{3/2}$ and **B)** Mg 1s.

Furthermore, a high-resolution XPS study was conducted to confirm the oxidation state of iron and the presence of magnesium in the final structure of magnesium-doped MIL-53 (Fe) nanoparticles. **Figure 67A** presents the high-resolution XPS profiles recorded for iron. The iron $2p_{3/2}$ orbit show an asymmetric peak, consisting of a source peak at 711.3 eV, which is consistent with the value reported in the literature corresponding to iron (III) oxide. **Figure 67B** presents the high-resolution XPS profiles recorded for magnesium. The Mg 1s spectral profile revealed the presence of a peak at 1305.6 eV, which correspond exactly to the value reported in the literature.

20. Conclusions and future perspectives

The development and optimization of a micellar based synthetic approach has enabled the synthesis of multiple MOFs with nanoscale dimensions. The primary benefit of this method is the use of aqueous solvents, which promotes eco-sustainability, reduces environmental impact, and allows for MOF synthesis at room temperature and atmospheric pressure. Most importantly, this approach enables a control synthesis of MOFs at the nanoscale, a feat not achievable with conventional solvothermal methods. For the synthesis of Cu-CAT-1, a cationic model was developed using the surfactant CTAB. In the presence of the anionic surfactant, SDS, the structural properties are altered, since this surfactant remains trapped in the MOF structure. Conversely, a catanionic system has been developed and optimized for the synthesis of Mn-BTC, MIL-100 (Fe) and MIL-53 (Fe) nanoparticles. As indicate above, the optimal SDS/CTAB ratio of 97:3 was used for these synthesis. Thanks to the use of this catanionic system it was possible to obtain structures that mimic the typical characteristics of these MOFs produced using standard synthetic protocols, such as good crystallinity, large surface area and excellent thermal stability. A thorough characterisation was carried out from a chemical and morphological perspective, and the outcomes were compared to those reported in the literature. Using the micellar approach, it is possible to obtain a direct control of the synthesis and growth of the considered MOFs, otherwise impossible with conventional approaches. In fact, using the micellar approach, we obtained nanoparticles with a diameter lower than or equal to 100 nm, alternatively if we used conventional methods, we would obtain fibres or crystals of a few microns. This decrease in size is advantageous for their processing, which could favour the generation of highly efficient electrodes for supercapacitor application and nanoscaled drug delivery

agents. For instance, we are currently evaluating the electrochemical properties of Cu-CAT-1 and Mn-BTC nanoparticles, comparing them to the electrochemical performance of microcrystalline powders of these MOFs produce via conventional synthetic methods reported in the literature. It is known that Cu-CAT-1 obtained through the conventional approach presents good electrochemical properties, the same is true for Mn-BTC, even if in the latter case it is reported in the literature that this does not present a high electrochemical efficiency as in the case of Cu-CAT-1. If we can enhance the electrochemical performance of Cu-CAT-1 and Mn-BTC nanoparticles, our next objective will be to fabricate an asymmetric supercapacitor. In this configuration, Cu-CAT-1 would serve as the negative electrode and Mn-BTC as the positive electrode. Achieving this could lead to the development of high-performance supercapacitors, leveraging the unique properties of these materials.

Additionally, we also synthesized MIL-100 (Fe) and MIL-53 (Fe) nanoparticles, using a micellar approach. This method also proved effective for generating bimetallic nanoscale MOF crystals, such as magnesium-doped MIL-100 (Fe) and MIL-53 (Fe) nanoparticles. The bimetallic systems were characterized chemically and morphologically, with techniques confirming the presence of the magnesium in the structure. The goal in this case is to evaluate the biocompatibility and toxicity of MIL-53 (Fe) and MIL-100 (Fe) nanoparticles to different cell lines. While it is well-documented, that these systems are used as drug-carriers, the real advantage of this research lies in utilizing nanoparticles that can penetrate cells. Finally, we aim to determine how the presence of a secondary metal, magnesium, can influence the biocompatibility and toxicity.

21. References

- [1] D. Maspoch, D. Ruiz-Molina, J. Veciana. *Chemical Society Reviews* **2007**, 36, 770-818.
- [2] J. Hong-Cai, S. Kitagawa. *Chemical Society Reviews* **2014**, 43, 5415-5418.
- [3] O. M. Yaghi, M. O'Keeffe, N. W. Ockwig, H. K. Chae, M. Eddaoudi, J. Kim. *Nature* **2003**, 423, 705.
- [4] N. L. Rosi, J. Kim, M. Eddaoudi, B. L. Chen, M. O'Keeffe, O. M. Yaghi. *Journal of the American Chemical Society* **2005**, 127, 1504.
- [5] M. O'Keeffe, M. Eddaoudi, H. L. Li, T. Reineke, O. M. Yaghi. *Journal of Solid-State Chemistry* **2000**, 152, 3.
- [6] S. Noro, R. Kitaura, M. Kondo, S. Kitagawa, T. Ishii, H. Matsuzaka, M. Yamashita. *Journal of the American Chemical Society* **2002**, 124, 2568.
- [7] M. Dinca, A. F. Yu, J. R. Long. *Journal of the American Chemical Society* **2006**, 128, 8904.
- [8] B. L. Chen, N. W. Ockwig, A. R. Millward, D. S. Contreras, O. M. Yaghi. *Angewandte Chemie-International Edition* **2005**, 44, 30, 4745-4749.
- [9] G. Ferey. *Chemical Society Reviews* **2008**, 37, 191.
- [10] G. Ferey, M. Haouas, T. Loiseau, F. Taulelle. *Chemical Materials* **2014**, 26, 299-309.
- [11] L. Cronin, P. Kögerler, A. Müller. *Journal of Solid-State Chemistry* **2000**, 152, 57-67.
- [12] C. P. Raptopoulou. *Materials* **2021**, 14, 2, 310.
- [13] Z. Hong-Cai, J. R. Long, O. M. Yaghi. *Chemical Reviews* **2012**, 112, 2, 673-674.
- [14] G. Ferey. *Chemical Materials* **2001**, 13, 3084.
- [15] M. Eddaoudi, D. B. Moler, B. Chen, T. M. Reineke, M. O'Keeffe, O. M. Yaghi. *Accounts of Chemical Research* **2001**, 34, 319.

- [16] J. R. Long, O. M. Yaghi. *Chemical Society Reviews* **2009**, 38, 1213.
- [17] C. Baerloche, W. M. Meier, D. H. Olson. *Atlas of Zeolite Framework Types* **2001**.
- [18] D. Rodriguez-San-Miguel, C. Montoro, F. Zamora. *Chemical Society Reviews* **2020**, 49, 2291-2302.
- [19] A. T. Colak, G. Pamuk, O. Z. Yesilel, F. Yuksel. *Solid State Science* **2011**, 13, 2100.
- [20] F. A. Almeida, J. Kilnowski. *Journal of Solid-State Chemistry* **2004**, 177, 3423.
- [21] G. Férey, C. Mellot, C. Serre, F. Millange, J. Dutour, S. Surble, I. A. Margiolaki. *Science* **2005**, 309, 2040.
- [22] K. K. Gangu, S. Maddila, S. B. Mukkamala, S. B. Jonnalagadda. *Inorganic Chimica Acta* **2016**, 446, 61-74.
- [23] D. Sud, G. Kaur. *Polyhedron* **2021**, 193, 114897.
- [24] O. M. Yaghi, H. Li. *Journal of the American Society Chemistry* **1995**, 117, 10401-10402.
- [25] D. M. P. Mingos. *Chemical Society Reviews* **1991**, 20, 1.
- [26] C. O. Cappa. *Chemical Society Reviews* **2008**, 37, 1127.
- [27] A. Garcia Marquez, A. Demessence, A. E. Platero-Prats, D. Heurtaux, P. Horcajada, C. Serre, J.-S. Chang, G. Férey, V. A. de la Peña-O'Shea, C. Boissière, D. Grosso, C. Sanchez. *European Journal of Inorganic Chemistry* **2012**, 32, 5165-5174.
- [28] P. Horcajada, T. Chalati, C. Serre, B. Gillet, C. Sebrie, T. Baati, J. F. Eubank, D. Heurtaux, P. Clayette, C. Kreuz, J. S. Chang, Y. K. Hwang, V. Marsaud, P. N. Bories, L. Cynober, S. Gil, G. Férey, P. Couvreur, R. Gref. *Nature Materials* **2010**, 9, 172.
- [29] S. H. Jhung, J. H. Lee, J. W. Yoon, C. Serre, G. Férey, J. S. Chang. *Advanced Materials* **2007**, 19, 121.
- [30] S. C. Jung, J. S. Won, K. Jahoen, S. A. Wha. *Journal of the Korean Physical Society* **2008**, 116, 727.

- [31] P. Wasserscheid, T. Welton. *Wiley-VCH* **2003**.
- [32] K. Akhabari, M. Ali, R. Pascal. *Ultrasonics Sonochemistry* **2013**, *20*, 1428.
- [33] M. Martos, J. Morales, L. Sanchez, R. Ayouchi, D. Leinen, F. Martin, J. R. Ramos Barrado. *Electrochemistry Acta* **2001**, *46*, 2939.
- [34] C. Vaitsis, G. Sourkouni, C. Argirusis. *Ultrasonics Sonochemistry* **2019**, *52*, 106-119.
- [35] D. W. Jung, D. A. Yang, J. Kim, W. S. Ahn. *Dalton Transactions* **2010**, *39*, 2883.
- [36] W. J. Son, J. Kim, W. S. Ahn. *Chemical Communication* **2008**, 6336-6338.
- [37] U. Mueller, H. Puetter, M. Hesse, H. Wessel. *Journal of Materials* **2006**, *7*.
- [38] U. Mueller, M. Schubert, F. Teich, H. Puetter, K. Schierle, J. Pastre. *Journal of Material Chemistry* **2006**, *16*, 626.
- [39] R. A. Sheldon. *Green Chemistry* **2005**, *7*, 267.
- [40] A. L. Garay, A. Pichon, S. L. James. *Chemical Society Reviews* **2007**, *36*, 846.
- [41] J. F. F. Bertran. *Chemistry of pure applications* **1999**, *71*, 581.
- [42] C. P. Raptopoulou. *Materials* **2021**, *14*,2, 310.
- [43] P. A. Julien, C. Mottillo, T. Friščic. *Green Chemistry* **2017**, *19*, 2729-2747.
- [44] H. Reinsch, S. Waitschat, S. M. Chavan, K. P. Lillerud, N. Stock, A. Facile. *European Journal of Inorganic Chemistry* **2016**, 4490-4498.
- [45] S. Wang, C. Serre. *ACS Sustainable Chemistry & Engineering* **2019**, *7*, 11911-11927.
- [46] P. Rocío-Bautista, I. Taima-Mancera, J. Pasan, V. Pino. *Separations* **2019**, *6*, 33, 33.
- [47] C. Belyakov-Berzina. *Crystals* **2020**, *10*, 37.
- [48] A. J. Howarth, Y. Liu, P. Li, Z. Li, T. C. Wang, J. T. Hupp, O. K. Farha. *Natures Reviews Materials* **2016**, *1*, 15018.
- [49] D. Yang. *ACS Catalysis* **2019**, *9*, 1779-1798.

- [50] A. Bagno, G. Scorrano. *Journal of the American Chemical Society* **1988**, 119, 4577-4582.
- [51] M. J. Raymond, C. S. Slater, M. J. Salveski. *Green Chemistry* **2010**, 12, 1826-1834.
- [52] A. Babayigit, A. Ethirajan, M. Muller, B. Conings. *Nature Materials* **2016**, 15, 247-251.
- [53] Y. Tao, G. Huang, H. Li, M. R. Hill. *ACS Sustainable Chemistry & Engineering* **2019**, 7, 16, 13627-13632.
- [54] M. Tobiszewski, J. Namiesnik, F. Pena-Pereira. *Green Chemistry* **2017**, 19, 1034-1042.
- [55] M. A. Rasool, I. F. J. Vankelecom. *Green Chemistry* **2019**, 21, 1054-1064.
- [56] E. V. Ramos-Fernandez, A. Grau-Atienza, D. Farrusseng, S. Aguardo. *Journal of Materials Chemistry A* **2018**, 6, 5598-5602.
- [57] H. Chevreau, A. Permyakova, F. Nouar, P. Fabry, C. Livage, F. Ragon, A. Garcia-Marquez, T. Devic, N. Steunou, C. Serre, P. Horcajada. *CrystEngComm* **2016**, 18, 4094-4101.
- [58] M. Sanchez, N. Getachew, K. Diaz, M. Diaz-Garcia, Y. Chebule, I. Diaz. *Green Chemistry* **2015**, 17, 1500-1509.
- [59] X. Qian, F. Sun, J. Sun, H. Wu, F. Xiao, X. Wu, G. Zhu. *Nanoscale* **2017**, 9, 2003-2008.
- [60] S. Waitschat, H. Reinsch, N. Stock. *Chemical Communications* **2016**, 52, 12698-12701.
- [61] V. Benoit, R. S. Pillai, A. Orsi, P. Normand, H. Jobic, F. Nouar, P. Billefont, E. Bloch, S. Burrelly, T. Devic, P. A. Wright, G. De Weireld, C. Serre, G. Maurin, P. L. Llewellyn. *Journal of Materials Chemistry A* **2016**, 4, 1383-1389.
- [62] H. Y. Guan, R. J. LeBlanc, S. Y. Xie, Y. Yue. *Coordination Chemistry Reviews* **2018**, 369, 76-90.

- [63] S. Abou-Shehada, J. H. Clark, G. Paggiola, J. Sherwood. *Organic Process Research & Development* **2016**, *99*, 88-96.
- [64] A. Capuzza, M. Maffei, A. Occhipinti. *Molecules* **2013**, *18*, 7194-7238.
- [65] B. Li, W. Guo, W. Song, E. D. Ramsey. *Journal of Chemical & Engineering Data* **2016**, *61*, 2128-2134.
- [66] M. F. Dapaah, B. Liu. *Journal of Inorganic and Organometallic Polymers and Materials* **2019**, *30*, 581-595.
- [67] K. Matsuyama, M. Motomura, T. Kato, T. Okuyama, H. Muto. *Microporous Mesoporous Materials* **2016**, *225*, 26-32.
- [68] A. Lopez-Periago, O. Vallcorba, C. Frontera, C. Domingo, J. A. Ayllon. *Dalton Transactions* **2015**, *44*, 7548-7553.
- [69] N. Portoles-Gil, S. Gowing, O. Vallcorba, C. Domingo, A. M. Lopez-Periago, J. A. Ayllon. *Journal of CO₂ Utilization* **2018**, *24*, 444-453.
- [70] M. Dasic, I. Stankovic, K. Gkagkas. *Physical Chemistry Chemical Physics* **2019**, *21*, 4375-4386.
- [71] A. Figoli, T. Marino, S. Simone, E. Di Nicolò, X. M. Li, T. He, S. Tornaghi, E. Drioli. *Green Chemistry* **2014**, *16*, 4034-4059.
- [72] T. Erdmenger, C. Guerrero-Sanchez, J. Vitz, R. Hoogenboom, U. S. Schubert. *Chemical Society Reviews* **2010**, *39*, 3317-3333.
- [73] E. A. Turner, C. C. Pye, R. D. Singer. *Journal of Physical Chemistry A* **2003**, *107*, 2277-2288.
- [74] R. S. Varma, V. V. Namboodiri. *Chemical Communications* **2001**, 643-644
- [75] A. Lopez-Periago, P. Lopez-Dominguez, J. Perez Barrio, G. Tobias, C. Domingo. *Microporous Mesoporous Materials* **2016**, *234*, 155-161.
- [76] J. Liu, Y. Li, Z. Lou. *Sustainability* **2022**, *14*, 10, 5768.
- [77] M. Bharathi, S. Indira, G. Vinoth, K. Shanmuga Bharathi. *Journal of Porous Materials* **2019**, *26*, 1377-1390.

- [78] J. Zhu, P. C. Wang, M. Lu. *Catalysis Science & Technology* **2015**, 5, 3383-3393.
- [79] K. Kaneda, T. Mizugaki. *Green Chemistry* **2019**, 21, 1361-1389.
- [80] F. P. Byrne, S. Jin, G. Paggiola, T. H. M. Petchey, J. H. Clark, T. J. Farmer, A. J. Hunt, C. R. McElroy, J. Sherwood. *Sustainable Chemical Processes* **2016**, 4, 7.
- [81] S. Kumar, S. Jain, M. Nehra, N. Dilbaghi, G. Marrazza, K. Ki. *Coordination Chemistry Reviews* **2020**, 420, 213407.
- [82] H. Reinsch, B. Bueken, F. Vermoortele, I. Stassen, A. Lieb, K. P. Lillerud, D. De Vos. *CrystEngComm* **2015**, 17, 4070-4074.
- [83] H. Reinsch. *European Journal of Inorganic Chemistry* **2016**, 4290-4299.
- [84] M. Sanchez, N. Getachew, K. Díaz, M. Díaz -García, Y. Chebude, I. Díaz. *Green Chemistry* **2015**, 17, 1500-1509.
- [85] S. L. Anderson, K. C. Stylianou. *Coordination Chemistry Reviews* **2017**, 349, 102-128.
- [86] M. Zhang, Z. Y. Gu, M. Bosch, Z. Perry, H. C. Zhou. *Coordination Chemistry Review* **2015**, 293-294, 327-356.
- [87] J. An, S. J. Geib, N. L. Rosi. *Journal of American Chemical Society* **2010**, 132, 38-39.
- [88] J. An, S. J. Geib, M. G. Kim, S. Y. Choi, W. T. Lim. *Journal of Porous Materials* **2015**, 22, 867-875.
- [89] H. An, M. Li, J. Gao, Z. Zhang, S. Ma, Y. Chen. *Coordination Chemistry Reviews* **2019**, 384, 90-106.
- [90] N. Yan, X. Chen. *Nature* **2015**, 524, 155-157.
- [91] Q. Wang, M. Fu, X. Li, R. Huang, R. E. Glaser, L. Zhao. *Journal of Computational Chemistry* **2019**, 40, 1599-1608.
- [92] F. D. Pileidis, M. M. Titirici. *ChemSusChem* **2016**, 9, 562-582.
- [93] S. T. Morthensen, B. Zeuner, A. S. Meyer, H. Jorgensen, M. Pinelo. *Separation and Purification Technology* **2018**, 194, 73-80.

- [94] Y. Wang, W. Cao, J. Luo, B. Qi, Y. Ean. *Bioresource Technology* **2019**, 272, 398-406.
- [95] N. Huang, P. Wang, D. Jiang. *Nature Reviews Materials* **2016**, 1, 10.
- [96] B. J. Smith, L. Parent, A. C. Overholts, P. A. Beaucage, R. P. Bisbey, A. D. Chavez, N. Hwang, C. Park, A. M. Evans, N. C. Gianneschi, W. R. Dichtel. *ACS Central Science* **2017**, 3, 1, 58-65.
- [97] Y. Sakata, S. Furukawa, M. Kondo, K. Hirai, N. Horike, Y. Takashima, H. Uehara, N. Lovanio, M. Meilikhov, T. Tsuruoka, S. Isoda, W. Kosaka, O. Sakata, S. Kitagawa. *Science* **2013**, 339, 6116, 193-196.
- [98] M. Sindoro, N. Tanai, J. Ah-Young, S. Granick. *Accounts of Chemical Research* **2014**, 47, 2, 459-469.
- [99] C. R. DeBlase, W. R. Dichtel. *Macromolecules* **2016**, 49, 15, 5297-5305.
- [100] C. Franco, D. Rodriguez-San-Miguel, A. Sorrenti, S. Sevim, R. Pons, A. E. Platero-Prats, M. Pavlovic, I. Szilagyi, M. L. Ruiz Gonzalez, J. M. Gonzalez-Calbet, D. Bochicchio, L. Pesce, G. M. Pavan, M. Cano-Sarabia, D. MasPOCH, S. Pané, A. J. De Mello, F. Zamora, J. Puigmartí-Luis. *Journal of the American Chemical Society* **2020**, 142, 7, 3540-3547.
- [101] D. Rodriguez-San-Miguel, A. Yazdi, V. Guillermin, J. Perez-Carvajal, V. Puentes, D. MasPOCH, F. Zamora. *Chemistry-A European Journal* **2017**, 23, 36, 8623-8627.
- [102] P. Horcajada, S. Surble, C. Serre, D.-Y. Hong, Y.-K. Seo, J.-S. Chang, J.-M. Greneche, I. Margionalki, G. Férey. *Chemical Communications* **2007**, 27, 2820-2822.
- [103] G. Llauradó-Capdevila, A. Veciana, M. A. Guarducci, A. Mayoral, R. Pons, L. Hertle, H. Ye, M. Mao, S. Sevim, D. Rodríguez-San-Miguel, A. Sorrenti, B. Jang, Z. Wang, X.-Z. Chen, B. J. Nelson, R. Matheu, C. Franco, S. Pané and J. Puigmartí-Luis. *Advanced Materials* **2023**, 2306345.

- [104] M. Hadiseh, S. Tayebbeh, M. Ali, S. Ghasem. *Journal of Materials Science: Materials in Electronics* **2021**, *32*, 22840-22859.
- [105] Z. XiaoJing, F. XiaoLiang, W. BingHui, Z. LanSun, Z. NanFeng. *Science China Chemistry* **2013**, *57*, 141-146.
- [106] R. Freund, O. Zaremba, G. Arnauts, R. Ameloot, G. Skorupski, M. Dinca, A. Bavykina, J. Gascon, A. Ejsmont, J. Goscianska, M. Kalmutzki, U. Lachelt, E. Ploetz, C. S. Dierks, S. Wuttke. *Angewandte International Edition Chemie* **2021**, *60*, 45, 23975-24001.
- [107] H. Li, K. Wang, Y. Sun, C. T. Lollar, J. Li, H. C. Zhou. *Materials Today* **2018**, *21*, 108-121.
- [108] H. Furukawa, K. E. Cordova, M. O'Keeffe, O. M. Yaghi. *Science* **2013**, *341*, 1230444.
- [109] H. Li, M. Eddaoudi, M. O'Keeffe, O. M. Yaghi. *Nature* **1999**, *402*, 276-279.
- [110] T. De Villenoisy, Z. Xioran, V. Wong, S. Mofarah, H. Arandiyani, Y. Yamauchi, P. Koshy, C. Sorrell. *Advanced Materials* **2023**, *35*, 24, 2210166.
- [111] U. K. Demir, A. Goldman, L. Esrafil, M. Gharib, A. Morali, O. Weingart, C. Janiak. *Chemical Society Reviews* **2020**, *49*, 2751-2798.
- [112] H. Li, L. Li, R. B. Link, W. Zhou, Z. Zhang, S. Xiang, B. Chen. *Energy Chemistry* **2019**, *1*, 100006.
- [113] Y. He, F. Chen, B. Li, G. Qian, W. Zhou, B. Chen. *Coordination Chemistry Reviews* **2018**, *373*, 167-198.
- [114] J. A. Mason, M. Veenstra, J. R. Long. *Chemical Science* **2014**, *5*, 32-51.
- [115] A. R. Millward, O. M. Yaghi. *Journal of the American Chemical Society* **2005**, *127*, 17998-17999.
- [116] A. O. Yazaydin, R. Q. Snurr, T. H. Park, K. Koh, J. Liu, M. D. LeVan, A. I. Benin, P. Jakubczak, M. Lanuza, D. B. Galloway, J. J. Low, R. R. Willis. *Journal of the American Chemical Society* **2009**, *131*, 18198-18199.

- [117] J. Antonio Zàrate, E. Sàncnez-Gonzalez, T. Jurado-Vazquez, A. Gutierrez-Alejandre, E. Gonzalez-Zamora, I. Castillo, G. Maurin, I. A. Ibarra. *Chemical Communications* **2019**, 55, 3049-3052.
- [118] J. Li, X. Han, X. Zhang, A. M. Sheveleva, Y. Cheng, F. Tuna, E. J. L. McInnes, L. J. McCormick, S. J. McPherson, S. J. Teat, L. L. Daemen, A. J. Ramirez-Cuesta, M. Schroder, S. Yang. *Nature Chemistry* **2019**, 11, 1085-1090.
- [119] Y. Khabzina, J. Dhainaut, M. Ahlhelm, H. J. Richter, H. Reinsch, N. Stock, D. Farrusseng. *Industrial & Engineering Chemistry Research* **2018**, 57, 8200-8208.
- [120] L. Alaerts, E. Seguin, H. Poelman, F. Thibault-Starzyk, P. A. Jacobs, D. E. De Vos. *Journal of European Chemistry* **2006**, 12, 7353 - 7363.
- [121] A. M. Rasero-Almansa, M. Iglesias, F. Sanchez. *RSC Advances* **2016**, 6, 106790-106797.
- [122] M. Gimenez-Marques, A. Santiago-Portillo, S. Navalon, M. Alvaro, V. Briois, F. Nouar, H. Garcia, C. Serre. *Journal of Materials Chemistry A* **2019**, 7, 20285-20292.
- [123] A. Bavykina, N. Kolobov, I. S. Khan, J. A. Bau, A. Ramirez, J. Gascon. *Chemical Reviews* **2020**, 120, 8468-8535.
- [124] P. Horcajada, C. Serre, M. Vallet-Regi, M. Sebban, F. Taulelle, G. Ferey. *Angewandte International Edition Chemie* **2006**, 45, 5974-5978.
- [125] P. Horcajada, T. Chalati, C. Serre, B. Gillet, C. Sebrie, T. Baati, J. F. Eubank, D. Heurtaux, P. Clayette, C. Kreuz, J. S. Chang, Y. K. Hwang, V. Marsaud, P. N. Bories, L. Cynober, S. Gil, G. Ferey, P. Couvreur, R. Gref. *Nature Materials* **2010**, 9, 172-178.
- [126] R. Zhao, Z. Liang, R. Zou, Q. Xu. *Joule* **2018**, 2, 2235-2259.
- [127] A. E. Baumann, D. A. Burns, B. Liu, V. S. Thoi. *Communications Chemistry* **2019**, 2, 86.
- [128] H. Wang, Q. L. Zhu, R. Zou, Q. Xu. *Chem* **2017**, 2, 52-80.

- [129] R. W. Day, D. K. Bediako, M. Rezaee, L. R. Parent, G. Skorupskii, M. Q. Arguilla, C. H. Hendon, I. Stassen, N. C. Gianneschi, P. Kim, M. Dinca. *ACS Central Science* **2019**, *5*, 1959-1964.
- [130] M. Hmadeh, Z. Lu, Z. Liu, F. Gandara, H. Furukawa, E. Wan, V. Augustin, L. Liao, F. Zhou, E. Perre, V. Ozolin, K. Suenaga, D. Xiangfeng, B. Dunn, Y. Yamamoto, O. Terasaki, O. M. Yaghi. *Chemistry of Materials* **2012**, *24*, *18*, 3511-3513.
- [131] L. Guo, J. Sun, W. Zhang, L. Hou, L. Liang, Y. Liu, C. Yuan. *ChemSusChem* **2019**, *12*, *22*, 5051-5058.
- [132] W. H. Li, T. Han-Rui, S. Yao, B. Nath, W. H. Deng, W. Yaobin, L. Xu. *Advanced Functional Materials* **2017**, *27*, *27*, 1702067.
- [133] Z. Cui, Q. Liu, C. Xu, R. Zou, J. Zhang, W. Zhang, G. Guan, J. Hu, Y. Sun. *Journal of Materials Chemistry A* **2017**, *5*, 21699.
- [134] F. Zheng, S. Xu, Z. Yin, Y. Zhang, L. Lu. *RSC Advances* **2016**, *6*, 93532-93538.
- [135] B. Sambandam, V. Soundharrajan, J. Song, S. Kim, J. Jo, D. P. Tung, S. Kim, V. Mathew, J. Kim. *Inorganic Chemistry Frontiers* **2016**, *3*, 1609.
- [136] M. Zahir Iqbal, U. Aziz, S. Siddique, S. Aftab, S. M. Wabaidur. *Materials Science in Semiconductor Processing* **2023**, *162*, 107511.
- [137] C. Honghong, J. Li, T. Meng, D. Shu. *Nano-Micro Small* **2024**, *20*, *20*, 2308804.
- [138] M. Hmadeh, Z. Lu, Z. Liu, F. Gandara, H. Furukawa, S. Wan, V. Augustyn, R. Chang, L. Liao, F. Zhou, E. Perre, V. Ozolins, K. Suenaga, X. Duan, B. Dunn, Y. Yamamoto, O. Terasaki, O. M. Yaghi. *Chemistry of Materials* **2012**, *24*, *18*, 3511-3513.
- [139] B. Chen, X. Yang, X. Zeng, Z. Huang, J. Xiao, J. Wang, G. Zhan. *Chemical Engineering Journal* **2020**, *397*, 125424.
- [140] B.H. Toby, R. B. Von Dreele. *Journal of Application Crystallography* **2013**, *46*, 544.

- [141] G.S. Pawley. *Journal of Application Crystallography* **1981**, *14*, 357.
- [142] X. Zhang, A. Yuan, X. Mao, Q. Chen, Y. Huang. *Sensors and Actuators B: Chemical* **2019**, *299*, 126928.
- [143] B. Chen, X. Yang, X. Zeng, Z. Huang, J. Xiao, J. Wang, G. Zhan. *Chemical Engineering Journal* **2020**, *397*, 125424.
- [144] K. Song, K. Guo, S. Mao, D. Ma, Y. Lv, C. He, H. Wang, Y. Cheng, J-W Shi. *ACS Catalysis* **2023**, *13*, 7, 5020-5032.
- [145] A. Fateeva, J. Clarisse, G. Pilet, J-M. Grenèche, F. Nouar, B. K. Abeykoon, F. Guegan, C. Goutaudier, D. Luneau, J. E. Warren, M. J. Rosseinsky, T. Devic. *Crystal Growth & Design* **2015**, *15*, 4, 1819-1826.
- [146] D. Yu, M. Wu, Q. Hu, L. Wang, C. Leopoli, L. Zhang. *Journal of Hazardous Materials* **2019**, *367*, 456-464.
- [147] N. V. Maksimchuk, K. A. Kovalenko, V. P. Fedin, O. A. Kholdeeva. *Chemical Communications* **2012**, *48*, 54, 6812-6814.
- [148] J.-W. Li, C.-C. Cheng. *Chinese Journal of Structural Chemistry* **2018**, *37*, 10, 1635-1644.
- [149] H. Xu, P. A. Zhao-Rui. *Chinese Journal of Structural Chemistry* **2019**, *38*, 12, 2121-2128.
- [150] T. A. Makal, J.R. Li, W. Lu, H.C. Zhou. *Chemical Society Reviews* **2012**, *41*, 23, 7761-7779.
- [151] Z. Shuo, Z. Yuan, B. Fayaz, L. Tian-Fu. *Crystal Growth & Design* **2021**, *21*, 5, 3100-3122.
- [152] C. Janiak, J. K. Vieth. *New Journal of Chemistry* **2010**, *34*, 2366-2388.
- [153] P. Horcajada, C. Serre, M. Vallet-Regi, M. Sebban, F. Taulelle, G. Férey. *Angewandte Chemie International Edition* **2006**, *45*, 36, 5974-5978.
- [154] C. Janiak, J. K. Vieth. *New Journal of Chemistry* **2010**, *34*, 11, 2366-2388.

- [155] J. Shi, S. Hei, H. Liu, Y. Fu, F. Zhang, Y. Zhong, W. J. Zhu. *Journal of Chemistry* **2013**, 2013.
- [156] S. Thomas, R. Thomas, A. K. Zachariah, R. Kumar. *Elsevier* **2017**, 3.
- [157] K. Matsuyama, N. Hayashi, M. Yokomizo, T. Kato, K. Ohara, T. Okuyama. *Journal of Materials Chemistry B* **2014**, 2, 43, 7551-7558.
- [158] J. Yu, X. Weiping, L. Xin, Y. Zhaohui, Z. Jiao, J. Meiyong, X. Rui, Z. Yanru. *Microporous and Mesoporous Materials* **2019**, 290, 109642.
- [159] Y. Esra, S. Emine, A. Ferhan Sami. *Journal of the Taiwan Institute of Chemical Engineers* **2016**, 65, 323-330.
- [160] Y. Fang, Z. Yang, H. Li, X. Liu. *Environmental Science and Pollution Research* **2020**, 27, 4703-4724.
- [161] S. Huang, K-L. Yang, X. Fang, H. Pan, H. Zhang, S. Yang. *Royal Society of Chemistry* **2017**, 7, 5621-5627.
- [162] Y. Jin, X. Mi, J. Qian, N. Ma, W. Dai. *ACS Applied Materials & Interfaces* **2022**, 14, 42, 48285-48295.
- [163] S. Tomar, V. K. Singh. *Materials Today: Proceedings* **2021**, 43, 5, 3291-3296.
- [164] K. Ariga, A. Vinu, Y. Yamauchi, Q. Ji, J. P. Hill. *Bulletin of the Chemical Society of Japan* **2012**, 85, 1, 1-32.
- [165] J. Gordon, H. Kazemian, S. Rohani. *Materials Science and Engineering: C* **2015**, 47, 172-179.
- [166] A. Li, X. Yang, J. Chen. *Royal Society of Chemistry* **2021**, 11, 10540-10547.
- [167] H. P. N. Thi, H. D. Ninh, C. V. Tran, B. T. Le, S. V. Bhosale, D. D. La. *Chemistry Select* **2019**, 4, 8, 2333-2338.
- [168] X. Leng, X. Dong, W. Wang, N. Sai, C. Yang, L. You, H. Huang, X. Yin, J. Ni. *Molecules* **2018**, 23, 10, 2490.
- [169] T. Araya, M. Jia, I. Yang, P. Zhao, K. Cai, W. Ma, Y. Huang. *Applied Catalysis B: Environmental* **2017**, 203, 768-777.

- [170] Y. Zhang, G. Li, H. Lu, Q. Lv, Z. Sun. *Royal Society of Chemistry* **2014**, 4, 7594-7600.
- [171] J. Tang, J. Wang. *Chemosphere* **2019**, 241, 125002.
- [172] Z. Jiao, Z. Miao, H. Un, Q. Li, X. Meng. *Environmental Technology & Innovation* **2022**, 28, 102847.
- [173] H. Li, T. Wang, Y. Wang, F. Liu, Y. Li, Y. Wang, M. Guo, G. Li, X. Ma. *Fuel* **2023**, 334, 1, 15.
- [174] T. Steenhaut, S. Hermans, Y. Filinchuk. *New Journal of Chemistry* **2020**, 44, 3847.
- [175] G. Prince, C. Chaudhari, C. Pradip. *Journal of Materials Science* **2018**, 53, 11694-11714.
- [176] S. Soury, A. Firoozichahak, D. Nematollahi, S. Alizadeh, H. kakaei, A. Abbasi. *Microchemical Journal* **2021**, 171, 106866.
- [177] M. Forghani, A. Azizi, M. J. Livani, L. A. Kafshagari. *Journal of Solid State Chemistry* **2020**, 291, 121636.
- [178] L. Weifeng, T. Zhang, L. Lv, C. Yanxiao, T. di Weinxiang, S. Tang. *Colloids and Surface A: Psycochemical and Engineering Aspects* **2021**, 624, 126791.
- [179] E. Bellido, T. Hidalgo, M. V. lozano, M. Guillevic, R. Simon-Vazquez, M. J. Santander-Ortega, A. Gonzalez-Fernandez, C. Serre, M. J. Alonso, P. Horcajada. *Advanced Healthcare Materials* **2015**, 4, 8, 1246-1257.

General conclusions and perspectives

In conclusion, different materials with progressively more complex structures and with variable applications have been discussed. The simplest system involves the creation of a new chiral stationary phase, for which two Pirkle-type selectors have been designed. In fact, two molecules have been synthesized that could mimic the same interactions of the currently marketed Whelk-O1 structure. The obtained chiral molecules were anchored on silica and an accurate physicochemical characterization was completed to evaluate the loading of selector and the thermostability. Chromatographic columns were then packed and tested in the separation of various enantiomeric mixtures. $^1\text{H-NMR}$ and molecular docking investigations were performed to further validate the recognition capabilities of the developed selectors and to evaluate the interactions with the selectands. In particular, the $^1\text{H-NMR}$ study on the equimolar mixture consisting of one enantiopure selector and ibuprofen racemic mixture revealed the formation of two transient diastereoisomeric complexes. Subsequently, in order to study the specific selector/selectand interactions, the molecular docking studies were made on the selector/selectand pair that showed the best experimentally obtained resolution. The results of docking agreed with experimental observations (e.g., the elution order). From a material science perspective, this study focuses on the surface modification of solid materials. Specifically, in the chromatographic field, we examine how controlling surface chemistry (using pre-designed selector) can be effectively achieved, even with pre-designed structural selector/selectand models. The future goal is to improve the structure of these chiral selectors to increase the chromatographic performance. This will be possible thanks to the combination of different techniques that will allow us to understand the recognition capabilities, such as NMR, and/or molecular docking studies.

In the second part, a novel covalent organic polymer (COP) was developed and synthesized. Chemical and morphologically analysis revealed that the synthesized systems are non-porous, amorphous, exhibit thermal stability, a possess a polymeric structure and, most importantly, show a strong affinity for copper adsorbed on their surface. The lack of porosity and amorphous nature of the material are likely due to the rapid kinetics of bond formation, which prevent the development of an ordered material with a crystalline structure. Due to its insolubility in common organic solvents, the application of this polymer in the context of heterogeneous organo-metallic catalysis has been an advantage. Consequently, it has been applied to prepare a small library of triazole derivatives through CuAAC “click” reaction. As added value, looking to a progressive reduction of use of organic solvent, in the final step of preparation of copper-coordinated support and in the developed protocol for the synthesize triazoles aqueous solvents were used. Furthermore, the purification of the reaction product occurs through a crystallization process, avoiding the use of silica-based chromatographic columns, which are expensive and time consuming. Novel COP synthetic strategies, in presence also of modulator agents, are under investigation with the aim to control the kinetics of the reaction and to favour the production of an ordered crystalline structure.

Finally, a protocol for the synthesis of micelles, as documented in the literature, has been optimized to synthesize MOF crystals with nanoscale dimensions. This approach offers several advantages, such as using aqueous solvents with anionic and cationic surfactants that aggregate to form micelles, which create a confined space where MOFs grows as nanoscale particles. With conventional systems, the fine-tuning of nanoscale MOF crystals is not straightforward. Moreover, the reaction proceeds under mild conditions (room temperature and atmospheric pressure), promoting a more sustainable green chemistry process. In brief, we

synthesized nanoscale-MOFs such as Cu-CAT-1, Mn-BTC, MIL-100 (Fe) and MIL-53 (Fe). In addition to the last MIL MOFs, we also produced corresponding bimetallic versions by doping them with magnesium, which was specifically chosen for its biocompatibility. Chemical and morphological characterization has been conducted, and the results have been compared with literature reports. This comparison demonstrates that, despite differences in the synthesis of these systems, the properties of crystallinity, porosity and large surface area are maintained. Using the micellar approach, nanoparticles with diameters of 100 nm or less were obtained, whereas traditional solvothermal methods produced nanorods several microns in length. Cu-CAT-1 and Mn-BTC are well-documented in the literature for their electrochemical properties in micron-sized crystal form. Currently, we are evaluating how the morphological and nanoscale dimensions of the particles produced using our micellar approach influence their electrochemical properties. We plan to use these nanoscale MOFs supercapacitors applications, with Cu-CAT-1 serving as the negative electrode and Mn-BTC as the positive electrode. On the other hand, MIL-100 (Fe) and MIL-53 (Fe) nanoparticles will be investigated as drug delivery carriers. Alongside their bimetallic versions, these nanoparticles are currently being studied to evaluate their potential biotoxicity and cellular biocompatibility as well as cellular uptake.

Future efforts should not only aim to complete each project according to its objectives but also to create new materials that combine the desirable qualities of individual systems, such as chirality, crystallinity, porosity, and large surface area. This would involve employing synthetic approaches aligned with eco-friendly chemistry. Controlling the synthesis of materials with defined properties and functions is extremely challenging due to the numerous uncontrollable variables involved, as demonstrated throughout this thesis. However, creating

ordered structures, such as crystals, can help achieve this goal. Therefore, a future objective could be the generation of porous crystalline materials with specific sizes and shapes to attain desired properties and functions.

In conclusion, this work represents a significant step forward in exploring complex materials. Each project builds on existing knowledge while opening new avenues for improvement. Although challenges remain, particularly in controlling the structure and behaviour of materials like COPs and MOFs, the progress made so far provides a solid foundation for future developments.

**List of publications and contributions
to conferences**

1. Core Research

Part of the work described in this thesis was also previously published in the following articles:

1. **M. A. Guarducci**, S. Manetto, M. Pierini, G. Mazzocanti, C. Villani. Design, Synthesis, and Applications of Bis-Amido HPLC Pirkle-Type Chiral Stationary Phases. *Chirality* **2024**, 36, 9.
2. G. Llauradó-Capdevila, A. Veciana, **M. A. Guarducci**, A. Mayoral, R. Pons, L. Hertle, H. Ye, M. Mao, S. Sevim, D. Rodríguez-San-Miguel, A. Sorrenti, B. Jang, Z. Wang, X.-Z. Chen, B. J. Nelson, R. Matheu, C. Franco, S. Pané, J. Puigmartí-Luis. Tailored Design of a Water-Based Nanoreactor Technology for Producing Processable Sub-40 nm 3D COF Nanoparticles at Atmospheric Conditions. *Advanced Materials* **2024**, 36, 14.

2. Other publications

1. **M. A. Guarducci**, A. Fochetti, A. Ciogli, G. Mazzocanti. A Compendium of the Principal Stationary Phases Used in Hydrophilic Interaction Chromatography: Where Have We Arrived?. *Separation* **2022**, 10, 1, 22

3. Conferences and contributions

Oral presentation

1. **Tailored Design of a Water-Based Nanoreactor Technology for Producing Processable Sub-40 nm 3D COF Nanoparticles at Atmospheric Conditions.** (XLVIII "A. Corbella" International Summer School on Organic Synthesis- ISOS 2024 Gargnano (BS), Palazzo Feltrinelli 26th-20th June 2024).

Poster

1. **Synthesis and evaluation of chiral recognition capabilities of a bis-amido Pirkle-Type selector.** (XIX Ischia Advanced School of Organic Chemistry IASOC 2022, Ischia (NA) 23rd -26th September 2022).
2. **Chiral enantiopure molecules bound on silica matrices through coordination mediated by metal cations: their possible application as both enantiopure catalysts in heterogeneous phase and chiral stationary phases in enantioselective chromatography.** (33rd International Symposium on Chirality- CHIRALITY 2023, Rome (RM) 24th-27th July 2024).